TECHNISCHE UNIVERSITÄT MÜNCHEN
Fakultät für Physik
Max-Planck-Institut für Plasmaphysik

Transport of Super-thermal Particles and their Effect on the Stability of Global Modes in Fusion Plasmas

Mirjam Simone Schneller

Vollständiger Abdruck der von der Fakultät für Physik
der Technischen Universität München zur Erlangung des akademischen Grades eines

Doktors der Naturwissenschaften (Dr. rer. nat.)

genehmigten Dissertation.

Vorsitzende:		Univ.-Prof. Dr. K. Krischer
Prüfer der Dissertation:	1.	Hon.-Prof. Dr. S. Günter
	2.	Univ.-Prof. Dr. A. Peeters, Universität Bayreuth

Die Dissertation wurde am 02.05.2013 bei der Technischen Universität München eingereicht und durch die Fakultät für Physik am 18.07.2013 angenommen.

Max-Planck-Institut
für Plasmaphysik
EURATOM Assoziation

Bereich Tokamakphysik

TECHNISCHE
UNIVERSITÄT
MÜNCHEN

Fakultät für Physik

PhD Thesis

Transport of Super-thermal Particles and their Effect on the Stability of Global Modes in Fusion Plasmas

Mirjam Schneller
mirjam.schneller@ipp.mpg.de

Erstbetreuer: Prof. Sibylle Günter
Zweitbetreuer: Dr. Philipp Lauber

Eingereicht am 2. Mai 2013
Verteidigt am 2. August 2013

Abstract

In thermonuclear plasmas, a population of super-thermal particles generated by external heating methods or fusion reactions can lead to the excitation of global instabilities. The transport processes due to nonlinear wave-particle interactions and the consequential particle losses reduce the plasma heating and the efficiency of the fusion reaction rate. Furthermore, these *energetic* or *fast particles* may cause severe damages to the wall of the device.

This thesis addresses the resonance mechanisms between these energetic particles and global MHD and kinetic MHD waves, employing the hybrid code HAGIS. A systematic investigation of energetic particles resonant with multiple modes (*double-resonance*) is presented for the first time. The double-resonant mode coupling is modeled for waves with different frequencies in various overlapping scenarios. It is found that, depending on the radial mode distance, double-resonance is able to significantly enhance, both the growth rates and the saturation amplitudes. Small radial mode distances, however can lead to strong nonlinear mode stabilization of a linear dominant mode.

For the first time, simulations of experimental conditions in the ASDEX Upgrade fusion device are performed for different plasma equilibria (particularly for different q profiles). An understanding of fast particle behavior for non-monotonic q profiles is important for the development of advanced fusion scenarios. The numerical tool is the extended version of the HAGIS code, which computes the particle motion in the vacuum region between vessel wall in addition to the internal plasma volume. For this thesis, a consistent fast particle distribution function was implemented, to represent the fast particle population generated by the particular heating method (ICRH). Furthermore, HAGIS was extended to use more realistic eigenfunctions, calculated by the gyrokinetic eigenvalue solver LIGKA. One important aim of these simulations is to allow fast ion loss measurements to be interpreted with a theoretical basis. Fast particle losses are modeled and directly compared with experimental measurements. The phase space distribution and the mode-correlation signature of the fast particle losses allows them to be characterized as prompt, resonant or diffusive (non-resonant). It is found that a large number of diffuse losses occur in the lower energy range (at around 1/3 of the birth energy) particularly in multiple mode scenarios (with different mode frequencies), due to a domino-like transport process. In inverted q profile equilibria, the combination of radially extended global modes and large particle orbits leads to losses with energies down to 1/10th of the birth energy.

The HAGIS code is a perturbative hybrid code, which models the nonlinear interaction between a distribution of energetic particles and a set of Alfvén eigenmodes. The wave eigenfunctions are assumed to be invariant, but its amplitude and frequency evolve in time, as determined by kinetic wave-particle nonlinearities. To solve the particle equations of motion, the 6D phase space is reduced to a 5D description, using the guiding center approach. The change in the fast particle distribution function is modeled using

a δf-method, to significantly reduce numerical noise and the number of simulation markers. As in ideal MHD, the HAGIS model previously neglected any parallel electric field perturbation $\tilde{E}_{\parallel}$. This approximation is dropped within this work, by implementing a non-vanishing $\tilde{E}_{\parallel}$ term, employing the electric and magnetic perturbation structure given by LIGKA. In this way, a more advanced damping effect is introduced into the HAGIS model, which is not only individual for each poloidal harmonic, but is also characterized by a radial structure. The implementation of this damping is the first step towards a HAGIS-LIGKA hybrid model, which can overcome the limit of fixed radial mode structures.

Kurzfassung

In thermonuklearen Fusionsplasmen existieren energiereiche Teilchen, hervorgerufen durch externe Heizmethoden, sowie durch die Fusionsreaktionen selbst. Diese Population an *schnellen Teilchen* kann globale Plasmainstabilitäten anregen. Nichtlineare Welle-Teilchen-Wechselwirkungen führen dabei zu Transportprozessen der schnellen Teilchen im Plasma mit der Konsequenz von Teilchenverlusten, was eine Reduktion der Plasmaheizung und der Fusionsrate bewirkt. Außerdem besteht die Gefahr, dass es zu Schäden an der Gefäßwand kommt.

Ziel dieser Arbeit ist ein tieferes Verständnis für die Resonanzmechanismen dieser Teilchen mit globalen MHD Wellen und kinetischen Moden. Mit dem hybrid Code HAGIS werden erstmals systematische Studien durchgeführt, welche die Wechselwirkung von Teilchen mit mehreren Wellen verschiedener Frequenz untersuchen. Die resonante Kopplung an zwei verschiedene Wellen (*Doppel-Resonanz*) wird für verschiedene Modenkonstellationen untersucht. Es zeigt sich, dass Doppel-Resonanz zu signifikant höheren Anwachsraten und Sättigungsamplituden führen kann. Der zu Grunde liegende Effekt ist abhängig vom radialen Abstand der Wellen, und kann bei sehr geringem Abstand auch bewirken, dass eine linear dominante Welle nichtlinear stabilisiert wird.

Erstmals werden Simulationen für realistische Plasmabedingungen durchgeführt, welche auf neuen Erkenntnissen am Fusionsexperiment ASDEX Upgrade beruhen. Ein wichtiges Ziel ist es, experimentelle Messungen der Verluste schneller Teilchen theoretisch zu interpretieren. Dabei werden verschiedene Plasmagleichgewichte untersucht, vor allem unter dem Aspekt unterschiedlicher q Profile welche in sogenannten “advanced scenarios” für künftige Fusionsreaktoren von Bedeutung sein können. Nummerische Grundlage ist eine erweiterte HAGIS Version, die nicht auf das Innere des Plasmas beschränkt ist, sondern die Teilchenbewegung bis hin zur Gefäßwand berechnet. Im Rahmen dieser Arbeit wird eine konsistente Verteilungsfunktion für schnelle Teilchen implementiert, wie sie durch die ICRH Heizung entsteht. Außerdem werden realistischere Eigenfunktionen für die Plasmawellen verwendet, berechnet mit Hilfe des Gyrokinetische Eigenwertlösers LIGKA. Die simulierten Teilchenverluste können dann zum ersten Mal direkt mit solchen aus experimentellen Messungen verglichen werden. Eine detaillierten Untersuchung der Phasenraumverteilung und des zeitlichen Signals der numerisch berechneten Verluste erlaubt es, diese zu charakterisieren. Dabei unterscheidet man Verluste, die “prompt” auftreten von solchen, die entweder durch resonante Wechselwirkung mit den Wellen oder auf Grund von Stochastisierungsprozessen (diffusiv) das Plasma verlassen. Dabei zeigt sich, dass vor allem in Szenarien mit mehreren Wellen (mit verschiedener Frequenz) eine große Menge von diffusive Verlusten auftritt, v.a. im niederen Energiebereich von c.a. 1/3 der Entstehungsenergie. Dies wird verursacht von Kaskaden-artigen Transportprozessen, begünstigt durch ein invertiertes q Profil, aus welchem global ausgedehnte Wellen und große Teilchenorbits folgen. Besonders durch die radial ausgedehnten Moden mit mehreren Harmonischen kommt es sogar zu Verlusten bis in den niedrigsten Energiebereich von 1/10 der Entstehungsenergie.

HAGIS ist ein störungstheoretischer Hybrid-Code, der die nichtlineare Wechselwirkung zwischen einer Verteilung von energiereichen Teilchen und Alfvénischen Eigenmoden als Plasmawellen modelliert. Die Eigenfunktion der Welle wird dabei als invariant vorausgesetzt, jedoch entwickeln sich Amplitude sowie Frequenz selbstkonsistent auf Grund der nichtlinearen, kinetischen Welle-Teilchen-Wechselwirkung. Um die Bewegungsgleichung der schnellen Teilchen zu lösen wird der 6-dimensionale Phasenraum mit Hilfe des Guiding-Center-Ansatzes auf 5 Dimensionen reduziert. Die Verwendung der δf-Methode reduziert das numerische Rauschen und die Anzahl der notwendigen Marker, indem nur die *Änderung* der Verteilungsfunktion berechnet wird. Wie in der idealen MHD vernachlässigt das HAGIS Modell jede parallele elektrische Feldstörung $\tilde{E}_{||}$. Im Rahmen dieser Arbeit wird diese Näherung überwunden, indem ein nichtverschwindender $\tilde{E}_{||}$ Term implementiert wird. Unter Verwendung der von LIGKA berechneten elektrischen und magnetischen Störung kann $\tilde{E}_{||}$ berstimmt werden. Damit wird ein komplexerer Dämpfungseffekt in das Modell integriert. Gleichzeitig ist es der erste Schritt auf dem Weg zu einem Hybrid-Modell bestehend aus HAGIS und LIGKA, welches erlaubt, auch die Wellenstruktur während der Simulation zeitlich weiterzuentwickeln.

Contents

CHAPTER 1

Introduction: Nuclear Fusion

1.1 Global Energy Situation

> *"History will judge us on our ability to manage this energy environment, and mitigate the worst effects of climate change. It is the great challenge of our generation."*
>
> José Manuel Durão Barroso[1]

Life on Earth currently faces a threat on a truly global scale: climate change. A scientific consensus is emerging that civilization must reduce its emissions of greenhouse gases by more than half in less than the next five decades if we are to stand a chance of retaining a global climate as stable as that of the past 10 000 years [3].
Maintaining civilization relies on energy supply and since the industrial revolution, humanity's need for energy is growing steadily – to the same degree, technical advancement is achieved.
But in spite of all the progress, the main source of our energy still remains the same as it was centuries ago: the combustion of fossil fuels. Coal, natural gas and, to some extent, uranium became the fuels of choice for electricity generation (fig. 1.1) – in developing or technologically advanced countries alike.
After two centuries of world-wide fossil fuel burning, concentrations of global warming gases such as methane, carbon dioxide, and nitrous oxide have increased markedly and now exceed by far the natural range determined from ice cores spanning many thousands of years before industrialization [4]. Although there have always been oscillations in these values throughout geological timescales[2], analysis of climate models together with constraints from observations (see fig. 1.3) have made a scientific consensus possible that 'most of the warming over the last 50 years is *very likely* to have been caused by anthropogenic increases in greenhouse gases', as stated by the Intergovernmental Panel on Climate Change (IPCC) [4, 5]. But we are far even from stabilizing the concentrations, mainly for two different reasons: Global population is growing[3], and with it, the demand for energy. Secondly: newly industrializing countries have an extremely rapid growth in energy demand, but energy consumption of countries within

[1] President of the European Commission, in January 2008 [1] and in his speech during the World Energy Congress in Rome, November 12, 2007 [2].

[2] Which can be explained by plate tectonics, variations in the geometry of the Earth's orbit, solar activity, greenhouse gases e.g. due to volcanism and feedback factors such as reflecting glacial areas, CO_2 releasing, melting permafrost and others.

[3] World population has more than doubled since 1950 and is set to increase by 40% by 2050 [6].

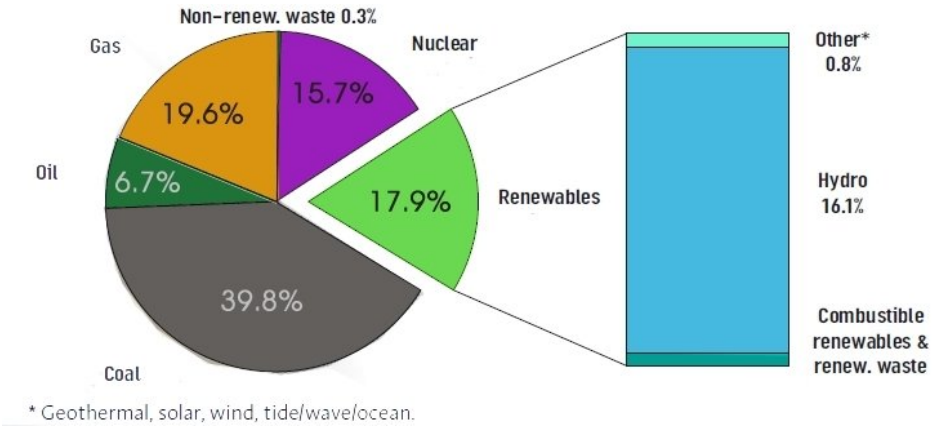

Figure 1.1: *Global electricity generation by fuel in the year 2004. Source: [7]*

the OECD is projected to rise as well, summing up to an estimated increase of global energy demand by 44% until 2030 (compared to 2006 values) [8] (see fig. 1.2). It is assumed, that by 2015, growth in the production of easily accessible oil and gas will not match the projected rate of increase in demand, and the question arises of how supply-demand tensions will be resolved [6]. Political and market forces already favor the development of coal as a still widely available, low-cost energy option [9].
To draw hope from nuclear fission energy might be delusive, as in this case as well, the resource is not inexhaustible and far from being distributed homogeneously over the globe [10] – plus the problem of massive damage, the mining of uranium causes to the surrounding nature [11]. However, the most prominent heavy drawbacks of nuclear fission are the risk of accidents, which we are aware of since the catastrophes of Chernobyl (1986) and Fukushima (2011) and the – after 55 years of civil use of nuclear fission energy – still unsolved problem of hazardous waste disposal. Fusion energy might become, together with renewable energy sources and fission energy, one of the three alternatives to fossil fuels. However, for the second half of the 21st century, renewable energy sources are by far not expected to be able to meet the total energy demand [7, 12]. The need for fusion power as a globally available, stable base load energy source will grow.

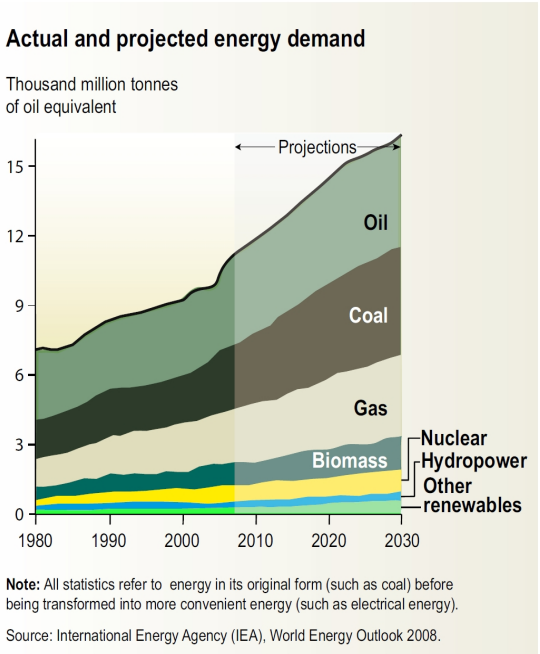

Figure 1.2: *2004 global primary energy consumption by sector. Source: [7]*

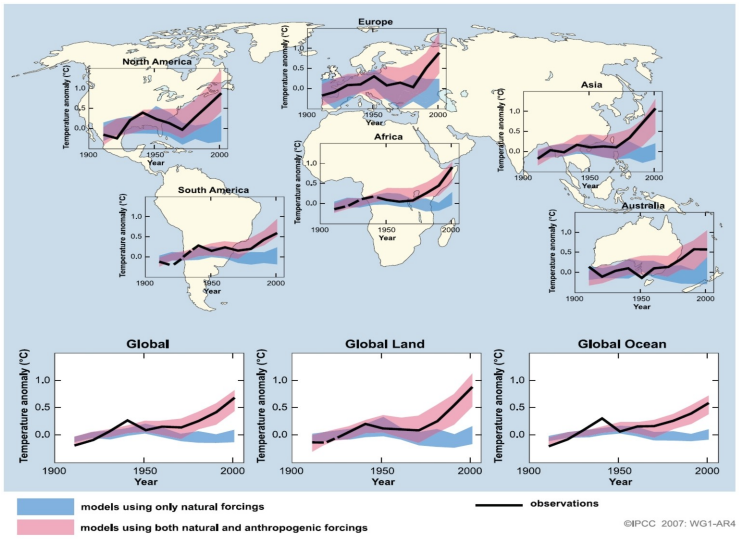

Figure 1.3:

"Comparison of observed continental- and global-scale changes in surface temperature with results simulated by climate models using natural and anthropogenic forcings. Decadal averages of observations are shown (black line) [...]. Blue shaded bands show the 5-95% range for 19 simulations from five climate models using only the natural forcings due to solar activity and volcanoes. Red shaded bands the 5-95% range for 58 simulations from 14 climate models using both natural and anthropogenic forcings". Source for text and figure: [4]

1.2 Nuclear Fusion – From a Star to a Terrestrial Power Plant

1.2.1 Stellar Fusion and Principal Energy Source

For a long time – mainly since the 1950s – the idea exists to follow the example of the stars and to generate energy by nuclear fusion. Like the sun and other stars, one would then set energy free by nuclear fusion which corresponds to the difference in nuclear binding energies between the fusing elements and the product element. Due to the fact that the binding energy results from the attraction of the nucleons via the strong force, this is a significant amount of energy: compared to chemical burning of fossil fuels, where one sets free only the binding energy of the shell electrons, resulting from the electromagnetic interaction, the energy set free in nuclear transformations is six orders of magnitude larger. To maintain a gigawatt power plant, 7000 tons of coal are necessary per day but only one kilogram of nuclear fusion fuel.
The nuclear binding energy depends on the composition of the particular isotope and has a global minimum for iron (^{56}Fe), see fig. 1.4. Therefore, energy can be set free either by fissioning nuclei heavier than iron *or* by fusing nuclei with a mass number lower than iron. The energy is – in both cases – on the scale of MeV. A net energy gain can, in principle, be obtained from nearly all fusions of light nuclei, but only few of them can be realized in practice, as there is the Coulomb barrier to be overcome. The ionized nuclei repel one another because of the repulsive electrostatic force between their positively charged protons.

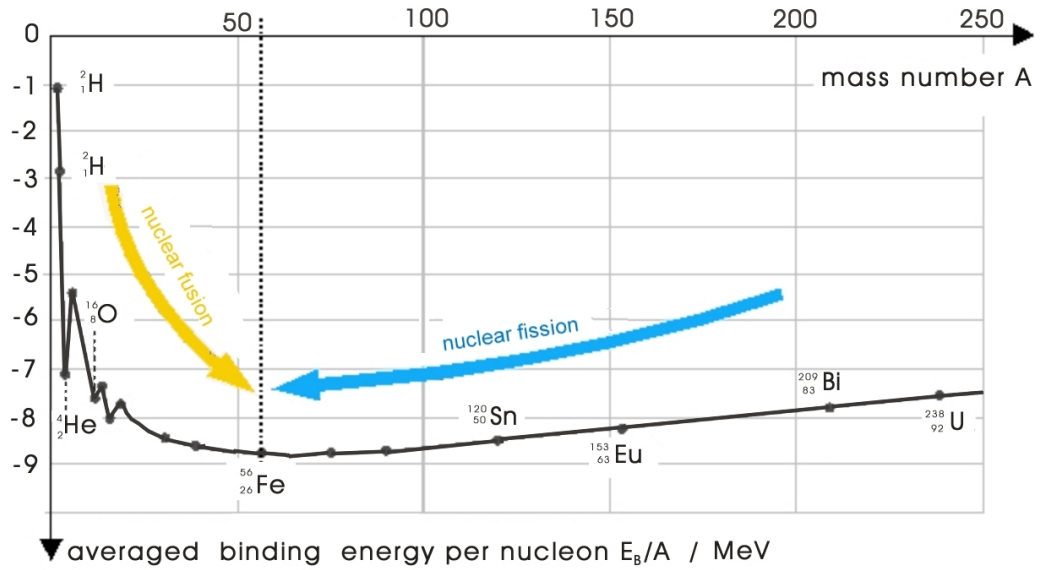

Figure 1.4: *The binding energy E_B of atomic nuclei per nucleon plotted against the number of nucleons (mass number A). This curve can be explained with the Bethe-Weizsäcker formula. To understand the existence of the peaks, one needs to use the nuclear shell model. Net energy can be gained by fissioning heavy nuclei or by fusion of light nuclei.*

An estimate for the Coulomb barrier to be overcome shows that temperatures in the scale of a billion Kelvin are necessary to make light nuclei fuse. In fact, fusion can already be achieved at considerably lower temperatures, mainly due to two effects: the Maxwellian tail in the Maxwell-Boltzmann distribution and the effect of quantum tunneling, explained by Gamow in 1928. On the sun, the main reactions are:

$$\mathrm{p} + \mathrm{p} \longrightarrow \mathrm{D} + \mathrm{e}^{+} + \nu_{\mathrm{e}} + 0.42\ \mathrm{MeV}$$
$$\mathrm{D} + \mathrm{p} \longrightarrow {}^{3}\mathrm{He} + \gamma + 5.49\ \mathrm{MeV}$$

and, as half as frequently as the above:

$${}^{3}\mathrm{He} + {}^{3}\mathrm{He} \longrightarrow {}^{4}\mathrm{He} + 2\mathrm{p} + 14.86\ \mathrm{MeV}$$

which gives – including matter-antimatter annihilation of the e^{+} with an e^{-} – a total of 26.7 MeV and is called the first pp-chain. Thus, the sun fuses four protons to one Helium nucleus, transforming this way 4.3 million tons of mass to energy every second. An important feature of the energy production in the sun is the role of the weak interaction which transforms protons to neutrons in the first of the above reactions and involves the emission of neutrinos. As the weak interaction is very slow, this contributes to the long lifetime of the sun. But why not utilize these reactions for terrestrial fusion? For energy production on Earth the weak interaction has to be avoided since it would lead to unacceptably small fusion rates.

1.2.2 Terrestrial Fusion Reactions

The sun, like all other stars overcomes this problem by its huge mass[4], thus the stellar fusion reactions are not feasible on Earth. Possible candidates for terrestrial fusion reactions are the following:

$$
\begin{aligned}
\mathrm{D} + \mathrm{D} &\longrightarrow {}^{3}\mathrm{He} + \mathrm{n} && + 3.27\ \mathrm{MeV}\\
\text{or} &\longrightarrow \mathrm{T} + \mathrm{p} && + 4.03\ \mathrm{MeV}\\
\mathrm{D} + \mathrm{T} &\longrightarrow {}^{4}\mathrm{He} + \mathrm{n} && + 17.6\ \mathrm{MeV}\\
\mathrm{T} + \mathrm{T} &\longrightarrow {}^{4}\mathrm{He} + 2\mathrm{n} && + 11.3\ \mathrm{MeV}\\
\mathrm{D} + {}^{3}\mathrm{He} &\longrightarrow {}^{4}\mathrm{He} + \mathrm{p} && + 18.4\ \mathrm{MeV}
\end{aligned}
$$

since the highest energy gain can be expected for the fusion of the lightest nuclei (see fig. 1.4). As can be seen in fig. 1.5, the deuterium-tritium (D-T) fusion has by far the largest cross section at the lowest energies. The reason for this can be found in the energy levels of the unstable ^{5}He nucleus: it has an excited state just 64 keV above the sum of the masses of tritium and deuterium. Due to the a resonance-like mechanism, the D-T fusion reaches its maximum at this energy difference. As a consequence, the D-T fusion is the most promising candidate for the terrestrial use of nuclear fusion.

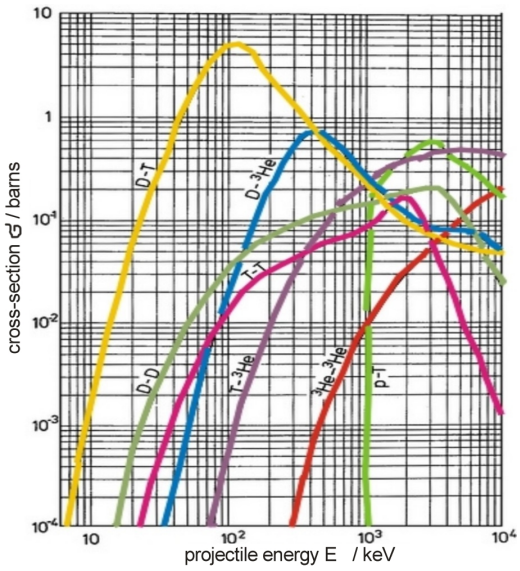

Figure 1.5: *Measured cross sections σ in barns (10^{-28} m^2) for different fusion reactions as a function of the center of mass energy E. Source: [13]*

1.2.3 Fusion Fuel

Deuterium appears with a weight fraction of 0.033% in water. Given the water of the oceans as 1.4×10^{21} kg, the mass of deuterium on Earth is 4×10^{16} kg. In D-T reactors with a thermal efficiency of about one third, this amount would allow for a production of $4\times10^{16}/m_{\mathrm{D}} \times 17.6\ \mathrm{MeV} \times 1/3 \approx 10^{33}$ J of electric energy. Assuming a constant energy demand from onward, one could supply the world with energy for more than the next 10^{10} years (calculation see ref. [14]). Moreover, the extraction of deuterium is easier than the enrichment of uranium (^{235}U), due to the high relative mass difference of the isotopes.
Tritium – super heavy hydrogen ^{3}H – in contrast, does not exist naturally as its half-life is only 12.3 years. However, it can be bred from lithium using neutron-induced fission reactions – for example with the help of fusion generated neutrons that are moderated

[4] This concept is called 'gravitational confinement'.

to thermal energies [5]:

$$^{6}\mathrm{Li} \; + \; \mathrm{n}_{\mathrm{thermal}} \; \longrightarrow \; \mathrm{T} \; + \; ^{4}\mathrm{He} \; + \; 4.8\ \mathrm{MeV}$$

The natural abundance of lithium is 7.4% ^{6}Li and can be found in the Earth's crust to an averaged percentage of[6] 0.006%. Seawater contains an estimated 230 billion tons of lithium, though at a low concentration of 0.1 to 0.2 ppm [15, 16]. The energy contained in 1 kg ^{6}Li is roughly 22 MeV/m_{Li}. Thus, at a thermal efficiency of about one third, 1 kg of natural lithium would give around 7×10^{3} GJ of electric energy.
Summing up, one asserts that the fuels for fusion are widespread and abundantly available, fair distributed all over the world and nearly inexhaustible, as they can be extracted from seawater (deuterium) and out of the Earth's crust (lithium). To assuage todays energy demand, five thousand 1 GW fusion power plants worldwide would be sufficient, each using 110 kg of deuterium and 380 kg of lithium per year (at perfect efficiency)[7].

1.2.4 Fusion Waste and Safety Aspects

Having discussed the fuels for terrestrial nuclear fusion, one should now have a look at the waste: The D-T reaction leads to very small quantities of Helium, which is an inert gas, and highly energetic[8] neutrons which are like in a fission power plant the principal performers in the process of producing hot steam to generate electricity in a common generator.
In contrast to nuclear fission, the working principle of the processes is not a chain reaction. There is only a very small amount of fuel used during the operation state, and therefore no risk of explosion and meltdown as known from nuclear fission. Even if there is a leak in the coolant cycle, only about 5 g of tritiated water (HTO or T_2O) will be released into the environment. The only concern arises from the reactor walls which will be activated over time due to the high neutron fluxes. As a consequence, materials will have to be disposed after the shutdown of the reactor. However, while fission plant components (and especially the waste) remain extremely hazardous for millennia, the storage period for fusion plant components is not of a geological time scale. It is estimated to be less than 100 years (see fig. 1.6), depending on the achievements of material research.

[5] Since fusion reactors would operate at optimal temperature, a self-energizing runaway reaction like in nuclear fission is not possible.

[6] Salts of lithium can be found mainly in salt lakes with a natural abundance of 1%. The most important technically available deposit of lithium is in the Salar de Uyuni area of Bolivia (5.3 million tons) which holds half of the world's reserves, the Salar de Atacama in Chile (3 million tons), China, and the U.S.A.

[7] Compared to 66 500 t of (natural) uranium required worldwide in 2013 ref. [17].

[8] As the fusion energy is distributed to the products inversely proportional to their mass ratio.

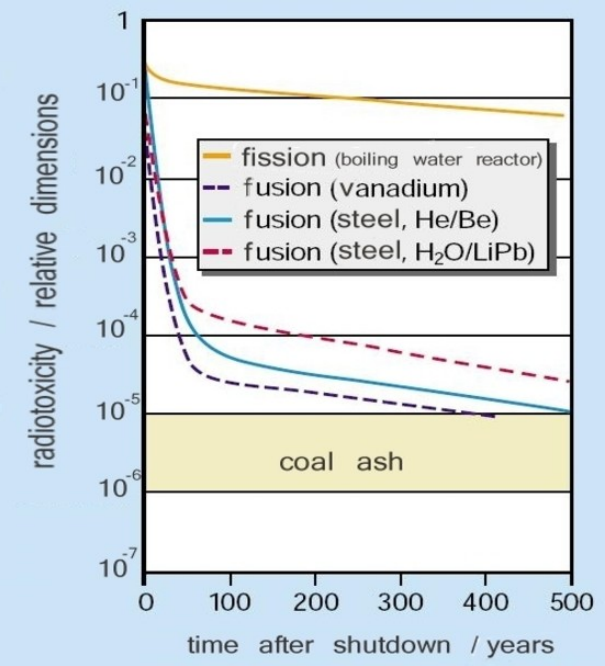

Figure 1.6: *Comparison between the time evolution of radiotoxicity of all waste produced up to after shutdown (including replaced units) from three fusion power plant concepts differing in the material of the vacuum vessel and from the most common fission power plant type (all with equal power output). The radiotoxicity is referring to ingestion. The three fusion power plant materials are: 1) vanadium alloy; 2) helium cooled blanket and steel that is more resistant to activation; 3) water cooled blanket, with the same steel. Source: [18]*

1.3 Conceptional Approaches to a Fusion Reactor

As mentioned above, the *gravitational confinement* cannot be realized on Earth. In principle, there are two types of confinement left: *inertial confinement* and *magnetic confinement*. As this thesis is set in the context of magnetic confinement fusion, only this concept is explained in the following.

1.3.1 Criteria for Energy Gain

To be able to use nuclear fusion in a power plant, it is very helpful to operate in a (quasi) stationary state, using considerably less energy for its creation and maintenance than the fusion plant is providing to the grid.
An estimate for the required conditions was given by J. D. Lawson in 1957 [19]: The so-called *Lawson Criterion* gives a state in which the energy losses to the environment are (over-) compensated by the energy released in the fusion reactions – it is therefore an ignition criterion. Having passed the threshold of Lawson Criterion, the plasma is called 'burning' or *ignited* . This should not be confused with the *breakeven point*, i.e. the operation state which gives as much energy from fusion reactions than energy is required to reach and maintain this state. Breakeven is easier to achieve than ignition. The fusion power output is the product of the fusion reaction rate $R = n_D n_T \langle \sigma v_r \rangle$ and the energy gain per fusion reaction. The plasma is burning, if energy losses via electromagnetic radiation (with c_B the constant of bremsstrahlung) and convection are (over-)compensated by the heating of the α particles, i.e. Helium nuclei. Thus, the

Lawson Criterion can be written as

$$n\,\tau_{\mathrm{E}} > \frac{3k_{\mathrm{B}}T}{1/4\,\langle\sigma(v_r)\cdot v_r\rangle E_\alpha - c_{\mathrm{B}}\,T^{1/2}} \tag{1.1}$$

for an ideal plasma without impurities. n is the plasma density, τ_{E} the so-called confinement time [9], and σ is the cross section of the respective fusion reaction and depends on the relative velocity v_{r} between the reactants. E_α is the energy carried by each helium nucleus, T the temperature.

To take the α particles into account which remain as 'ash' in the plasma, the Lawson criterion, eq. (1.1) can be expanded. The density of the α particles is expressed as a fraction f of the electron density n_{e}. As it reduces the fusion probability, the heating power is reduced, too, i.e. in mathematical terms it has to be multiplied by a factor of $(1-2f)^2$. The losses due to electromagnetic radiation increase by a factor of $(1+2f)$, the convection power decreases by $(1-f/2)$. Taking these factors into account, a new Lawson Criterion is found:

$$n\,\tau_{\mathrm{E}} > \left(1-\frac{f}{2}\right)\frac{3k_{\mathrm{B}}T}{1/4\,(1-2f)^2\langle\sigma(v_{\mathrm{r}})\cdot v_{\mathrm{r}}\rangle E_\alpha - (1+2f)c_{\mathrm{B}}\,T^{1/2}}$$

The right hand side has an absolute minimum at a temperature of $T \approx 3.2\times10^{18}$ K or ≈ 27 keV[10]. As the reaction parameter $\langle\sigma v_{\mathrm{r}}\rangle$ is roughly proportional to T^2 at these temperatures, one can take the so-called *triple product* as an ignition condition (see fig. 1.7):

$$nT\tau_{\mathrm{E}} \geq 3.5\times10^{21}\text{keV s m}^{-3} = 4.06\times10^{28}\text{ K s m}^{-3}$$

Typical parameters to reach are $T \sim 10$ keV, $n \sim 10^{20}$ m^{-3}, $\tau \sim 5$ s. Within the last decades, the triple product could be raised over more than three orders of magnitude and today only needs to be increased by a factor of five to reach the threshold.
Note that the fusion power scales with $\propto (nT)^2$ and the costs of a power plant approximately with $\propto B$, the magnetic field.
The closest to a burning plasma that has been achieved was in the JET experiment, the Joint European Torus, currently the largest fusion experiment in the world. The triple product in JET is only a factor of five short of the ignition criterion. The next worlds largest fusion experiment is under construction and shall reach the breakeven point. It is an international project, realized by a number of nations (China, the European Union, India, Japan, South Korea, Russia, and the USA) and called ITER [11] [20].

[9] Defined by the confined energy divided by the heating power.
[10] from now on, the Boltzmann constant k_{B} will be absorbed in T, such that temperatures have the unit of eV.
[11] formerly standing for *International Thermonuclear Experimental Reactor*, but also Latin for 'way'.

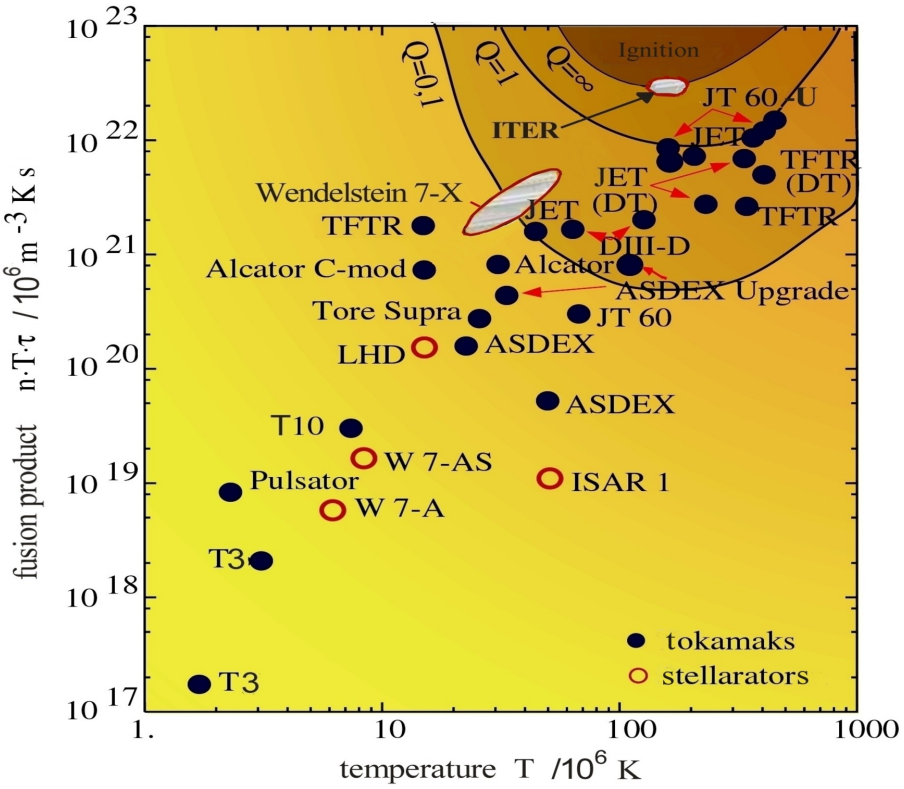

Figure 1.7: *The triple product for different fusion devices throughout fusion research history; Q is the fraction of total output energy to input energy. For the acronyms of the various machines, see app. A. Adapted from: [21, 22]*

1.3.2 Magnetic Confinement

At the extremely high temperatures necessary for ignition, the fusion fuel is in the state of a fully ionized[12] plasma[13]. On a scale greater than the so-called *Debye* scale, the plasma is electrically neutral (*quasi-neutrality*, *Debye-shielding*). As such, they are subject to electric and magnetic forces. This feature of the plasma particles is used to confine the fusion fuel. The Lorentz force acts on charged (charge q), moving (velocity $\boldsymbol{v}$) particles in a magnetic field $\boldsymbol{B}$: $\boldsymbol{F} = q\ \boldsymbol{v} \times \boldsymbol{B}$. In a homogeneous field, moving particles are forced on helical trajectories. The motion along the magnetic field lines is not affected, whereas perpendicular to the field lines, it is limited to the *gyroradius* ρ, resulting from the Lorentz force acting as a centripetal force. The gyroradius, or *Larmor radius*

$$\rho = \frac{m v_\perp}{eB} \tag{1.2}$$

[12] Up to the atomic number of argon, all elements are completely ionized in a fusion plasma.

[13] Throughout this thesis, the plasma can be considered *ideal*, i.e. it is not relativistic and not quantum-mechanically degenerated, as the velocity and the density respectively do not exceed a certain value.

of an ion moving with ion sound speed $v_s = \sqrt{T_e/m_i}$ is a frequently used normalization value in fusion research (T_e is the electron temperature, m_i the ion mass). In the case of deuterium ions, ρ_s is typically a few millimeters[14], whereas that of the electrons is smaller by a factor of $\sqrt{m_e/m_{i(D)}} \approx 1/60$.
This limits the motion in the perpendicular direction, whereas in the parallel direction, the charged particles can still move freely. A quite obvious method to avoid high loss rates at the ends of any fusion device is to fold a cylindrical vessel to a torus. However, the bending of the confining arrangement leads to an inhomogeneous, curved magnetic field. As will be shown in sec. 2.2.1, a purely toroidal magnetic field will cause particle drift movements, leading to a charge separation within the plasma. Due to the resulting electric forces, the plasma will drift out of the confinement region. To prevent the charge separation, there is the idea of twisting the field lines helically. The additional circulating movement of the particles, that follow the magnetic field lines, leads to the compensation of the drift movements. A further advantage of such helical magnetic configuration is the better magneto-hydrodynamic stability.

To obtain a helical magnetic field, two concepts were developed almost simultaneously, in the early 1950s: the so-called "*Stellarator*" and the so-called "*TOKAMAK*". The Stellarator[15] concept was developed in 1951 by the U.S.-American astrophysicist Lyman Spitzer [23], and the first experiments were built the same year in the Princeton Plasma Physics Laboratory (PPPL) in the USA. In a Stellarator, the magnetic field necessary to confine the plasma is generated completely by external coils. The problem of particle drift is addressed in this concept by establishing a very complex magnetic field that minimizes radial particle diffusion.
The TOKAMAK [24] concept was developed in 1952 by the Soviet physicists Andrei Sakharov and Igor Yevgenyevitch Tamm (who had been inspired by an original idea from Oleg Lavrentyev) at the Kurtschatow Institute. In the early 1950s, first TOKAMAK experiments were run in the Soviet Union. The most famous among them are T-3 and its larger version T-4, tested in Novosibirsk, conducting the first ever quasi-stationary thermonuclear fusion reaction in 1968[16]. In a TOKAMAK device (see fig. 1.8), the twist of the field lines is not achieved by a complicated coil configuration, but by superimposing a simple toroidal magnetic field, generated by the so-called 'toroidal field coils' with a poloidal one. The poloidal magnetic field is created by a toroidal electric current carried by the plasma itself. This current is driven by the transformer principle (induced with the help of a variable magnetic field from the 'poloidal field coils': the plasma itself can be viewed as the secondary winding of a transformer). The current, and therefore the magnetic confinement, can only be maintained for a distinct time span[18]. Therefore, TOKAMAKs either operate inherently pulsed or have to rely on other means of current drive.

[14] In ASDEX Upgrade: $\sim$ 3mm in the plasma core.

[15] From Latin: *stella* , star

[16] The word 'TOKAMAK' is a transliteration of the Russian 'Токамак', which is an acronym for 'Тороидальная Камера в Магнитных Катушках'[17] meaning 'toroidal chamber with magnetic coils'. Furthermore, the word 'ток' is Russian for 'current'.

[18] In the case of ASDEX Upgrade, this is approximately 10 s; in the case of superconducting coils like in Tore Supra it can be several minutes.

The development of the TOKAMAK concept has advanced considerably. Thus, research does no longer only concentrate on reaching the fusion criterion but also on common problems of the power plant operating state, e.g. the development of long-life wall materials that can stand the extreme thermal stresses and the progress of the so-called *advanced TOKAMAK* concept. This concept is characterized by the features needed for a viable fusion power plant. Primarily it implies a (quasi-) steady-state operating system by generating the toroidal plasma current not inductively and therefore not pulsed. Such non-inductive current drive is important with regard to desirable steady-state operating TOKAMAKs, but also to access advanced regimes of superior confinement which often rely on certain current profiles.

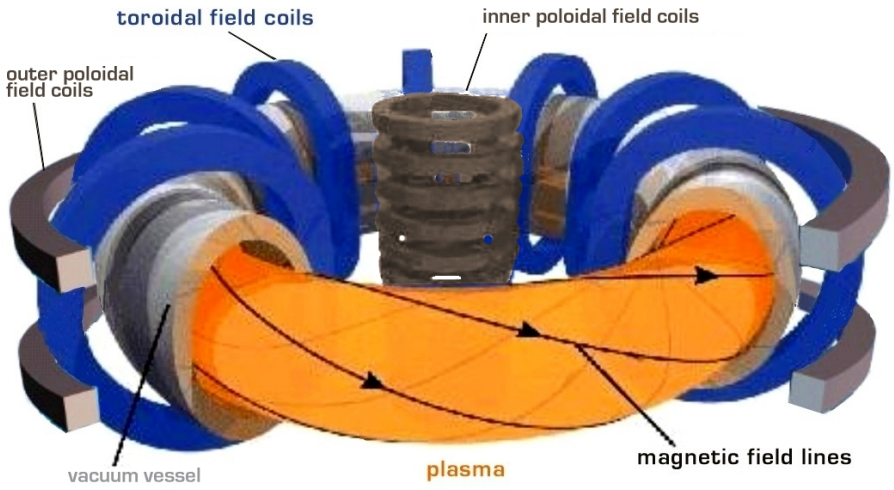

Figure 1.8: *The TOKAMAK concept: Shown are the field coils (blue) generating the toroidal field and the current for the poloidal field, the plasma itself (yellow) and the vacuum vessel (gray). Adapted from: [25, 26]*

1.3.3 Plasma Heating

As mentioned above, the fusion born α particles remain as electrically charged particles in the magnetic cage and release their energy of 3.5 MeV via collisions to the background plasma. Thus α particle heating is a by-product of fusion itself. However, to heat a plasma to temperatures where ignition becomes possible in the first place, other methods have to be employed, as will be described shortly.

Ohmic Heating

As the plasma has a non-zero electric resistivity, the toroidal plasma current induced in tokamaks contributes to the plasma heating. This fact is called *ohmic heating* [14]. The heat generated depends on the electrical resistivity, which is $\propto T^{-3/2}$, thus decreases with rising electron temperature[19]. As a consequence, the maximum plasma temperature attainable by pure ohmic heating lies between 20 and 30 million degrees Celsius. To obtain fusion temperatures, additional heating methods must be used.

Radiofrequency (RF) Heating

Radiofrequency heating, short RF, makes use of high power electromagnetic waves to excite resonances with the gyromotion of plasma ions or electrons [14]. An antenna in the plasma vessel which receives power from a remote generator radiates the electromagnetic wave into the plasma, where it is damped by particles with a gyromotion satisfying the resonance condition. The resonances lie in the range of Alfvén waves ($1-10$ MHz), the ion cyclotron frequency (ICRH, $30-100$ MHz), electron cyclotron frequency (ECRH, $20-200$ GHz), as well as the so-called lower hybrid range (the intermediate between the ion and the electron cyclotron frequency, $1-10$ GHz). Lower hybrid heating excites oscillations of electrons along the magnetic field in phase with ion oscillations across. Depending on the choice of the frequency, plasma density and composition at the position of the wave energy deposition, different constituents of the plasma are heated. Heating the lower concentration species (e.g. protons in a deuterium plasma) is often advantageous [27]. This method is called *minority heating*.

But RF is not only used for heating, it is also one non-inductive way for current drive: if the waves are launched predominantly in one direction with respect to the main magnetic field, the current profile is also changed.

Neutral Beam Injection (NBI) Heating

The concept of Neutral Beam Injection, short NBI, was suggested in the 1950s and is nowadays the major work horse for plasma heating at most fusion experiments (see fig. 1.9) [14]: Atoms, being electrically neutral, are not affected by the Lorentz force and can penetrate through the confining magnetic field until they become ionized in the plasma via collisions with electrons and ions. If their kinetic energy is large compared

[19] The current is mainly carried by electrons, as the resistivity is proportional to the square root of the particle mass.

to the plasma temperature, they will deliver their energy to the plasma, thus heat it up. In general, the beams have energies up to several ten keV, in very large devices even several hundred keV.

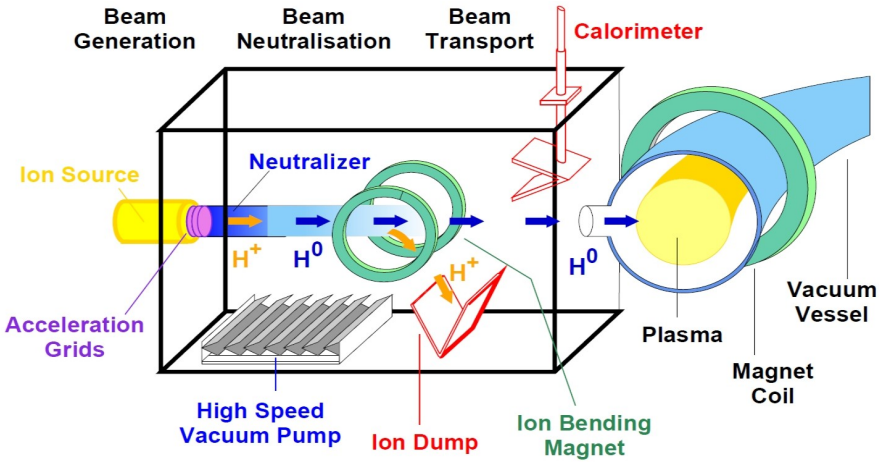

Figure 1.9: *Schematic view of the* NBI *heating system. Source: [21, 26]*

Another non-negligible aspect of the NBI concept is the re-fueling of the fusion plasma with ions and, as in the case of RF, current drive. If a neutral beam is injected at an oblique angle, the current profile can be changed.

As a side effect, the NBI beam can be used for diagnosing the fast particle distribution function by measuring the Doppler-shifted Balmer-alpha light, that is emitted when fast ions charge-exchange with neutral beam ions. This technique is called FIDA [28, 29].

1.4 Thesis Outline

In a fusion plasma, due to the described external heating methods and eventually due to fusion born α particles, a population of higher energetic particles is present. They have energies significantly above the thermal ion energy. It is necessary that these super-thermal ("fast") particles are well confined until they transfer their energy to the background plasma. Fast particle populations can interact with global electromagnetic waves, what was described first by ref. [30]. Through inverse Landau-damping, the wave-particle interaction can lead to the growth of MHD-like and kinetic instabilities. The respective transport processes enhance fast particle losses. As a consequence, fusion power is reduced and there is the risk of damages at the machine wall.

It is important to investigate the fast particle loss mechanisms for different reasons: on the one hand, a deeper understanding of the mechanisms might provide an opportunity to extract the α particle ash efficiently [31]. On the other hand, fast ion losses need to be controlled to mitigate their negative effects on confinement and wall. This could be done e.g. via tailoring the plasma current to control the MHD modes, once their role concerning fast ion losses is understood.
ASDEX Upgrade [32, 33] and other machines of similar size (e.g. DIII-D [34]), have the advantage to allow for a direct measurement of the fast ion losses caused by core-localized MHD activity, since the particle orbits are relatively large compared to the machine size. The fast ion loss detector (FILD) at ASDEX Upgrade measures fast ion losses resolved in pitch angle and gyroradius [35].
From the theoretical point of view, these measurements are of great importance: comparing numerically obtained losses with experimentally measured ones can be regarded as a code validation against the experiment. The basic connection between numerical predictions and experimental results provides a deeper understanding of physical mechanisms and a validation of theoretical models. Therefore, this thesis not only addresses the comparison of simulated with experimentally measured losses. It also presents a study to reveal the underlying transport mechanisms in relatively complex multi-mode scenarios.

The thesis is organized as follows: chapter 2 introduces TOKAMAK geometry and the general particle motion in this geometry. In chapter 3, the theoretical background on MHD waves and wave-particle interaction is given. After providing this general basis, chapter 4 presents the HAGIS model with the inclusion of a non-vanishing parallel electric field. In chapter 5, a numerical study is carried out, investigating resonance mechanisms for wave-particle interaction, especially in the presence of multiple modes with different frequencies. Finally, in chapter 6, simulations are carried out under conditions that are as realistic as possible. The resulting fast particle transport processes are studied and the consequential losses compared with experimentally measured data, in particular with FILD data from the ASDEX upgrade discharge #23824.

CHAPTER 2

Particle Motion in Toroidal Magnetic Fields

2.1 Geometry of a Tokamak

One important quantity to characterize a TOKAMAK device is the so-called *aspect ratio A*. It is defined as the ratio of major plasma radius R_{mag} to minor plasma radius a (see fig. 2.1):

$$A := \frac{R_{\text{mag}}}{a}. \tag{2.1}$$

The limit of a very large-aspect ratio $A \to \infty$ corresponds to a cylindrical device. The vertical symmetry axis (z in fig. 2.1) is the *torus axis*, the center of the plasma ($r = 0$ and $R = R_{\text{mag}}$ in fig. 2.1) is called the *magnetic axis*. The inner part of the torus, where $R < R_{\text{mag}}$ is called the *high field side* (HFS), as the magnetic field strength is higher there, compared to the so-called *low field side* (LFS), $R > R_{\text{mag}}$. The R-φ plane of horizontal symmetry is called the *outboard midplane* for $R > R_{\text{mag}}$. For the last closed flux surface, the acronym LCFS is used frequently. The boundary between closed and open field lines, separating the toroidally confined region from the region where field lines connect to material surfaces is called *separatrix*.
The *safety factor* q quantifies the helicity of the magnetic field by giving the number of toroidal turns the magnetic field traverses until one poloidal turn is complete,

$$q := \frac{N_{\text{t}}}{N_{\text{p}}}. \tag{2.2}$$

In other words, $q := \Delta\varphi/(2\pi)$, where $\Delta\varphi$ is the change of the toroidal angle for one poloidal revolution ($\Delta\vartheta = 2\pi$). The ratio of the toroidal to the poloidal magnetic field[1] is $B_{\text{t}}/B_{\text{p}} = R\mathrm{d}\varphi/r\mathrm{d}\vartheta$. If one assumes a large-aspect ratio TOKAMAK, where $R_{\text{mag}} \gg a$, and thus $R \approx R_{\text{mag}}$, $B_{\text{t}}(R) \approx B_{\text{t}}(R_{\text{mag}})$, the safety factor reads [36]

$$q = \frac{\mathrm{d}\varphi(\text{B line})}{\mathrm{d}\vartheta(\text{B line})} \approx \frac{r}{R_{\text{mag}}}\frac{B_{\text{t}}}{B_{\text{p}}}. \tag{2.3}$$

This is equal to the rate of change of toroidal flux Ψ_{t} with poloidal flux Ψ_{p} (for definitions, see app. C, apply eqs. (C.1) and (C.5) in the toroidal coordinate system),

$$q = \frac{\mathrm{d}\Psi_{\text{t}}}{\mathrm{d}\Psi_{\text{p}}}. \tag{2.4}$$

[1] B_{t} is the toroidal, B_{p} the poloidal component of the magnetic field, according to Ampère's law $B_{\text{p}}(r) = \mu_0 I/(2\pi r)$ for a current I passing through a circular area.

Typically, $|q| \gtrsim 1$, and q depends on the radial location r in the TOKAMAK. q is negative if the helicity of the magnetic field twist is left handed, i.e. the current direction is opposite to the toroidal magnetic field direction.

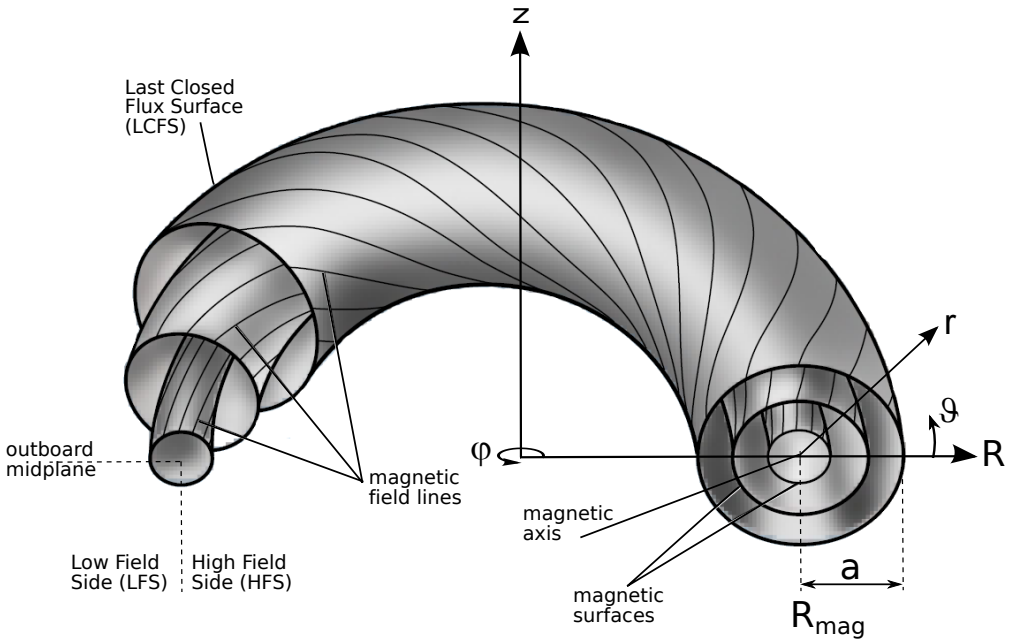

Figure 2.1: *Magnetic surfaces in a TOKAMAK and two different toroidal coordinate systems: toroidal coordinates (r, ϑ, φ) and cylindrical coordinates (R, z, φ); the angle φ denotes the* toroidal *direction, ϑ the* poloidal *direction. Adapted from: [18].*

In the TOKAMAK ASDEX Upgrade, the characteristic values are:

$$a \approx 0.5 \text{ m}, \qquad R_{\text{mag}} \approx 1.65 \text{ m}, \quad B_{\text{t}} \approx 2.5 \text{ T}, \quad B_{\text{p}} \approx 0.4 \text{ T}, \quad q \approx -2.$$

As the electron temperature decreases with increasing r, the electric conductivity decreases with r, leading to a lower current density j towards the plasma edge compared to the plasma core. Therefore, the total current I increases less than quadratically with r, and thus B_{p} less than linearly. B_{t} can be approximated to decrease with $1 - r$. Thus, $q(r)$ usually increases monotonically from the magnetic axis to the plasma edge leading to a differential helicity of the magnetic field lines, that is called magnetic *shear* $\hat{s}$:

$$\hat{s}(r) \equiv \frac{r}{q} \frac{\mathrm{d}q}{\mathrm{d}r} \,. \tag{2.5}$$

However, by means of different current drives, hollow radial current density profiles can be tailored, resulting in non-monotonic, *inverted q profiles*. These may play a role in future TOKAMAKs, especially with long-pulse operation since non-inductive current drives often lead to hollow radial current density profiles (for an overview, see ref. [37]).

As each magnetic field line can be connected to a certain q value and due to the fact that magnetic field lines cannot cross each other, a *magnetic surface* can be defined (see fig. 2.1). Since the magnetic flux within each such surface must be constant through any cross section, they are also referred to as *flux surface*. The magnetic surfaces are toroidally symmetric. In the poloidal projection, they are nested flux surfaces[2]. This becomes clear when considering one magnetic field line with an irrational q value. This field line covers the entire magnetic surface. A surface where q takes a rational value is called *rational surface*. Rational surfaces, especially those with q being a fraction of small integers, $1/2$, $4/3$, 1, ... play an important role in TOKAMAK stability, since they are resonant surfaces for plasma instabilities. Physical variables that are constant on magnetic surfaces are called *flux functions*. Besides q, the pressure p is a flux function[3]: if ideal MHD is valid, in a static equilibrium, the pressure gradient is balanced by the Lorentz force, $\boldsymbol{j} \times \boldsymbol{B} = \nabla p$ (see eq. (3.1b)), and $\boldsymbol{j}$ and $\boldsymbol{B}$ are perpendicular to ∇p, i.e. lie in surfaces of constant pressure which are the magnetic surfaces. Via this MHD static force balance, applied to an axis symmetric static[4] magnetic equilibrium cast in terms of the poloidal flux Ψ_p , the magnetic surfaces can be calculated. The resulting equation is the so-called *Grad-Shafranov equation* (for derivation see ref. [36]):

$$\Delta^* \Psi_\mathrm{p} + \frac{\mu_0^2}{4\pi^2} I_\mathrm{p} \cdot I_\mathrm{p}' + \mu_0 R^2 p' = 0, \tag{2.6}$$

with I_p, the flux function of the poloidal current and the operator[5]

$$\Delta^* \equiv \frac{\partial^2}{\partial R^2} - \frac{1}{R}\frac{\partial}{\partial R} + \frac{\partial^2}{\partial z^2}.$$

The primes ($'$) denote derivatives with respect to Ψ_p.

2.2 Guiding Center Motion

This section is dedicated to single particle movement, which is important in many fundamental aspects of wave-particle resonance. However, for a more comprehensive introduction, one may consult ref. [38].
In a strong magnetic field, it is advantageous to describe the motion of a charged particle as a superposition of its guiding center motion and its fast gyration around this guiding center (see fig. 2.2). In many theories, the exact dynamics of the fast gyromotion is neglected, because it is sufficient to examine the guiding center motion only. This not only leads to more analytic simplicity but also saves many orders of magnitude in both spacial and temporal resolution.
The so-called *guiding center approximation* is such a theory (also referred to as *driftkinetic formulation*). It is a perturbative ansatz, dating back to Hannes Alfvén, who

[2] and even circular in the simple TOKAMAK model without additional shaping, such as *elongation* or *triangularity*.
[3] thus, magnetic surfaces are identical to isobaric surfaces.
[4] Static means $\partial/\partial t = 0$ *and* $\boldsymbol{u} = 0$.
[5] Note: the $\partial/\partial\varphi$ term is zero.

recognized its validity in temporally and spatially varying fields (B) as long as the variations are small during one gyroperiod, i.e. $\nabla B \ll B/\rho$ and $\dot{B} \ll \Omega \cdot B$, with the gyroradius ρ and the gyrofrequency Ω.
Ref. [39] presents a rigorous derivation for the guiding center motion using the variational principle $\delta \int L dt = 0$. The resulting equations of motion (the drift equations) possess exact conservation laws for phase volume, energy (for time-independent systems), and angular momentum (for azimuthally symmetric systems). The Lagrangian

$$\mathscr{L} = \sum_i p_i \dot{q}_i - \mathscr{H},$$

(where q and p are conjugated canonical variables) for a charged particle (charge e, mass m) in an electromagnetic field takes the form (details see sec. 4.3)

$$\mathscr{L} = (m\boldsymbol{v} + e\boldsymbol{A}) \cdot \dot{\boldsymbol{x}} - \frac{1}{2} m v^2 - e\Phi \tag{2.7}$$

with $\boldsymbol{x}$, $\boldsymbol{v}$, $\boldsymbol{A}$, Φ the exact particle position, velocity, the vector and scalar potential.

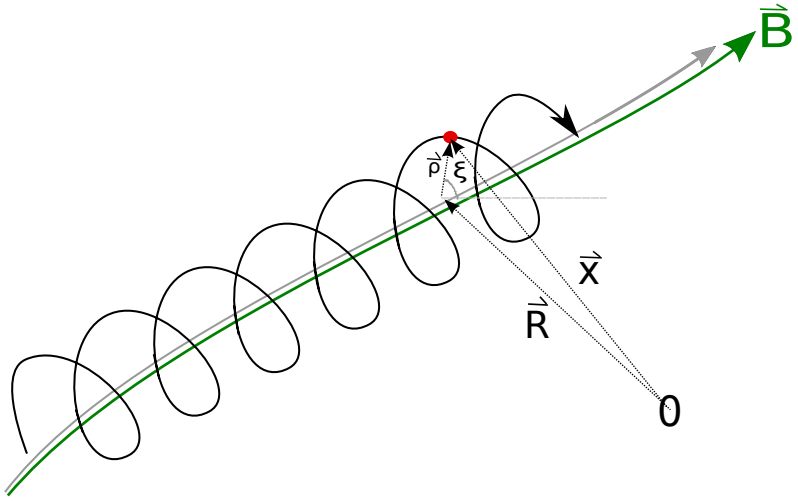

Figure 2.2: *Helical trajectory of a charged particle around a magnetic field line. The arrows denote the space vectors used for the guiding center ansatz.*

In the guiding center approximation, the motion of the guiding center (spacial coordinate $\boldsymbol{R}$) is separated from the gyromotion (expressed by the gyroradius $\boldsymbol{\rho}$) as visualized in fig. 2.2,

$$\boldsymbol{x} = \boldsymbol{R} + \boldsymbol{\rho} \tag{2.8a}$$

$$\text{with the gyroradius :} \quad \boldsymbol{\rho} = \rho\hat{\boldsymbol{\rho}} \equiv \frac{m\boldsymbol{v}_\perp}{eB} = \frac{v_\perp}{\Omega}\hat{\boldsymbol{\rho}} \tag{2.8b}$$

$$\text{with the known gyrofrequency :} \quad \Omega \equiv \frac{eB}{m} \tag{2.8c}$$

$$\text{and a unity vector :} \quad \hat{\boldsymbol{\rho}} = \cos\xi\, \boldsymbol{e}_x + \sin\xi\, \boldsymbol{e}_y. \tag{2.8d}$$

$\boldsymbol{e}_x(\boldsymbol{R}, \xi)$ and $\boldsymbol{e}_y(\boldsymbol{R}, \xi)$ are unity vectors in the plane perpendicular to the magnetic field lines. As the fields and potentials are assumed not to vary strongly over one gyroorbit,

it is sufficient to Taylor expand the potentials around the gyrocenter up to the first order:

$$\boldsymbol{A}(\boldsymbol{x}) = \boldsymbol{A}(\boldsymbol{R}) + (\rho \cdot \nabla)\boldsymbol{A}(\boldsymbol{R}) \tag{2.9a}$$

$$\Phi(\boldsymbol{x}) = \Phi(\boldsymbol{R}) + (\rho \cdot \nabla)\Phi(\boldsymbol{R}) \tag{2.9b}$$

Still, there are six phase space coordinates, three spacial components of the guiding center position $\boldsymbol{R}$, the parallel velocity of the guiding center $v_\parallel$, the perpendicular velocity of the particle $\boldsymbol{\rho} \propto v_\perp$, and the gyrophase angle ξ. However, under the conditions where the guiding center approximation is valid, the gyromotion is an exact periodic motion, and therefore associated to an *adiabatic invariant* (according to $\oint p\mathrm{d}q$, see textbooks like ref. [40]). This adiabatic invariant is the magnetic moment μ of the gyrating charged particle (see textbooks like ref. [36]),

$$\boldsymbol{\mu} := \frac{1}{2}\int \boldsymbol{r} \times \boldsymbol{j}\mathrm{d}^3 r \tag{2.10}$$

$$\boldsymbol{\mu} = \frac{1}{2} m v_\perp^2 / B \; \hat{\boldsymbol{b}} \;\equiv \mathscr{E}_\perp / B \; \hat{\boldsymbol{b}}. \tag{2.11}$$

As μ is related to $v_\perp$, it can be substituted for it, reducing the number of evolving phase-space coordinates to four: three components of $\boldsymbol{R}$ and the parallel velocity $v_\parallel$ of the guiding center. The gyrophase angle is irrelevant to the guiding center motion, and averaged out in the following.
Inserting the Taylor expansion of the fields given above as well as the magnetic moment μ and averaging over the gyromotion (then, the average of the gyroradius over one gyroorbit vanishes $<\boldsymbol{\rho}>=0$), one obtains the particle Lagrangian as (details see app. E.1)

$$\mathscr{L} \;=\; (m v_\parallel \hat{\boldsymbol{b}} \;+\; e\boldsymbol{A}(\boldsymbol{R}))\cdot \dot{\boldsymbol{R}} \;+\; \frac{\mu B}{\Omega}\dot{\xi} \;-\; \frac{1}{2} m v_\parallel^2 \;-\; \mu B \;-\; e\Phi(\boldsymbol{R}). \tag{2.12}$$

The variation principle is now applied for the guiding center coordinate $\boldsymbol{R}$ to this Lagrangian,

$$0 \;=\; \frac{\mathrm{d}}{\mathrm{d}t}\frac{\partial \mathscr{L}}{\partial \dot{\boldsymbol{R}}} - \frac{\partial \mathscr{L}}{\partial \boldsymbol{R}}, \tag{2.13}$$

using the definition

$$\boldsymbol{B}^* := \boldsymbol{B} + \underbrace{\frac{m}{e} v_\parallel \nabla \times \hat{\boldsymbol{b}}}_{\mathscr{O}(1)}. \tag{2.14}$$

The result can be cast into the following form (see app. F.3):

$$\dot{\boldsymbol{R}} = v_\parallel \hat{\boldsymbol{b}} + \frac{B}{B_\parallel^*}\left(\boldsymbol{v}_{\mathrm{E\times B}} + \boldsymbol{v}_{\nabla B} + \boldsymbol{v}_{\mathrm{curv}}\right), \tag{2.15}$$

which is split into two parts: the parallel motion given by $m\dot{\boldsymbol{v}}_\parallel = \boldsymbol{F}_\parallel$ and a motion perpendicular to the magnetic field (other terms, that all contain "$\times\boldsymbol{B}$" as seen below), called *drifts*. They are frequently combined into the *drift velocity* $\boldsymbol{v}_{\mathrm{d}}$. A closer look on these drift velocities is taken in the next section.

2.2.1 Particle Drifts

The drift velocities appearing in the guiding center equation of motion eq. (2.15) are of the general structure

$$\boldsymbol{v}_{\mathrm{d}} = \frac{\boldsymbol{F} \times \boldsymbol{B}}{eB^2}, \tag{2.16}$$

where $\boldsymbol{F}$ is a force that is specified in more detail in the following (for a more rigorous derivation see app. F.3). Due to the cross product, only the perpendicular part of $\boldsymbol{F}$ is relevant.
As a first example, an electric field is considered to cause the force, resulting in the so-called *E-cross-B drift*:

$$\boldsymbol{v}_{\mathrm{E\times B}} = \frac{\boldsymbol{E} \times \boldsymbol{B}}{B^2}. \tag{2.17}$$

The E-cross-B drift is independent of the particle's charge e and therefore a threat for plasma confinement, since it leads to a drift of the whole plasma in the same direction.
In a spatial inhomogeneous magnetic field with growing field strength, there is a force $\boldsymbol{F} = -\mu \nabla B$ on all particles, due to their magnetic moment μ (eq. (2.10)). The resulting drift, called *grad-B drift* reads:

$$\boldsymbol{v}_{\nabla B} = -\frac{m\, v_\perp^2}{2eB^3} \nabla B \times \boldsymbol{B}. \tag{2.18}$$

Since $\nabla \cdot \boldsymbol{B} = 0$, the existence of a gradient in the magnetic field is always coupled to a curvature of the field lines. The local curvature radius R_C is given by $1/R_C \boldsymbol{e}_C = -\nabla B/B$ (with $\boldsymbol{e}_C$ being the unity vector in the direction perpendicular to the curve and its tangent). With the centripetal force $\boldsymbol{F}_{\mathrm{R}} = m v_\parallel^2 / R_C \, \boldsymbol{e}_C$, one obtains:

$$\boldsymbol{v}_{\mathrm{curv}} = -m\boldsymbol{v}_\parallel^2 \frac{\boldsymbol{B} \times (\boldsymbol{B} \cdot \nabla) B}{eB^4} \equiv -\frac{m\boldsymbol{v}_\parallel^2}{eB^3} (\nabla B \times \boldsymbol{B}), \tag{2.19}$$

which is called the *curvature drift*.
As curvature and grad-B drift act in different directions depending on the sign of the particle's electric charge. Thus, if not compensated, they lead to a charge separation and to the establishment of an electric field E. This field in turn causes E-cross-B drift, which is independent of the charge and conducts the whole plasma radially outwards.
A different kind of drift, as caused by a fluid effect, arises in the presence of a pressure gradient ∇p. There is a force $\boldsymbol{F}$ affecting a volume element δV, resulting from a pressure difference per area: $\boldsymbol{F} = -\nabla p \cdot \delta V$. One single particle feels the force $\boldsymbol{F} = -\nabla p / n$. This leads to the so-called *diamagnetic drift*

$$\boldsymbol{v}_{\mathrm{diam}} = -\frac{\nabla p \times \boldsymbol{B}}{enB^2}. \tag{2.20}$$

2.2.2 Magnetic Mirror Effect

Due to the particle gyration, it can be viewed as magnetic dipole, connected to a magnetic moment as defined in eq. (2.10). This dipole experiences a force arising from the magnetic field's inhomogeneity, $\boldsymbol{F}_\mathrm{m} = -\mu\nabla B$. This force is called *magnetic mirror force* and changes the potential energy μB of the magnetic moment. At the same time, the particle's total kinetic energy $\mathscr{E} = \mathscr{E}_\parallel + \mathscr{E}_\perp$ remains constant (in the absence of collisions, as magnetic fields cannot perform work on charged particles). As mentioned above, μ is an adiabatic invariant, and thus constant as well. To keep both $\mu = \mathscr{E}_\perp/B$ and the particle energy $\mathscr{E} = \mathscr{E}_\parallel + \mathscr{E}_\perp$ constant, the parallel energy of the particle, $\mathscr{E}_\parallel$ decreases when moving to regions of higher magnetic field strength B. If the B field becomes strong enough, the parallel velocity may reduce to zero and then be reversed, before the particle is accelerated in the direction of the weaker field. This effect is called *magnetic mirror* and results in a bounce movement of the particle. The turning point, or *bounce point*, is determined by the local magnetic field B_b and the angle of the particles initial velocities $v_{\parallel,\mathrm{i}}/v_{\perp,\mathrm{i}}$

$$\frac{B_\mathrm{b}}{B_\mathrm{i}} = 1 + \left(\frac{v_{\parallel,\mathrm{i}}}{v_{\perp,\mathrm{i}}}\right)^2, \tag{2.21}$$

where B_i is the magnetic field at the initial position [14]. The ratio of a particle's perpendicular velocity (containing drifts and gyromotion) to its parallel velocity is referred to as *pitch* λ or *pitch angle* λ^o:

$$\lambda := \frac{v_\parallel}{v}, \quad \text{or} \quad \cos\lambda^o := \frac{v_\parallel}{v}. \tag{2.22}$$

Although the pitch is sometimes used as second velocity space coordinate (besides the energy), one has to keep in mind, that it changes along the gyroorbit. At the reflection point, $\lambda = 0$.
Particles being *trapped* in inhomogeneous magnetic fields occur in cosmic phenomena such as the Van Allen radiation belt, and also in magnetic fusion devices, as explained in the next section.

2.2.3 Particle Orbits

Having introduced the concepts of drift (sec. 2.2.1) and magnetic mirror (sec. 2.2.2), particle trajectories in a twisted toroidal magnetic field, as it is in a TOKAMAK, can be sketched [14]. The magnetic field of a TOKAMAK has an intrinsic inhomogeneity leading to a magnetic mirror effect, as the field decreases with the radius R. As a consequence, there are two types of particle trajectories, the so-called *passing particles* and the *trapped particles*, as will be explained in the following.
In TOKAMAKs and – although in a more complicated way also in stellarators – the trapped particles bounce on the LFS within the well of the magnetic field. The minimum of the well is located at the outboard midplane ($\vartheta = 0$ in fig. 2.3), the maximum at the opposite side ($\vartheta = \pm\pi$). The trapped particles have insufficient parallel kinetic energy compared with their perpendicular energy to penetrate into the HFS of

the torus. Only particles with a parallel velocity that is high enough to let the particle overcome the mirror force $\boldsymbol{F}_{\mathrm{m}}$ can complete a poloidal revolution. These are the passing particles (for $v_{\parallel} > 0$, they are *co-passing* , for $v_{\parallel} < 0$ *counter-passing*).

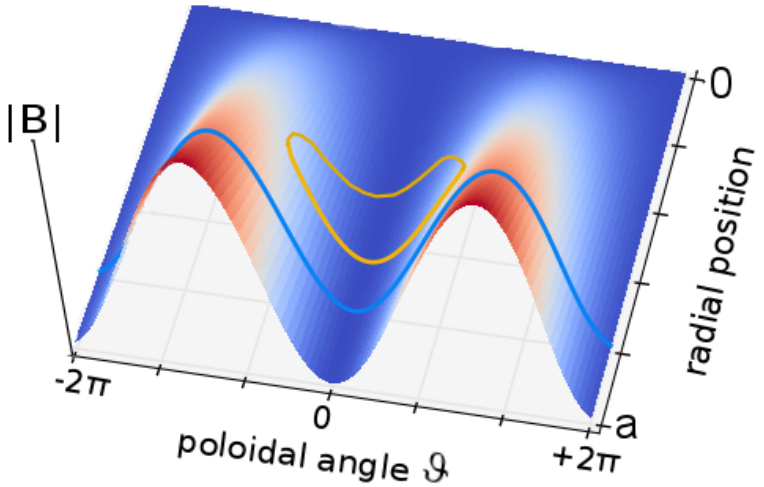

Figure 2.3: *Passing (blue) and trapped (yellow) particle orbits in a TOKAMAK's magnetic field (projection to the r-ϑ plane).*

The fraction of these trapped particles depends on the position $\varepsilon := r/R_{\mathrm{mag}}$ in the TOKAMAK [14],

$$f_{\mathrm{t}}(\epsilon,\vartheta) = \sqrt{\frac{\varepsilon + \varepsilon\cos\vartheta}{1+\varepsilon\cos\vartheta}}, \qquad \text{if} \quad B(\varepsilon,\vartheta) \approx B_{\mathrm{mag}}/(1+\varepsilon\cos\vartheta), \tag{2.23}$$

thus, increases with increasing r.

The helical movement of the particles is superimposed by a vertical drift movement due to the combined effects of field curvature and gradient. This leads to toroidally symmetric *drift surfaces* – surfaces defined by the particle trajectories. In the poloidal projection they resemble (almost) circles (in case of the passing particles) or so-called *banana orbits* (for the trapped particles respectively), see fig. 2.4, fig. 2.5. Note, that the magnetic surfaces do not coincide with the drift surfaces.

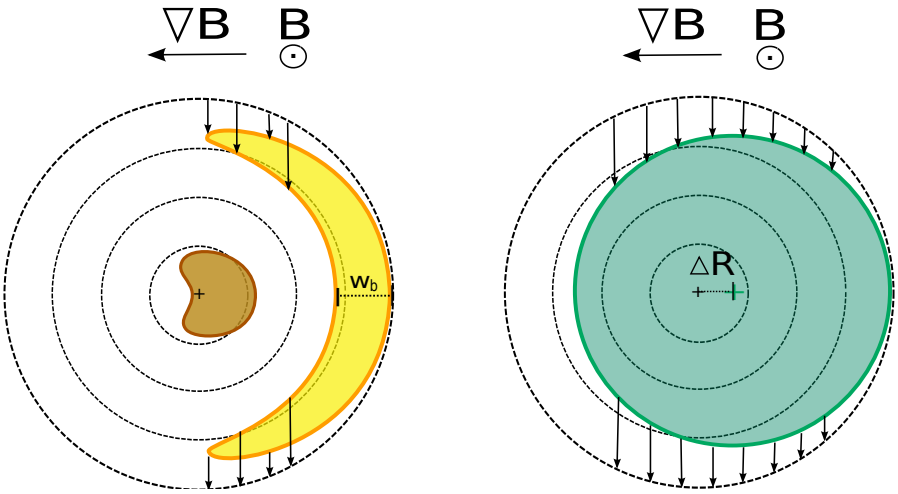

Figure 2.4: *Poloidal projections of the orbits of trapped (left) and passing (right) ions (thus the toroidal movement of the particles on the drift surfaces around the TOKAMAK cannot be seen here). The black lines represent a poloidal cut of the magnetic surfaces, the arrows indicate the drifts, leading to a deviation between the drift surfaces and the magnetic surfaces.*

Additional to the poloidally periodic movement, as seen in fig. 2.4, the particles also move periodically in the toroidal direction. This movement is visualized in fig. 2.5. Since the particle does not stay exactly on the field line, its orbit does not close on itself after one poloidal turn, but drifts to another field line. This implies that the particle undergoes a slow precession in the φ direction (see fig. 2.5), the *toroidal precession*. The toroidal precession frequency ω_{tp} is (see ref. [41]):

$$\omega_{tp} \approx \frac{q v_\perp^2}{2 r R_{mag} \Omega}. \tag{2.24}$$

Another important property of the particle movement is its orbit or *bounce frequency* ω_b, defined by the inverse of the transit time of one poloidal turn. In the following, a very rough estimation for the bounce frequency is given. For a more formal derivation of eq. (2.27) and eq. (2.34), involving elliptic integrals, in a large-aspect ratio approximation assuming circular flux surfaces can be found e.g. in [41]).
For strongly passing particles, the bounce frequency results from

$$\omega_b = \frac{2\pi}{T} = \frac{2\pi}{L_c / v_\parallel}, \tag{2.25}$$

where L_c is the connection length of the magnetic field helix. Considering one toroidal turn $N_t = 1$, the connection length can be given as $L_c \approx 2\pi R_{mag}/N_p$ with N_p the number of poloidal turns. Using the safety factor, eq. (2.2) this equals:

$$L_c = 2\pi q R_{mag}. \tag{2.26}$$

Thus,

$$\omega_b = \frac{v_\parallel}{q R_{mag}}. \tag{2.27}$$

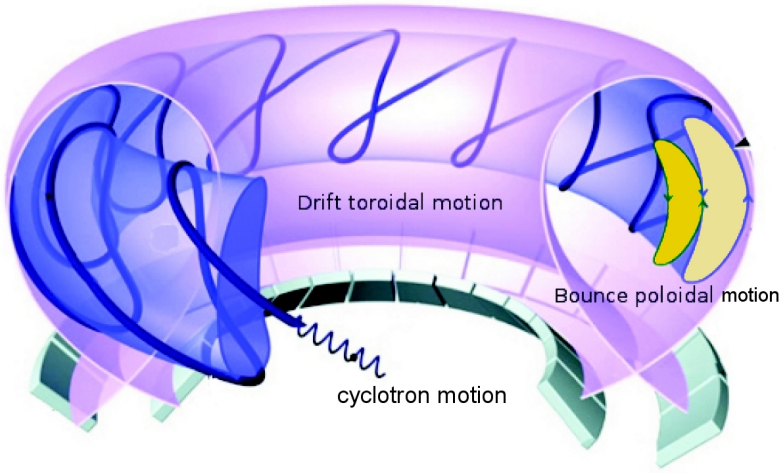

Figure 2.5: *A trapped particle's orbit in 3D to visualize the toroidal drift motion in addition to the poloidal bounce movement. Source: [42].*

For the wave particle interaction, the shifts caused by the drift movement are often crucial – for passing particles, this is the radial shift ΔR, for trapped particles it results in the banana orbit width W_b. In the following, a closer look is taken on it. One can focus on a poloidal cut, i.e. on a $\boldsymbol{e}_\mathrm{R}$-$\boldsymbol{e}_\mathrm{z}$ plane, knowing already that the drift v_d is in the z direction (eqs. (2.18) and (2.19)). The equations of motion are thus:

$$\begin{aligned} R &= R_\mathrm{mag} + \cos(\omega_\mathrm{b} t), \\ z &= v_\mathrm{d} t + \sin(\omega_\mathrm{b} t). \end{aligned} \tag{2.28}$$

The time derivative is then:

$$\begin{aligned} \dot{R} &= -z\omega_\mathrm{b} - v_\mathrm{d} t \omega_\mathrm{b}, \\ \dot{z} &= (R - R_\mathrm{mag})\omega_\mathrm{b} + v_\mathrm{d}. \end{aligned} \tag{2.29}$$

As the vertical drift will cancel out over the toroidal movement, it is valid to look at this poloidal cut at the initial time $t = 0$ only. One can easily prove, that the following circle equation is valid:

$$(R - R_\mathrm{mag} + v_\mathrm{d}/\omega_\mathrm{b})^2 + z^2 = \text{const.}, \tag{2.30}$$

meaning, that in this approximation, where the passing particle's orbit is a circle of the radius of the flux surface, the orbit is shifted from the magnetic axis R_mag by

$$\Delta R = \frac{v_\mathrm{d}}{\omega_\mathrm{b}} \approx \frac{v_\parallel^2 + \frac{1}{2} v_\perp^2}{v_\parallel v_\perp} \rho q \propto \rho q. \tag{2.31}$$

A trapped particle's bounce movement in the well of the magnetic field minimum can be treated as harmonic oscillator with the mirror force $F_\mathrm{R} = -\mu \, \partial / \partial s \, B$ as restoring force, acting on the magnetic moment μ along the particle trajectory s. As the change of

the magnetic field along the trajectory is crucial, one can not assume $B \approx B_{\mathrm{mag}}$ here, but may take $B(r) \approx B_{\mathrm{mag}}(1 - r/R_{\mathrm{mag}} \cos\vartheta)$ as given in eq. (4.15). Taylor expanding this around ϑ reads $B(r) \approx B_{\mathrm{mag}}(1 - r/R_{\mathrm{mag}} + r/R_{\mathrm{mag}}(\mathrm{d}\vartheta)^2/2$. As long as q is significantly above 1, one can approximate the distance traveled by a particle along the magnetic field line ds with its toroidal projection $R\mathrm{d}\varphi$, and thus after eq. (2.3), d$s = R_{\mathrm{mag}} q \mathrm{d}\vartheta$. In the expression for the magnetic field, dϑ can now be expressed by ds, the derivative of the magnetic field with respect to s leads to

$$F_{\mathrm{R}} = -\mu \frac{B_{\mathrm{mag}} r}{q^2 R_{\mathrm{mag}}^3} s. \tag{2.32}$$

The differential equation of motion of a harmonic oscillator with this restoring force reads

$$m\ddot{s} = -\mu \frac{B_{\mathrm{mag}} r}{q^2 R_{\mathrm{mag}}^3} s, \tag{2.33}$$

leading to an eigenfrequency of

$$\omega_{\mathrm{b}} = \frac{v_\perp}{q R_{\mathrm{mag}}} \sqrt{\frac{r}{2R_{\mathrm{mag}}}}. \tag{2.34}$$

This is the approximated bounce frequency of deeply trapped particles.
With the differential equation of motion, the angular movement along the magnetic field lines is known (one can consider now φ, instead of s, as they were assumed equivalent): $\varphi(t) = \hat{\varphi} \sin(\omega_{\mathrm{b}} t)$. However, the drift movement across the flux surface r was not taken into account so far. To cast the vertical movement (see fig. 2.4) into an expression for r, one can assume $\dot{r} = v_{\mathrm{d}} \sin\varphi \approx v_{\mathrm{d}} \varphi$. To obtain the projection of the particle orbit in the $\boldsymbol{e}_r$-$\boldsymbol{e}_\varphi$ plane, one has to calculate

$$\frac{\mathrm{d}r}{\varphi} = \frac{\mathrm{d}r/\mathrm{d}t}{\varphi/\mathrm{d}t} = \frac{v_{\mathrm{d}}}{\omega_{\mathrm{b}} \sqrt{(\hat{\varphi}/\varphi)^2 - 1}}. \tag{2.35}$$

After the φ integration, the banana orbit can be identified as

$$\left(\frac{r}{\hat{\varphi} v_{\mathrm{d}}/\omega_{\mathrm{b}}}\right)^2 + \left(\frac{\varphi}{\hat{\varphi}}\right)^2 = 1, \tag{2.36}$$

which is the equation of an ellipse with the two axes $\hat{\varphi}$ and $\hat{\varphi} v_{\mathrm{d}}/\omega_{\mathrm{b}}$ in the φ and the r direction respectively. The maximal width of the banana is twice the axis in the radial direction,

$$\begin{aligned} W_{\mathrm{b}} &= 2\frac{\hat{\varphi} v_{\mathrm{d}}}{\omega_{\mathrm{b}}}, \\ W_{\mathrm{b}} &\propto q\rho \sqrt{2R_{\mathrm{mag}}/r}. \end{aligned} \tag{2.37}$$

Thus, it is a factor of $q/\sqrt{\varepsilon}$, with $\varepsilon := r/R_{\mathrm{mag}}$ larger than the gyroradius.

After having introduced main aspects of particle motion in this chapter, the next chapter is dedicated to the second actor within the fast particle-wave interplay, the waves.

CHAPTER 3

MHD Waves and their Interaction with Fast Particles

A well established model for understanding the large scale physics of plasmas is the *magnetohydrodynamic* (MHD) theory [43]. In this theory, the plasma is seen as a current-carrying, conductive *fluid*. The basic idea is to look only at macroscopic dimensions such as density, fluid velocity and temperature. Thus, a velocity space dependence is neglected and a collisional plasma[1] assumed.
The general equations that describe the ideal[2] plasma this way are called MHD equations:

$$\frac{\partial}{\partial t}\rho = -\nabla\cdot(\rho\boldsymbol{v}), \qquad \text{continuity equation (=mass conserv.)} \tag{3.1a}$$

$$\rho\left(\frac{\partial}{\partial t}+\boldsymbol{v}\cdot\nabla\right)\boldsymbol{v} = -\nabla p+\boldsymbol{j}\times\boldsymbol{B}, \qquad \text{momentum conservation} \tag{3.1b}$$

$$\left(\frac{\partial}{\partial t}+\boldsymbol{v}\cdot\nabla\right)p = -\gamma p\nabla\cdot\boldsymbol{v}, \qquad \text{adiabatic equation for an ideal gas} \tag{3.1c}$$

$$\frac{\partial}{\partial t}\boldsymbol{B} = \nabla\times(\boldsymbol{v}\times\boldsymbol{B}), \qquad \text{Faraday's induction law} \tag{3.1d}$$

$$\boldsymbol{E} = -\boldsymbol{v}\times\boldsymbol{B}, \qquad \text{Lorentz trafo to a co-moving frame} \tag{3.1e}$$

$$\boldsymbol{j} = \frac{1}{\mu_0}\nabla\times\boldsymbol{B}, \qquad \text{Ampère's law (non-relativistic)} \tag{3.1f}$$

$$\nabla\cdot\boldsymbol{B} = 0, \qquad \text{non-existence of magnetic monopoles} \tag{3.1g}$$

Here, ρ is the plasma mass density, n the plasma particle density, $\boldsymbol{v}$ the velocity of the plasma, p the pressure, γ the adiabatic coefficient, $\boldsymbol{B}$ and $\boldsymbol{E}$ the magnetic and electric field, ρ_{el} the charge density, and $\boldsymbol{j}$ the current density.
The ideal MHD in this case is a so-called *single-fluid model*, as the plasma's composition of different particle species is not taken into account. Considering ions and electrons as different species is possible within the MHD as well: one assumes two different fluids penetrating each other, what is called a *multi-fluid model*.

Every motion of the plasma will give rise to electromagnetic forces, as it consists of charged particles. The emerging currents will, due to the magnetic field, lead to

[1] Thus a plasma in which a Maxwellian distribution is always established.
[2] i.e. without any energy dissipation: an infinite electric conductivity is assumed, as well as zero heat conductivity and zero viscosity.

mechanical forces that change the state of motion of the plasma. Thus, a *combined electromagnetic-hydrodynamic wave* is created, a fact pointed out first by Hannes Alfvén in 1942 [44]. These *Alvfén waves* are ubiquitous in astrophysical as well as in laboratory plasmas. The next sections are dedicated to approach Alfvén waves and – more general – MHD waves, as they exist specifically in fusion devices.

3.1 Theory of MHD Waves

The equations of ideal MHD, eqs. (3.1), are nonlinear, but they can be used in a linearized form to identify classes of waves. Such approximation is valid for the examination of perturbations with relatively small magnitudes: The *bulk plasma*, i.e. the initial, non-perturbed state, can then be considered static on timescales that are large compared to those associated with the small scale perturbation dynamics. Thus, all quantities $Q(\boldsymbol{x},t)$ can be separated into an equilibrium part $Q_0(\boldsymbol{x})$ and a small, first-order time-dependent perturbation: $\tilde{Q}(\boldsymbol{x},t)$. All higher order terms are neglected, assuming $|\tilde{Q}| \ll |Q_0|$. Furthermore, a global plasma motion is neglected: $\boldsymbol{v}_0 = 0$. After introducing a *displacement vector*:

$$\tilde{\boldsymbol{v}} =: \frac{\partial \boldsymbol{\xi}}{\partial t}, \tag{3.2}$$

the linearized momentum conservation, eq. (3.1b), adiabatic equation, eq. (3.1c) and Faraday's law, eq. (3.1d) read

$$0 = \rho_0 \frac{\partial^2 \boldsymbol{\xi}}{\partial t^2} + \nabla \tilde{p}, + \frac{1}{\mu_0}(\tilde{\boldsymbol{B}} \times (\nabla \times \boldsymbol{B}_0)) + \boldsymbol{B}_0 \times (\nabla \times \tilde{\boldsymbol{B}}), \tag{3.3a}$$

$$0 = \tilde{p} + \boldsymbol{\xi} \cdot \nabla p_0 + \gamma p_0 \nabla \cdot \boldsymbol{\xi}, \tag{3.3b}$$

$$0 = \tilde{\boldsymbol{B}} + \nabla \times (\boldsymbol{B}_0 \times \boldsymbol{\xi}). \tag{3.3c}$$

One can now resolve eq. (3.3b) for $\tilde{p}$ and substitute this, together with $\tilde{\boldsymbol{B}}$ from eq. (3.3c) into eq. (3.3a), and obtain the so-called force-operator equation,

$$\rho_0 \frac{\partial^2}{\partial t^2} \boldsymbol{\xi} = \boldsymbol{F}(\boldsymbol{\xi}). \tag{3.4}$$

$\boldsymbol{F}(\boldsymbol{\xi})$ is the hermitian force operator

$$\begin{aligned} \boldsymbol{F}(\boldsymbol{\xi}) := \nabla(\boldsymbol{\xi} \cdot \nabla p_0 + \gamma p_0 \nabla \cdot \boldsymbol{\xi}) \; + \; & \frac{1}{\mu_0}[(\nabla \times \boldsymbol{B}_0) \times (\nabla \times (\boldsymbol{\xi} \times \boldsymbol{B_0})) \\ & + (\nabla \times (\nabla \times (\boldsymbol{\xi} \times \boldsymbol{B}_0))) \times \boldsymbol{B}_0] \end{aligned} \tag{3.5}$$

The linear stability of waves can be studied as a normal mode problem, assuming a time variation of all perturbed quantities to be of the form $\tilde{Q}(\boldsymbol{x},t) = Q(\boldsymbol{x}) \exp(-i\omega t)$. Eq. (3.4) can then be written as eigenvalue problem for the eigenvalue ω^2:

$$-\omega^2 \boldsymbol{\xi} = \frac{1}{\rho_0} \boldsymbol{F}(\boldsymbol{\xi}), \tag{3.6}$$

As the force operator is Hermitian, the eigenvalue is real, which leads to ω taking either purely real values (if $\omega^2 > 0$) or purely imaginary values (if $\omega^2 < 0$). The first case represents an oscillating wave, the latter a growing/damped instability.

3.1.1 MHD Waves in a Homogeneous Plasma

Let us assume a homogeneous magnetic field $\boldsymbol{B}$ in an infinite, homogeneous, stationary plasma. After Fourier transforming the force-operator equation, eq. (3.4), according to $\boldsymbol{\xi} = \hat{\boldsymbol{\xi}} \exp(-i\omega t - i\boldsymbol{k}\cdot\boldsymbol{x})$, one obtains:

$$\begin{aligned} -\rho_0\omega^2\hat{\boldsymbol{\xi}} &= \nabla(\hat{\boldsymbol{\xi}}\cdot\nabla p_0 - \mathrm{i}\gamma p_0 \boldsymbol{k}\cdot\hat{\boldsymbol{\xi}}) \\ &\quad + \frac{1}{\mu_0}\left[(\nabla\times\boldsymbol{B}_0)\times(-i\boldsymbol{k}\times(\hat{\boldsymbol{\xi}}\times\boldsymbol{B}_0)) + (-i\boldsymbol{k}\times(-i\boldsymbol{k}\times(\hat{\boldsymbol{\xi}}\times\boldsymbol{B}_0)))\times\boldsymbol{B}_0\right]. \end{aligned} \tag{3.7}$$

In a homogeneous plasma, all derivatives of equilibrium quantities, such as ∇p_0 or $\nabla\times\boldsymbol{B}_0$ vanish. Without loss of generality, we can assume the equilibrium magnetic field to be parallel to the z direction, i.e. $\boldsymbol{B}_0 = B_0\boldsymbol{e}_z$ and $\boldsymbol{k} = k_\perp\boldsymbol{e}_y + k_\parallel\boldsymbol{e}_z$. We further take the *Alfvén velocity* v_A and the *adiabatic sound velocity* v_S, which are

$$v_\mathrm{A} := \frac{B_0}{\sqrt{\mu_0\rho_0}}, \tag{3.8}$$

$$v_\mathrm{S} := \sqrt{\frac{\gamma p_0}{\rho_0}}, \tag{3.9}$$

and rewrite the eq. (3.7) to

$$0 = \begin{pmatrix} \omega^2 - v_\mathrm{A}^2k_\parallel^2 & 0 & 0 \\ 0 & \omega^2 - v_s^2k_\perp^2 - v_\mathrm{A}^2k^2 & -v_\mathrm{S}^2k_\perp k_\parallel \\ 0 & -v_\mathrm{S}^2k_\perp k_\parallel & \omega - v_\mathrm{S}^2k_\parallel^2 \end{pmatrix} \begin{pmatrix} \hat{\xi}_x \\ \hat{\xi}_y \\ \hat{\xi}_z, \end{pmatrix} \tag{3.10}$$

or, as a system of equations:

$$0 = (\omega^2 - v_\mathrm{A}^2k_\parallel^2)\,\hat{\xi}_x, \tag{3.11a}$$

$$0 = (\omega^2 - v_s^2k_\perp^2 - v_\mathrm{A}^2k^2)\,\hat{\xi}_y - v_\mathrm{S}^2k_\perp k_\parallel\,\hat{\xi}_z, \tag{3.11b}$$

$$0 = -v_\mathrm{S}^2k_\perp k_\parallel\,\hat{\xi}_y + (\omega - v_\mathrm{S}^2k_\parallel^2)\,\hat{\xi}_z. \tag{3.11c}$$

It can be seen now that the x component of $\hat{\boldsymbol{\xi}}$ decouples from the other two spacial directions.
Non-trivial solutions for $\hat{\boldsymbol{\xi}}$ to this eigenvalue equation require a vanishing determinant of the matrix in eq. (3.10),

$$(\omega^2 - v_\mathrm{A}^2k_\parallel^2)\left[\omega^4 - (v_\mathrm{A}^2 + v_\mathrm{S}^2)k^2\omega^2 + (v_\mathrm{A}v_\mathrm{S}k_\parallel k)^2\right] \stackrel{!}{=} 0. \tag{3.12}$$

Each solution of this equation represents a mode plasma perturbation, and since it is cubic in ω^2, three types are expected. The first solution is seen easily, as the $\hat{\xi}_x$ branch decouples:

$$\omega^2 = v_\mathrm{A}^2k_\parallel^2. \tag{3.13}$$

giving the dispersion relation of the so-called *Shear-Alfvén wave* in a homogeneous plasma. As the right hand side is a quadrature and therefore always positive, the perturbation is oscillatory. Further, it is independent of $k_\perp$, even if $k_\perp \gg k_\parallel$, meaning that

the propagation direction is along the equilibrium magnetic field: $\boldsymbol{k} = k_{\parallel}\boldsymbol{e}_z$.
Since it is decoupled from the y and z direction, the plasma displacement of the Shear-Alfvén wave is purely perpendicular to the equilibrium field, $\hat{\xi}_x \perp \boldsymbol{B}_0 = B_0\boldsymbol{e}_z$. Substituting $\hat{\boldsymbol{\xi}} = \hat{\xi}_x\boldsymbol{e}_x$ into eq. (3.3c) gives a $\tilde{\boldsymbol{B}} = -i\hat{\xi}_x k_{\parallel} B_0 \boldsymbol{e}_x$ which is $\perp \boldsymbol{B}_0$, thus reveals the purely transverse nature of the Shear-Alfvén wave's field perturbation. Substituting $\hat{\boldsymbol{\xi}}$ into eq. (3.3b) reveals $\tilde{p} = 0$, and thus the incompressible nature of the Shear-Alfvén wave.
Summarized, the Shear-Alfén wave is an incompressible oscillation of the plasma inertia against the magnetic field line tension producing a restoring force. Both the field line perturbation $\tilde{\boldsymbol{B}}$ and the plasma displacement $\hat{\boldsymbol{\xi}}$ are perpendicular to the propagation direction $\boldsymbol{k}$, which is parallel to the equilibrium magnetic field $\boldsymbol{B}_0$.

The two other solutions result from the square bracket in eq. (3.10):

$$\omega^2 = \frac{1}{2}k^2(v_{\mathrm{A}}^2 + v_{\mathrm{S}}^2)\left[1 \pm \sqrt{1 - 4\underbrace{\frac{k_{\parallel}^2}{k^2}\frac{v_{\mathrm{A}}^2 v_{\mathrm{S}}^2}{(v_{\mathrm{A}}^2 + v_{\mathrm{S}}^2)^2}}_{:=\delta(>0)}}\right]. \tag{3.14}$$

With the plus sign, one obtains the dispersion relation for the *fast magnetosonic wave*, with the minus the *slow magnetosonic wave*. The magnetosonic wave emerges from the coupling between the magnetic compression (Alfvénic) and the fluid compression (sonic). In contrast to the Shear-Alfvén wave, the magnetosonic waves are characterized by transversal as well as longitudinal components of both, the plasma displacement $\hat{\boldsymbol{\xi}}$ and the magnetic perturbation $\tilde{\boldsymbol{B}}$, and are compressible, i.e. $\tilde{p}$ and $\nabla \cdot \tilde{\boldsymbol{v}} \neq 0$. In any case, the fast magnetosonic wave oscillates ($\omega^2 > 0$), and its frequency is higher than that of the Shear-Alfvén wave.
In the next step, a limiting situation is considered, the limit of a low-plasma 'beta' parameter, β which is the ratio of plasma pressure to the magnetic field pressure:

$$\beta = \frac{2\mu_0\, p}{B^2}. \tag{3.15}$$

Inserting p and B from the definition of the adiabatic sound velocity, eq. (3.9) and the Alfvén velocity, eq. (3.8) respectively, β reads

$$\beta = \frac{2}{\gamma}\frac{v_{\mathrm{S}}^2}{v_{\mathrm{A}}^2}. \tag{3.16}$$

Most astro- or geophysical observations are related to a high β value, meaning that the plasma fluid is '*frozen*' to the magnetic field lines. In fusion plasmas, one has to deal with the opposite case in general, the low-β limit resulting in the ratio $v_{\mathrm{S}}^2/v_{\mathrm{A}}^2 \ll 1$. This ratio can thus be chosen as smallness parameter ε. It can then be seen, that the δ term

is of the order $\mathcal{O}(\geq \varepsilon)$, too:

$$\delta = 4 \underbrace{\frac{k_\parallel^2}{k_\parallel^2 + k_\perp^2}}_{<1} \underbrace{\frac{1}{(1+\varepsilon)^2}}_{\text{Taylor exp.}} \varepsilon. \\ \simeq (1+4\varepsilon) \tag{3.17}$$

Therefore, the whole square-root term in eq. (3.14) can be Taylor expanded giving (up to the order of $\mathcal{O}(\varepsilon)$) $\sqrt{1-\delta} \simeq 1 - 1/2\delta$. Thus, the slow wave's dispersion relation becomes in the low-β limit:

$$\omega^2 \;=\; k_\parallel^2 \frac{v_S^2}{1+\varepsilon} \;\simeq\; k_\parallel^2 v_S^2. \tag{3.18}$$

In the zero-th order in v_S^2/v_A^2 approximation, the slow magnetosonic wave's dispersion relation yields

$$\omega^2 \;\simeq\; k_\parallel^2 v_S^2, \tag{3.19}$$

which is the familiar *ion sound wave*'s dispersion relation. Inserting ω^2 from eq. (3.19) into eq. (3.11c) gives deeper insight into the nature of the slow wave: it can only be valid if either $k_\perp = 0$ or $\hat{\xi}_z = 0$. However, the latter would lead to a $\hat{\xi}_y = 0$ as well (second of eqs. (3.11)), resulting in no wave at all, whereas $\hat{\xi}_y = 0$ and $k_\perp = 0$ still allow for a parallel displacement vector $\hat{\xi}_z$. The slow wave therefore propagates parallel to the equilibrium field ($k_\parallel$) at the speed v_S. It is characterized by a pure longitudinal plasma displacement $\hat{\xi}_z$. Using these findings in $\tilde{\boldsymbol{B}} = -i\boldsymbol{k} \times (\boldsymbol{B}_0 \times \hat{\boldsymbol{\xi}})$ (eq. (3.3c) in Fourier space) results in $\tilde{\boldsymbol{B}} = 0$. This means, there is no magnetic field perturbation involved at all, the energy oscillates within the plasma between kinetic and internal energy.

Analogously to the "− branch" of the magnetosonic wave in eq. (3.14), one can derivate for the "+ branch", the fast wave

$$\omega^2 \;=\; \frac{k^2\varepsilon^2 + (k^2 + k_\perp^2)\varepsilon + k^2}{1+\varepsilon} v_A^2, \tag{3.20}$$

giving in the zero-th order in v_S^2/v_A^2 approximation the dispersion relation of the fast magnetosonic wave (in this limit the *compressional Alfvén wave*):

$$\omega^2 \;\simeq\; k^2 v_A^2. \tag{3.21}$$

The fast magnetosonic wave propagates isotropically with the speed v_A. Inserting here again ω^2 from eq. (3.21) into eq. (3.11c) and dividing by v_A^2, one can easily see that the parallel plasma displacement $\hat{\xi}_z$ is of order v_S^2/v_A^2 compared to the perpendicular one $\hat{\xi}_y$. Thus, the plasma motion is almost transverse. Fast waves describe the interchange between the energy needed to bend and compress the magnetic field with perpendicular plasma energy.

As could be seen, ideal MHD waves display a strong anisotropy. Since all three types of MHD waves have constant phase velocities $v_{\mathrm{Ph}} = \omega/k$ (at least along a fixed direction of $\boldsymbol{k}$), given by eq. (3.13) and eq. (3.14), there is no wave dispersion.

As $\omega^2 > 0$, the waves described above are stable in homogeneous equilibria. However, this is not generally the case in fusion relevant geometries, which are the topic of the next section.

3.1.2 Shear-Alfvén Waves in Fusion Plasmas – TAE and RSAE

In magnetic fusion devices, the plasma cannot be considered as homogeneous. Considering an inhomogeneous plasma geometry, one might begin with asking about the presumably least damped types of waves. A first guess can be made by examining the dispersion relations in the homogeneous geometry, eqs. (3.13) and (3.14), and viewing the wave numbers as effective spring constants: the larger the spring constant in a wave equation, the less is the wave destabilized under external perturbation. As $k_\parallel \leq \sqrt{k_\parallel^2 + k_\perp^2}$, the Shear-Alfvén waves are expected to be less stable than the compressional waves, especially in TOKAMAKs, where $k_\parallel < k_\perp$. The presence of inhomogeneities in the plasma density and magnetic field strongly affects the character of the waves, making both k and v_{A} space dependent. Assuming a local limit, were a *local* dispersion relation is considered valid $\omega = k_\parallel(r) v_{\mathrm{A}}(r)$, one can easily see, that no wave packet of non-vanishing width (spectral or radial) can persist for a long time, as each slice of the wave has to fulfill its local dispersion relation. The different slices move with different velocities and in different directions. This effect is called *phase mixing* and leads to the damping of any initial wave. However, the effect of toroidal geometry introduces some new physical effects, that cannot be anticipated with the help of this simple picture.
To derive the force-operator equation similar to eq. (3.10), but in fusion-relevant toroidal geometry is far more involved even when applying several approximations. Helpful milestones of the derivation are given in the technical report of Berk, ref. [45]. Here, a short overview is given in the following.

Toroidicity-induced Shear-Alfvén Eigenmode

Just like in the homogeneous plasma, one considers small perturbations $\tilde{\boldsymbol{B}} \ll \boldsymbol{B}_0$ only, allowing for a linearization of the MHD equations. Again, the equations to start with are the momentum balance equation (eq. (3.1b)) and the MHD continuity equation (eq. (3.1a)). Further the potential definitions, Maxwell's equations and the linearized E-cross-B drift velocity (eq. (2.17)) are used, assuming that the fluid velocity $\tilde{\boldsymbol{v}}$ is mainly given by the perturbed $\tilde{\boldsymbol{E}} \times \boldsymbol{B}_0$ motion. The theory is restricted to Shear-Alfvén waves as described in subsec. 3.1.1. This allows to neglect density perturbations $\tilde{p}$, to set $\tilde{B}_\parallel = 0$, as well as $\tilde{E}_\parallel = 0$ (due to the divergence-free nature of the electric field in ideal MHD, $\boldsymbol{k} \cdot \boldsymbol{E} = 0$ and $\boldsymbol{k} \| \boldsymbol{B}_0$). Again, a steady-state equilibrium is assumed, neglecting equilibrium electrostatic potentials ($\Phi_0 = 0$) and equilibrium plasma movement ($\boldsymbol{v}_0 = 0$). Further, the low-β limit is considered, that allows one to ignore the

equilibrium plasma pressure ($p_0 = 0$) terms.
All quantities are rewritten in a straight field line coordinate system (see sec. 4.2.2), under the assumption of a large-aspect ratio (see eq. (2.1)), i.e. one can chose the inverse (local) aspect ratio as a smallness parameter $\varepsilon := r/R_{\text{mag}}$. In the presented first order approximation of toroidicity, all terms of $\mathcal{O}(\varepsilon^2)$ and higher are neglected. The terms of order $\mathcal{O}(\varepsilon)$ are kept only if there is a second derivative in the perturbed quantity. The electric potential perturbation is then assumed to depend on the radial position r in its amplitude, and to be periodic in the toroidal ζ as well as the poloidal θ direction. Thus, it can be expressed as a Fourier composition of all poloidal harmonics m and toroidal harmonics n:

$$\tilde{\Phi} = \sum_{n,m} \Phi_{n,m}(r) \exp(-\mathrm{i}m\theta + \mathrm{i}n\zeta). \tag{3.22}$$

As will be seen later, the mode (n,m) is coupled only poloidally, and in this approximation, only to the neighboring poloidal harmonic $m \pm 1$. Due to axis symmetry, they are completely independent on each other in the toroidal direction, and therefore, one can calculate $\tilde{\Phi}$ for each n individually. In the following, we focus on the calculation of one arbitrary n, i.e. drop the sum over n for simplicity. A new wave function is introduced,

$$\tilde{E}_m(r) = \frac{1}{r}\Phi_m(r), \tag{3.23}$$

giving a set of equations, one equation for each poloidal harmonic. This set is coupled: each equation for the mth poloidal harmonic $\tilde{E}_m$ includes terms of the neighboring harmonics $\tilde{E}_{m\pm1}$ as well. At this point, a parallel wave vector is introduced,

$$k_{\parallel} = \frac{1}{R_{\text{mag}}}\left(n - \frac{m}{q(r)}\right). \tag{3.24}$$

It is shown in app. C, sec. C.2, that $k_{\parallel}$ is the parallel wave vector of the cylindrical limit, i.e. the wave equation in zeroth-order approximation (leaves away all terms $\mathcal{O}(\geq \varepsilon)$). To get rid of the dependence of θ and ζ, one multiplies with the complex conjugate $\exp(\mathrm{i}m\theta - \mathrm{i}n\zeta)$ and integrates over both angles. In a last step, in small terms, such as those with the radial derivative of the Shafranov shift as well as those $\propto r/R_{\text{mag}}$, the wave vector is replaced by its gap value. The *gap* is the position where the wave vector of m equals those of the neighboring harmonics $m+1$. Its value is then given by the Shear-Alfvén dispersion relation. At all other radial positions, terms of the order $\mathcal{O}(\varepsilon)$ can be neglected.
The final form of the Shear-Alfvén wave equation in the low-β limit in large-aspect ratio toroidal geometry reads [45]:

$$0 = \begin{pmatrix} P_m & Q \\ Q & P_{m+1} \end{pmatrix} \begin{pmatrix} \tilde{E}_m \\ \tilde{E}_{m+1} \end{pmatrix}. \tag{3.25}$$

The diagonal elements P and the off-diagonal elements Q are the following differential operators:

$$\begin{aligned} P_m &= \frac{\mathrm{d}}{\mathrm{d}r} r^3 \left(\frac{\omega^2}{v_A^2} - k_{\parallel m}^2 \right) \frac{\mathrm{d}}{\mathrm{d}r} \; - \; (m^2-1) r \left(\frac{\omega^2}{v_A^2} - k_{\parallel m}^2 \right) \; + \; \left(\frac{\omega^2}{v_A^2} \right)' r^2, \\ Q \;\; &= \frac{5}{2} \varepsilon \frac{\mathrm{d}}{\mathrm{d}r} \frac{\omega^2}{v_A^2} \frac{r^4}{a} \frac{\omega^2}{v_A^2}. \end{aligned} \tag{3.26}$$

The prime ($'$) denotes the radial derivation. This is the Shear-Alfvén wave equation for the first order toroidal approximation. The first order of toroidicity is kept in all terms of the second derivative $\mathrm{d}^2\tilde{E}_m/\mathrm{d}r^2$, since they become significant only in the gap regions, i.e. the regions where the second derivatives almost vanish. In all other terms, toroidicity is neglected. These wave equations are coupled to the neighboring poloidal harmonic due to the toroidal geometry imposed by the toroidal system.
In the cylindrical limit, the off-diagonal elements vanish, leaving a decoupled system of equations [46]:

$$\begin{aligned} 0 &= P_m \; \tilde{E}_m, \\ 0 &= \frac{\mathrm{d}}{\mathrm{d}r} r^3 \left(\frac{\omega^2}{v_A^2} - k_{\parallel m}^2 \right) \frac{\mathrm{d}}{\mathrm{d}r} \; \tilde{E}_m \; - \; (m^2-1) r \left(\frac{\omega^2}{v_A^2} - k_{\parallel m}^2 \right) \; \tilde{E}_m \; + \; \left(\frac{\omega^2}{v_A^2} \right)' r^2 \; \tilde{E}_m. \end{aligned} \tag{3.27}$$

In the following, the physical nature of Shear-Alfvén modes in toroidal devices is investigated. The wave equation eq. (3.25) is a second order linear ordinary differential equation for the wave amplitude $\tilde{E}$ depending on the radial coordinate r. If the coefficient in front of the second derivative becomes zero, the equation is fulfilled only by $\tilde{E}(r) = 0 \; \forall r$. The condition that leads to this case, forbidding the existence of any Shear-Alfvén wave, is called the *Shear-Alfvén continuum*. As the wave equation is a coupled system of equations, this condition can be calculated by setting the determinant of the coefficients in front of the second derivative terms equal zero [47]:

$$0 = \underbrace{r^3 \left(\frac{\omega^2}{v_\mathrm{A}^2} - k_{\parallel m} \right)}_{\text{from } P_m} \underbrace{r^3 \left(\frac{\omega^2}{v_\mathrm{A}^2} - k_{\parallel m+1} \right)}_{\text{from } P_m+1} \; - \; \underbrace{\left(\frac{5}{2} \frac{\omega^2}{v_\mathrm{A}^2} \varepsilon \frac{r^4}{a} \right)^2}_{Q^2}. \tag{3.28}$$

Solving for ω^2 gives

$$\omega^2(r) = \underbrace{\frac{k_{\parallel m}^2 + k_{\parallel m+1}^2 \; \pm \; \sqrt{(k_{\parallel m}^2 - k_{\parallel m+1}^2)^2 + 4 \left(\frac{5}{2} \varepsilon \frac{r}{a} \right)^2 k_{\parallel m}^2 k_{\parallel m+1}^2}}{2 \left(1 - \left(\frac{5}{2} \varepsilon \frac{r}{a} \right)^2 \right)}}_{\bar{k}_\parallel} \; v_\mathrm{A}^2. \tag{3.29}$$

In the cylindrical limit, the Q term within the determinant does not exist, leading to a decoupling of m and $m+1$. Performing the transition from first order toroidicity to

cylinder means setting $\varepsilon \to 0$. This simplifies Eq. (3.29) to

$$\omega^2(r) = \begin{cases} +k_{\parallel m}^2 \quad v_{\mathrm{A}}^2 \\ -k_{\parallel m+1}^2 v_{\mathrm{A}}^2. \end{cases} \tag{3.30}$$

Note two important facts: through $k_{\parallel m}$ and v_{A}, the Shear-Alfvén continuum eq. (3.29) depends on the q profile and the density profile $n(r)$. Also, the wave vector is now space dependent. Second: although eq. (3.30) formally looks like the dispersion relation for the Shear-Alfvén wave in an homogeneous plasma (eq. (3.13)), these equations for the Shear-Alfvén continua express the contrary, resonant absorption of the Alfvénic waves (evoked by the inhomogeneous plasma geometry). The Shear-Alfvén continuum gives those frequencies $\omega(r)$ that are strongly damped (at least in the frame of this theory). Therefore, the damping is referred to as *continuum damping* [48]. The effect of phase mixing is smallest in regions where the Shear-Alfvén continuum is flat. This is the case, where both $q(r)$ and $n(r)$ are relatively flat. These locations can be viewed as a potential site for a Shear-Alfvén mode. Thus, n- and q profile affect strongly the radial structures of Shear-Alfvén modes.

In the MHD model, the radial structure of the wave field perturbation $\tilde{E}$ (obtained from eq. (3.25) or also eq. (3.27)) has a singularity at the radial surface where the mode frequency is resonant with the local continuum, $\omega = k_{\parallel}(r)v_{\mathrm{A}}(r)$ – the resonant layer. Ideal MHD does not allow the wave to propagate perpendicular to the magnetic field ($\omega \neq \omega(k_{\perp})$), but causes resonant absorption. Within the MHD model, the singularity is resolved only outside the continuum. However, if one goes beyond MHD, accounting for kinetic effects, the singularity in the vicinity of the resonant layer can be resolved. In this region, the perpendicular wavelength $2\pi/k_{\perp}$ is non-negligible, since it becomes comparable to the ion gyroradius ρ_i, and finite Larmor radius (FLR) effects become important. The ions do not need to follow the magnetic field lines any more, whereas the electrons do (due to their smaller gyroradius). This results in a charge separation and a coupling to the Kinetic Alfvén Waves (KAW). Mathematically, the singularity is resolved in eq. (3.25) and eq. (3.27) due to higher order derivatives. At the resonance layer, the concept of phase-mixing is replaced by the concept of *mode conversion* [49] from an MHD eigenmode to a short wavelength KAW. Thus, the KAW can intersect the continuum.

When plotting the Shear-Alfvén continuum for the toroidal case, one can see the disappearance of the crossing point, giving rise to a gap instead, the *Shear-Alfvén gap*. Within this model, Alfvén modes in toroidal geometry such as a TOKAMAK can be excited only at frequencies, where there is a gap in this continuum and therefore, the continuum damping is weak (typically $\gamma/\omega = 0.01 \ldots 0.1\%$) [49]. These waves are called *Toroidicity-induced Alfvén eigenmodes* (TAE) [50, 51]. However, in case the mode spreads over a wide radial range, parts of its structure might intersect with a local Alfvén resonance. The eigenmode then experiences a small amount of continuum damping [52–54].

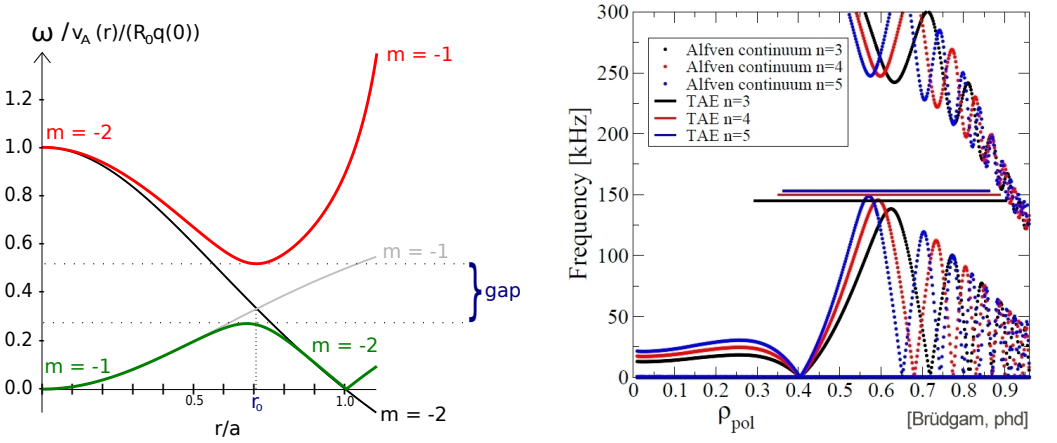

(a) *given analytically.* (b) *given numerically (by the* CASTOR *code) [55].*

Figure 3.1: *Toroidal Shear-Alfvén continuum (a) for a safety factor profile* $q = 1 + (r/a)^2$*, constant density profile* $n(r) = \text{const.}$ *and* $B = B_0(1 - r/R_{\text{mag}})$*; the cylindrical spectra (gray curves) for m=-1 and m=-2, with n=-1 cross at the flux surface where* $q = 1.5$*. (b) numerically calculated for an* ASDEX *Upgrade equilibrium.*

Fig. 3.1a shows both, the Shear-Alfvén continuum in cylindrical (gray curves) and in toroidal (colored curves) geometry. The two curves for the neighboring harmonics in the cylindrical case cross at a radial position, say r_0, which is the position of the gap in the toroidal geometry. Via

$$k_{\parallel m} v_A \stackrel{!}{=} -k_{\parallel m+1} v_A$$

one obtains an expression for q at this radial position r_0,

$$q(r_0) = \frac{m + \frac{1}{2}}{n}. \tag{3.31}$$

It is also possible to calculate the frequency of the crossing-point (eq. (3.30)), which is approximately the TAE frequency ω_{TAE}:

$$\omega_{\text{TAE}} = \omega(r_0) = \frac{v_A}{2qR_{\text{mag}}}. \tag{3.32}$$

Inserting $k_{\parallel m+1} = -k_{\parallel m}$ into the toroidal Shear-Alfvén continuum eq. (3.29) gives the width of the gap $\Delta\omega$:

$$\begin{aligned} \omega(r_0) &= \frac{k_{\parallel m} v_A}{\sqrt{1 \mp \frac{5}{2}\varepsilon\frac{r}{a}}} \simeq k_{\parallel m} v_A \left(1 \pm \frac{1}{2}\frac{5}{2}\varepsilon\frac{r}{a}\right) \\ \Rightarrow \Delta\omega &= |\omega_+(r_0) - \omega_-(r_0)| \approx k_{\parallel m} v_A \frac{5}{2}\varepsilon\frac{r}{a}. \end{aligned} \tag{3.33}$$

TAEs are characterized by global radial extent with their maximum located at the radial position r_0 of the gap, which strongly depends on the q profile. In the spectrum, their frequencies are located at either gap boundary (usually 100-300 kHz). Due to the coupling, each mode consists of two neighboring poloidal harmonics in this model. If both harmonics are in phase – which is the case for modes with frequencies at the lower gap boundary – the mode is called *even*. If their phase is opposite to each other – that happens for frequencies at the upper gap boundary – the mode is *odd* (both see fig. 3.2). As a consequence, even modes interfere constructively only on the LFS, an effect that is often referred to as *ballooning*. Even TAEs are more frequently observed than odd TAE, which exist only in low-shear plasmas [56]. It becomes clear, that the alignment of the gap structure strongly affects the mode structure also in the poloidal direction.

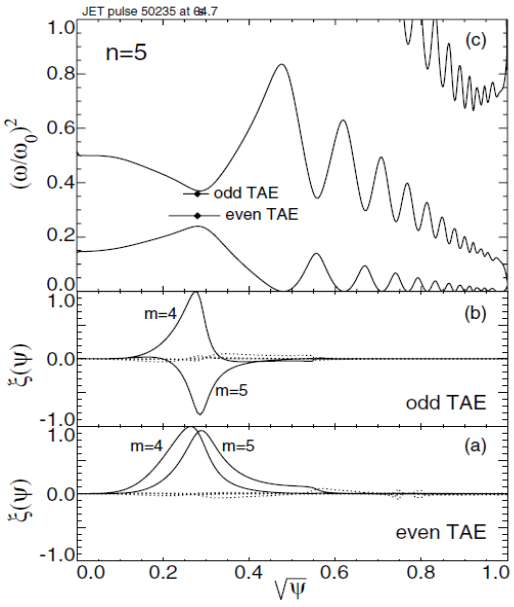

Figure 3.2: *The Shear-Alfvén continuum of a* JET *discharge with an even and an odd TAE frequency indicated, as well as their radial structures. Source: [56]*

As we saw in this section, the gap arises due to the toroidicity, when bending a cylindrical plasma to a torus. In realistic fusion devices, however, the plasma shape is in general more complex. Mostly, the circular cross section is elongated, and even the up-down symmetry might be broken. These two geometry features give rise to further gaps, as shown in fig. 3.3.

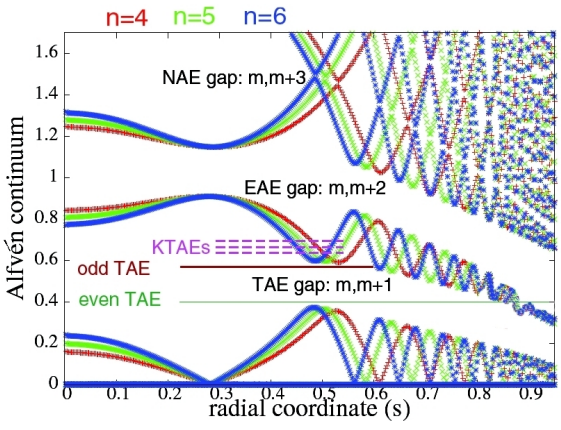

Figure 3.3: *Shear-Alfvén continuum of the* AUG *discharge #21067 at 2.99 s shows the toroidicity-induced gap (which is closed at the plasma edge) but also the ellipticity-induced gap and a small gap due to non-up-down symmetry. Source: [49]*

Reversed Shear-Alfvén Eigenmode or Alfvén Cascade

In the late 1990s, an experimental discovery of Shear-Alfvén modes with a *frequency sweeping* upwards on the equilibrium evolution time scale was made in different TOKAMAKs, first in JT-60 [57]. In JET [58], the same upwards sweeping frequency was found during q relaxation (i.e. decrease, due to current ramp-up). Thus, the new mode was called *Alfvén cascade* (AC).
This mode differs considerably in its mode structure from the TAE: especially, it is thinner (as it appears at positions, where the q profile is not flat, but reversed) and located further inside (where $\hat{s}$ is smaller). ACs typically emerge in 'bunches' outside the TAE frequency gap, thus the AC sweeping starts at frequencies significantly below the TAE frequency. In the course of the q profile relaxation, the frequency grows, until a transition from AC into TAE takes place.
In ref. [59], the excitation of these modes is explained through energetic particle drive in a reversed shear equilibrium, therefore, ACs are also called *Reversed Shear-Alfvén Eigenmodes* (RSAE). However, today it is known that the existence of the mode does not necessarily require the reversal of the q profile nor the existence of energetic particles, but depends also on the background temperature and density profiles [60]. The theoretical description resembles that for TAEs, but takes into account also second-order toroidicity MHD effects, i.e. $\mathcal{O}(\varepsilon^2)$ terms [60]. However, the RSAE are weakly damped and easily destabilized by energetic particles [59]. The assumption of a very localized (thin) mode at a position of shear $\hat{s} \approx 0$ leads to decoupling, and therefore the RSAE mode is cylindrical without a coupling to its neighbor poloidal harmonics.

3.1.3 Magneto-acoustic Waves in Fusion Plasmas – BAE

By ignoring the parallel plasma displacement $\xi_\parallel$, all *acoustic* parts within the Alfvén waves are neglected. However, it can be seen from the second branch in the plasma wave dispersion relation (eq. (3.14) for homogeneous plasmas) that there is a coupling between Shear-Alfvén waves and acoustic waves through the presence of both a magnetic (v_A) and a compressional (v_S) term. This mixing of the Alfvén and the acoustic branch depends on the ratio of v_S/v_A and thus on β (eq. (3.16)). It is stronger in the lower frequency range for fusion-relevant β values [61], where the compressional, acoustic part cannot be neglected any more. Due to the finite β, the Shear-Alfvén continuum with the poloidal mode number m couples to the sound continuum with the mode numbers $m-1$ and $m+1$, leading to another type of instability. As it requires $\beta \neq 0$, it is called *Beta-induced Alfvén eigenmode* (BAE). Due to the compressibility, it has an additional parallel component $\xi_\parallel$ with the poloidal harmonics $m \pm 1$. However, in case of low-β plasmas, the perpendicular displacement is still larger $\xi_\perp > \xi_|$, leading to one dominant poloidal harmonic m. Nevertheless, the BAE is neither pure Alfvénic, nor pure acoustic.
Experimentally, it is observed in many TOKAMAKs, first described in ref. [62] as a dangerous instability with similar properties but at around 30-50% of the TAE frequency (30-70 kHz) appearing in a spectral gap that is created by finite-β effects.
For frequencies close to the thermal ions' toroidal precession frequency $\omega_{\mathrm{tp,i\ th}}$, the MHD approximation becomes invalid, due to existing resonances. A kinetic description

of the BAE continuum is given in ref.s [63, 64]. The full kinetic BAE continuum (see ref. [49]) can be approximated to take the following form, if q is large and $k_{\|}$ is small [65]:

$$\omega^2_{\mathrm{BAE}} = \frac{v^2_{\mathrm{th,i}}}{R^2_{\mathrm{mag}}}\left(\frac{7}{4} + \frac{T_{\mathrm{e}}}{T_{\mathrm{i}}}\right), \tag{3.34}$$

with v the velocity and T the temperature of the plasma background ions (index i) and electrons (index e). The kinetic BAE description reveals the *geodesic curvature*-induced coupling of the Alfvén wave to the sound wave. However, in this approximation, the diamagnetic and shaping effects together with trapped particle contributions were neglected. They modify the dispersion relation in a non-trivial way, leading to a downshift of the BAE continuum frequency, that has to be taken into account when comparing to experimentally measured BAE frequencies [64].
The BAE is a core-localized, electromagnetic mode with an extent of around 20 to 40% of the minor radius. As the dominant harmonic does not couple to its neighbor poloidal harmonics, there is no ballooning on the LFS opposite to the case of the TAE, i.e. the BAE is a cylindrical mode.
Further described by the same continuum relation (in the long wavelength limit) is the so-called *geodesic acoustic mode* (GAM), a mostly electrostatic $n = 0$ BAE, usually located at the plasma edge.
Due to the lower frequencies of the magneto-acoustic waves, the energy which is necessary for background particles to resonate with the wave is lower. This results in a stronger damping of BAE/GAM compared to Shear-Alfvén modes. The next section is dedicated to damping mechanisms.

3.2 Fast Particle Resonance, Mode Drive and Damping

3.2.1 Mode Background Damping Mechanisms

One of the major damping mechanisms, the resonant absorption of Alfvén waves, evoked by the inhomogeneous plasma geometry – continuum damping – has already been discussed in sec. 3.1.2. But further damping mechanisms exist and are shortly presented in the following.

Radiative Damping

In the kinetic description of plasma waves (however still in the limit $v_{\mathrm{i,th}} \ll v_{\mathrm{A}}$), the inclusion of finite Larmor radius (FLR) effects lead to a modification of the continuum curve [66, 67], from eq. (3.29) to

$$\omega = \pm \bar{k}_{\|m} v_{\mathrm{A}} \left[1 + \left(\frac{3}{4} + \frac{T_{\mathrm{e}}}{T_{\mathrm{i}}}\right)(k_\perp \rho_{\mathrm{i}})^2\right] \tag{3.35}$$

The term in square brackets evokes a finite radial group velocity, as $\partial\omega/\partial k_\perp \neq 0$. Although this makes the mode existence within the continuum possible in the first

place (as explained in sec. 3.1.2), it can also lead to the damping of a TAE: a TAE with a frequency close to the local continuum frequency can be converted into a KAW, an effect called *tunneling*. Due to $\partial\omega/\partial k_\perp \neq 0$ energy is carried radially away from the localization of the TAE in the from of an outgoing radiative kinetic Alfvén wave (KAW). Therefore, the effect is called *radiative damping* [68].

Ion Landau Damping

A negative slope in a particle velocity distribution function $\partial f/\partial E$ is known to cause Landau damping [69, 70] (see textbooks as e.g. [36]) if particles are resonant with the wave. However, the distribution function of the thermal ions in a typical fusion plasma provides only a small number of particles that are fast enough to fulfill the resonance condition with the AE, $v_{i\|} = v_A$, since most ions have $v_{i\|} \ll v_A$. It is only due to the magnetic field curvature, which modifies the resonance condition, that ion Landau damping becomes relevant [30, 71]: the drift velocity v_d enters the resonance condition, giving $\omega = k_\| v_\| + k_\perp \cdot \boldsymbol{v}_d$. This extra term allows sub-Alfvénic particles with $v_{i\|} = v_A/3$ to resonate with the wave.
Though it is small and difficult to predict, it is expected to be the most important stabilizing effect for global modes in ignited TOKAMAK plasmas [72].

Electron Landau Damping and Trapped Electron Collisional Damping

In typical TOKAMAK plasmas, the thermal velocity of background electrons exceeds by far the Alfvén velocity $v_{e\|} \gg v_A$. Therefore, only a small fraction of electrons – those with $v_{e,\|} \ll v_{e,\perp}$ satisfy the resonance condition $\omega = k_\| v_{e\|}$, causing electron Landau damping [73]. However, the electron Landau damping is very difficult to predict, as at rational surfaces, $k_\|$ can become very small (see eq. (3.24)) and thus, very high velocities $v_{e\|}$ may fulfill the resonance condition there. This resonance is located radially at $q = m/n$, and not exactly in the TAE gap $q = (m+1/2)/n$, so that only the tails of radially extended TAEs are affected. For radially localized modes, the electron Landau damping effect can be neglected, similar to the effect of continuum damping.
As all electrons with $v_{e,\|} \ll v_{e,\perp}$ are trapped (see sec. 2.2.2,sec. 2.2.3), an alternative damping mechanism was proposed, caused by the transition of electrons from trapped to passing orbits due to collisions, *trapped electron collisional damping* [74, 75]. It can play a role in higher density plasmas or at lower temperatures.

3.2.2 Mode Drive and Fast Particle Transport

To determine the effect of fast particles, i.e. particles with $v \gg v_{th,i}$ – also referred to as *energetic particles* – on the stability of MHD, a very common and straightforward way is a *hybrid model*. The MHD instabilities are calculated as explained previously in this chapter. As MHD does not cover the intrinsic Alfvénic wave-particle resonances, the fast particles are taken into account using drift- or gyrokinetic models. It is sufficient, to introduce the fast particle dynamics only via their pressure tensor. This simplification is valid, since in typical fusion plasmas, the number density of the fast particles is small compared to the background plasma, but due to their high energies, the fast particle

pressure is of the same order as the background pressure. Thus, when using *driftkinetic*, a linear operator $L_k(\omega)$ enters eq. (3.25) to calculate the pressure terms. With $\tilde{f}$ being the perturbed particle distribution function, $\boldsymbol{v}_\mathrm{d}$ the curvature drift velocity in the low-β limit, and s the different species, it has the following form [47]:

$$L_k(\omega) = \frac{-4\pi \mathrm{i}\omega r^2}{c^2} \sum_s e \int d^3\, v \boldsymbol{v}_{\mathrm{ds}} \cdot \nabla \tilde{f}_s \;=\; \mathrm{i} L_k(\omega) \xi_m. \tag{3.36}$$

In the driftkinetic model, ref. [47] did an estimation for the linear growth rate, using α particles with a slowing-down energy distribution function in the large-aspect ratio limit. The TAE is then highly peaked around the $q = (2m+1)/(2n)$ surface. The resulting linear mode growth γ (relative to its unperturbed frequency ω_0) can be estimated by the analytical formula ('fp' stands for the fast particle species):

$$\frac{\gamma}{\omega_0} = \frac{9}{4}\beta_\mathrm{fp}\left(\frac{\omega_{*,\mathrm{fp}}}{\omega} - \frac{1}{2}\right) F(v_\mathrm{A}/v_\mathrm{fp}) - \beta_\mathrm{e}\frac{v_\mathrm{A}}{v_\mathrm{e}}, \tag{3.37}$$
$$\gamma \propto \omega_{*,\mathrm{fp}} \propto \text{mode harmonics } m.$$

The diamagnetic drift frequency $\omega_{*,s}$ is

$$\omega_{*,s} = \frac{m_s c}{eB} \boldsymbol{k} \times \boldsymbol{B} \frac{\nabla f_{0,s}}{f_{0,s}}, \tag{3.38}$$

$$\tag{3.39}$$

containing the equilibrium distribution function $f_{0,s}$ of the species s.
The function F is

$$F(x) = x(1 + 2x^2 + 2x^4)e^{-x^2}.$$

Inserting the wave vector as it will be introduced in subsec. 4.4.1, $\boldsymbol{k} = n\nabla\xi - m\nabla\theta$, the magnetic field in Boozer coordinates eqs. (4.17), and $\nabla f_{0,\mathrm{fp}} = \partial f_{0,\mathrm{fp}}/\partial\psi \; \nabla\psi$, the diamagnetic drift frequency becomes[3]

$$\omega_{*,\mathrm{fp}} \propto \frac{-nI - mg}{\mathfrak{J}} \frac{\partial f_{0,\mathrm{fp}}}{\partial \psi}, \tag{3.40}$$

which is always a positive expression, as long as $\partial f_{0,\mathrm{fp}}/\partial\psi < 0$, i.e. the fast particle distribution function decreases with the radius. Thus, this term is an instability *driving* term in eq. (3.38). The second term $(-1/2)$ comes from the negative slope in the slowing-down energy distribution function, and is always < 0, i.e. (Landau) *damping*. The last term of eq. (3.37) represents the *bulk electron Landau damping*. However, most electrons have $v_\mathrm{e} \gg v_\mathrm{A}$ and cannot resonate with the wave. As a consequence, this term is very small. The *Landau damping caused by thermal ions* is neglected in eq. (3.37), as most ions have $v_\mathrm{i} \ll v_\mathrm{A}$ and only very few thermal ions, those in the Maxwellian tail, are fast enough, to resonate with the Alfvén waves.

[3] ψ is the radial coordinate, which will be introduced in sec. 4.2.

To understand the driving mechanism caused by the negative slope ($\partial f_{0,\mathrm{fp}}/\partial\psi < 0$) of the radial distribution function, it is important that the radial position ψ is always connected with a toroidal momentum, p_ζ (will be shown in eq. (4.45b)): $p_\zeta \propto -\psi$. This means, whenever a particle loses toroidal momentum to the wave (p_ζ decreases), ψ will increase, i.e. the particle moves outwards. The inverse process – a particle gains momentum from the wave and moves inwards – is possible as well. However, in a distribution function that decreases radially, the dominating process is the first one. Since the energetic particle density is higher in the center, it provides a source of free energy for mode drive – as a consequence the wave amplitude grows. As will be shown in sec. 4.4.2, each change in the toroidal momentum of a particle is related to a change in particle energy. In the nonlinear stage of the mode evolution, the *radial particle redistribution* leads to *plateau formation* of the distribution function if other sources and sinks are absent. This process is visualized in fig. 3.4.

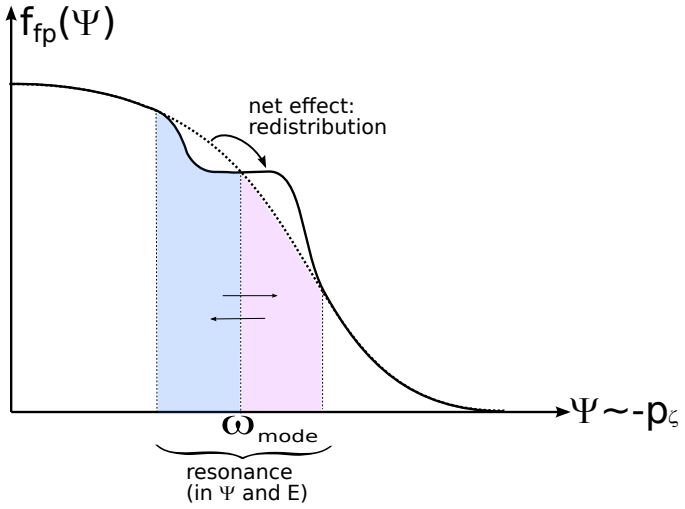

Figure 3.4: *Schematic radial fast particle redistribution due to wave-particle interaction.*

The given growth rate was estimated in the limit of small particle orbits, i.e. for orbit width W_b that are smaller than the *mode width* W_m , $W_\mathrm{b} \ll W_\mathrm{b}$. The mode width is given by

$$W_m = \frac{r^2}{m\,\hat{s}\,R_\mathrm{mag}}. \tag{3.41}$$

If the particle orbit is comparable to the mode width, $W_\mathrm{b} \approx W_\mathrm{m}$, the growth rates scales linear with the poloidal mode harmonic $\gamma \propto m$ [76]. If the orbit is much larger, $W_\mathrm{b} \gg W_\mathrm{m}$, the growth rates scales with $\gamma \propto 1/m^2$ [77]. Thus, the maximal mode growth is obtained for modes, that have a radial extent comparable to the resonating particles' bounce orbits, as shown in fig. 3.5. This is quite plausible, as a small particle orbit can pass the mode twice during one poloidal surrounding, leading to a mutual canceling of each interaction effect. A particle with an orbit much broader than the mode extent might not pass through the mode at all.

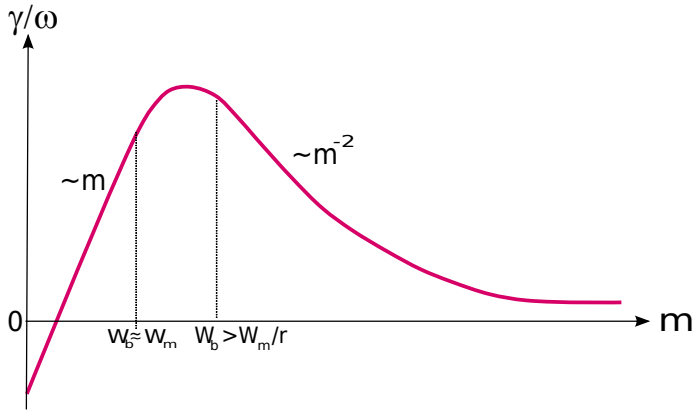

Figure 3.5: *Scaling of the linear mode growth rate with ratio of orbit width to radial mode width (for passing particles) [72, 77, 78].*

3.2.3 Fast Particle-Wave Resonance

As mentioned above, the fast particle-wave interaction requires a distinct resonance condition to be fulfilled: $v_{\|} \approx v_{\mathrm{A}}$. Using the driftkinetic approach and dividing the distribution function into a linearized part and a *non-adiabatic part*, ref. [79] rewrites the particles' bounce movement as a Fourier series

$$\propto \exp(-\mathrm{i}\omega\tau - \mathrm{i}p\omega_{\mathrm{b}}\tau - \mathrm{i}n < \dot{\zeta} > \tau). \tag{3.42}$$

There, ω is the wave frequency, ω_{b} the bounce frequency , $\omega_{\mathrm{tp}} \approx < \dot{\zeta} >$ the bounce averaged toroidal precession frequency and τ is the time parameter to be integrated over, in order to average out the bounce movement. Then, the non-adiabatic part can be seen to be

$$\propto \frac{\exp(-\mathrm{i}(\omega + n\omega_{\mathrm{tp}} + p\omega_{\mathrm{b}})t)}{\omega + n\omega_{\mathrm{tp}} + p\omega_{\mathrm{b}}}. \tag{3.43}$$

It is also shown, that the resonance for trapped particles requires

$$\omega - n\omega_{\mathrm{tp}} - p\omega_b \approx 0, \tag{3.44}$$

and, for passing particles,

$$\omega - n\omega_{\mathrm{tp}} - (p + nq)\omega_b \approx 0. \tag{3.45}$$

The bounce harmonic p comes from the Fourier decomposition of the bounce movement, thus can take any integer value $p = 0, \pm 1, \pm 2$, but the most important are the lower harmonics.

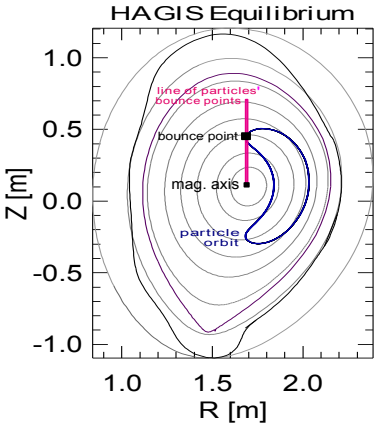

(a) *How the radial parameter for a resonance plot is obtained (pink line).*

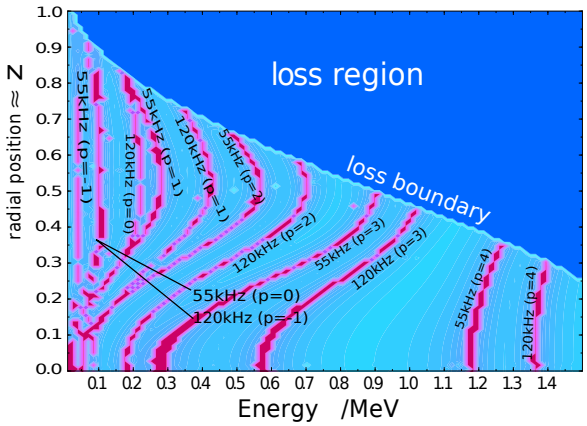

(b) *Resonances (pink) in phase space for a 120 kHz $n = 4$ and a 55 kHz $n = 4$ mode in the* AUG *equilibrium #23824, $t = 1.16$ s. The blue region is the loss area for this equilibrium.*

Figure 3.6: *The bounce point location of trapped particles bouncing vertically above the mag. axis (a) is used as radial parameter (vertical axis) for the resonance plot (b). As second coordinate, the energy is chosen to be displayed (horizontal axis). (Note: the resonance plot was created with* HAGIS*, without its vacuum extension.)*

The bounce frequency (see eq. (2.34)) depends on the particles perpendicular energy via $\omega_b \propto \sqrt{\mathcal{E}_\perp}, 1/q(\psi)$, whereas its toroidal precession frequency (see eq. (2.24)) is $\omega_{tp} \propto \mathcal{E}_\perp, q(\psi)$. A convenient (but not the only) way to visualize the resonances in phase space is to contour plot eq. (5.2) in the energy-radius space [80]. To get rid of the pitch λ and the poloidal coordinate θ, the resonance condition is evaluated (by the HAGIS Code) along a radial line from the magnetic axis vertically upwards (see fig. 3.6a). Thereby, it is assumed, that all particles have their bounce point in this region, i.e. have $\lambda \approx 0$. Of course, this is an approximation that is only true for ICRH-heated scenarios, where the fast particles are indeed generated in this region with $\lambda \approx 0$. Further, the line then serves as radial coordinate, as the bounce averaged radial position of a particle is approximately remaining on one flux surface. In this reduced phase space (from 5D to 2D), the regions where the resonance condition is fulfilled form the so-called *resonance lines* (pink in fig. 3.6b). Areas where no particles can be situated, as they would not be confined are *loss regions* (turquoise). The loss region is separated from the *confined region* by the *loss boundary*.

The resonance lines as well as the loss region depend strongly on the q profile. They help to predict and explain the fast-particle interaction with waves at certain radial positions and with certain frequencies. However, they do not contain information about how dense the resonant areas are populated, nor if other requirements for wave-particle interaction are fulfilled, such as a radial gradient at the wave position. To model not only the possibility of wave-particle interaction but also the interaction processes, the full HAGIS code will be used. The next chapter is dedicated to describe the HAGIS model.

CHAPTER 4

The HAGIS Model and the Inclusion of an $\tilde{E}_{||}$ Term

For a complete nonlinear description of fast particle-wave interaction, the spatial resolution has to cover several orders of magnitude, from millimeters to the scale of meters. Also the time and velocity space require high resolution, due to the high wave frequencies and the distinct phase space resonances. The nonlinear multi-scale problem cannot be solved in a fully consistent way so far. Rather, so-called *hybrid models* are used, which either base on an MHD model, where the fast particle dynamics is introduced via an energetic particle pressure tensor. Or, the fast particle distribution is evolved in a drift- or gyrokinetic model and the wave contribution enters the problem via a set of pre-calculated modes. This way, the energetic particle nonlinearities are kept, but the MHD nonlinearities are usually dropped. The HAGIS code follows this latter principle: only the energy transfer between waves and fast particles is accounted for. This leads to a redistribution of the fast particle population in phase space and to the evolution of the mode amplitudes and their real frequencies. However, the wave structures and so far also their damping is kept fix during a simulation. Saturation is reached in the nonlinear stage due to the local flattening of the driving gradient in the radial fast particle distribution. Further, the stochastization of the fast particle orbits caused by overlapping resonances with different modes influences the saturation level.

The scenarios considered in chapter 5 and chapter 6 are weakly nonlinear with wave damping rates that are negligibly small ($\lesssim 1\%$). Thus, the dependency of the linear background damping from the radial mode structure does not play a role so far. However, this changes when studying strongly damped modes, such as acoustic low-frequency electrostatic modes (GAMs) or the nonlinear behavior of linearly stable modes. Of special interest is not only the study of waves near the marginal stability threshold [81, 82], but also the investigation of the strong nonlinear regime, i.e. the behavior of strongly damped non-MHD-like modes, such as energetic particle modes (EPMs). When trying to answer the question under which conditions the strong nonlinear regime will be dominating – probably with avalanche-like transport, the inclusion of the background damping with non-local structure into the model is crucial. With a view to future studies in this direction, the approximation of a vanishing parallel electric field $\tilde{\boldsymbol{E}}_{||}$ in the HAGIS model is dropped in this chapter, giving rise to an effective radial damping structure.

This chapter is organized as follows: after a short technical overview over the HAGIS code, the Boozer coordinates are introduced as the relevant coordinate system. The

equations of motion for the guiding center of the fast particles are derived in sec. 4.3, using the Hamiltonian formalism in the Boozer coordinate system. Afterwards, the effect of the fast particles on the waves is calculated, following the description given by Pinches [72], but dropping the approximation of a vanishing parallel electric field $\tilde{\boldsymbol{E}}_{\parallel}$. At the end of the chapter, an outlook is given, concerning on-going work.

4.1 HAGIS Overview

The HAGIS code [72, 83] models the interaction between a distribution of energetic particles and a set of Alfvén Eigenmodes. It calculates the linear growth rates as well as the nonlinear behavior of the mode amplitudes and frequencies, and the fast ion distribution function evolution, determined by kinetic wave-particle nonlinearities. It is fully updated to work with MHD equilibria given by the recent HELENA [84] version. The plasma equilibrium for HAGIS is based on the CLISTE code [85, 86], then transformed via HELENA to straight field line coordinates and to Boozer coordinates by HAGIS. Some details about HAGIS:

- nonlinear, driftkinetic, perturbative (delta-f), particle-in-cell (PIC) code, written in FORTRAN (current release: no. 10.4).
- newly updated (for this thesis) to recent RWSHOT and HELENA versions.
- extended version by M. Brüdgam with vacuum region: possibility to track particles re-entering the plasma [55], and investigate losses including finite larmor radius effects.
  Within this thesis, this vacuum extension was brought to use in combination with realistic ASDEX Upgrade equilibrium geometry.

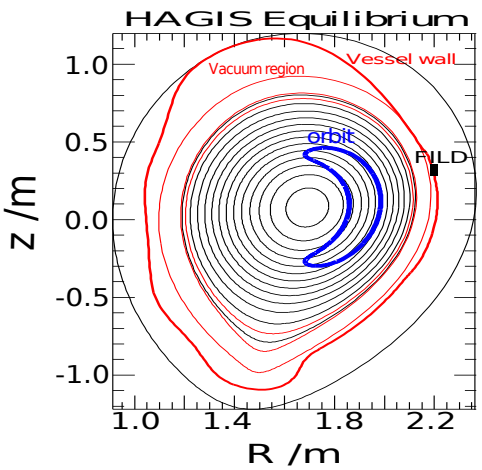

Figure 4.1: HAGIS *equilibrium*

- Implemented for this thesis: possibility to read LIGKA eigenfunctions (electric and magnetic part) and to simulate with non-vanishing $\tilde{E}_{\parallel}$ term[1]. This new feature is implemented from HAGIS Version 2440 (development branch) on[2].
- Implemented for this thesis: ICRH-like distribution function through a consistent loading & weighting scenario[3].
- Built in the frame of this thesis: Comprehensive DIAGNOSTICS tool for post-processing, written in PYTHON 2 language. Its graphical user interface is based on the toolkit TKINTER. For further details see the manual.

[1] Affects the files *readsp.F, spif.m* and *falpha.m*
[2] Most important changes in files *falpha.m*, and *rhs_waves.F*; require the input parameter *spcpet==15*
[3] Most important changes affect the file *f0_method0.m*.

4.2 The Coordinate System

4.2.1 Magnetic Flux Coordinates

If it is a valid approximation to consider good magnetic surfaces Ψ_p only (see sec. 2.1), the poloidal magnetic flux function $\Psi_p(\psi,\theta,\zeta)$ can be reduced to be a function of the radius only: $\psi_p(\psi)$. The coordinate ψ can be interpreted as the toroidal flux inside a magnetic surface, and $\psi_p(\psi)$ represents then either the poloidal flux outside the magnetic surface, or the (equal) poloidal flux through a surface that is spanned by the minor radius and the magnetic axis (see fig. C.1).

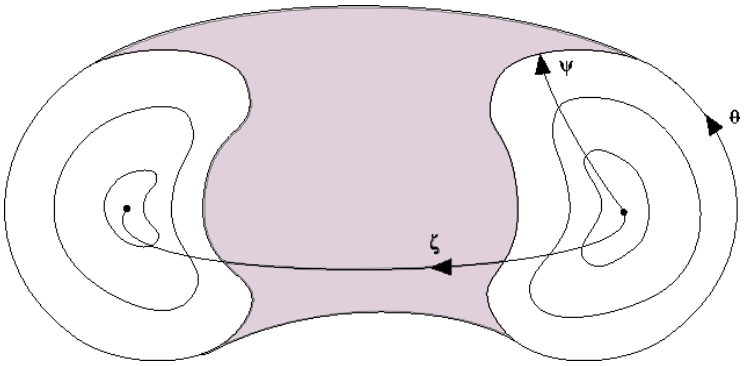

Figure 4.2: *Schematic view of a torus, with flux surfaces and a set of toroidal coordinates. Adapted from: [72].*

Thus, *flux coordinates* are curvilinear coordinate systems, in which one of the coordinates, usually denoted ψ, the *flux label*, is constant over each flux surface. As the magnetic field lines lie within the surface, it holds[4] $\boldsymbol{B}\cdot\nabla\psi = 0$, in other words: the contravariant component of the magnetic field direction vanishes $B^\psi = 0$ and $\psi = \text{const.}$ defines a sequence of nested tori. The other two coordinates form a grid within each flux surface such that they close upon themselves once around the poloidal (θ) as well as the toroidal (ζ) direction, shown in fig. 4.2.
Flux coordinates are advantageous, as they enable the fast streaming of particles along the magnetic field lines to be separated from the slow perpendicular drift movement. Any function f that fulfills the condition $\boldsymbol{B}\cdot\nabla f = 0$ is a *flux function*.

The divergence-free nature of the magnetic field, $\nabla\cdot\boldsymbol{B} = 0$ then implies that

$$\nabla\cdot\boldsymbol{B} = \frac{1}{\mathfrak{J}}\left[\frac{\partial}{\partial\theta}(\mathfrak{J}B^\theta) + \frac{\partial}{\partial\zeta}(\mathfrak{J}B^\zeta)\right] = 0 \tag{4.1}$$

with $\mathfrak{J}$ being the Jacobian of the coordinate system. It follows, that the magnetic field might be defined with the help of a stream function ν:

$$\mathfrak{J}B^\theta = -\frac{\partial\nu}{\partial\zeta}\ , \qquad \mathfrak{J}B^\zeta = \frac{\partial\nu}{\partial\theta} \tag{4.2}$$

[4] analogously: $\boldsymbol{j}\cdot\nabla\psi = 0$.

4.2.2 Straight Field Line Coordinates

Coming from the idea of a magnetic flux coordinate system, one can further specify the 'angular' coordinates θ and ζ, such that the magnetic field lines appear as straight lines on a flux surface. This is achieved by choosing the stream function ν of eq. (4.2) to be linear in θ and linear in ζ , as shown in fig. 4.3.

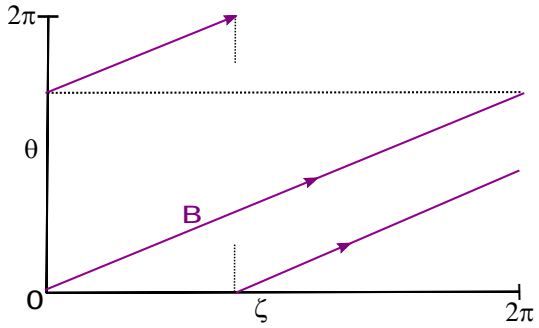

Figure 4.3: *A toroidal flux (ψ = const.) surface with straight magnetic field lines in the appropriate $\theta - \zeta$ coordinates.*

The stream function can then be written as $\nu = u(\psi)\theta + w(\psi)\zeta$. The magnetic field $\boldsymbol{B} = B^{\psi}\boldsymbol{e}_{\psi} + B^{\theta}\boldsymbol{e}_{\theta} + B^{\zeta}\boldsymbol{e}_{\zeta}$ becomes then, using the relation eqs. (B.3a):

$$\boldsymbol{B} = \frac{\partial \nu}{\partial \zeta}\nabla\psi \times \nabla\zeta + \frac{\partial \nu}{\partial \theta}\nabla\psi \times \nabla\theta \tag{4.3}$$

And with the chain rule applied on ν,

$$\nabla\nu = \frac{\partial \nu}{\partial \psi}\nabla\psi + \frac{\partial \nu}{\partial \theta}\nabla\theta + \frac{\partial \nu}{\partial \zeta}\nabla\zeta \tag{4.4}$$

one obtains

$$\boldsymbol{B} = \nabla\psi \times \nabla\nu \tag{4.5}$$

which is the *Clebsch form* for the magnetic field. Calculating the poloidal and the toroidal flux , the meaning of ν becomes clear: The toroidal flux between the adjacent surfaces ψ and $\psi + \mathrm{d}\psi$ is (see eq. (C.4)):

$$\begin{aligned}
\mathrm{d}\Psi_{\mathrm{t}} &= \frac{1}{2\pi}\int_{\psi}^{\psi+\mathrm{d}\psi}\int_{0}^{2\pi}\int_{0}^{2\pi}\underbrace{\boldsymbol{B}\cdot\nabla\zeta}_{B^{\zeta}}\mathrm{d}x^3 \\
&= \frac{\mathrm{d}\psi}{2\pi}\iint\frac{1}{\mathfrak{J}}\underbrace{\frac{\partial \nu}{\partial \theta}}_{=u(\psi)}\mathfrak{J}\mathrm{d}\theta\mathrm{d}\zeta \\
&= 2\pi\, u(\psi)\mathrm{d}\psi
\end{aligned}$$

$$\Rightarrow u(\psi) = \frac{1}{2\pi}\frac{\mathrm{d}\Psi_\mathrm{t}}{\mathrm{d}\psi} \tag{4.6}$$

and similarly with the poloidal flux, eq. (C.6):

$$w(\psi) = -\frac{1}{2\pi}\frac{\mathrm{d}\Psi_\mathrm{p}}{\mathrm{d}\psi} \tag{4.7}$$

Using the prime to denote the derivative with respect to ψ, $\boldsymbol{B}$ is then written as

$$\boldsymbol{B} = \frac{\psi_\mathrm{t}'}{2\pi}\nabla\psi\times\nabla\theta - \frac{\psi_\mathrm{p}'}{2\pi}\nabla\psi\times\nabla\zeta \tag{4.8}$$

$$\boldsymbol{B} = \boldsymbol{B}_\mathrm{t} + \boldsymbol{B}_\mathrm{p} \tag{4.9}$$

where $\boldsymbol{B}_\mathrm{t}$ is the toroidal magnetic field and $\boldsymbol{B}_\mathrm{p}$ the poloidal magnetic field .
The co-variant components of the vector potential are then flux functions $B_\theta = B_\theta(\psi)$ and $B_\zeta = B_\zeta(\psi)$, and all variation of $\boldsymbol{B}$ upon a flux surface is then hidden in the basis vectors $\nabla\theta$ and $\nabla\zeta$.

4.2.3 Boozer Coordinates

At the beginning of the 1980s, Boozer [87, 88] introduced a specific coordinate system, now called the *Boozer coordinates*: as a certain type of straight field line coordinates, the Boozer coordinates have the property that the magnetic field components required to describe the particle motion can be chosen to be functions of ψ_p alone. Additionally, the last degree of freedom is used to chose the Jacobian to be a flux function. White and Chance [89] used the Boozer coordinate system with the further assumption of toroidal symmetry. This implies that all equilibrium quantities such as the metric tensor and field components are independent of the azimuthal angle ζ .
In an axis symmetric toroidal device, ζ coordinate surfaces are vertical planes, so that $\nabla\zeta$ points in the symmetry direction. It therefore holds $\nabla\psi\cdot\nabla\zeta = 0$ (implying the metric tensor components $\mathfrak{g}^{\psi\zeta} = 0$). To obtain physical quantities independent on ζ, the poloidal coordinate must be chosen such, that $\nabla\theta\cdot\nabla\zeta = 0$ (again, implying $\mathfrak{g}^{\theta\zeta} = 0$).
The magnetic field can then be written as a composition of a horizontal and a orthogonal component (see app. D.1) [90]:

$$\boldsymbol{B} = B_\mathrm{h}(\psi,\theta)\,\nabla\psi\times\nabla\theta \;+\; B_\mathrm{O}(\psi,\theta)\,(\nabla\psi\times\nabla\theta)\times\nabla\psi \tag{4.10}$$

The divergence-free nature $\nabla\cdot\boldsymbol{B}$ allows to calculate B_O (see app. D.1):

$$B_\mathrm{O} \;=\; \frac{\Gamma(\psi)}{\mathfrak{J}(\nabla\psi\times\nabla\theta)^2}, \tag{4.11}$$

with Γ a so far undetermined flux function. However, $\Gamma(\psi) = 1$ if one chooses the poloidal flux Ψ_p to serve as flux label coordinate ψ, say $\psi = \Psi_\mathrm{p}/(2\pi)$.
As mentioned above, equilibrium force balance implies $\boldsymbol{j}\cdot\nabla\psi = 0$, i.e. the plasma current is a flux function as well. Using the Maxwell relation $\boldsymbol{j} = \nabla\times\boldsymbol{B}$, B_h is found (see app. D.1):

$$B_\mathrm{h} \;=\; \frac{g(\psi)}{\mathfrak{J}(\nabla\psi\times\nabla\theta)^2}, \tag{4.12}$$

with g as another undetermined flux function.

Knowing this, the magnetic field can be written with its co-variant components,

$$\boldsymbol{B} = B_\psi \nabla\psi + B_\theta \nabla\theta + B_\zeta \nabla\zeta. \tag{4.13}$$

These are obtained by taking the scalar product of eq. (4.10) with the appropriate co-variant basis vector $\boldsymbol{e}_i$ (see app. D.2).
In the same way, one obtains the contra-variant components of $\boldsymbol{B}$ (see app. D.3), and then calculates B^2 from $B^2 = B_\psi \cdot B^\psi + B_\theta \cdot B^\theta + B_\zeta \cdot B^\zeta$,

$$B^2 = \frac{1}{\mathfrak{J}^2(\nabla\psi \times \nabla\theta)^2}[(\nabla\psi)^2 + g^2]. \tag{4.14}$$

Evaluating this in cylindrical coordinates $(R, \varphi, z) = (R_{\text{mag}} + \psi\cos\theta, -\zeta, \psi\sin\theta)$ gives the familiar large-aspect ratio approximation for the magnetic field

$$B(r) \approx B_0(1 - r/R_{\text{mag}}\cos\theta) \tag{4.15}$$

As Boozer coordinates are meant to be a type of straight field line coordinates, the magnetic field lines have to be straight in the $\boldsymbol{e}_\theta - \boldsymbol{e}_\zeta$ – plane, i.e. $B^\zeta/B^\theta = \text{const.}$ on one flux surface. This constant is named $q(\psi)$ in the following. The B^ζ component (of eq. (D.11c)) becomes then quite simple, using eq. (D.11b) in $B^\zeta = q\, B^\theta$:

$$B^\zeta = \frac{q}{\mathfrak{J}} \tag{4.16}$$

Calculating the toroidal magnetic flux (according to eq. (C.4)) reveals that the constant $q = B^\zeta/B^\theta$ is the familiar safety factor of eq. (2.4) in Boozer coordinates.
Together with eq. (4.14), both representations of B^ζ (eq. (D.11c) and eq. (4.24)) can be used to recalculate B_θ (eq. (D.9), see app. D.3). By demanding $\boldsymbol{B} \cdot \nabla\psi = 0$, the B_ψ component can be rewritten, using the contra-variant metric coefficients, which are (eq. (B.6a)) $\mathfrak{g}^{\psi\psi} = (\nabla\psi)^2$, $\mathfrak{g}^{\psi\theta} = \nabla\psi \cdot \nabla\theta$ and $\mathfrak{g}^{\psi\zeta} = \nabla\psi \cdot \nabla\zeta$. Summarized, it is found that

$$B_\psi = \delta, \tag{4.17a}$$
$$B_\theta = I, \tag{4.17b}$$
$$B_\zeta = g, \tag{4.17c}$$

with

$$I := \mathfrak{J}B^2 - qg, \tag{4.18}$$

and (from eq. (D.14))

$$\delta := -\frac{I\mathfrak{g}^{\psi\theta} + g\mathfrak{g}^{\psi\zeta}}{\mathfrak{g}^{\psi\psi}}. \tag{4.19}$$

And $\boldsymbol{B}$ can be written in its co-variant components:

$$\boldsymbol{B} = \delta\nabla\psi + I\nabla\theta + g\nabla\zeta. \tag{4.20}$$

As one can see, B^ψ is related to the degree of orthogonality of the system, and is in general a small quantity – the smaller the more circular the cross section of the equilibrium.
Note: as mentioned at the beginning of this section, the metric of the Boozer coordinate system was chosen such, that $\mathfrak{g}^{\psi\zeta} = \mathfrak{g}^{\theta\zeta} = 0$. Geometrically, this translates into orthogonality of the respective contra-variant basis vectors. Furthermore, the angular co-variant components I and g depend on the coordinate ψ alone, which is an important feature of this system, especially within the development of the Hamiltonian formulation. The Jacobian might be written in terms of these co-variant components:

$$\mathfrak{J} = \frac{I + gq}{B^2} \tag{4.21}$$

It can be shown (see app. D.4), that I is closely related to the toroidal current penetrating one poloidal cross section, whereas g represents the total poloidal current penetrating one toroidal surface.

For the contra-variant components, it is found (see app. D.3):

$$B^\psi = 0, \tag{4.22}$$
$$B^\theta = 1/\mathfrak{J}, \tag{4.23}$$
$$B^\zeta = q/\mathfrak{J}. \tag{4.24}$$

A frequently used form for the magnetic field $\boldsymbol{B}$ is obtained, when writing it as composition of its contra-variant components, i.e.

$$\begin{aligned} \boldsymbol{B} &= B^\psi \boldsymbol{e}_\psi + B^\theta \boldsymbol{e}_\theta + B^\zeta \boldsymbol{e}_\zeta \qquad (4.25)\\ \boldsymbol{B} &= 0 - \frac{1}{\mathfrak{J}}\,\mathfrak{J}(\nabla\psi \times \nabla\zeta) + \frac{q}{\mathfrak{J}}\,\mathfrak{J}(\nabla\psi \times \nabla\theta) \end{aligned}$$

$$\boldsymbol{B} = \nabla(\zeta - q(\psi)\theta) \times \nabla\psi \tag{4.26}$$

The fact, that q is dependent only on ψ leads to $\nabla q = \partial q/\partial\psi\ \nabla\psi$, which is parallel to $\nabla\psi$ and could therefore be interchanged with the first derivation.

4.3 Guiding Center Equations

In the following, the guiding center Lagrangian for the fast ion movement is derived from that for a free charged particle moving in an electromagnetic field. Canonical variables are identified and the gyro-averaging procedure is performed as usual for the driftkinetic approximation [39], reducing phase space by one dimension. The equations of motions are obtained via the Hamiltonian formalism, i.e. differentiating the guiding center Hamiltonian with respect to these canonical variables.
The Boozer coordinate system is used as a reference frame.

4.3.1 The Guiding Center Hamiltonian

In a stationary reference frame, the exact particle Lagrangian of the form

$$\mathscr{L} = \sum_i p_i \dot{q}_i - \mathscr{H}$$

reads

$$\mathscr{L} = (m\boldsymbol{V} + e\boldsymbol{A}_S)\cdot\dot{\boldsymbol{X}} - \frac{1}{2}mV^2 - e\Phi_S \tag{4.27}$$

with $\boldsymbol{X}$, $\boldsymbol{V}$, $\boldsymbol{A}_S$, Φ_S the exact particle position, velocity, the vector and scalar potential in this reference frame S. Now we transform these quantities into a possibly time-dependent reference frame (such as e.g. a time-dependent magnetic flux coordinate system) with the coordinates χ_i: the particle position and velocity relative to this frame are named $\boldsymbol{x}$ and $\boldsymbol{v}$, and are related to the coordinates in the stationary frame via

$$\begin{aligned}\boldsymbol{V} &= \frac{\partial \boldsymbol{x}}{\partial t} + \frac{\partial \boldsymbol{x}}{\partial \chi_i}\dot{\chi}^i \\ \boldsymbol{V} &= \boldsymbol{v} + \boldsymbol{V}_B\end{aligned} \tag{4.28}$$

with $\boldsymbol{V}_B$ the velocity of the frame (e.g. the magnetic field). By defining the field potentials as

$$\boldsymbol{A} = \boldsymbol{A}_S + \frac{m}{e}\boldsymbol{V}_B \quad \text{and} \quad \Phi = \Phi_S - \boldsymbol{A}_S\cdot\boldsymbol{V}_B - \frac{1}{2}\frac{m}{e}V_B^2 \tag{4.29}$$

it is possible to write the Lagrangian in its well-known form

$$\mathscr{L} = (m\boldsymbol{v} + e\boldsymbol{A})\cdot\dot{\boldsymbol{x}} - \frac{1}{2}mv^2 - e\Phi \tag{4.30}$$

similar to its appearance in a stationary reference frame, although the coordinates $(\boldsymbol{x}, \boldsymbol{v})$ are defined with respect to the new, non-inertial system. All terms of inertia that arise naturally in every accelerated frame are packed into the new definition of the field potentials, eq. (4.29).
In the following, the relative magnitudes of these terms of inertia should be considered: recalling the Larmor radius $\rho = mv_\perp/(eB)$ and the common estimation of the magnetic field strength $B \approx A/L$ (from $\boldsymbol{B} = \nabla\times\boldsymbol{A}$), with L a typical scale length upon which the field varies, one finds the relative magnitude of the term of inertia in $\boldsymbol{A}$ to the first term:

$$\frac{|m\boldsymbol{V}_B|}{|e\boldsymbol{A}_B|} \approx \frac{\boldsymbol{V}_B}{\boldsymbol{v}_\perp}\frac{\rho}{L} \tag{4.31}$$

As both, V_B/v and ρ/L being small, it can be assumed that $\boldsymbol{A} \simeq \boldsymbol{A}_S$, and also $\Phi \simeq \Phi_S - \boldsymbol{A}_S\cdot\boldsymbol{V}_B$.
If the driftkinetic approximation is valid, i.e. the field varies only on temporal and spacial scales much larger than the gyromotion ($\nabla\boldsymbol{B} \ll B/\rho$ and $\dot{B} \ll \Omega\cdot B$), the magnetic moment $\mu = m\boldsymbol{v}_\perp/(2B)$ is invariant (see sec. 2.2). As it couples to external forces by means of the mirror force, $\boldsymbol{F}_m = -\nabla(\mu B)$, the term $\mu B = 1/2mv_\perp^2$ can be

interpreted rather as potential energy than as kinetic energy. The Lagrangian can then be written as

$$\mathscr{L} = \frac{1}{2}mv_{\parallel}^2 + e\boldsymbol{A}(\boldsymbol{x},t)\cdot\boldsymbol{v} - \mu B - e\Phi(\boldsymbol{x},t), \tag{4.32}$$

a form that was first given in ref. [91]. Originally, there were six phase space coordinates, which could have been expressed e.g. by three spacial components of the guiding center position $\boldsymbol{x}$, the parallel velocity of the guiding center $v_{\parallel}$, the magnetic moment, i.e. the perpendicular kinetic energy of the particle $\propto v_{\perp}^2$, and the gyrophase angle ξ. However, in driftkinetic theory, μ is an invariant quantity, and the gyrophase angle can be neglected since it is irrelevant to the motion of the guiding center $\boldsymbol{R}$. Thus, the number of independent phase space coordinates reduces to four: three components of $\boldsymbol{x}$ and the parallel velocity $v_{\parallel}$ of the guiding center. $\boldsymbol{x}$ can be composed of

$$\begin{aligned} &\boldsymbol{x} = \boldsymbol{R} + \boldsymbol{\rho} \\ &\quad \text{with the gyroradius :} \quad \boldsymbol{\rho} = \rho\hat{\boldsymbol{\rho}} \equiv \frac{m\boldsymbol{v}_{\perp}}{eB} = \frac{v_{\perp}}{\Omega}\hat{\boldsymbol{\rho}} \\ &\quad \text{with the known gyrofrequency :} \quad \Omega \equiv \frac{eB}{m} \\ &\quad \text{and a unity vector :} \quad \hat{\boldsymbol{\rho}} = \cos\xi\ \boldsymbol{e}_x + \sin\xi\ \boldsymbol{e}_y \end{aligned} \tag{4.33}$$

$\boldsymbol{e}_x(\boldsymbol{R},\xi)$ and $\boldsymbol{e}_y(\boldsymbol{R},\xi)$ are unity vectors in the plane perpendicular to the magnetic field lines. Note also, that the average of the gyroradius over one gyroorbit vanishes $<\boldsymbol{\rho}>=0$.
Within the frame of driftkinetic theory, the fields and potentials are assumed not to vary strongly over one gyroorbit. Therefore, the potentials can be Taylor expanded around the gyrocenter up to the first order only:

$$\begin{aligned} \boldsymbol{A}(\boldsymbol{x}) &= \boldsymbol{A}(\boldsymbol{R}) + (\rho\cdot\nabla)\boldsymbol{A}(\boldsymbol{R}) \\ \Phi(\boldsymbol{x}) &= \Phi(\boldsymbol{R}) + (\rho\cdot\nabla)\Phi(\boldsymbol{R}) \end{aligned} \tag{4.34}$$

(4.35)

Inserting this into the Lagrangian eq. (4.30) yields:

$$\begin{aligned} \mathscr{L} \ &= e\boldsymbol{A}(\boldsymbol{R})\cdot\dot{\boldsymbol{R}} + e(\rho\cdot\nabla)\boldsymbol{A}(\boldsymbol{R})\cdot\dot{\boldsymbol{R}} + e\boldsymbol{A}(\boldsymbol{R})\cdot\dot{\boldsymbol{\rho}} + e(\rho\cdot\nabla)\boldsymbol{A}(\boldsymbol{R})\cdot\dot{\boldsymbol{\rho}} \\ &\quad + m\boldsymbol{v}\cdot\dot{\boldsymbol{R}} + m\boldsymbol{v}\cdot\dot{\boldsymbol{\rho}} - \frac{1}{2}mv_{\parallel}^2 - \mu B - e\Phi(\boldsymbol{R}) \end{aligned} \tag{4.36}$$

The first order term of Φ can be dropped, since the electric field is of one order higher in perturbation when assuming a vanishing equilibrium electric field, $\Phi_0 = 0$.
The canonical variables to keep within the formulation are $\boldsymbol{R}$ and $\dot{\boldsymbol{R}}$. As it is not necessary to retain the fast gyromotion within the equations, an averaging over the gyroangle is performed, indicated by '<>'. This so called *gyro-averaging* reduces the

phase-space coordinates by eliminating the gyroangle ξ:

$$\mathscr{L} = e\underbrace{<\boldsymbol{A}(\boldsymbol{R})\cdot\dot{\boldsymbol{R}}>}_{\text{independent of }\xi} + e\underbrace{<(\rho\cdot\nabla)\boldsymbol{A}(\boldsymbol{R})\cdot\dot{\boldsymbol{R}}>}_{=0\text{ (see app. E.1)}} + e\underbrace{<\boldsymbol{A}(\boldsymbol{R})\cdot\dot{\boldsymbol{\rho}}>}_{=0\text{ (see app. E.1)}} + e\underbrace{<(\rho\cdot\nabla)\boldsymbol{A}(\boldsymbol{R})\cdot\dot{\boldsymbol{\rho}}>}_{=2\mu B/\Omega\ \dot{\xi}}$$
$$+ \underbrace{m<\boldsymbol{\nu}\cdot\dot{\boldsymbol{R}}>}_{=m\nu_\parallel^2\text{ indep. of }\xi} + \underbrace{m<\boldsymbol{\nu}\cdot\dot{\boldsymbol{\rho}}>}_{=-\mu B/\Omega\ \dot{\xi}} - \frac{1}{2}m\underbrace{<\nu_\parallel^2>}_{\text{indep. of }\xi} - \underbrace{<\mu B>}_{\text{indep. of }\xi} - e\underbrace{<\Phi(\boldsymbol{R})>}_{\text{indep. of }\xi} \quad (4.37)$$

The first and the three last terms are independent of ξ, and thus, the averaging brackets are obsolete. For the remaining terms, the averaging is performed in app. E.1.
The vector $\hat{\boldsymbol{b}} = \boldsymbol{B}/B$ is a unit vector in the direction of the equilibrium magnetic field. This leads to a Lagrangian of the form

$$\mathscr{L} = (m\nu_\parallel\hat{\boldsymbol{b}} + e\boldsymbol{A}(\boldsymbol{R}))\cdot\dot{\boldsymbol{R}} + \frac{\mu B}{\Omega}\dot{\xi} - \frac{1}{2}m\nu_\parallel^2 - \mu B - e\Phi(\boldsymbol{R}). \quad (4.38)$$

With $\mathscr{L} = \sum_i p_i\dot{q}_i - \mathscr{H}$, it is possible to identify the Hamiltonian $\mathscr{H} = \frac{1}{2}m\nu_\parallel^2 + \mu B + e\Phi(\boldsymbol{R})$
Furthermore, we define a formal parallel analogon to the gyroradius:

$$\boldsymbol{\rho}_\parallel \equiv \frac{m\boldsymbol{\nu}_\parallel}{eB} = \frac{\nu_\parallel}{\Omega}\hat{\boldsymbol{b}}, \quad (4.39)$$

which makes the Lagrangian

$$\mathscr{L} = e(\rho_\parallel\boldsymbol{B}(\boldsymbol{R}) + \boldsymbol{A}(\boldsymbol{R}))\cdot\dot{\boldsymbol{R}} + \frac{\mu B}{\Omega}\dot{\xi} - \frac{1}{2}m\nu_\parallel^2 - \mu B - e\Phi(\boldsymbol{R}). \quad (4.40)$$

Now we fill in the contra-variant notation of the magnetic field in Boozer coordinates $\boldsymbol{A} = \Psi_t/(2\pi)\nabla\theta - \Psi_p/(2\pi)\nabla\zeta$, eq. (D.19) and $\boldsymbol{B} = \delta\nabla\psi_p + I\nabla\theta + g\nabla\zeta$, eqs. (4.17), as well as the co-variant decomposition of the gyrocenter position $\dot{\boldsymbol{R}} = \dot{\psi}\boldsymbol{e}_{\psi_p} + \dot{\theta}\boldsymbol{e}_\theta + \dot{\zeta}\boldsymbol{e}_\zeta$.
With the use of $\nabla u^i\boldsymbol{e}_j = \delta^i_j$, one obtains[5]:

$$\mathscr{L} = e\rho_\parallel\delta\dot{\psi}_p + e(\rho_\parallel I + \psi_t)\dot{\theta} + e(\rho_\parallel g - \psi_p)\dot{\zeta} + \frac{m}{e}\mu\dot{\xi} - \mathscr{H}. \quad (4.41)$$

However, in this expression, only the equilibrium fields have entered the Lagrangian. We are now also taking into account the perturbed part of the field potentials, i.e. $\boldsymbol{A} = \boldsymbol{A}_0 + \tilde{\boldsymbol{A}}$, with $\boldsymbol{A}_0$ as given above, and $\tilde{\boldsymbol{A}} = \tilde{A}_{\psi_p}\nabla\psi_p + \tilde{A}_\theta\nabla\theta + \tilde{A}_\zeta\nabla\zeta$, as well as $\Phi = \Phi_0 + \tilde{\Phi}$. This leads to a Lagrangian of the form

$$\mathscr{L} = e(\rho_\parallel\delta + \tilde{A}_{\psi_p})\dot{\psi}_p + e(\rho_\parallel I + \psi_t + \tilde{A}_\theta)\dot{\theta} + e(\rho_\parallel g - \psi_p + \tilde{A}_\zeta)\dot{\zeta} + \frac{m}{e}\mu\dot{\xi} - \mathscr{H}, \quad (4.42)$$

with a Hamiltonian written in the form

$$\mathscr{H} = \frac{1}{2}\rho_\parallel^2 B^2 + \mu B + e\tilde{\Phi}(\boldsymbol{R}), \quad (4.43)$$

[5] Note: $\psi_t := \Psi_t/(2\pi)$ and $\psi_p := \Psi_p/(2\pi)$. The first expression is also referred to as ψ.

when excluding any equilibrium electrostatic potential $\Phi_0 = 0$. In this form, one could now immediately identify the conjugated momenta p_i. However, it is also obvious, that there are four terms of the form $p_i \dot{q}_i$. To resolve this problem, the particle motion is reproduced only to second order in ρ, but the Hamiltonian is conserved exactly. This is achieved by modifying the guiding center velocity $\dot{\boldsymbol{R}} = \boldsymbol{v}$ with $\boldsymbol{v} \longrightarrow \boldsymbol{v} + \boldsymbol{w}$. The arising additional term in eq. (4.40) is of the form $e\boldsymbol{A}(\boldsymbol{R}) \cdot \boldsymbol{w}$. The additional w may be chosen such that

$$\boldsymbol{A} \cdot \boldsymbol{w} = -\delta \rho_{\parallel} \dot{\psi}_{\mathrm{p}}. \tag{4.44}$$

This trick removes the $\dot{\psi}_{\mathrm{p}}$ term from the Lagrangian.
As the Lagrangian in eq. (4.42) is exactly written in the form $\mathscr{L} = \sum_i p_i \dot{q}_i - \mathscr{H}$, the three conjugated momenta are simply:

$$p_\theta = e\rho_{\parallel} I + e\psi_{\mathrm{t}} + e\tilde{A}_\theta \tag{4.45a}$$
$$p_\zeta = e\rho_{\parallel} g - e\psi_{\mathrm{p}} + e\tilde{A}_\zeta \tag{4.45b}$$
$$p_\xi = \mu \tag{4.45c}$$

These expressions show a familiar structure: compared to the conjugated momentum of a free particle in an electromagnetic field, $\boldsymbol{p} = m\boldsymbol{v} + e\boldsymbol{A}$, eqs. (4.45), are composed in the same way: concerning the vector potential, one has to take into account, that ψ_{t} and $-\psi_{\mathrm{p}}$ are the co-variant components of the unperturbed vector potential $\boldsymbol{A}_0$ for the coordinates θ and ζ. Concerning the classical momentum $m\boldsymbol{v}$, it is worth knowing that I also stands for the co-variant component of the magnetic field, B_θ, whereas g represents B_ζ. Therefore, the term $e\rho_{\parallel} I = ev_{\parallel} m/(eB) B_\theta \propto mv_{\parallel}$ and analogously for the g term. Hence, the particle momenta corresponding to θ and ζ are $v_{\parallel} I$ and $v_{\parallel} g$.

4.3.2 The Equations of Motion for the Guiding Center Coordinates

According to the Hamiltonian formalism, the equations of motion are obtained via

$$\dot{q}_i = \frac{\partial \mathscr{H}}{\partial p_i} \qquad\qquad \dot{p}_i = -\frac{\partial \mathscr{H}}{\partial q_i} \tag{4.46}$$

with q_i in our case being θ, ζ and ξ for the canonical variables, p_i being p_θ, p_ζ and p_ξ for the conjugated canonical momenta. However, the Hamiltonian is not given in terms of these canonical variables, and therefore, one first has to evaluate the partial derivatives of ψ_{p} and $\rho_{\parallel}$ with respect to these variables. Note that g, I and ψ_{t} are flux coordinates, and thus functions of ψ_{p} alone. ψ_{p} in turn depends, as well as $\rho_{\parallel}$ on θ, ζ, p_θ and p_ζ.
From eqs. (4.45), one can eliminate $\rho_{\parallel}$:

$$g(p_\theta - e\psi_{\mathrm{t}} - e\tilde{A}_\theta) = I(p_\zeta + e\psi_{\mathrm{p}} - e\tilde{A}_\zeta). \tag{4.47}$$

Differentiating this expression with respect to θ, ζ, p_θ and p_ζ gives the ψ_{p} derivatives (see app. F.1). Differentiating eqs. (4.45) with respect to θ, ζ, p_θ and p_ζ gives the derivatives of $\rho_{\parallel}$ (see app. F.2). Thereby, it is convenient, to summarize the term:

$$D \equiv \rho_{\parallel}(gI' - g'I) + I + qg - I\tilde{A}'_\zeta + g\tilde{A}'_\theta, \tag{4.48}$$

where q is the well-known safety factor, in Boozer coordinates $q = \partial\psi_t/\partial\psi_p$.
Having derived the partial derivatives of ψ_p and $\rho_\parallel$ with respect to the canonical variables $x = \theta, \zeta, p_\theta$ and p_ζ, it is now possible, to obtain the equations of motion via the Hamiltonian formalism, as recalled in eq. (4.46), using the chain rule:

$$\frac{\partial \mathscr{H}}{\partial x} = \frac{\partial \mathscr{H}}{\partial \psi_p}\frac{\partial \psi_p}{\partial x} + \frac{\partial \mathscr{H}}{\partial \rho_\parallel}\frac{\partial \rho_\parallel}{\partial x}. \tag{4.49}$$

This gives the equations of motion for the four guiding center coordinates:

$$\dot{\theta} = \frac{1}{eD}\left[\rho_\parallel B^2\,(1-\rho_\parallel g' - \tilde{A}'_\zeta) + g\left((\rho_\parallel^2 B+\mu)B' + \tilde{\Phi}'\right)\right], \tag{4.50a}$$

$$\dot{\zeta} = \frac{1}{eD}\left[\rho_\parallel B^2\,(q+\rho_\parallel I' - \tilde{A}'_\theta) - I\left((\rho_\parallel^2 B+\mu)B' + \tilde{\Phi}'\right)\right], \tag{4.50b}$$

$$\dot{\psi}_p = \frac{1}{D}\left[\left(I\frac{\partial \tilde{A}_\zeta}{\partial\theta} - g\frac{\tilde{A}_\theta}{\partial\theta}\right)\dot{\theta} + \left(I\frac{\partial \tilde{A}_\zeta}{\partial\zeta} - g\frac{\tilde{A}_\theta}{\partial\zeta}\right)\dot{\zeta} + \frac{g}{e}\dot{p}_\theta - \frac{I}{e}\dot{p}_\zeta\right], \tag{4.50c}$$

$$\dot{\rho}_\parallel = \frac{1}{I}\left[\dot{p}_\theta - e\frac{\partial \tilde{A}_\theta}{\partial\theta}\dot{\theta} - e\frac{\partial \tilde{A}_\theta}{\partial\zeta}\dot{\zeta} - e\dot{\tilde{A}}_\theta - e(q+\tilde{A}'_\theta + \rho_\parallel I')\dot{\psi}_p\right]. \tag{4.50d}$$

Eqs. (4.50) define the particle trajectories via the functions $I(\psi_p)$, $g(\psi_p)$, $q(\psi_p)$, $B(\psi_p,\theta)$, $\tilde{\boldsymbol{A}}(\psi_p,\theta,\zeta,t)$, $\tilde{\Phi}(\psi_p,\theta,\zeta,t)$. To describe the particle paths in the inertial laboratory frame of reference, the transformation function $\boldsymbol{x}(\psi_p,\theta,\zeta)$ has to be known.

4.3.3 Specialization to Low-β Shear-Alfvén Waves

The equations of motion derived above describe in a very general form the particle motion in a toroidal magnetic geometry in the presence of any perturbed vector potential $\tilde{\boldsymbol{A}}$. However, by choosing a more specific form for the magnetic perturbation, these equations can be simplified at the expense of their generality. By choosing as perturbation a low-β Shear-Alfvén wave, one imposes a constraint on the perturbed magnetic field, as these kind of waves have a perpendicular field line displacement, oscillating against the plasma inertia. As a consequence, $\tilde{\boldsymbol{B}} = \tilde{\boldsymbol{B}}_\perp$. The fact, that $\tilde{B}_\parallel = 0$ allows to chose a vector potential of the form $\tilde{\boldsymbol{A}} = \tilde{\boldsymbol{A}}_\parallel$ and thus

$$\tilde{\boldsymbol{A}} \equiv \tilde{\alpha}(\boldsymbol{x},t)\boldsymbol{B}_0 \tag{4.51}$$

This definition ties $\tilde{\alpha}$ closely to the parallel component of the perturbed vector potential and it follows for the resulting perturbed magnetic field, that

$$\tilde{\boldsymbol{B}} = \nabla\times\tilde{\alpha}(\boldsymbol{x},t)\boldsymbol{B}_0 \tag{4.52}$$

As mentioned above, $\tilde{\alpha}$ was introduced to simplify the equations of motion. To insert $\tilde{\alpha}$ into those, one first has to find the respective co-variant components of eq. (4.51):

$$\tilde{A}_\theta = \tilde{\alpha}B_\theta = \tilde{\alpha}I, \tag{4.53a}$$

$$\tilde{A}_\zeta = \tilde{\alpha}B_\zeta = \tilde{\alpha}g. \tag{4.53b}$$

Note that when deriving $\tilde{A}$ with respect to ψ_p (indicated by the prime $'$), the product rule must be applied. The arising terms $\tilde{\alpha}g'$ and $\tilde{\alpha}I'$ are then absorbed within the definition of a new quantity, ρ_c:

$$\rho_\mathrm{c} = \rho_\parallel + \tilde{\alpha}' \tag{4.54}$$

Using this definition, D can be written simpler:

$$D = \rho_\mathrm{c}(gI' - g'I) + I + qg \tag{4.55}$$

Inserting the co-variant components of $\tilde{A}$ from eqs. (4.53) into the equations of motion, eqs. (4.50a) and (4.50b) and using eq. (4.54), one obtains:

$$\dot{\theta} = \frac{1}{eD}\left[\rho_\parallel B^2\,(1 - \rho_\mathrm{c}g' - \tilde{\alpha}') + g\left((\rho_\parallel^2 B + \mu)B' + \tilde{\Phi}'\right)\right], \tag{4.56a}$$

$$\dot{\zeta} = \frac{1}{eD}\left[\rho_\parallel B^2\,(q + \rho_\mathrm{c}I' - \tilde{\alpha}') - I\left((\rho_\parallel^2 B + \mu)B' + \tilde{\Phi}'\right)\right]. \tag{4.56b}$$

In the next step, the same is done (inserting eqs. (4.53)) in equation for $\dot{\psi}_\mathrm{p}$ and $\dot{\rho}_\parallel$. Starting with $\dot{\psi}_\mathrm{p}$ eq. (4.50c) the terms with $\dot{\theta}$ and $\dot{\zeta}$ will cancel, leaving only the $\dot{p}_\theta$ and $\dot{p}_\zeta$ terms, which can be replaced (by eq. (F.24) and eq. (F.25)), again substituting the components of $\tilde{A}$ (eqs. (4.53)).
For $\dot{\rho}_\parallel$ eq. (4.50d), the derivation is equally simple but more tedious, as terms cancel only after expanding all the equations for $\dot{\theta}$ eq. (4.50a), $\dot{\zeta}$ eq. (4.50b), $\dot{p}_\theta$ eq. (F.24) and $\dot{\psi}_\mathrm{p}$ eq. (4.57a). The results are:

$$\begin{aligned}\dot{\psi}_\mathrm{p} = \frac{1}{eD}\Bigg[&\rho_\parallel B^2\left(g\frac{\partial\tilde{\alpha}}{\partial\theta} - I\frac{\partial\tilde{\alpha}}{\partial\zeta}\right) + \left(g\frac{\partial\tilde{\alpha}}{\partial\theta} - I\frac{\partial\tilde{\alpha}}{\partial\zeta}\right)\\ &- g(\rho_\parallel^2 B + \mu)\frac{\partial B}{\partial\theta} + g\left((\rho_\parallel^2 B + \mu)B' + \tilde{\Phi}'\right)\Bigg],\end{aligned} \tag{4.57a}$$

$$\begin{aligned}\dot{\rho}_\parallel = -\frac{1}{D}\Bigg[&\left(g\frac{\partial\tilde{\alpha}}{\partial\theta} + I\frac{\partial\tilde{\alpha}}{\partial\zeta}\right)\left\{(\rho_\parallel^2 B + \mu)B' + \tilde{\Phi}'\right\} + (q + \rho_\mathrm{c}I' - \tilde{\alpha}')\frac{\partial\tilde{\Phi}}{\partial\zeta}\\ &+ (1 - \rho_\mathrm{c}g' - \tilde{\alpha}')\left\{(\rho_\parallel^2 B + \mu)\frac{\partial B}{\partial\theta} + \frac{\partial\tilde{\Phi}}{\partial\theta}\right\}\Bigg] - e\dot{\tilde{\alpha}}.\end{aligned} \tag{4.57b}$$

With these equations of motion, implemented numerically[6] the HAGIS code calculates the trajectories of the fast particles in the presence of a magnetic perturbation imposed on the equilibrium magnetic field B. The perturbation, as well as the other equilibrium functions – poloidal current g, toroidal current I, safety factor q – are given externally by MHD codes that solve the Grad-Shafranov equation. The structure of the perturbation as well is calculated by external codes (such as the MHD code CASTOR [92] or the gyrokinetic LIGKA solver [93]).

[6] in *rhs_markers.F*.

4.4 Wave evolution (with a Non-vanishing Parallel Electric Field)

The amplitude evolution of the perturbations is evaluated by HAGIS self-consistently, calculating the effect of the moving particles on the waves. I.e. the amplitude evolution of the waves is a response to their collective interaction with the particles. In turn, the wave evolution then determines the particle motion in the perturbed field.
This section is dedicated to the derivation of the wave equations, in response to the wave-particle interaction. If follows ref. [72] but drops the approximation of a vanishing parallel electric field $\tilde{E}_{\parallel}$. Like the particle motion, the wave evolution can be derived within the Lagrange Formalism. The total system Lagrangian $\mathscr{L}$ consists of the fast particle Lagrangian $\mathscr{L}_{\mathrm{fp}}$ and the wave Lagrangian $\mathscr{L}_{\mathrm{w}}$, which in turn contains the background (=bulk) plasma contribution to the Alfvén waves and the electromagnetic wave energy. Both parts are derived in subsec. 4.4.3. The actual wave-particle interaction is contained within a third Lagrangian $\mathscr{L}_{\mathrm{int}}$, describing the effect of the Alfvén waves upon the particle motion. It is derived in subsec. 4.4.4. The total Lagrangian then reads

$$\mathscr{L} = \overbrace{\mathscr{L}_{\mathrm{fp}} + \underbrace{\mathscr{L}_{\mathrm{int}}}_{\text{wave evolution}}}^{\text{particle motion}} + \mathscr{L}_{\mathrm{W}}$$

4.4.1 Wave representation, Potential Definitions and Notation

In the following, the notation is set up. In all terms concerned with the energetic part of the plasma, j is the particle index, m and e the particle mass and electric charge . As a subscript to the potentials, j indicates, that it has to be evaluated at the respective particle position. The subscript 0 denotes an equilibrium quantity, whereas a *tilde* indicates a perturbed quantity.
The electric field equilibrium part is equal zero, leading to an electric field of: $\boldsymbol{E} = \tilde{\boldsymbol{E}}_{\parallel} + \tilde{\boldsymbol{E}}_{\perp}$. The magnetic field $\boldsymbol{B}$ consists of a (per definition parallel) equilibrium part, and a perturbed part, which is perpendicular: $\boldsymbol{B} = \boldsymbol{B}_{0\parallel} + \tilde{\boldsymbol{B}}_{\perp}$. For simplicity the $\perp,\parallel$ subscripts of B are left away.
The same applies for the velocity $\boldsymbol{v} = \boldsymbol{v}_{0\parallel} + \tilde{\boldsymbol{v}}_{\perp}$, with $\tilde{\boldsymbol{v}} = (\boldsymbol{B} \times \boldsymbol{E})/B^2$, the E-cross-B drift velocity eq. (2.17), which is perpendicular to the unperturbed magnetic field.
The perturbed fields and potentials can be written as a sum over all perturbations k, which reads $\tilde{\boldsymbol{B}} = \sum_k \boldsymbol{B}_k$ and $\tilde{\boldsymbol{E}} = \sum_k \boldsymbol{E}_k$ respectively. Expanding the fields and take up to the 2nd order of perturbation – considering only perpendicular terms of $\tilde{v}$, one obtains:

$$\boldsymbol{v} = \boldsymbol{v}_0 + \sum_k \frac{\boldsymbol{E}_{k\perp} \times \boldsymbol{B}_0}{B_0^2} + \sum_{k,k'} \frac{\boldsymbol{E}_{k\parallel} \times \boldsymbol{B}_{k'}}{B_0^2} \tag{4.58}$$

Analogously to ref. [72], all fields are expressed through potentials, using the definition of $\tilde{\alpha}$, which makes use of the fact, that the perturbed vector potential must be parallel

to the equilibrium magnetic field to result in a perpendicular perturbed magnetic field:

$$\begin{aligned} & \boldsymbol{A_k} = \alpha_k(\boldsymbol{x},t)\,\boldsymbol{B_0}, \\ \Leftrightarrow\ & \boldsymbol{B_k} = \nabla\times(\alpha_k \boldsymbol{B_0}), \end{aligned} \tag{4.59}$$

The perturbed fields then read [7]:

$$\boldsymbol{B}_k = \nabla\times\boldsymbol{A}_k, \tag{4.60}$$

$$\boldsymbol{B}_k = \nabla\times(\alpha_k\boldsymbol{B_0}),$$

$$\boldsymbol{B}_k = \underbrace{\alpha_k B_0\ \nabla\times\hat{\boldsymbol{b}}}_{\text{small (of order } \varepsilon)} - \hat{\boldsymbol{b}}\times\nabla(\alpha_k B_0), \tag{4.61}$$

$$\boldsymbol{E}_k = \nabla\Phi_k - \frac{\partial}{\partial t}\boldsymbol{A}_k,$$

$$\boldsymbol{E}_k = \nabla\Phi_k - \frac{\partial}{\partial t}(\alpha_k\boldsymbol{B_0}), \tag{4.62}$$

$$\boldsymbol{E}_{\perp k} = \nabla_\perp\Phi_k. \tag{4.63}$$

So far, it was assumed in the HAGIS code, that the parallel electric field $\tilde{\boldsymbol{E}}_\parallel$ vanishes, due to the fast parallel dynamics of the particles along the equilibrium magnetic field lines. Then, the magnetic and the electric potential are correlated via the potential definition eq. (4.62):

$$\boldsymbol{E}_{\parallel k} \equiv 0 = \nabla_\parallel\Phi_k - \frac{\partial}{\partial t}(\alpha_k\boldsymbol{B}_0). \tag{4.64}$$

As each wave is characterized by a distinct toroidal eigenfunction (index k), and represented as a sum of poloidal harmonics m, one can compose its electric potential, as it enters the HAGIS code such that

$$\begin{aligned} \Phi_k &= \sum_m \Phi_{km}(\psi_\mathrm{p})\ \ \mathrm{e}^{\mathrm{i}(\boldsymbol{k}_{nm}\cdot\boldsymbol{x}-\omega_k t)}, \\ \Phi_k &= \sum_m \Phi_{km}(\psi_\mathrm{p})\ \ \mathrm{e}^{\mathrm{i}(n_k\zeta - m\theta - \omega_k t)}. \end{aligned} \tag{4.65}$$

with the real wave vector $\boldsymbol{k}_{nm} = n\nabla\xi - m\nabla\theta$. The wave frequency is ω_k, which might be complex, if there is a damping term γ, otherwise, it is real.
Using this wave decomposition for $\tilde{\Phi}$ and analogously for $\tilde{\alpha}$, eq. (4.64) turns into

$$\begin{aligned} 0 &= \sum_m \mathrm{i}\boldsymbol{k}_{\parallel nm}\Phi_{km}\ \ \mathrm{e}^{\mathrm{i}(\boldsymbol{k}_{nm}\cdot\boldsymbol{x}-\omega_k t)} - \mathrm{i}\omega_k\alpha_{km}\boldsymbol{B}_0\ \ \mathrm{e}^{i(\boldsymbol{k}_{nm}\cdot\boldsymbol{x}-\omega_k t)} \\ \Rightarrow \alpha_{km} &= \frac{k_{\parallel nm}}{\omega B_0}\Phi_{km}. \end{aligned} \tag{4.66}$$

This means, the magnetic perturbation can be obtained from the electric perturbation input data[8].

If one wants to drop this approximation and keep $\boldsymbol{E}_{\parallel\boldsymbol{k}} \neq 0$, this is not valid any more: magnetic as well as electric perturbation have to be given. Instead of eq. (4.66), one can calculate the (small) parallel electric field (using the same wave decomposition as

[7] Reminder: $\hat{\boldsymbol{b}} = \boldsymbol{B}/B$ is the unit vector in the direction of the equilibrium magnetic field.
[8] used in *falpha.m*

for the potential):

$$\sum_m \boldsymbol{E}_{\parallel \boldsymbol{k}\boldsymbol{m}} = \sum_m \mathrm{i}\boldsymbol{k}_{\parallel nm}\Phi_{km}\ \ \mathrm{e}^{\mathrm{i}(\boldsymbol{k}_{nm}\cdot\boldsymbol{x}-\omega_k t)} - \mathrm{i}\omega_k\alpha_{km}\boldsymbol{B}_0\ \ \mathrm{e}^{\mathrm{i}(\boldsymbol{k}_{nm}\cdot\boldsymbol{x}-\omega_k t)}$$

$$\Rightarrow \alpha_{km} = \frac{k_{\parallel nm}}{\omega_k B_0}\Phi_{km} + \mathrm{i}\frac{E_{\parallel km}}{\omega_k B_0}. \tag{4.67}$$

The relation between $\tilde{\Phi}$ and $\tilde{\alpha}$ make it later possible to eliminate the magnetic perturbation $\tilde{\alpha}$ from the wave equation, which is extremely useful, especially if $\tilde{E}_{\parallel} = 0$. Otherwise, it also allows one to eliminate $\tilde{\alpha}$, but a small correction term $\tilde{E}_{\parallel}$ has to be retained within the formulation.
To be able to expand the perturbation potential in the ordering of powers of the slowly varying wave amplitude, and the small wave frequency shift (see below), it is useful to further decompose the wave potential. First, one can define:

$$\Phi_k =: \frac{\partial}{\partial t}\chi_k, \tag{4.68}$$

and χ consisting of a slowly varying Amplitude A , a spatial eigenfunction $\hat{\chi}$ and the oscillation term of the exponential function, which also contains a frequency shift σ:

$$\chi_k = A_k(t)\ \hat{\chi}_k\ \mathrm{e}^{-\mathrm{i}\omega_k t - \mathrm{i}\sigma_k(t)}. \tag{4.69}$$

The same slow complex time variation is introduced for each wave's electric potential:

$$\Phi_k = A_k(t)\ \Phi_{km}\mathrm{e}^{\mathrm{i}(n_k\zeta_j - m\theta_j - \omega_k t - \sigma_k(t))}. \tag{4.70}$$

The slow variation is separated into its real and an imaginary part by defining an X and Y such that

$$\begin{aligned} X_k(t) &:= \quad \Re e[A_k\ \mathrm{e}^{-\mathrm{i}\sigma_k}] &= A_k\ \cos(\sigma_k), \\ Y_k(t) &:= -\Im m[A_k\ \mathrm{e}^{-\mathrm{i}\sigma_k}] &= A_k\ \sin(\sigma_k). \end{aligned} \tag{4.71}$$

Thus,

$$A_k\ \mathrm{e}^{-\mathrm{i}\sigma_k} = X_k(t) - \mathrm{i}Y_k(t). \tag{4.72}$$

In case of a non-vanishing parallel electric field, one has to do the same for $\tilde{E}_{\parallel}$ (otherwise, $E_{\parallel k} = 0$ and $\Sigma_k = 0$), i.e. defining:

$$E_{\parallel k} =: \frac{\partial}{\partial t}\Sigma_k, \tag{4.73}$$

$$\Sigma_k = C_k(t)\ \hat{\Sigma}_k\ \mathrm{e}^{-\mathrm{i}\omega_k t - \mathrm{i}\sigma_k(t)}. \tag{4.74}$$

With these definitions, eq. (4.62) results in

$$\begin{aligned} \alpha_k &= -\frac{\nabla_{\parallel}\chi_k}{B_0} + \frac{\Sigma_k}{B_0}, \\ \alpha_k &= -\frac{(\hat{\boldsymbol{b}}\cdot\nabla)\chi_k}{B_0} + \frac{\Sigma_k}{B_0}. \end{aligned} \tag{4.75}$$

It is convenient to introduce the following notation for the real and the imaginary part of Φ_k:

$$C_{jkm} := \Re e[\Phi_{km}(\psi_{pj})\, e^{i(n_k\zeta_j - m\theta_j - \omega_k t)}], \tag{4.76}$$
$$S_{jkm} := \Im m[\Phi_{km}(\psi_{pj})\, e^{i(n_k\zeta_j - m\theta_j - \omega_k t)}]. \tag{4.77}$$

This definition results in the following notation for the real and the imaginary part of the wave electric potential:

$$\begin{aligned} \Re e\ \ \Phi_k &= \sum_m [X_k(t)\, C_{jkm}\ +\ Y_k(t)\, S_{jkm}], \\ \Im m\ \ \Phi_k &= \sum_m [X_k(t)\, S_{jkm}\ -\ Y_k(t)\, C_{jkm}]. \end{aligned} \tag{4.78}$$

4.4.2 System Invariants

In the presence of a perturbation, the particle energy is no longer conserved, as there can be an energy exchange between wave and particle. However, a new constant of motion exists, as will be shown in the following [72]: The following differential operator gives zero

$$\partial_t + (\omega_k/n_k)\partial_\zeta \equiv 0, \tag{4.79}$$

as can be seen when acting on the wave as defined in eq. (4.65):

$$\Phi_{jkm} \propto e^{i(n_k\zeta - m\theta - \omega_k t)}.$$

Applying this operator on $\mathscr{H}$, and using $\partial_\zeta \mathscr{H} = -\dot{p}_\zeta$, one obtains for one particle j:

$$\begin{aligned} &\frac{\mathrm{d}}{\mathrm{d}t}\left(\mathscr{E}_j - \frac{\omega_k}{n_k} p_{\zeta j}\right) = 0 \\ \Longrightarrow\quad &\mathscr{E}_j - \frac{\omega_k}{n_k} p_{\zeta j} = \text{const.} \end{aligned} \tag{4.80}$$

This means, if the particle loses energy, it also loses toroidal momentum and vice versa. However, the relative change in momentum is much larger than the relative change in the particle energy:

$$\frac{\Delta p_{\zeta j}}{p_{\zeta j}} = \frac{n_k}{\omega_k}\frac{\mathscr{E}_j}{p_{\zeta j}}\frac{\Delta \mathscr{E}_j}{\mathscr{E}_j}, \tag{4.81}$$

(as long as n_k is in the usual range of 10) since $\mathscr{E}_j \propto \Omega$ and the gyrofrequency is much higher than the Alfvén wave frequency, $\Omega \ll \omega_k$.

4.4.3 Wave Lagrangian

This section carries out the derivation of the Lagrangian $\mathscr{L}_{\mathrm{W}}$ for Alfvén waves. As these waves represent a balance between field line tension and plasma inertia, the wave Lagrangian must consist of an electromagnetic part, as well as a contribution from the bulk plasma particles:

$$\mathscr{L}_{\mathrm{W}} = \sum_j \underbrace{\underbrace{\frac{1}{2} m_j \boldsymbol{v}_j^2}_{\text{kin. part}} + \underbrace{e(\boldsymbol{A}_j \cdot \boldsymbol{v}_j - \Phi_j)}_{\text{potential part}}}_{\text{bulk plasma}} + \underbrace{\frac{1}{2\mu_0} \int_V \left(\frac{1}{c^2} E^2 - B^2 \right) d^3x}_{\text{el.mag. part}}. \tag{4.82}$$

Now, the drift velocity (eq. (4.58)) and the fields as composition of an equilibrium and a perturbed part (given in subsec. 4.4.1) are substituted. For simplicity, the sum over k is left away, using the *tilde* instead. Furthermore, the sum over all bulk plasma particles j is replaced by an integration over the volume V, using $\sum_j m_j = \int_V n_s m_s \, \mathrm{d}^3x$ for each particle species s (electrons are neglected, due to their small inertia). Note, that many terms vanish due to orthogonality, as e.g. $\tilde{\boldsymbol{B}}$ and $\tilde{\boldsymbol{E}}_{\perp}$ are perpendicular to $\boldsymbol{B}_0$. The same applies for $\boldsymbol{A}_0$, due to the choice of the equilibrium gauge $\Phi_0 \equiv 0$. The latter leads to $\boldsymbol{A}_0 \cdot \tilde{\boldsymbol{E}} \times \tilde{\boldsymbol{B}} = 0$, as the vectors are co-planar. Sorted according to the perturbation ordering, $\mathscr{L}_{\mathrm{W}}$ reads:

$$\begin{aligned}
\mathscr{L}_{\mathrm{W}} = \int_V \Bigg[& \underbrace{\frac{1}{2} n_s m_s \boldsymbol{v}_0^2}_{\text{0th order}} + \underbrace{\frac{1}{2} n_s m_s \frac{\tilde{E}_{\perp}^2}{B_0^2}}_{\text{2nd order}} \\
& \underbrace{+ n_s e \boldsymbol{v}_0 \tilde{\boldsymbol{A}} - n_s e \tilde{\Phi} + \frac{n_s e}{B_0^2} \boldsymbol{A}_0 \cdot (\tilde{\boldsymbol{E}}_{\perp} \times \boldsymbol{B}_0)}_{\text{1st order}} + \underbrace{\frac{n_s e}{B_0^2} \boldsymbol{A}_0 \cdot (\tilde{\boldsymbol{E}}_{\parallel} \times \tilde{\boldsymbol{B}})}_{\text{2nd order}} \Bigg] \mathrm{d}^3x \\
& + \frac{1}{2\mu_0} \int_V \Bigg[\underbrace{B_0^2}_{\text{0th order}} + \underbrace{\frac{1}{c^2} \tilde{E}_{\parallel}^2 + \frac{1}{c^2} \tilde{E}_{\perp}^2 - \tilde{B}^2}_{\text{2nd order}} \Bigg] \mathrm{d}^3x.
\end{aligned} \tag{4.83}$$

The 0th order terms represent the MHD equilibrium and cancel by force balance. The first order perturbations vanish, since linear waves are stable within ideal MHD. Second order terms are the first non-zero contribution to $\mathscr{L}_{\mathrm{W}}$ within this model. With the use of the definition of the Alfvén velocity (eq. (3.8)), $v_{\mathrm{A}} := B_0 / \sqrt{\mu_0 m_s n_s}$, with n being the number density of the plasma , and m_s the mass of a particle of the species s, the Lagrangian becomes

$$\mathscr{L}_{\mathrm{W2}} = \frac{1}{2\mu_0} \int_V \Bigg[\underbrace{\frac{1}{v_{\mathrm{A}}^2} \tilde{\boldsymbol{E}}_{\perp}^2}_{\text{kin. term}} + \underbrace{\frac{1}{c^2} \tilde{\boldsymbol{E}}_{\perp}{}^2 + \frac{1}{c^2} \tilde{\boldsymbol{E}}_{\parallel}{}^2 - \tilde{B}^2}_{\text{wave energy term}} + \underbrace{\frac{1}{v_{\mathrm{A}}^2} \frac{e}{m_s} \boldsymbol{A}_0 \cdot (\tilde{\boldsymbol{E}}_{\parallel} \times \tilde{\boldsymbol{B}})}_{\text{potential term}} \Bigg] d^3x. \tag{4.84}$$

The fact, that $v_{\mathrm{A}} \ll c$, allows to neglect the terms containing $1/c^2$.
Substituting the Fourier sums (hidden in *tilde* terms), the Lagrangian reads

$$\mathscr{L}_{\mathrm{W2}} = \frac{1}{2\mu_0}\sum_{k,k'}\int_V \left[\frac{1}{v_{\mathrm{A}}^2}\boldsymbol{E}_{\perp\boldsymbol{k}}^{\mathbf{2}} - B_k^2 + \frac{1}{v_{\mathrm{A}}^2}\frac{e}{m_j}\boldsymbol{A}_0\cdot(\boldsymbol{E}_{k\parallel}\times\boldsymbol{B}_{k'})\right] d^3x. \tag{4.85}$$

The orthogonality of the MHD eigenfunctions ensures, that all cross terms of squared field quantities due to the double sum k, k' are zero. Note, that when setting $k' = k$, every term is counted twice, therefore, a factor of $1/2$ enters $\mathscr{L}_{\mathrm{W}}$.
Since $\tilde{\boldsymbol{E}}_\parallel$ is small compared to $\tilde{\boldsymbol{E}}_\perp$, which appears in the first term, it is a valid approximation within the chosen ordering, to neglect the last term. Thus, it turns out, that $\tilde{\boldsymbol{E}}_\parallel$ does not contribute significantly to the wave Lagrangian in second order of perturbation, and $\mathscr{L}_{\mathrm{W}}$ has not changed compared to its expression with vanishing parallel electric field, presented in [72], p. 56.
Substituting eqs. (4.61) and (4.63) into eq. (4.85) yields:

$$\mathscr{L}_{\mathrm{W2}} = \frac{1}{4\mu_0}\sum_{k}\int_V \left[\frac{1}{v_{\mathrm{A}}^2}\left|\nabla_\perp\Phi_k\right|^2 - \left|\hat{\boldsymbol{b}}\times\nabla(\alpha_k\boldsymbol{B}_0)\right|^2\right] d^3x \tag{4.86}$$

Using eqs. (4.68) and (4.75) further gives:

$$\mathscr{L}_{\mathrm{W2}} = \frac{1}{4\mu_0}\sum_{k}\int_V \left[\frac{1}{v_{\mathrm{A}}^2}\left|\nabla_\perp\frac{\partial\chi_k}{\partial t}\right|^2 - \left|\hat{\boldsymbol{b}}\times\nabla((\hat{\boldsymbol{b}}\cdot\nabla)\chi_k) + \hat{\boldsymbol{b}}\times\nabla\Sigma_k\right|^2\right] d^3x \tag{4.87}$$

Thanks to the notations 4.69 and 4.74, the slowly varying complex amplitude terms A and C are made explicit, as well as the small frequency shift σ. It is therefore possible, to expand χ and Σ in powers of the small fractions $\dot{A}_k/(\omega_k A_k)$ and σ_k/ω_k (see app. G). In zeroth order, A_k is constant in time. Taking only the *first* order, one obtains (the last term does not have any order higher than zero!):

$$\mathscr{L}_{\mathrm{W2}} = \frac{1}{2\mu_0}\sum_{k}\int_V \frac{1}{v_{\mathrm{A}}^2}\left[\frac{\dot{\sigma}_k}{\omega_k}\Big(\underbrace{\omega_k\left|\nabla_\perp\chi_k\right|}_{=\omega_k^2 A_k^2|\nabla_\perp\hat{\chi}|^2}\Big)^2\right] \mathrm{d}^3x. \tag{4.88}$$

With $\hat{\chi}$ being the radial structure of the electric perturbation, the expression becomes

$$\mathscr{L}_{\mathrm{W2}} = \frac{1}{2\mu_0}\sum_{k}\int_V \frac{1}{v_{\mathrm{A}}^2}\left[\frac{\dot{\sigma}_k}{\omega_k}A_k^2\left|\nabla_\perp\sum_m\Phi_{km}\right|^2\omega_k^2\right] d^3x. \tag{4.89}$$

With the definition of the (time independent) wave energy

$$\mathscr{E}_\perp = \frac{1}{2\mu_0}\int_V \frac{1}{v_{\mathrm{A}}^2}\left|\nabla_\perp\sum_m\Phi_{km}\right|^2\mathrm{d}^3x, \tag{4.90}$$

one obtains

$$\mathscr{L}_{\mathrm{W2}} = \sum_k \frac{1}{v_{\mathrm{A}}^2}\frac{\mathscr{E}_k}{\omega_k}\left[A_k^2\,\dot{\sigma}_k\right]\omega_k^2. \tag{4.91}$$

From the wave potential decomposition performed in subsec. 4.4.1, it is obvious that:

$$\begin{aligned} A_k^2 &= X_k^2 + Y_k^2, \\ \sigma_k &= \arctan\left(\frac{Y_k}{X_k}\right). \end{aligned} \tag{4.92}$$

This gives for the temporal derivative of the frequency shift σ

$$\dot{\sigma}_k = \frac{X_k \dot{Y}_k \; - \; \dot{X}_k Y_k}{A_k^2}. \tag{4.93}$$

With this equation filled into the equation for $\mathscr{L}_{\mathrm{W2}}$, eq. (4.91), one obtains

$$\mathscr{L}_{\mathrm{W2}} \; = \sum_k \frac{1}{v_{\mathrm{A}}^2} \frac{\mathscr{E}_k}{\omega_k} \left[X_k \dot{Y}_k \; - \; \dot{X}_k Y_k \right] \omega_k^2. \tag{4.94}$$

4.4.4 Interaction Lagrangian

The interaction Lagrangian $\mathscr{L}_{\mathrm{int}}$ expresses the interaction of an ensemble of particles (labeled by the subscript j) and a spectrum of waves (subscript k). The Lagrangian for a free particle in an electromagnetic field consists of a kinetic term and a potential term. The part containing the perturbed fields of the latter is responsible for the wave-particle interaction and thus forms the interaction Lagrangian:

$$\mathscr{L}_{\mathrm{int}} = \sum_j (\tilde{\boldsymbol{A}}_j \cdot \boldsymbol{v}_j - \tilde{\Phi}_j). \tag{4.95}$$

The equation can now be re-written, using the definition of $\tilde{\alpha}$, eq. (4.59).

$$\mathscr{L}_{\mathrm{int}} = \sum_j (\tilde{\alpha}_j \boldsymbol{B}_0 \cdot \boldsymbol{v}_j - \tilde{\Phi}_j). \tag{4.96}$$

As the perturbed velocity $\tilde{\boldsymbol{v}}$ is perpendicular to the equilibrium magnetic field, their scalar product vanishes, leaving only the equilibrium velocity $\boldsymbol{v}_0 = \boldsymbol{v}_{\parallel}$. With the relation between the electric and the magnetic potential, eq. (4.67) one obtains:

$$\mathscr{L}_{\mathrm{int}} = \sum_j \sum_k \frac{1}{\omega_k} \sum_m (k_{\parallel m} v_{\parallel j} - \omega_k) \Phi_{km}(\psi_{\mathrm{p}j}) + \mathrm{i} v_{\parallel j} E_{\parallel km}(\psi_{\mathrm{p}j}). \tag{4.97}$$

Note the appearance of the resonance condition here and the decisive role of the radial (ψ_{p}) envelope of the mode in combination with the particle orbit.
In the following, the equation is separated according to its real and its imaginary part. Therefore, eq. (4.78) is used for the electric potential. A similar decomposed notation has to be introduced for the electric field as well (unless one assumes $\tilde{E}_{\parallel} = 0$).

$$D_{jkm} =: \Re e[E_{\parallel km}(\psi_{\mathrm{p}j}) \, \mathrm{e}^{\mathrm{i}(n_k \zeta_j - m\theta_j - \omega_k t)}], \tag{4.98}$$

$$F_{jkm} := \Im m[E_{\parallel km}(\psi_{\mathrm{p}j}) \, \mathrm{e}^{\mathrm{i}(n_k \zeta_j - m\theta_j - \omega_k t)}]. \tag{4.99}$$

In contrast to the case of the wave electric potential, the amplitude parallel electric field is not allowed to evolve in time self-consistently (i.e. independently). Thus, the physics of $\tilde{E}_\parallel$ is not contained within HAGIS, but given externally, assuming that the damping does not change. One only has to allow for a slowly evolving phase, which has to be the same as for the potential, $\sigma_k(t)$. The wave electric field then reads

$$E_{\parallel k} = E_{\parallel km} \mathrm{e}^{\mathrm{i}(n_k\zeta_j - m\theta_j - \omega_k t - \sigma_k(t))}. \tag{4.100}$$

To again separate this into a real and an imaginary part, one can separate the new factor by defining V and W such that

$$\begin{aligned} V_k(t) := \quad \Re e[\mathrm{e}^{-\mathrm{i}\sigma_k}] &= \cos(\sigma_k) \quad \Longrightarrow \quad V_k(t) \;=\; X_k(t)/A_k(t), \\ W_k(t) := -\Im m[\mathrm{e}^{-\mathrm{i}\sigma_k}] &= \sin(\sigma_k) \quad \Longrightarrow \quad W_k(t) \;=\; Y_k(t)/A_k(t). \end{aligned} \tag{4.101}$$

This definition results in the following notation for the real and the imaginary part of the wave electric potential:

$$\begin{aligned} \Re e \;\; E_{\parallel k} &= \sum_m [V_k(t)\, D_{jkm} \;+\; W_k(t)\, F_{jkm}], \\ \Im m \;\; E_{\parallel k} &= \sum_m [V_k(t)\, F_{jkm} \;-\; W_k(t)\, D_{jkm}]. \end{aligned} \tag{4.102}$$

The real part of the interaction Lagrangian is

$$\mathscr{L}_{\mathrm{int}} = \sum_j \sum_k \frac{1}{\omega_k} \sum_m (k_{\parallel m} v_{\parallel j} - \omega_k) \;\; \Re e[\Phi_{km}] + \mathrm{i}\,\mathrm{i} \;\; \Im m[E_{\parallel k}] v_{\parallel j}. \tag{4.103}$$

Using eq. (4.78) for the electric potential, and eq. (4.102) for the field, leads to

$$\begin{aligned} \mathscr{L}_{\mathrm{int}} = \sum_j \sum_k \frac{1}{\omega_k} \sum_m (k_{\parallel m} v_{\parallel j} - \omega_k) \, [X_k(t)\, C_{jkm} \;+\; Y_k(t)\, S_{jkm}] \\ - \; v_{\parallel j} \, [V_k(t)\, F_{jkm} \;-\; W_k(t)\, D_{jkm}]. \end{aligned} \tag{4.104}$$

Inserting the expressions for V and W of eq. (4.101) yields

$$\begin{aligned} \mathscr{L}_{\mathrm{int}} = \sum_j \sum_k \frac{1}{\omega_k} \sum_m (k_{\parallel m} v_{\parallel j} - \omega_k) \, [X_k(t)\, C_{jkm} \;+\; Y_k(t)\, S_{jkm}] \\ - \; \frac{v_{\parallel j}}{\sqrt{X_k^2 + Y_k^2}} \, [X_k(t)\, F_{jkm} \;-\; Y_k(t)\, D_{jkm}]. \end{aligned} \tag{4.105}$$

4.4.5 The Wave equations

The wave equations can be obtained by varying the relevant Lagrangian, which is $\mathscr{L}_{\mathrm{int}} + \mathscr{L}_w$, calculated in subsec. 4.4.4 and subsec. 4.4.3 respectively.
The relevant Lagrangian reads

$$\begin{aligned} \mathscr{L} = \sum_j \sum_k \frac{1}{\omega_k} \Big(\sum_m (k_{\parallel m} v_{\parallel j} - \omega_k) [X_k(t)\, C_{jkm} \;+\; Y_k(t)\, S_{jkm}] \\ - \; \frac{v_{\parallel j}}{\sqrt{X_k^2 + Y_k^2}} \, [X_k(t)\, F_{jkm} \;-\; Y_k(t)\, D_{jkm}] \\ + \mathscr{E}_k \, [X_k \dot{Y}_k \;-\; \dot{X}_k Y_k] \Big) \end{aligned} \tag{4.106}$$

The variation for Y,

$$0 = \frac{\mathrm{d}}{\mathrm{d}t}\frac{\partial \mathscr{L}}{\partial \dot{Y}} - \frac{\partial \mathscr{L}}{\partial Y} \tag{4.107}$$

gives

$$\begin{aligned} 0 = \sum_j \sum_k \frac{1}{\omega_k} \Bigg(\frac{\mathrm{d}}{\mathrm{d}t}\left[2\mathscr{E}_k X_k\right] + \mathscr{E}_k \dot{X}_k - \sum_m \Big[(k_{\parallel m} v_{\parallel j} - \omega_k) S_{jkm} \\ + \frac{v_{\parallel j}}{\sqrt{X_k^2 + Y_k^2}} D_{jkm} + \frac{v_{\parallel j}}{\sqrt{X_k^2 + Y_k^2}^3} (X_k F_{jkm} - Y_k D_{jkm}) \Big] \Bigg) \end{aligned} \tag{4.108}$$

Solving for $\dot{X}$ reads

$$\begin{aligned} \dot{X}_k = \frac{1}{2\mathscr{E}_k} \sum_j \sum_m \big[(k_{\parallel m} v_{\parallel j} - \omega_k) S_{jkm} \\ + \frac{v_{\parallel j}}{\sqrt{X_k^2 + Y_k^2}} D_{jkm} + \frac{v_{\parallel j}}{\sqrt{X_k^2 + Y_k^2}^3} (X_k F_{jkm} - Y_k D_{jkm}) \big] \end{aligned} \tag{4.109}$$

Analogously varying for X, one obtains $\dot{Y}$:

$$\begin{aligned} \dot{Y}_k = -\frac{1}{2\mathscr{E}_k} \sum_j \sum_m \big[(k_{\parallel m} v_{\parallel j} - \omega_k) C_{jkm} \\ - \frac{v_{\parallel j}}{\sqrt{X_k^2 + Y_k^2}} F_{jkm} + \frac{v_{\parallel j}}{\sqrt{X_k^2 + Y_k^2}^3} (X_k F_{jkm} - Y_k D_{jkm}) \big] \end{aligned} \tag{4.110}$$

These are the equations to solve for the wave evolution[9]. In case of $\tilde{E}_\parallel = 0$, the second line vanishes in both, and only S_{jkm} and C_{jkm} have to be provided as input data ($\Re e\ \Phi_{km}$ and $\Im m\ \Phi_{km}$) in the form of a radial wave structure (j indicates that the radial position is particle j's position) for each wave k and each poloidal harmonic m. Otherwise, D_{jkm} and F_{jkm} have to be known as well. Usually, the magnetic field perturbation structure ($\Re e\ \tilde{\Psi}_{km}$ and $\Im m\ \tilde{\Psi}_{km}$) is given (analogously to the electric potential structure $\tilde{\Phi}$), from which $\tilde{\alpha}$ is calculated via $\tilde{\alpha} = k_\parallel/(\omega B_0)$. Having $\tilde{\Phi}$ and $\tilde{\alpha}$, the relation eq. (4.67) gives the parallel electric field structure, thus D_{jkm} and F_{jkm}:

$$E_{\parallel km}(\psi_\mathrm{p}) = \mathrm{i}\big(k_{\parallel nm}\ \Phi_{km}(\psi_\mathrm{p}) - \omega_k B_0\ \alpha_{km}(\psi_\mathrm{p})\big). \tag{4.111}$$

4.4.6 Interpretation and First Consistency Check of the $\tilde{E}_\parallel$ Term

The electric perturbation field $\tilde{E}$ moves the particles out of the resonance, due to the electric force, and the $\tilde{E} \times B$ force, and has therefore the physical effect of damping. Particles in resonance with the wave (i.e. near the singularity in eq. (3.43)) exchange energy with it. If there is no slope in $f(E)$, the energy transfer to and from the wave cancels. Only with a slope, there is net energy transfer – from the wave to the particles

[9] implemented in *rhs_waves.F*

if the slope is negative (Landau damping).
An additional imaginary term as the $\tilde{E}_{\parallel}$ term shifts the singularity into the complex plane, like a damping term does. In the relation between $\tilde{\alpha}$ and $\tilde{\Phi}$, an imaginary term was derived, being formally equivalent to a damping component γ in the wave frequency ω:

$$\omega_k B\ \alpha_{km} = k_{\parallel m}\Phi_{km} + iE_{\parallel km}$$
$$\overbrace{f_k + i\gamma_k} \tag{4.112}$$

However, the non-vanishing $\tilde{E}_{\parallel}$ is not just another form of adding a damping to the wave frequency[10]: $\tilde{E}_{\parallel}$ is obtained from the electric and magnetic component of the MHD wave, given as input. Therefore, it has a radial structure, $\tilde{E}_{\parallel} = \tilde{E}_{\parallel}(\psi)$, that is different for each mode harmonic m. So far, the wave structure cannot evolve in time within a HAGIS simulation (only the wave amplitude and frequency changes self-consistently with time), and thus, $\tilde{E}_{\parallel}$ cannot either. However, it is planned to update the wave structure on a time scale slower than the particle's bounce time in the wave via coupling HAGIS to the LIGKA code. This will eventually lead to a time-evolving $\tilde{E}_{\parallel}$ term as well.

In order to test the new implementation, a first consistency check has been carried out. $\tilde{\alpha}$ and $\tilde{\Phi}$ are chosen to have the same radial shape but are assumed different by a constant factor:

$$\alpha_{km} = \text{factor}\ \frac{k_{\parallel m}}{\omega B_0}\Phi_{km}$$

As $\tilde{E}_{\parallel}$ is determined by the difference between $\tilde{\alpha}$ and $\tilde{\Phi}$, the parallel electric field also differs only by a constant factor, as shown in (fig. 4.4a) The resulting growth rates (fig. 4.4b) show the expected scaling $\gamma \propto$ factor, in agreement with the discussion above.

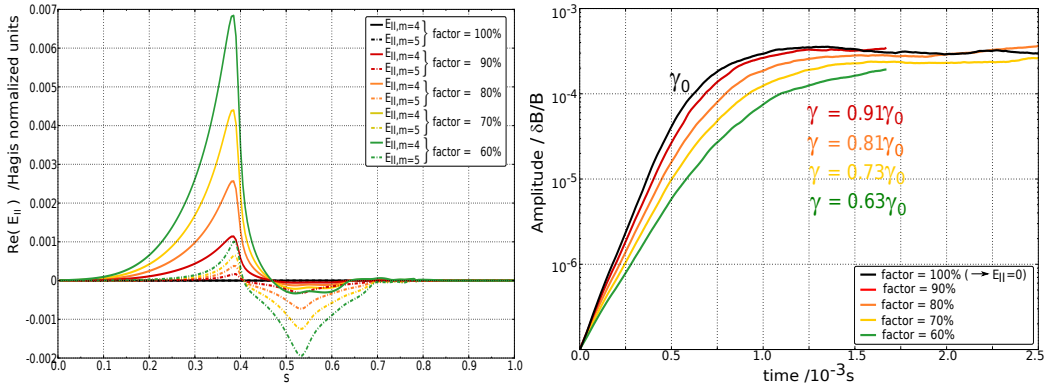

(a) *Radial $\tilde{E}_{\parallel}$ structure.* (b) *Amplitude evolution.*

Figure 4.4: *First consistency check for the new $\tilde{E}_{\parallel} \neq 0$ implementation: the growth rate scales with the same factor, that was chosen between $\tilde{\alpha}$ and $\tilde{\Phi}$. The difference between $\tilde{\alpha}$ and $\tilde{\Phi}$ determines $\tilde{E}_{\parallel}$ and thus the damping.*

[10] which can be done within HAGIS via setting *sgamma* < 0

4.5 HAGIS Outlook

Although the nonlinear wave-particle interaction is calculated self-consistently within HAGIS, other nonlinearities such as the wave *structure evolution* and the toroidal coupling of different n are not included. However, the first steps have been carried out towards a *hybrid model* that overcomes this deficiency. This model will be a hybrid between the nonlinear wave-particle modeling HAGIS code and the linear gyrokinetic eigenvalue solver LIGKA [93], that calculates the wave structures. HAGIS reads the LIGKA-given eigenfunctions (electric and magnetic parts), models the wave-particle interaction and gives back moments of the new fast particle distribution function to LIGKA, which then in turn re-evaluates the wave structures for the HAGIS input (fig. 4.5). What is achieved so far is the possibility to read the full LIGKA eigenfunctions, i.e. with an arbitrary amount of poloidal harmonics, and including not only their electric but also their magnetic potential, which allows to run HAGIS with a non-vanishing $\tilde{E}_{\parallel}$ term, thus a realistic damping structure. Since the calculation of the moments to give back to LIGKA is already included within HAGIS, in the next step, the HAGIS-LIGKA communication has to be addressed. Of special interest is the adequate iteration scheme for passing back and forth the eigenfunction as well as the distribution function to describe the nonlinear system behavior correctly. It has to be a compromise between easing LIGKA's iterative eigenvalue search by short exchange intervals (thus, the start eigenfunction for the search has not changed too much) and saving computational costs.

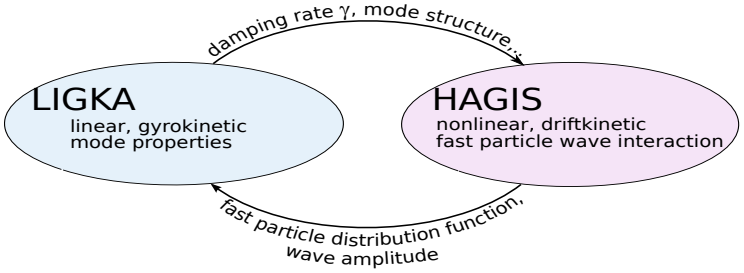

Figure 4.5: *Basic idea for the* HAGIS-LIGKA *hybrid model to allow the mode structure to evolve.*

The hybrid HAGIS-LIGKA model will be able to evolve the eigenmodes on a time scale slower than the mode frequencies. Although *chirping* effects – i.e. rapid frequency changes that occur in regimes near marginal stability[11] – can be simulated by HAGIS, as the frequency evolves in time, it will not be possible to update the wave structures on a time scale comparable to the mode frequencies. Whether or not these structures change during a chirping event is still an open question, since there is no experimental evidence yet. In contrast, the importance of a non-local damping mechanism for regimes near marginal stability is not doubted. With the use of the new $\tilde{E}_{\parallel}$ term, first studies can be carried out in the near future. Another aspect, that is still missing within the HAGIS model is a *source term* for fast particles – so far, there is no possibility to 'refill' fast particles, making it impossible to simulate on time scales of the slowing-down time [98] (≈ 0.1 s, see sec. 6.3.6).

[11] Experimental evidence is reported in ref.s [94, 95], simulations presented in ref.s [96, 97], the theory is covered by the Berk & Breizman model (1990s).

CHAPTER 5

Double-resonant Fast Particle-wave Interaction

The interaction of a fast particle population with MHD and MHD-like instabilities (see chapter 3) can lead to significant fast particle losses, as observed in many ASDEX Upgrade discharges. The study presented in this chapter applies the driftkinetic HAGIS code (see chapter 4)[72] with the aim of understanding the underlying resonance mechanisms, especially in the presence of multiple modes with different frequencies. Of particular interest is the resonant interaction of particles simultaneously with two different modes, referred to as *double-resonance*. Various mode overlapping scenarios with different q profiles are considered. It is found that, depending on the radial mode distance, double-resonance is able to enhance growth rates as well as mode amplitudes significantly. Surprisingly, no radial mode overlap is necessary for this effect. Quite the contrary is found: small radial mode distances can lead to strong nonlinear mode stabilization of a linearly dominant mode.
Sec. 5.1 gives an overview over the theoretical basis of these coupling mechanisms. Sec. 5.2 shortly introduces the AUG equilibrium, which the numerical study is based on. In sec. 5.3 and sec. 5.4, the preparation of the simulations is described concerning simulation conditions and numerical requirements. The last two sections are dedicated to the study itself, investigating first the single-mode situation, followed by the double-mode scenario and a short summary.

5.1 Theoretical Picture of Double-Resonance

Theory (e.g. ref. [76]) predicts that conversion of free energy to wave energy is enhanced in a multiple-mode scenario, i.e., the interaction of multiple modes produces energy conversion rates higher than what would be achieved with each mode acting independently. This can be partially explained by the principle of gradient (of the radial particle distribution) driven mode growth – according to[1] $\gamma \propto \nabla f(s)$ (see sec. 3.2.2) [47] – which was extended to multiple modes [76, 99–101]. So far, however, the investigation focused on modes with equal frequencies and radial overlap, a limitation that will be overcome in this chapter.

[1] Throughout this work, s refers to the radial coordinate as square root of the normalized poloidal flux: $s = (\psi_{\mathrm{pol}}/\psi_{\mathrm{pol,edge}})^{1/2} \in [0,1]$.

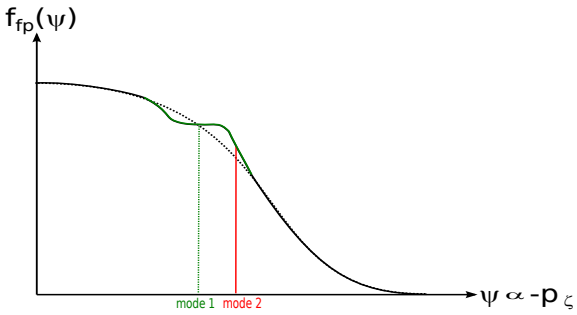

(a) Redistribution caused by mode 1

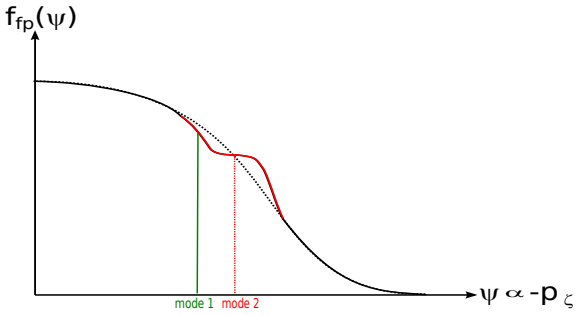

(b) Redistribution caused by mode 2

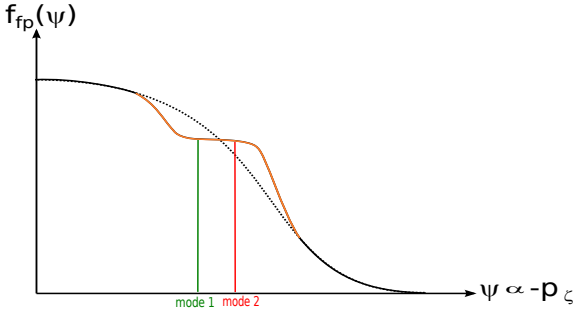

(c) Redistribution caused by both modes

Figure 5.1: *Simple scheme of gradient driven double-resonance to explain steeper gradients and higher saturation levels in the double-resonant mode case compared to the single-mode case.*

The picture of ***gradient driven double-resonance***, schematically visualized in fig. 5.1, is based on the precondition that modes share resonances in the same phase space area. Through the resulting redistribution by each mode, a steeper gradient is produced at the other mode's position, enhancing its drive. The overlapping of modes leads then to a much larger conversion of free energy to wave energy.

However, this mechanism can only work if there is also *spatial* mode overlap in the radial direction. In ref. [55] simulations were carried out, finding a double-resonant effect also without this precondition. Furthermore, an oscillation superimposed on the mode amplitudes was observed, clearly indicating mode-mode interaction. The modes without radial overlap are then coupled radially through the particles' trajectories: A population of particles that shares resonances in phase space with both modes and passes both mode locations at once, can transfer energy from one mode to the other [55]. Since the particle orbits are characterized by a certain width, it is not necessary that both modes have a radial overlap. In the following, this mechanism is called ***inter-mode energy transfer***:

By damping one mode (toroidal mode number n), particles gain energy E and also toroidal momentum p_ζ due to the relation (eq. (4.80))

$$\left(E - \frac{\omega}{n} p_\zeta\right) = \text{const.} \tag{5.1}$$

As Alfvénic mode frequencies (ω) are very low (compared to the particles' cyclotron frequency), momentum transfer dominates over energy transfer. Since a particle's toroidal momentum is related to its radial position, $p_\zeta \propto -\psi$ (see eq. (4.45b)), particles gaining energy from the wave (i.e. damping it), are redistributed radially inwards,

whereas particles losing energy to the wave (i.e. driving it), are redistributed radially outwards. The latter is the dominant process and is caused by the negative slope of the particles' radial distribution function. When passing through the second mode, the particles lose energy and toroidal momentum by the mode.

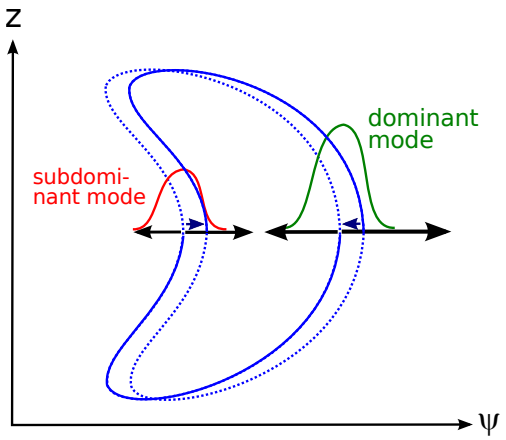

(a) *Scheme of inter-mode energy transfer. The black arrows represent the statistical relations of particle redistribution.*

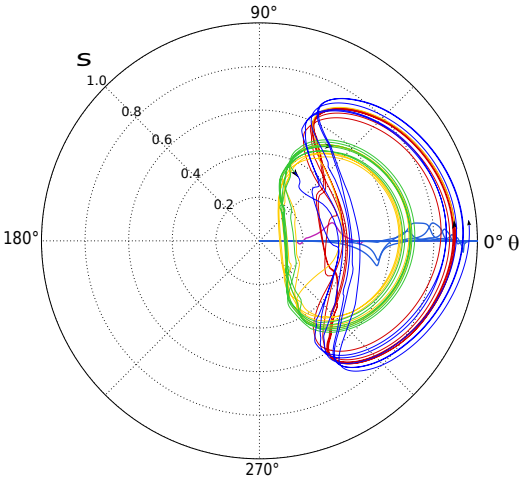

(b) *Orbit of a representative mode coupling particle ($E \approx 435$ keV) simulated by* HAGIS. *The radial mode structures are indicated on the axis ($\omega_1 = 55$ kHz and $\omega_2 = 120$ kHz).*

Figure 5.2: *Double-resonant mode coupling mechanism to explain the superimposed oscillation and steadily growing modes. The different colors in (b) and (c) give subsequent time intervals to visualize the back-and-forth redistribution.*

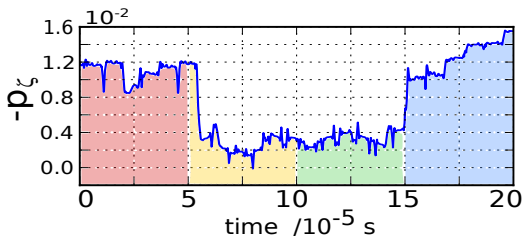

(c) *Evolution of the toroidal momentum (p_ζ) of the same particle.*

As long as the dominant mode is strong, this process can continue, keeping the particle trapped between both modes without a radial net drift, as seen in fig. 5.2. Therefore, this scenario is dominant over other possible combinations of mode-mode energy exchange. Particles that gain energy from both modes or lose energy to both modes soon leave the resonant phase space area. It is the exchange of energy between the modes that leads to the observed oscillation of their amplitudes: The mode receives energy in phase with the particle bounce motion, characterized by ω_b, which equals the beat frequency of both modes $\Delta\omega$ as shown in the following: Trapped particles with a bounce frequency ω_b and toroidal precession frequency ω_{tp} interact with MHD modes of a certain frequency ω, if the *resonance condition* (see eq. (5.2)) [79]

$$\omega - n\omega_{tp} - p\omega_b \approx 0 \tag{5.2}$$

is fulfilled, where n is the toroidal mode harmonic and p the particle bounce harmonic. For double-resonance, this resonance condition has to be fulfilled for both modes '1' and '2' simultaneously, leading to

$$\omega_{\mathrm{tp}}(n_1 - n_2) + \omega_{\mathrm{b}}(p_1 - p_2) = \omega_1 - \omega_2 \equiv \Delta\omega. \tag{5.3}$$

For the simplest case, the toroidal mode numbers n are considered equal, and $p_1 = 1$, $p_2 = 0$. This leads to $\omega_{\mathrm{b}} = \Delta\omega$. Indeed, the lowest bounce harmonics $p = 0, \pm 1$ are the most relevant ones; however, the issue of different toroidal mode numbers n will be discussed later (sec. 5.6.3).
For the example scenario in fig. 5.2b, i.e. a particle with an energy of 435 keV and two modes (both $n = 4$) of frequencies $\omega_1 = 55$ kHz and $\omega_2 = 120$ kHz, at the radial positions $s_1 \approx 0.2$ to 0.3 and at $s_2 \approx 0.4$ to 0.8, the resonances of importance are the $p_1 = 3$ and the $p_2 = 1$ resonance (consult fig. 3.6b). The bounce frequency of the particle can be seen e.g. from the plot (5.5 poloidal orbit surroundings per $\Delta t = 4.6 \cdot 10^{-5}$ s) as $\omega_{\mathrm{b}} \approx 120$ kHz. Thus, eq. (5.3) is fulfilled within this rough estimation.

5.2 Using the Hagis Code with an ASDEX Upgrade Plasma Equilibrium

The numerical investigations presented in this work are performed with the HAGIS code (for an overview, see sec. 4.1), current release 12.05, without using the vacuum extension of ref. [55] (explained in sec. 4.1).
The data for the MHD equilibria of all simulations presented in the following originate from the ICRH-minority-heated ASDEX Upgrade (AUG) discharge #23834, at time $t = 1.16$ s or $t = 1.51$ s. At the earlier time point, the q profile is slightly inverted (fig. 6.2, black solid line), whereas at the later time point, it is monotonic, with lower absolute values (fig. 6.2, blue dashed line).

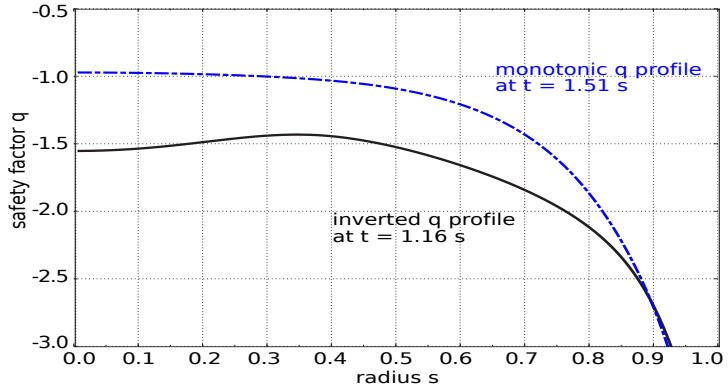

Figure 5.3: *q profile according to experimental measurements in AUG discharge #23824 at different times: $t = 1.16$ s (black solid line) and $t = 1.51$ s (blue dashed line): the q profiles differ in shape (the earlier one is inverted, the later one monotonic), but also in the absolute values (the inverted q profile has higher absolute q values). Note: the negative q values result from the AUG magnetic field's helicity.*

The plasma equilibrium, and in particular the q profile is determined by Alfvén spectroscopy of the RSAEs: magnetic pick-up coil data and soft X-ray emission measurements are used to determine the q profile's minimum value and location.
This particular discharge was chosen due to the availability of especially detailed experimental data concerning fast particle-mode interaction. A detailed comparison between numerical and experimental results is carried out in chapter 6. In this chapter, a numerical study is presented, which is based on an AUG reference case: the q profile, as well as the mode frequencies, harmonics and width are chosen according to experimental observation. However, significant simplifications are made: the mode structures are chosen analytically, as well as the particle distribution functions. Furthermore, mode saturation is based completely on the depletion of the particle distribution function, no collisions, nor turbulence as saturation mechanisms are taken into account, and there is no source term for energetic particles. Therefore, it has to be noted, that the simulated time is significantly lower than the slowing-down time of the fast particles.

5.3 Simulation Conditions

As the question of understanding double-mode resonance is very fundamental, the simulations are performed under quite simple, but still realistic physical conditions: the background plasma[2] is chosen to consist of 94% deuterium and 6% hydrogen ions[3], whereas the fast particle population is simulated as hydrogen ions (concerning mass and charge) with a volume averaged fast particle beta of $\beta_{\mathrm{fp}} = 1\%$. To avoid different mode drive at different radial mode positions only due to a steeper gradient in the distribution function, a radial particle distribution $f(\psi)$ with constant gradient is chosen (fig. 5.4a). The only damping mechanism that is accounted for is the local flattening of the driving gradient in the radial fast particle distribution. However, as explained in sec. 3.2.1, background damping is negligible for the considered scenario.

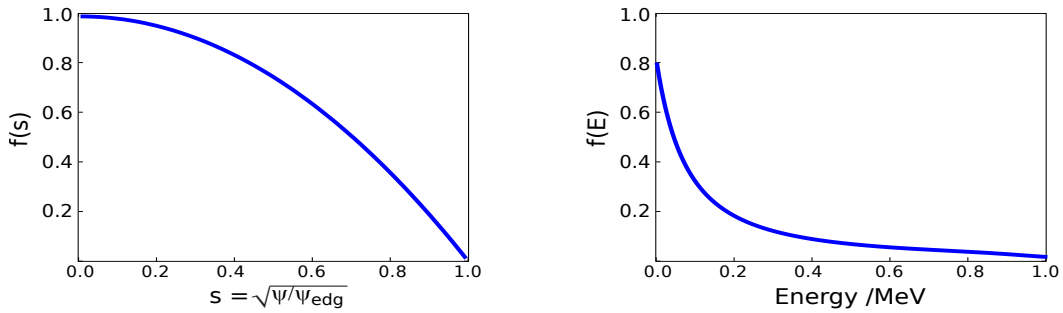

(a) *Radial distribution $f(s)$: constant in s^2*

(b) *Energy distribution $f(E)$: slowing-down*

Figure 5.4: *Fast particle distribution function (marker weighting) in phase space for the numerical study.*

[2] $n_{\mathrm{i}} = 5.4 \cdot 10^{19}\ m^{-3}$, $T_{\mathrm{i}} = T_{\mathrm{e}} = 2$ keV
[3] This is only important for the slowing-down parameters in the energy distribution function.

As energy distribution function $f(E)$ a slowing-down function [102, 103] is used, as shown in fig. 5.4b:

$$f(E) = \frac{1}{E^{3/2} + E_c^{3/2}} \mathrm{erfc}\left(\frac{E - E_0}{\Delta E}\right). \tag{5.4}$$

The parameter E_0 is the most probable maximal energy of the fast particles (*birth energy*) and chosen to be $E_0 = 1.0$ MeV. ΔE depends on the background plasma temperature T, and is (for $T = 2.0$ keV) $\Delta E = 149.9$ keV. The *cross-over energy* E_c takes into account the drag of the electrons on the fast ions. It depends on the background electron temperature T_e (in the following simulations $T_e = 2.0$ keV) and on the fraction of hydrogen to deuterium ions in the background (in the following simulations 0.06 : 0.94). It is $E_c = 19.34$ keV throughout this work. The particles are distributed isotropically in pitch angle (as e.g., fusion born α particles would be).

As MHD perturbations (see chapter 3), analytic, Gauss-shaped functions are used (see fig. 5.5), without background damping. The mode frequencies are chosen to match experimental data: at both time points within the considered discharge #23824, a high frequency TAE with 120 kHz is found ($n = 4$), as well as a lower frequency mode at 55 kHz. Ref. [64] describes this mode as an $n = 4$ RSAE at $t = 1.16$ s and as $n = 4$ BAE at $t = 1.51$ s. The widths of the modes are based on the MHD eigenfunctions, calculated with the linear eigenvalue solver LIGKA [93].

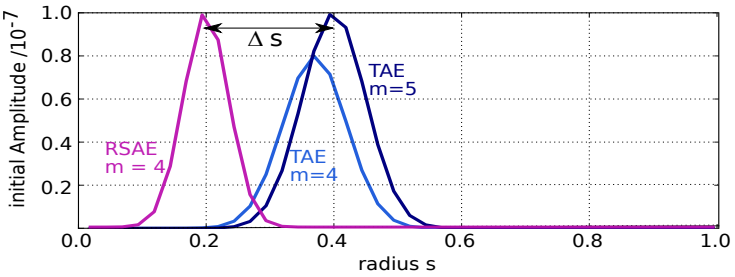

Figure 5.5: *Analytical, Gauss-shaped perturbation as used in the simulations.*

5.4 Numerical Requirements

Before starting the study, convergence in the numerical parameters is tested.
For time stepping, values around 50 to 100 per wave period in the major time discretization[4] and 150 for the orbit integration time stepping[5] are chosen. Concerning error tolerance, values of 10^{-2} for the orbit integration accuracy, and 10^{-4} for the wave amplitude accuracy and magnetic field lines were used[6]. Their convergence is validated by reducing all of them by a factor of 10^{-2}. However, most important for resolution is the number of simulation markers. Fig. 5.6 shows a convergence test for a double-mode simulation with 84 000, 120 000 and 160 000 markers. One can

[4] *n_interm*=50 or 100
[5] *n_integ*=150
[6] *toler_1,2,3*

see, that even the 84 000 marker simulation gives a roughly similar result, compared to the 160 000 marker simulation. The amplitude evolution for the 120 000 marker simulation is in good agreement with the 160 000 marker simulation.

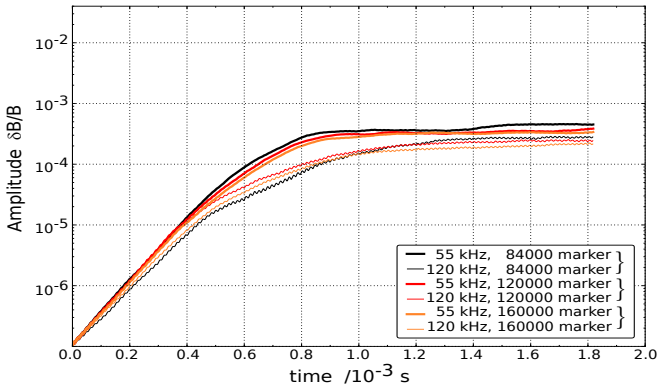

Figure 5.6: *Temporal mode evolution in a double-mode simulation (RSAE at $s = 0.3$, straight lines, and TAE at $s = 0.4$, dashed lines, $\beta_{\mathrm{fp}} = 0.3\%$) with different numbers of simulation markers: 84 000 (black curves), 120 000 (red) and 160 000 (orange): Convergence is found for 120 000 markers already.*

In fig. 5.7, the convergence test for a slightly different scenario is shown: RSAE radial mode position and fast particle beta β_{fp} are increased. This leads to a decreasing TAE amplitude in the saturation phase (as will be explained later). Due to the different amplitudes of both modes, resolution becomes more critical. However, a simulation with 120 000 markers gives perfect convergence for the RSAE amplitude and at the same time, resolves the decaying TAE sufficiently. In the following study, there is no need for a better resolution of decaying modes (which might cost even more than 160 000 markers). Thus, the convergence tests indicate that simulations with 120 000 markers are sufficient, leading to computational costs of a few hundred CPUh for each simulation.

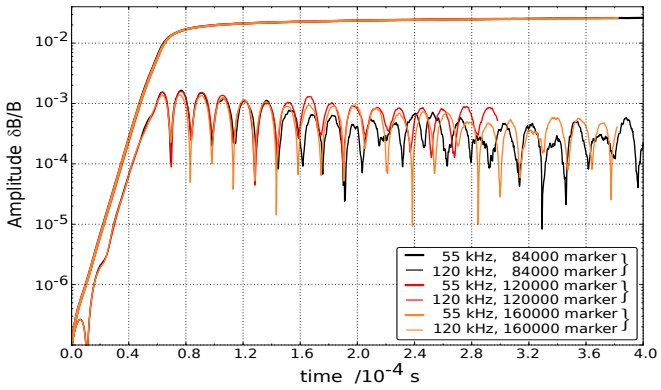

Figure 5.7: *Temporal mode evolution in a double-mode simulation (RSAE at $s = 0.35$, straight lines, and TAE at $s = 0.4$, dashed lines, $\beta_{\mathrm{fp}} = 2.0\%$) with different numbers of simulation markers: 84 000 (black curves), 120 000 (red) and 160 000 (orange): Convergence is good for 120 000 markers.*

5.5 Single-Mode Investigation

The first simulations are carried out with just one mode.
As shown in fig. 5.8, the mode growth rate rises strongly with radial position – the further it is located outside, the higher the growth rate and also the saturation level.

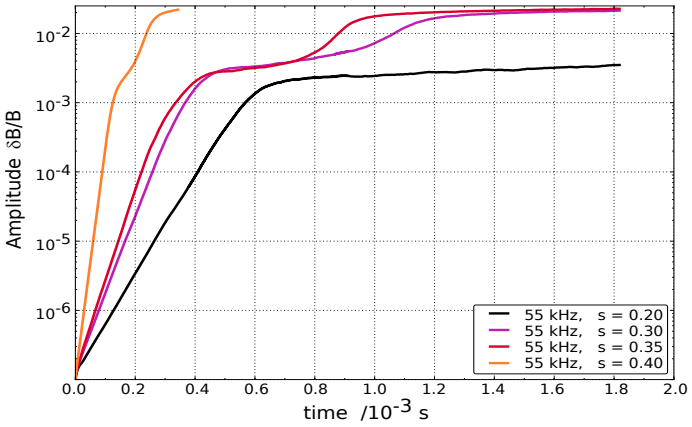

Figure 5.8: *RSAE mode amplitudes for different mode positions:* $s = 0.2$ *(black),* 0.3 *(pink),* 0.35 *(red),* 0.4 *(orange); one can see that more outside positions lead to higher growth rates and higher saturation levels.*

The gradient of the particle distribution is the same at every radial position, due to the linearity of $f(\psi)$. However, the q profile depends strongly on the radial position, and therefore also the particle orbit width. Particles further outwards have a more adequate orbit width for interacting with the given mode: for the circulating particles, the drift ΔR (see eq. (2.31)) is crucial, for the trapped particles, it is the banana width W_b (see eq. (2.37)),

$$\Delta R \propto q\rho \tag{5.5}$$

$$W_\mathrm{b} \propto \frac{q\rho}{\sqrt{\epsilon}} \tag{5.6}$$

For the q profile, it is a good approximation to assume $q \propto r^2$, whereas for the magnetic field B, it is $B \propto 1/R$. Hence, with $\rho = mv_\perp/(eB)$,

$$\Delta R \propto r^2 R \tag{5.7}$$

$$W_\mathrm{b} \propto \frac{r^2 R}{\sqrt{r/R_\mathrm{mag}}} \propto R\sqrt{r^3} \tag{5.8}$$

Especially for core-located modes, trapped particles have a significant contribution to mode drive (growth rate in the linear phase), whereas for modes further outside, this effect is slightly weaker (see fig. 5.9), although the fraction of trapped particles rises with the radial position. In simulations done for fig. 5.9, no trapped particles were initialized, and further, the code was modified to also neglect particles that become trapped in the course of the simulation.

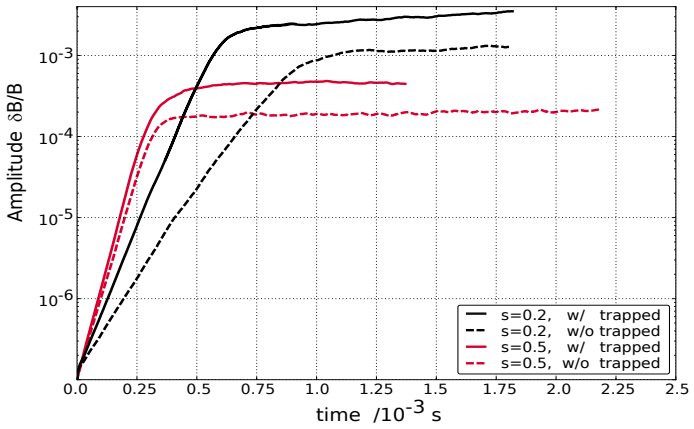

Figure 5.9: *Mode amplitudes in single-mode simulations with (solid lines) and without trapped particles (dashed lines) of a single RSAE at $s = 0.2$ (black) and at $s = 0.5$ (red). Note: β_{fp} =1.0% at the inner, and β_{fp}=0.35% at the outer position, to obtain comparable growth rates.*

The reason for the larger impact of trapped particles on mode drive at inner locations is the location of the resonance lines: at $s = 0.2$ the trapped particles' resonance lines lie densely in lower energy regions. Therefore, particles with smaller orbits, which are better confined are the resonant particles, that cause mode drive.

However, the influence of the q profile is the most important factor. Only the inverted q profile case has sufficient large absolute q values that lead to adequate orbit widths ($\propto q$) allowing the fast particles to drive the modes (see fig. 5.10). In the monotonic q profile, the fast particles' orbit width is much smaller than realistic mode widths, and therefore, fast particle-wave interaction is weaker. Additionally, the resonance lines are less dense in phase space in the monotonic q profile equilibrium (see fig. 6.8).

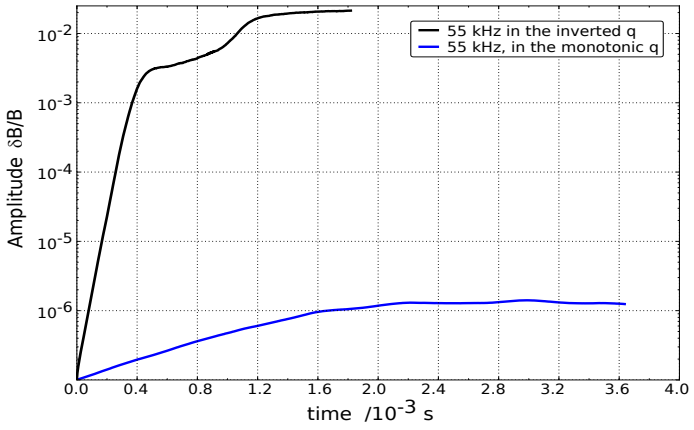

Figure 5.10: *Mode amplitudes of the RSAE (at $s = 0.35$) simulated in two equilibria with different q profiles: the inverted q profile leads to high growth rate and saturation level (black curve), whereas the monotonic q profile does not lead to significant mode drive (blue).*

In all simulations with amplitudes above certain values, one can perceive a significant 'step': after a first quasi-saturation phase, the amplitude is rising again to a higher level, where it saturates finally. This step is no numerical artifact, but has a physical background. It appears at an amplitude level of about $\delta B/B \approx 2 \cdot 10^{-3}$, in accordance with the theoretical predicted *stochasticity threshold* [76, 104], but fairly independent of q, the shear $\hat{s}$ or the radial mode position s. Looking at the redistribution in phase space *before* (at around the simulated time $t \approx 2.5 \cdot 10^{-3}$ s) and *after* the step ($t \approx 5.0 \cdot 10^{-3}$ s) explains what happens during the step: during the time before the step, when the quasi-saturation level is reached, the mode is in a *resonant phase*, i.e. it redistributes resonant fast particles interacting with the perturbation, as can be seen in fig. 5.11a: there are specific areas in phase space, where particles move away (blue color) from and others, more radially outward, where particles accumulate (red). The location of these areas matches with the location of the resonance lines (pink) in phase space showed in fig. 5.11a (for trapped particles). Later, however, no distinct redistribution is visible; particles are redistributed all over the energy range from a more inward position towards a more outward one, independent of their energy. Therefore, this phase, shown in fig. 5.11b, is called *stochastic regime*.

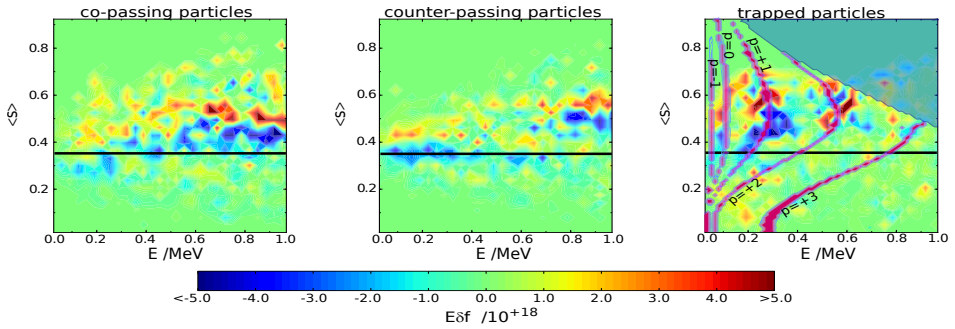

(a) *in redistribution phase,* $t \approx 5.4 \cdot 10^{-4}$ *s*

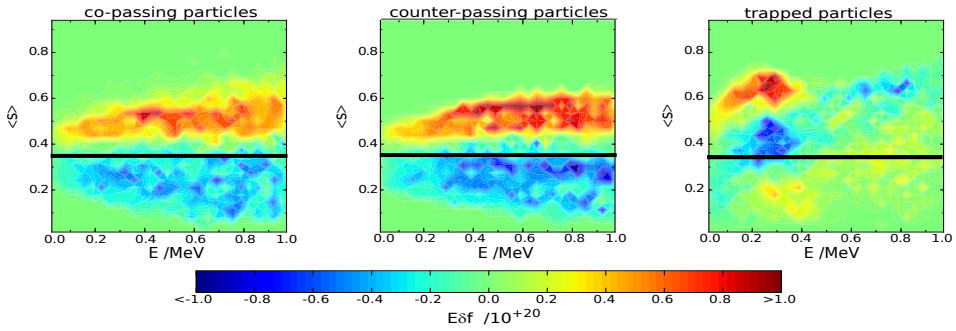

(b) *in stochastic phase,* $t \approx 5.0 \cdot 10^{-3}$ *s*

Figure 5.11: *Change of particle pressure* $E \cdot \delta f$ *in E-s phase space, separated by particle species (co-, counter-passing and trapped. Red: more particles, blue: less particles than initially. During the redistribution phase (a), one can see distinct areas of redistribution that match with the resonance lines (pink) of the resonance plot. In saturation phase (b), this pattern vanishes, leading to a broad redistribution over the energy range.*

Note: unlike the fast particle density, their pressure is comparable to the background pressure, due to their high energies. Thus, the pressure term, $E\delta f$, gives the relevant quantity for particle-mode interaction and is therefore plotted in the phase space plots, rather than the density redistribution δf.

To visualize the effect of stochastization on the particles, a representative particle orbit (left picture) and the particle's energy evolution (right) *before* and *after* the stochastization sets in is shown in fig. 5.12. One can clearly see the difference between the two phases: in the resonant phase, mode-particle interaction just shifts the whole orbit radially outwards (fig. 5.12a), while the particle loses energy. During the stochastic phase in contrast, the interaction with the mode additionally distorts the particle orbit (fig. 5.12b), and the energy loss occurs in bursts. Simulating far beyond amplitudes of $\delta B/B \approx 10^{-2}$ is not reasonable, as amplitudes reaching into the range of few percent compared to the background field are not considered 'small perturbations' any more, and the HAGIS code will be out of validity (due to the perturbation ansatz, described in sec. 3.1).

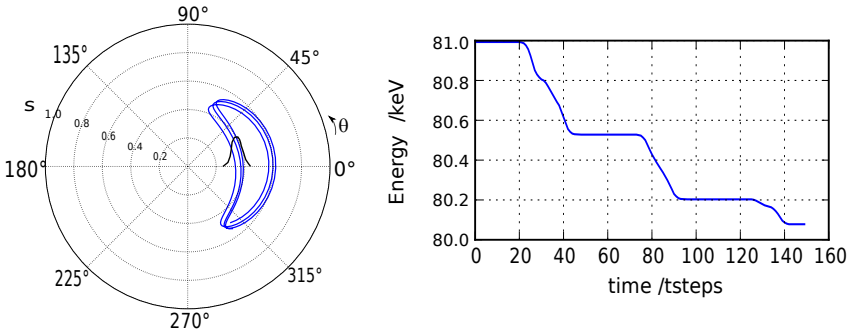

(a) *during resonant phase*

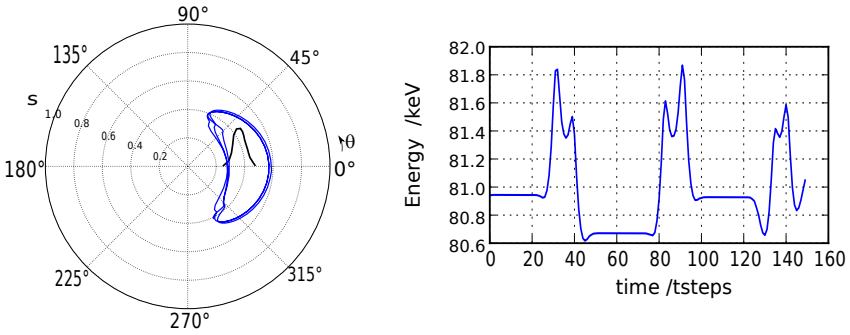

(b) *during stochastic phase*

Figure 5.12: *Representative particle orbit (left, blue line) and energy evolution (right) before (a) and after (b) the stochasticity threshold is reached: During the early saturation phase, the orbit is banana-shaped and shifted outwards, with the particle losing its energy. In the stochastic regime, the orbit becomes distorted and the particle's energy loss occurs in bursts. The black line in the left plots indicates radial envelope of the MHD mode.*

5.6 Multi-Mode Investigation

After getting familiar with the basics of mode drive with one single-mode in the previous section, the original aim of investigating multi-mode interaction is addressed in the following. Multi-mode simulations are carried out with different radial distances Δs between the Alfvénic modes.

5.6.1 The Effect of Radial Mode Distance on Double-resonance

It is helpful to look at the different stages within the simulation individually: although all simulations are performed including all particle nonlinearities, the nonlinear effects are small at the beginning of each simulation, leading to an amplitude evolution according to $\propto \exp(\gamma t)$ with γ the linear growth rate.

The linear regime The mode amplitudes in this linear regime, as depicted in fig. 5.13 confirm already some of the results presented in ref. [55]: at least one mode grows faster in the double-mode scenario compared to the single-mode simulation (the TAEs in fig. 5.13, dark colors).

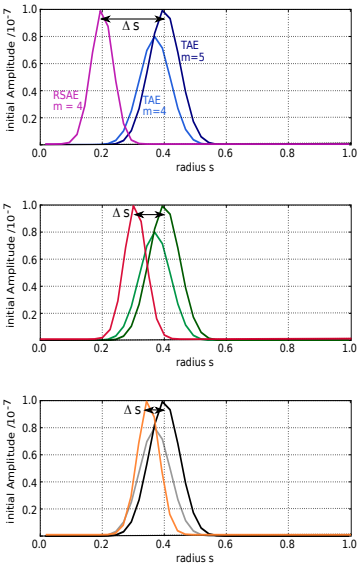

(a) *The analytic perturbations used for the multi-mode simulations presented in (b). The cases differ in the radial distances Δs between the two simultaneously used modes.*

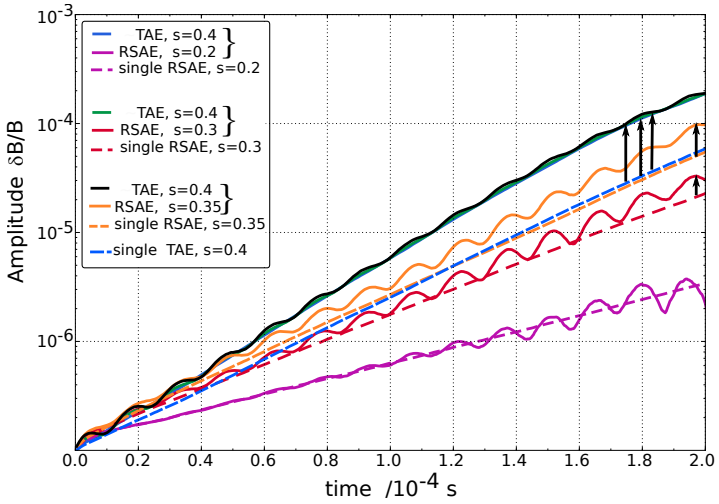

(b) *Mode amplitude evolution in linear growth phase for the different multi-mode (solid lines) scenarios according to (a). For comparison, the single-mode simulations are depicted as dashed lines. In all cases, the TAE (120 kHz at $s = 0.4$, dark colors) grows stronger in the double-mode scenario, the RSAE (55 kHz at various radial positions, reddish colors) in contrast, benefits most from the double-mode case, if Δs is small.*

Figure 5.13: *Three multi-mode (solid lines) scenarios in the inverted q profile equilibrium, differing in radial mode distances Δs.*

In most cases, both modes have larger growth rates in the double-mode scenario than in the single-mode simulation. Furthermore, it is usually the radially outer mode that is driven most strongly due to the double-mode resonance. This is because *gradient driven double-resonance* is most effective in driving the outer mode: through resonant particle redistribution, one mode produces steeper gradients at the other mode's position. Through the inner mode, particles are redistributed towards the outer position and supply it with more (resonant) particles, which can transfer their energy to the wave. At the inner mode's position, in contrast, the particle population decreases, and with it, the potential energy transfer to the wave.

However, in simulations with small growth rates (see linear phase of fig. 5.18), the stronger – and that is mostly the outer mode – was enhanced in mode drive less effectively than the subdominant one, or even weakened to the single-mode case. In these cases, the *inter-mode energy exchange* is the prevailing mechanism, conducting energy from the stronger to the weaker mode.

A superimposed oscillation is visible, strongest if the modes' growth rates are relatively different from each other. However, if they differ too much, the oscillation becomes jagged, due to the large impact of the dominant mode on the subdominant one. The oscillation frequency matches the beat frequency of both modes $\Delta\omega = \omega(\text{TAE}) - \omega(\text{RSAE}) = 65$ kHz, indicating the action of inter-mode energy transfer.
As stated in ref. [55], both mode numbers n have to be equal to lead to the oscillatory behavior, i.e. to double-mode resonance, as will be discussed later.

In the course of each simulation, nonlinear effects become more and more important, leading to a mode amplitude evolution different from $\propto \exp(\gamma t)$. The beginning of the nonlinear regime is observed, when the mode amplitude changes from evolving linearly (in a semilogarithmic plot) to saturating at a certain level.

The nonlinear regime The effect of the double-resonance in the nonlinear regime is clearly visible in fig. 5.14 ($\Delta s = 0.2$): in the double-mode scenario, the modes not only grow faster (in the case of the TAE), but also saturate at a higher level compared to the single-mode case (by about a factor of five to ten). The reason for this is the orbit *stochastization* at $\delta B/B \approx 2 \cdot 10^{-3}$ that was already observed in single-mode simulations: in the stochastic phase, non-resonant particles can become resonant due to distortions of their orbits and drive the mode as well. Thus, a new reservoir of free energy can be tapped. The stochasticity threshold is only reached in the double-mode scenario, not in the single-mode case, in accordance with the prediction by theoretical models [104].

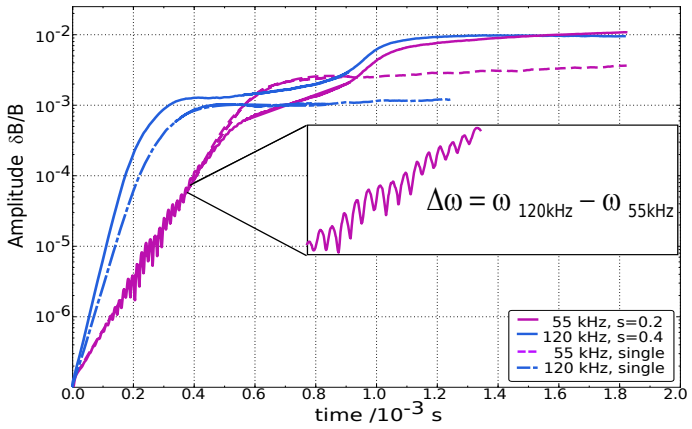

Figure 5.14: *Mode amplitudes evolution in double-mode (solid lines) versus single-mode (dashed) simulation, with an RSAE (pink) at* $s = 0.2$ *and a TAE (blue) at* $s = 0.4$ *for the inverted q profile equilibrium. In the double-mode case, one can clearly see a superimposed oscillation (insert) and higher saturation levels.*

The picture is not as simple in the second example considered ($\Delta s = 0.1$, fig. 5.15): at the beginning of the nonlinear regime, double-resonance is effective – mode amplitudes are higher by a factor of five compared to the single-mode simulation. At a later time point in the simulation however, the situation changes completely: the TAE amplitude vanishes and the RSAE saturates at a lower level compared to the amplitude it reached in the single-mode scenario during stochastization. This scenario was found frequently for close radial mode distances, and shows that a linearly dominant mode can be stabilized nonlinearly in a multi-mode scenario.

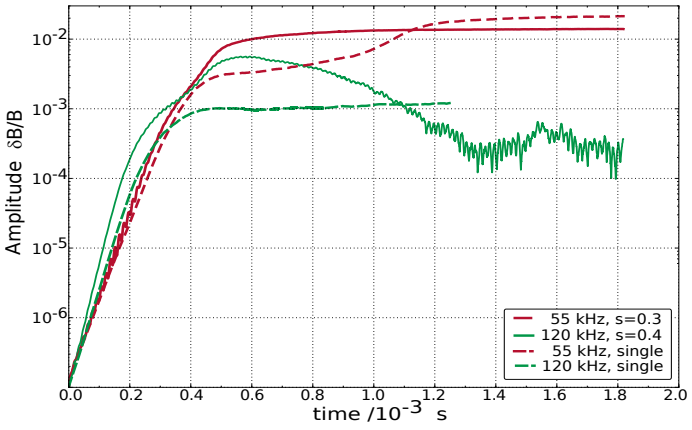

Figure 5.15: *Mode amplitudes evolution in double-mode (straight lines) versus single-mode (dashed) simulation, with an RSAE (red) at* $s = 0.3$ *and a TAE (green) at* $s = 0.4$ *for the inverted q profile equilibrium. Here, the TAE is 'destroyed' in the double-mode case.*

The reason for this behavior can be found in the radial particle redistribution: the single RSAE leads to a radial particle redistribution as depicted in fig. 5.16a. This redistribution leads to a flattened gradient (fig. 5.16b) at $s = 0.4$, the position of the TAE in the double-mode case of fig. 5.15. The reason for the stabilization of the TAE in this simulation is therefore its radial location too close to the RSAE. However, at all positions $s > 0.45$, the gradient becomes steeper in the course of the single-mode simulation. Indeed, simulating the RSAE with a TAE in this radial range leads to strong TAE drive.

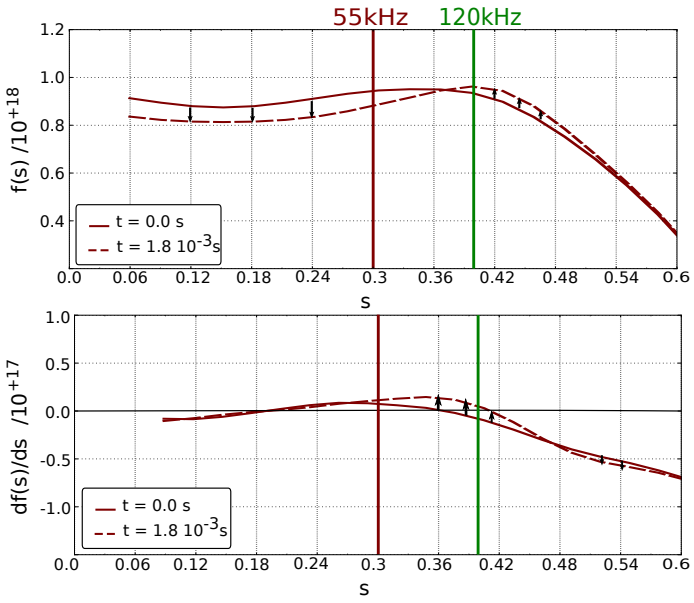

Figure 5.16: *Temporal evolution (early: solid, late: dashed) of the distribution function $f(s)$ in the single-mode simulation (inverted q profile equilibrium) with an RSAE at $s = 0.3$ (upper). Lower: the gradient $\mathrm{d}f(s)/\mathrm{d}s$ at $s = 0.4$ shows a transition from negative values (straight) to positive values (dashed), leading to a very low amplitude of the TAE mode at that position in the double-mode simulation.*

A scan over the radial mode distance reveals the effect of the double-resonance as shown in fig. 5.17: depicted are the ratios of the linear growth rates (a) and the amplitudes (b) in the double-mode case vs. the single mode case over the radial mode distance Δs. The amplitude level was compared after $\approx$ 300 TAE periods ($=$ 2.5 ms) of simulation time. This time is sufficient for the single amplitudes to saturate, but still significantly below energy slowing-down time $\approx$ 0.1 s. Therefore, the fact that no source term is implemented in the code does not disturb the simulation result.

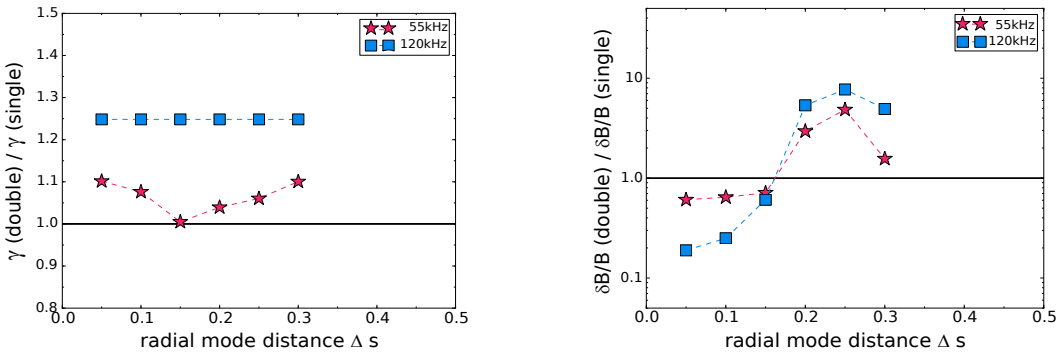

(a) *Growth rates enhancement*

(b) *Saturation amplitudes enhancement (at* $\approx$ 300 *TAE periods)*

Figure 5.17: *Mode evolution scanned over the radial mode distance* Δs *in the inverted q profile case. Depicted is the* Δs *dependence of the ratios of growth rates (a) and amplitudes (b) in double-mode simulations over those from single-mode simulations. Red: RSAE, blue: TAE. One can clearly see that larger radial mode distances lead to higher amplitudes, whereas amplitudes are even lower than in the single-mode case for* $\Delta s \leq 0.15$. *The linear growth rates, however, are higher than in the single-mode simulation throughout the* Δs *range. (The RSAE growth rate experiences a small drop at* $\Delta s \approx 0.15$.*)*

One can see that the growth rates of both the TAE and the RSAE are enhanced in all double-mode cases compared to the single-mode ones. However, the growth rate of the outer TAE is enhanced most strongly and independently of the radial mode distance – i.e. gradient driven double-resonance works even if there is no radial mode overlap. In contrast, the enhancement of the inner and weaker RSAE decreases with the radial mode distance for small Δs. Then it increases for $\Delta s > 0.15$. These larger mode distances match the double-resonant particle orbits and therefore enable inter-mode energy exchange, driving the weak mode. For higher Δs, the larger, i.e. higher energetic orbits fit the mode distance and lead to even more energy exchange. Furthermore, with larger radial mode distances, the modes are able to tap energy from a wider region. The amplitude ratios, however, are even lowered in the double-resonant case compared to the respective single-mode levels, if the radial mode distance is small. This happens due to the mutual gradient depletion at the other mode's radial position. If the modes cover a larger radial distance ($\Delta s > 0.15$), the double-mode scenario amplitudes are much higher compared to the single-mode amplitudes, both for the TAE and the RSAE. Both modes benefit from each other – most for a radial distance

of about $\Delta s \approx 0.25$. It is important to note that the distance $\Delta s = 0.25$ giving maximum amplitude ratios depends strongly on the absolute mode positions with respect to the radial distribution function, and especially on the amplitude regime (stochastic or non-stochastic) of each mode. The same applies for the value $\Delta s = 0.15$ at which the transition towards double-resonant amplitude enhancement takes place.

To summarize, the growth rates are generally enhanced by the presence of another mode, whereas for the nonlinear amplitudes, this is only the case, if the modes have a sufficient radial distance. For small distances, modes at radial positions, where the initial distribution function is already relatively flat, double-resonance leads to strong mode stabilization. If the amplitudes are enhanced, their amplification level is, however, mainly determined by whether the mode reaches the stochastic regime. The stochasticity threshold can be reached more easily, if a second mode is present.

However, if the growth rates are relatively low for some reason (e.g. small mode width, small fast particle beta), the particle redistribution is not strong enough to lead to a dominant gradient driven double-resonance. In these cases, the *inter-mode energy transfer* mechanism can prevail (even in a later phase). The dominant mode is weakened through inter-mode energy transfer to the subdominant mode, as depicted in fig. 5.18. The process saturates, as the mode amplitudes converge towards comparable levels. In this simulation, there is no strong fast particle redistribution.

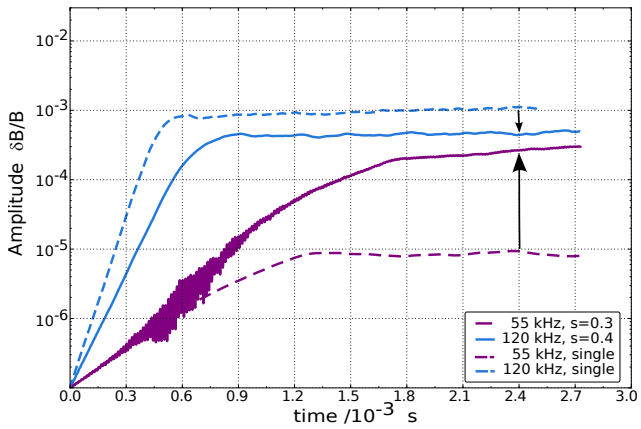

Figure 5.18: *Mode amplitudes over time in double-mode (solid lines) versus single mode (dashed) simulation with low growth rates (for monotonic q profile equilibrium ($\beta_{\mathrm{fp}} = 2.5\%$) with a BAE (pink) at $s = 0.3$ and a TAE (blue) at $s = 0.4$). Here, the redistribution is too weak to lead to significant gradient driven double-resonance. Inter-mode energy transfer (from the TAE to the BAE) dominates.*

As a proof, that it is not per default the drive of the inner mode, that gains energy from the inter-mode energy transfer, nor the low-frequency wave, fig. 5.19 is shown. Here, an RSAE is simulated as a radially broader perturbation, whereas the TAE has a relatively small radial width. These conditions result in a stronger growing RSAE compared to the TAE, and, eventually in the double-mode scenario to an inter-mode energy transfer from the inner RSAE to the outer TAE.

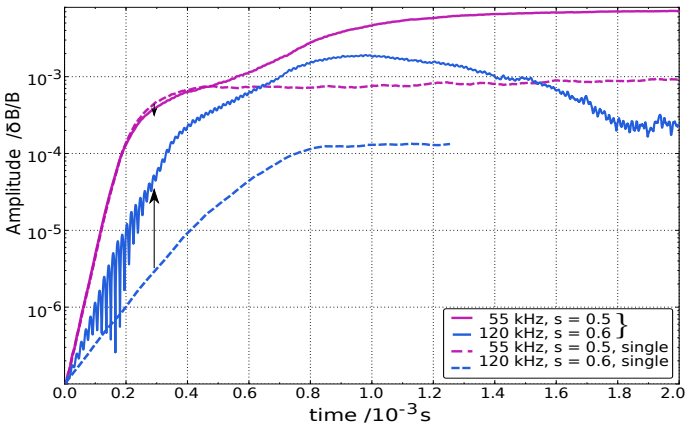

(a) Temporal evolution of the mode amplitudes.

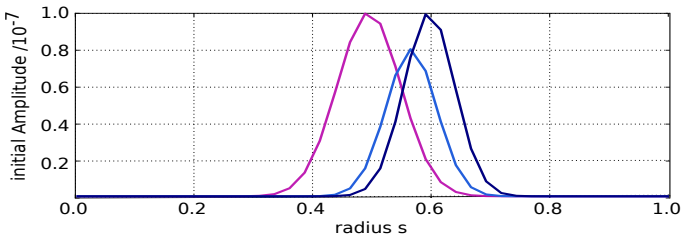

(b) Analytic perturbations used in a.

Figure 5.19: *Mode amplitudes over time in double-mode (solid lines) versus the single-mode (dashed) simulation (in the monotonic q profile equilibrium, $\beta_{\mathrm{fp}} = 1.1\%$), with a broad and therefore strong RSAE at $s = 0.5$ (pink) and a small, i.e. weak TAE at $s = 0.6$ (blue): here, the inter-mode energy transfer in the linear phase goes from the BAE radially outwards to the TAE. Later in the double-mode simulation, the BAE reaches the stochasticity threshold and outstrips the single BAE; the TAE amplitude decays due to the BAE's redistribution.*

A more complex case is shown in fig. 5.20, where two modes in the monotonic q profile equilibrium were simulated, with an increased β_{fp} value, to obtain higher amplitudes: the weaker but inner (BAE) mode is enhanced far stronger than the outer mode (TAE), but even the outer mode experiences an enhanced mode drive through double-mode resonance. A possible explanation is the interplay between both double-mode resonance mechanisms: at first, the BAE does not lead to sufficient redistribution for enhancing the outer TAE through gradient driven double-mode resonance. However, the radial mode distance and the q profile at the mode positions match for an effective inter-mode energy transfer from the TAE to the BAE. Due to the growth of the BAE, its redistribution can be increased (although exactly the particle population responsible for the inter-mode energy transfer is *not* redistributed, as explained earlier in this section) – and leads to a steeper gradient at the TAE position and eventually to enhanced mode drive also for the TAE.

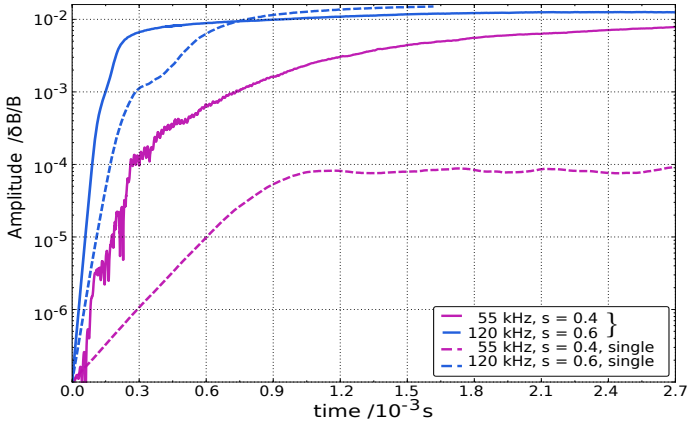

Figure 5.20: *Mode amplitudes evolution in double-mode (solid lines) versus single-mode (dashed) simulation with large radial mode distance (in the monotonic q profile equilibrium, $\beta_{\mathrm{fp}} = 2.5\%$) with a BAE at $s = 0.4$ (pink) and a TAE at $s = 0.6$ (blue): here, the weak mode's drive is enhanced stronger by double-resonance than the dominant one.*

The next example, fig. 5.21 investigates the effect of very different radial mode width. In the single-mode simulation, the mode with large radial extent saturates at almost the same level than the mode with small width. Only the time needed to reach this level is longer in the case of the thin mode. In the double-mode scenario in contrast, the saturation amplitude of the broad mode is higher by a factor of 20 compared to the thin mode. Since the broad mode can tap a wider reservoir of energy in phase space, it grows faster than the thin mode, and quite individually at the beginning. However, once the thin mode reaches a significant amplitude, it 'refills' the exhausted reservoir of resonant particles for the broad mode, i.e. counteracts the flattening of the broad mode. This mechanism does not work vice versa, as the thin mode's radial extent is very small and overlaps largely with the structure of the dominating broad mode.

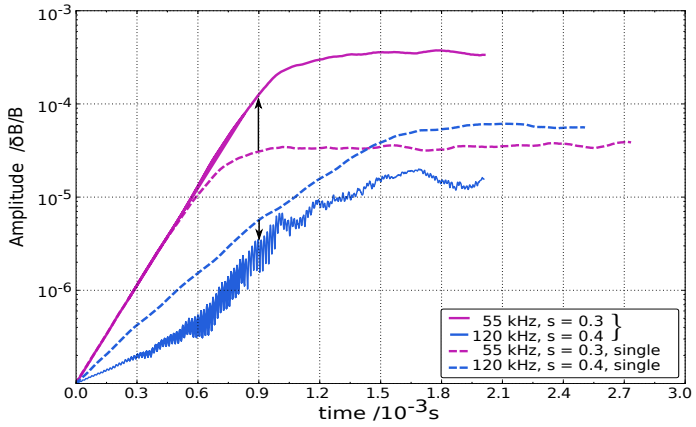

(a) Temporal evolution of the mode amplitudes.

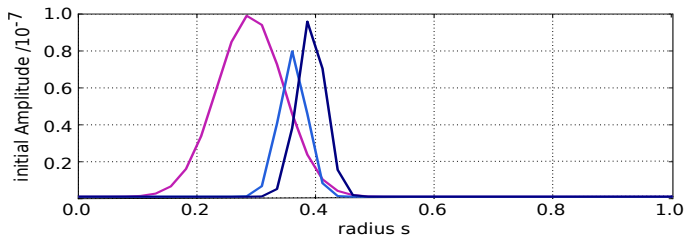

(b) Analytic perturbations used in a.

Figure 5.21: *Mode amplitudes over time in double-mode (solid lines) versus the single-mode (dashed) simulation (for the monotonic q profile equilibrium, $\beta_{fp} = 2.5\%$), with a broad and therefore strong BAE at $s = 0.5$ (pink) and a small, i.e. weak TAE at $s = 0.6$ (blue): here, the inter-mode energy transfer goes from the outside (but weak) TAE to the inside (but strong) BAE.*

5.6.2 The Role of Trapped Particles

Another question regards the role of trapped particles in the double-resonance mechanisms: Especially for the inter-mode energy exchange, the particles' orbit widths are crucial. Therefore, trapped and passing particles may have a different role within the double-resonance mechanism.

In the simulations presented in the following, no trapped particles were initialized, and the code was modified to even neglect particles that become trapped in the course of the simulation. It was found that for the linear phase, the absence of trapped particles leads to significantly lower growth rates (fig. 5.22). The effect is slightly stronger for inner mode positions, although there would be more trapped particles further outside. This is due to the fact that the orbit width broadens with radial position, and therefore also the loss region. But especially the resonance with a broader TAE is effective only with broader orbit particles that are more easily lost.

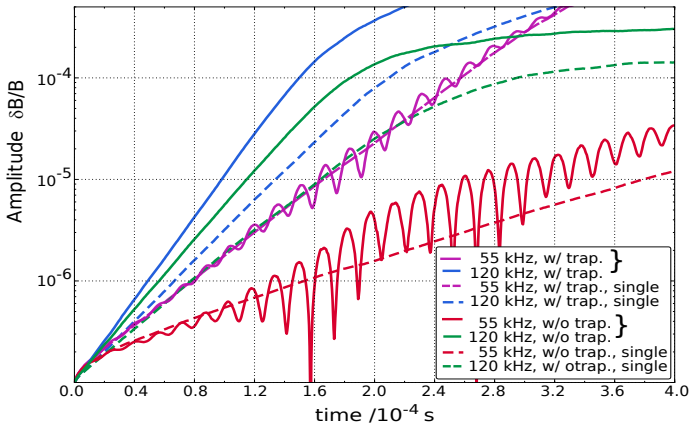

Figure 5.22: *The effect of double-mode resonance on the mode amplitudes evolution in a simulation neglecting trapped particles, using an RSAE at $s = 0.3$ (red solid line) and a TAE at $s = 0.5$ (green solid line). The same scenario is simulated with trapped particles (pink and blue solid lines respectively). The amplitude evolutions in the single-mode cases are shown for comparison (dashed lines).*

However, except for the effect of generally lower amplitudes in the scenario without trapped particles, the double-resonance also works with passing particles alone: the effect of double-resonance remains, which is reflected by the ratio of growth rates and amplitude levels in double-mode simulations compared to those from single-mode simulations. This means, passing as well as banana orbits can be adequate orbits for the double-resonance mechanism of inter-mode energy transfer: As for passing particles, the orbit does not close entirely on the low field side, the double-resonance mechanism must work with the higher poloidal harmonics m of one mode, located at the high field side. For the even TAE, there are no significant maxima at the HFS (see end of sec. 3.1.2). Core-localized modes, such as BAE and RSAE do not couple to the next harmonic $m \pm 1$ and are cylindrical modes, thus, they have comparable amplitudes at the HFS and the LFS (see sec. 3.1.3, sec. 3.1.2). There, double-resonant passing

particles can interact with the mode. Compared to the banana width W_b of a trapped particle eq. (2.37), the drift displacement ΔR of a passing particle's orbit (eq. (2.31) at the same energy) is significantly smaller. But, as the resonance condition is different for passing particles, higher energetic particles are responsible for double-resonance. These have a larger drift displacement that fits again the simulated radial mode distances Δs.

For the gradient driven (double as well as single) resonance, the trapped particles' resonances are very important. Without trapped particles, the saturation levels are much lower and do not reach the stochastic regime. This is due to the importance of the trapped particles' (single) resonances, leading to gradient driven mode-particle interaction. The importance of the trapped particles is consistent with the fact, that the TAE is an even TAE, which due to its ballooning structure interacts very strongly with trapped particles.

5.6.3 The importance of equal toroidal mode numbers

Especially for the inter-mode energy transfer, there has to be a population of particles that is resonant with both modes at once with orbits that pass through both modes. For two modes with different toroidal mode numbers n, the overlapping volume of resonances in phase space becomes smaller, and it becomes less probable to find particles that fulfill the resonance condition eq. (5.3) for two modes at once. Thus, it is expected that less double-mode resonance effects occur, if the modes differ in their toroidal mode number n. Fig. 5.23 shows the resulting amplitude in a double-mode simulation with different n for the RSAE ($n = 4$) and TAE ($n = 5$) in comparison with a simulation of both modes at $n = 4$.

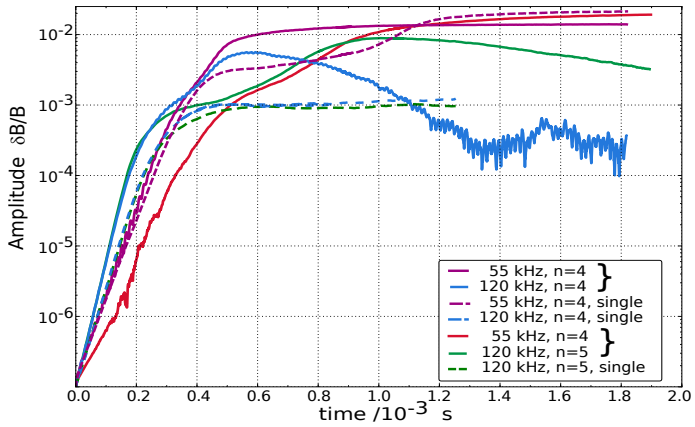

Figure 5.23: *The effect of double-mode resonance on the mode amplitudes evolution in a scenario with different toroidal mode numbers: an $n = 4$ RSAE at $s = 0.3$ (red solid line) was simulated together with and an $n = 5$ TAE at $s = 0.4$ (green solid line). For comparison, the result of the simulation, using an $n = 4$ RSAE and TAE (pink and blue solid lines respectively) is shown, as well as the single-mode cases (dashed lines).*

In the linear phase, one can see clearly that the amplitudes of the single TAE simulations are almost exactly equal, independent on n. However, in the double-mode scenario, the RSAE is enhanced (compared to the single-mode amplitude), and the TAE even more strongly – but only if both modes have equal n. If this is not the case, only the TAE is enhanced, whereas the RSAE actually decreases. Furthermore, the superimposed oscillation vanishes to a slightly jagged curve. This shows that gradient driven double-resonance still works with different toroidal n – the outer mode amplitude is still enhanced – but the inter-mode energy transfer mechanism breaks down, as the resonance condition cannot be easily fulfilled for both modes at once for particles with trajectories through both modes: the inner RSAE amplitude is not enhanced, but weakened. When reaching saturation, the effect of inter-mode energy transfer is overlapped by the dominance of the gradient driven double-resonance, and therefore, the saturation levels do not depend strongly on equal n. Simulations with different n show almost identical nonlinear behavior, although saturation is reached later. The stochasticity threshold does not seem to be influenced by the differing n, nor the effect that one mode can be damped by the redistribution of the other one. However, the differences again depend on the exact scenario.

5.7 Summary

The interaction of fast particles with Alfvén Eigenmodes of different frequencies was studied numerically with the HAGIS code in a simple, but physically realistic picture for two different MHD equilibria occurring during the ASDEX Upgrade discharge #23824. Double-resonant mode drive was compared to single-mode scenarios, verifying previous findings of double-resonance mechanisms: gradient driven double-resonance [76] and inter-mode energy transfer [55]. The latter was observed to prevail only in low amplitude cases, enhancing the weaker mode at the expense of the dominant one. A beat frequency oscillation superimposed on both mode amplitudes was found, as well as higher linear growth rates – at least for one mode – compared to the single-mode reference cases. The growth rate enhancement was observed to have only a very weak dependence on the radial mode distance. Concerning the amplitudes of the Alfvén Eigenmodes, the double-resonance can enhance modes to grow into the stochastic regime and therefore lead to much higher saturation levels compared to the single-mode scenarios, even if there is no radial mode overlap. However, close radial mode distances were found to 'destroy' linearly dominant modes when the nonlinear regime sets in. As a consequence, linearly weaker modes may become nonlinearly dominant. These results reveal a complex nonlinear evolution of multi-mode scenarios, rather than merely a simple continuation of the linear multi-mode behavior.

CHAPTER 6

Nonlinear Alfvénic Fast Particle Transport and Losses

In many discharges in different TOKAMAKs fast particle losses can be observed due to Toroidicity-induced Alfvén eigenmodes (TAE), Reversed Shear-Alfvén eigenmodes (RSAE) or core-localized Beta-induced Alfvén eigenmodes (BAE) (see chapter 3 for modes). They are driven by energetic particles and in turn enhance the losses. In the previous chapter, the mode-particle interaction was studied in different multi-mode scenarios. This chapter advances one step further: simulations under more realistic plasma conditions are presented for different plasma equilibrium conditions, in particular for different q profiles. Fast particle losses are simulated using the extended version of the HAGIS code [72, 83] (see chapter 4 for the code model).
To find out about the loss mechanisms, loss features such as phase space pattern and ejection frequency are analyzed. Both can help to learn about whether or not the losses are caused by mode-particle (double) resonance (*resonant losses*), phase space stochastization (*diffusive losses*) [105, 106] or none of both. Therefore, the losses are categorized: all particles that are unconfined solely due to their large orbit width – caused by a high birth energy – or a birth position radially far outside, are called *prompt losses*. They have no phase correlation with any mode, thus their ejection frequency is not related to any of the modes' frequencies, and the losses are therefore inherently *incoherent*. Losses that are caused due to wave-particle interaction can be both, either *coherent losses*, or incoherent as well. They are coherent, if they show a correlation with one of the mode frequencies or the beat frequency of different modes, but incoherent if they are ejected e.g. due to phase space stochastization. To learn about the role of the modes in the ejection mechanisms, the losses are further studied with respect to the number and type of modes present in the plasma and the q profile (as this determines particle orbit widths and also mode growth). Finally, the numerically obtained losses are compared directly to experimental loss measurements at ASDEX Upgrade [33].

The chapter is organized as follows: sec. 6.1 presents the experimental settings the numerical simulations are based on, as well as experimental loss observation. In sec. 6.2, the step-by-step advance towards more realistic simulations is documented, followed by sec. 6.3 where the final results are formulated, summarized and eventually compared to the experimental measurements.

6.1 Experimental Fast Ion Loss Measurement

To be able to compare the numerical loss results with experimental measurements, a specific experimental scenario with high quality loss data [33] is chosen as a basis for the simulations.

6.1.1 ASDEX Upgrade Discharge #23824

The ion cyclotron (ICRH) minority-heated ASDEX Upgrade (AUG) discharge #23824 is especially interesting for the investigation of fast particle-wave interaction and losses, as it has an inverted q profile after the current ramp-up phase and the q profile relaxes to a monotonic profile (q decreases) as the current density penetrates inwards (see fig. 6.2). As particle confinement depends largely on the q profile due to the proportionality between orbit width and q value, the inverted q profile with its higher absolute q values is expected to impact the amount of losses and also the wave-particle interaction. Further, an inverted q profile allows RSAEs to exist, which are known to interact with fast particles.

Except for the q profile, shot #23824 shows relatively similar plasma properties at two chosen time points ($t = 1.16$ s and $t = 1.51$ s), as can be seen in fig. 6.1.

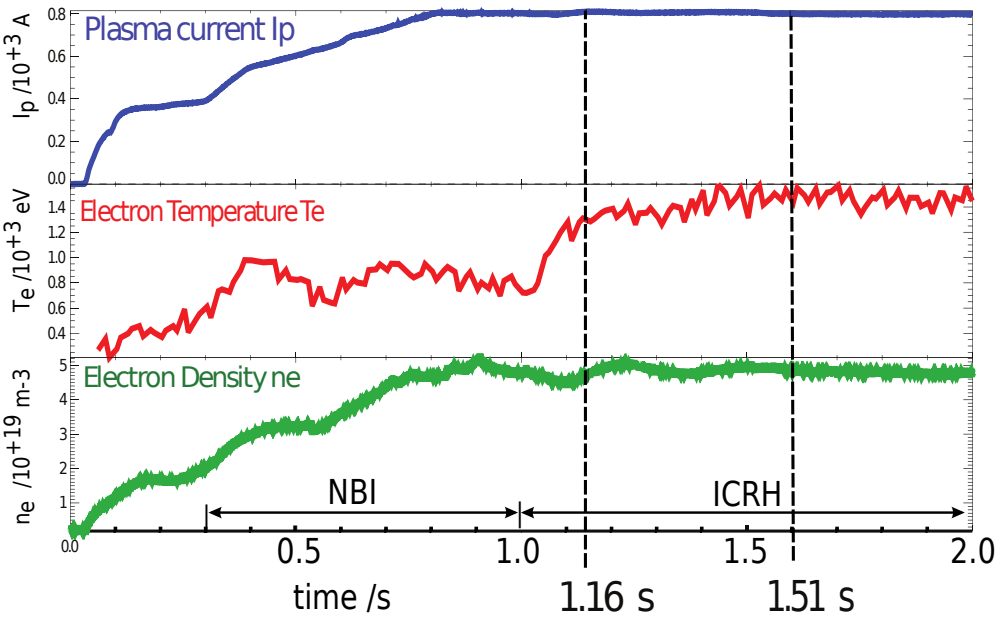

Figure 6.1: *Measured values over time for plasma current, electron temperature and density during AUG shot #23824 [107].*

The simulations are based on these two different MHD equilibria – at $t = 1.16$ s and $t = 1.51$ s (shown in fig. 6.3). The total plasma current is constant between both time points ($I = 800$ kA), only the current density penetrates inwards. Consequentially the inverted q profile at the earlier time point changes to a monotonic q profile at the later time point.

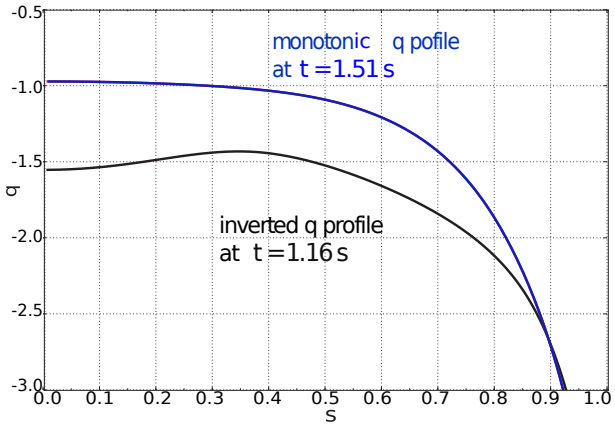

Figure 6.2: *q profile during* AUG *discharge #23824 at different time points, obtained from* CLISTE *calculation constrained by Alfvén spectroscopy measurements as described in detail in [64]. The black solid line shows the q profile at $t = 1.16$ s, whereas the blue dashed line refers to $t = 1.51$ s: the q profiles differ in the shape (the earlier one is inverted, the later one monotonic), but also in the absolute values (the inverted q profile has higher absolute q values in the plasma core).*

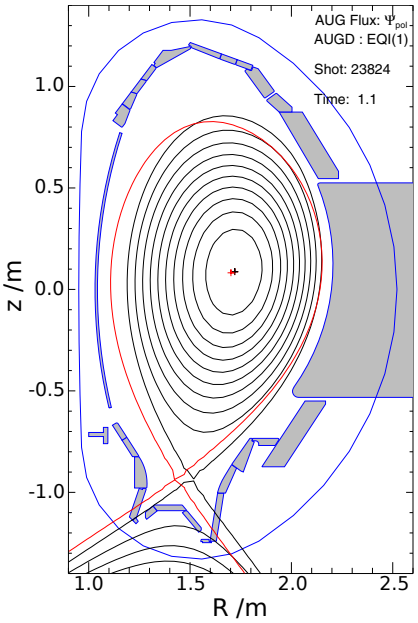

Figure 6.3: *MHD equilibrium of* AUG *discharge #23824 at time $t = 1.16$ s (black) and the separatrix at time $t = 1.51$ s (red) as obtained from the discharge database [107].*

6.1.2 Experimental Observation

In ASDEX Upgrade and other machines of similar size (e.g. DIII-D), a large number of fast ion losses occurs, which is directly measured: a new diagnostic in ASDEX Upgrade, the fast ion loss detector (FILD), provides energy and pitch angle resolved measurements of fast ion losses [35, 108]. The diagnostic consists of a scintillator plate that is contained within a cylindrical cup. The cup can be inserted via a movable manipulator up to a few millimeter behind the limiter, approximately 300 mm above the outboard mid plane (see fig. 6.5). Fast ions enter the detector through an aperture open in the cup and hit the scintillator. Their strike points depend on their gyroradius (i.e. their energy) and on their pitch angle, see fig. 6.4. A CCD camera observes the scintillating surface and provides a highly spatially resolved image. Furthermore, an array of 20 photomultipliers, which have a bandwidth of 1 MHz record the signal, providing a very high time resolution. The collimator geometry of the FILD allows for a detection of fast particles with a gyroradius of $\rho \in [30,120]$ mm. The corresponding energies depend on the magnetic field at the FILD position and on the particle species (their mass and

charge). Since there is no mass detection, different species, e.g. deuterium and hydrogen ions cannot be distinguished. The measured pitch angles are in the range of $\lambda^o \approx 30^o$ (passing) and $\lambda^o \approx 87^o$ (trapped).

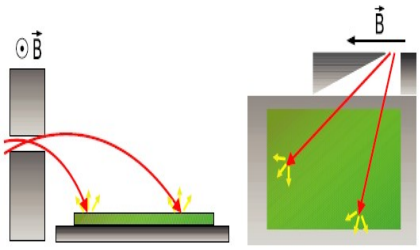

Figure 6.4: *Working principle of the* FILD *diagnostic. Two different particle trajectories are shown to demonstrate how the aperture works in the perpendicular and the parallel direction to the magnetic field. Source: [35]*

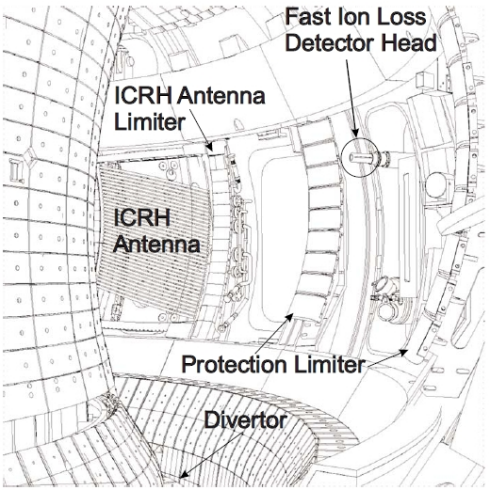

Figure 6.5: *Computer-aided design (CAD) view into the* ASDEX *Upgrade vacuum vessel (segments 8-10) to demonstrate the position of the* FILD. *Source: [108]*

When comparing the FILD measurements to numerical results from HAGIS, it is important to subtract from the experimental data 6^o to 9^o in (absolute) pitch angle and 6% in energy [55]. This deviation is due to the experimental method: deeply trapped particles (created in great number from ICRH heating), have a relatively high drift velocity. However, when measuring the particle's energy, the drift that takes place within the detector is neglected (see fig. 6.6): it is assumed, that the impact spot of the particle perpendicular to the magnetic field lines is caused solely by its gyroradius without any drift within the detector. Thus, the particle's gyroradius is overestimated: $\rho_{\text{exp}} = \rho + \rho'$. Further, the pitch angle changes along the trajectory through the detector. Therefore, to compare with the numerically calculated pitch angle λ^o (which corresponds to the one, the particle had at the detector entry position, λ_0), it is necessary to take this deviation into account, too: $\lambda_{\text{exp}} = \lambda_0 + \lambda'$. The overestimation of pitch angle and gyroradius is caused by the drift velocity v_{D}: $\rho' \approx v_{\text{D}}\Omega$, and $\lambda' \approx \arccos(v_{\text{D}}/v_{\parallel})$. Thus, since $v_{\text{D}} \propto \mathcal{O}(\rho/R)$, it depends on the gyroradius. With $\rho/R \approx 5\%$ for deeply trapped particles, it becomes relevant even on the scale of the detector size.
In ref. [55], λ' was calculated numerically for lost particles with different energies and initial positions, confirming the above estimate with the most relevant angle being λ' approximately $\in [6^o, 9^o]$. The overestimation ρ' of the gyroradii measured experimentally is in the same percentage range. Although λ' and ρ' depend on the pitch λ as well as on the gyroradius ρ (as v_{D} depends on ρ), they can be approximated with the values given above, which were reported in ref. [55].

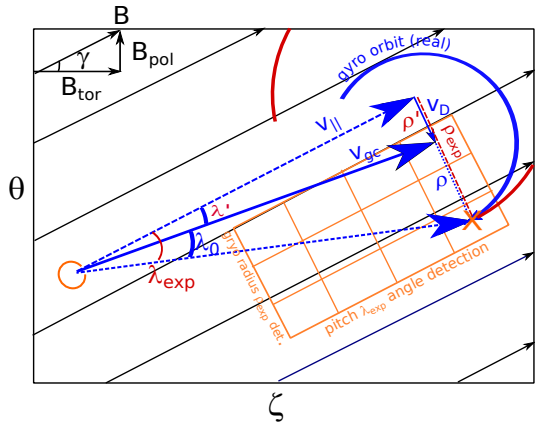

Figure 6.6: *The particle's pitch angle λ_0 (blue) when entering the detector (at the orange circle) deviates from the final pitch angle at the impact position (orange 'X'), λ_{exp} (red) by λ', due to the particle's drift within the detector. Also the* FILD *measured gyroradius ρ_{exp} (red) is overestimated by ρ' compared to the real gyroradius ρ (blue).*

For the AUG discharge #23824, ref. [33] reports a high raw signal with a vast majority of incoherent losses for times before $t \approx 1.4$ s, whereas, after this time, the raw signal is low, consisting of only coherent losses and no incoherent losses at all (figures showing the experimental results are given in sec. 6.3.6).
Fig. 6.7 shows the FILD spectrograms used to investigate the present modes and their frequencies during AUG discharge #23824. At the representative time point of $t = 1.16$ s, the major modes are a $n = 4$ TAE of 120 kHz and a $n = 4$ RSAE of 55 kHz. Later, at $t = 1.51$ s, there is a 160 kHz, $n = 5$ TAE and (though visible only with the Soft X-ray diagnostic method [109]) an 70 kHz, $n = 4$ BAE [64].

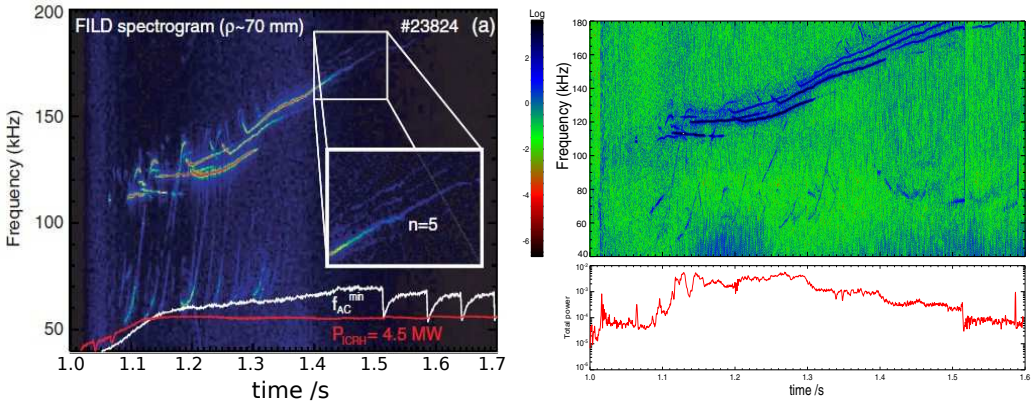

(a) FILD *spectrogram [33]* (b) *Mirnov spectrogram [110]*

Figure 6.7: *Spectrograms (over time) obtained via different measurement systems for AE frequencies during the* AUG *discharge #23824. Note that the frequencies in (b) include a small Doppler shift.*

The Mirnov coils [111] detect an integrated signal for electromagnetic fluctuations at the plasma edge. Thus, they can detect global modes with either a relatively high amplitude or a not too core-localized position, such as TAE. With the Soft-X ray diagnostic more core-localized modes, such as BAE and RSAE can be measured regarding their amplitude and radial position [109].

With HAGIS, the wave-particle resonances in phase space are calculated for these modes (as explained in sec. 3.2.3) in the respective MHD equilibria, AUG #23824, $t = 1.16$ s (see fig. 6.8a) and $t = 1.51$ s (see fig. 6.8b). Two important differences are visible: at the earlier time point, where the q profile is inverted, the loss boundary is larger, due to the higher $|q|$ value. Further, the resonance lines for the observed mode frequencies lie denser, due to the smaller difference in the frequency of both modes.

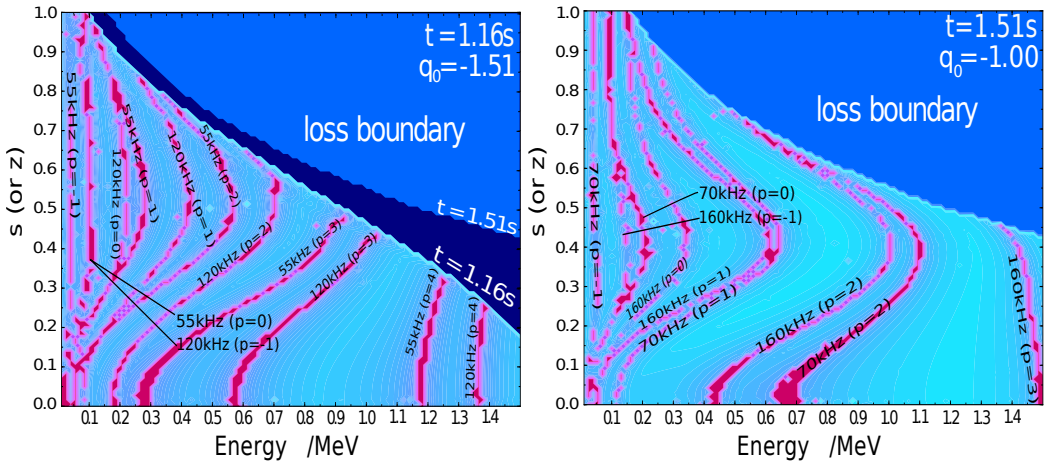

(a) *at $t = 1.16$ s – inverted q profile*

(b) *at $t = 1.51$ s – monotonic q profile*

Figure 6.8: *Resonance plots for two equilibria of* AUG *discharge #23824 at two different time points with different q profiles. Pink indicates resonant, cyan non-resonant areas, with respect to the main MHD modes as diagnosed experimentally ($n = 4$ TAE of 120 kHz, $n = 4$ RSAE of 55 kHz at $t = 1.16$ s and $n = 5$ TAE of 160 kHz, $n = 4$ BAE of 70 kHz at $t = 1.51$ s). Particles in the blue regions are lost. The loss region of the right picture is plotted superimposed in the left image to point out the difference. Note: the* HAGIS *version extended to the vacuum region was used.*

Thus, it appears evident, to observe fewer losses at the later time point. However, the detailed loss mechanism is not known yet: the large amount of losses at the earlier time point can be both – prompt and thus incoherent due to the large orbit widths, *or* caused by wave-particle interaction. In the latter case, the question arises, if the interaction is resonant, causing coherent losses, or diffusive, emerging from phase space stochastization and causing incoherent losses [105]. In the following sections, these questions will be investigated.

6.2 Numerical Implementation to Simulate Fast Particle Losses

As mentioned before, the simulation of fast particle losses with HAGIS requires the use of the extended version, which includes the *vacuum region* [55]. Therefore, the simulations are computationally more expensive (roughly between 120% and 300% compared to the simulations without the extended version). Otherwise, there is no possibility to track the particles across the separatrix and to decide whether they are lost or re-enter the plasma. As will be shown in sec. 6.2.4, losses can be overestimated up to 30%. I.e. around 30% of the particles that cross the separatrix and are *lost* in the original version of HAGIS are actually not lost, but re-enter the plasma.
Compared to chapter 5, not only the code itself is used differently, also the physical simulation conditions are adapted to the more realistic problem. This will be done in different steps: firstly, the distribution function is specialized, secondly the eigenmode input data. But first, a few lines about numerical requirements have to be given, as these may change while approaching more and more realistic simulation scenarios, compared to simpler studies.

6.2.1 Numerical Requirements

One of the most crucial parameters in a PIC code simulation is the number of markers, but also the time stepping as well as error tolerance allowed.
Concerning error tolerance, convergence is validated by reducing the orbit integration tolerance[1] from 10^{-2} to 10^{-4}: the number of losses does not change (100.4%), very small deviations in the mode amplitude evolution of the subdominant mode are visible.
For the time stepping, the numerical requirements are investigated by reducing the time step in the time discretization for calculating the energy transfer between particles and waves[2] from 50 to 150 per wave period (1/55 kHz). The losses obtained are reduced to around 98% only, without a qualitative change in the pattern. Very small deviations in mode amplitude evolution are visible only for the subdominant mode during the phase were both amplitudes differ significantly.
Concerning the number of markers[3]: increasing from 250 000 to 1 million results in exactly the same amplitude evolution (except for minor deviations with the subdominant mode during the phase were both amplitudes differ significantly) and loss appearance.

The reason for the use of the relatively large amount of markers is the idea to investigate the time correlation between mode amplitudes and losses via Fourier analysis. Therefore, the amount of loss events needs to be large enough, to provide good enough time resolved statistics, even after sorting the losses by energy (to not make the peak smeared out by different travel time of the particles). This is, however, not the only point why the desired Fourier analysis makes the simulations more expensive: for good frequency resolution, the selected time window has to be sufficiently large. As the frequency correlation between losses and mode is expected to occur especially

[1] *toler_1* parameter, used in *rkqs* subroutine
[2] *n_interm* parameter, loop in *follow.F*
[3] *nmrkrs* parameter

during the resonant phase, the modes have stay sufficiently long on this first saturation level, before the stochastization sets in. Thus, the growth rates have to be low and the simulated time interval large.

6.2.2 More Realistic Simulation Conditions – ICRH Distribution Function

The AUG discharge #23824 is characterized by the ion cyclotron resonance heating (ICRH), resulting in a very particular fast ion distribution function, different from the fast particle population generated by neutral beam injection (NBI). To be able to simulate the interaction of these ICRH-generated fast ions with Alfvénic waves, an adequate distribution function is implemented in HAGIS. Especially the anisotropy in the pitch λ is taken into account: the ICRH resonance with the background plasma depends on the ion gyrofrequency, and thus on the magnetic field strength. It is located in a small cone below and above the magnetic axis at the poloidal angles $\vartheta = 90^o$ and $\vartheta = 270^o$, radially between $s = 0$ and $s \approx 0.7$. Particles with a very small parallel velocity $v_\parallel$ stay longer in this area under the influence of the ICRH heating, and further, the resonance heating increases the perpendicular energy of the particle. Thus, the pitches of the newly generated fast ions are very small. This results in banana orbits (see sec. 2.2.3) with turning points in the area of the ICRH deposition layer. As a consequence, the ICRH-generated distribution function is highly anisotropic in both velocity and orbit topology. Usually, and also in the AUG discharge #23824, the ICRH resonates with the second harmonic of the proton cyclotron frequency, since this is the most efficient heating method (it is called *minority heating*). The major challenge one faces when trying to simulate an ICRH scenario is a two-part problem: first, it is difficult to find the real fast particle distribution function. Different from NBI-heated plasmas, the fast ion distribution function in ICRH-heated plasmas is almost unknown experimentally. Second, the distribution function has strong anisotropies in coordinates that are not constants of the motion (pitch λ and poloidal angle ϑ – coordinates of velocity and real space that change along the particle orbit), making it difficult to evolve such a distribution function in HAGIS.
To explain how these two problems are addressed, this section is split into two parts: the first part is about the implementation of the distribution function into HAGIS. The second part discusses the choice of the distribution function.

ICRH-like Distribution Function Implementation

In HAGIS, the fast ions are treated in a 5D phase space (see sec. 4.3), consisting of the three spacial coordinates: the radial coordinate as square root of the normalized poloidal flux $s = \sqrt{\psi/\psi_{\text{edge}}} \in [0,1]$, the poloidal angle $\theta \in [0,2\pi]$, and the toroidal angle $\zeta \in [0,2\pi]$, which is irrelevant due to axisymmetry. Velocity space is treated in spherical coordinates: $v = |\boldsymbol{v}| = \sqrt{2E/m}$ is the absolute value of the velocity and λ^o the known pitch angle $\lambda^o = \arccos(v_\parallel/v)$. The volume element of this coordinate system consists of the spacial Jacobian part $2\pi(I + gq)/B^2 \mathrm{d}s\mathrm{d}\theta$ (see eq. (4.21), where the $\mathrm{d}\zeta$ integration has been executed) and the velocity space part $2\pi v^2 \sin(\lambda^o)\mathrm{d}v\mathrm{d}\lambda^o$, which is equivalent to $2\pi v^2 \mathrm{d}v\mathrm{d}\lambda$.
As a PIC code and applying the *delta-f* method, HAGIS handles the distribution function

as sum of two parts: an unperturbed part f_0, and a perturbed part δf. This separation of a prescribed component f_0 and a numerically described component δf is formally valid without the assumption that the latter must be much smaller than the former. However, it is only for the case where $\delta f \ll f_0$ that substantial reductions in simulation noise are expected [83]. It is possible to represented only the perturbed part via 'particles', which follow the equations of motion presented in eqs. (4.57). The 'particles' are not equal to physical particles but represent a certain particle density in phase space and are therefore called 'markers'.
Concerning the markers in phase space, one has to distinguish between *loading* and *weighting*: the loading takes place at the beginning of the simulation and positions the markers at their initial position in phase space (see Sec. 3.4.1 of ref. [72]) using Hammersley's sequences[4]. Afterwards, the markers are restricted to the phase space regions specified in the input parameters[5]. All five coordinates are relevant for loading: s, θ, ζ, v and λ. All except the toroidal coordinate ζ can be restricted: $s \in [s_1, s_2]$, $\theta \in [\theta_1 - \Delta\theta, \theta_1 + \Delta\theta]$ (above the mag. axis) and $\theta \in [\theta_2 - \Delta\theta, \theta_2 + \Delta\theta]$ (below the mag. axis), $E \in [E_{\min}, E_{\max}]$ and $\lambda \in [\lambda_0 - \Delta\lambda, \lambda_0 + \Delta\lambda]$[6]. Especially for the θ coordinate, one has to take into account, that the Boozer coordinate θ does not transfer identically into the torus coordinate ϑ. The loading fills these phase space regions uniformly with markers, as can be seen in green in fig. 6.9 and fig. 6.10 (green).

In the unperturbed situation, an equilibrium energetic particle distribution profile is present during the discharge, i.e. one assumes either a balance between relaxation and heating source (which is not implemented in HAGIS) or sufficiently small simulated times ($\ll 0.1$ s). The unperturbed part of the distribution function, and also the weight of a marker is determined by the distribution function specified as analytical function $f_0(\psi, E, \Lambda)$ in the input parameters[7]. Each marker is assigned with a weight according to the value of this function at its current phase space position. However, for this position, the coordinates θ and λ are not 'good coordinates', as they change along the orbit. In contrast, the radial coordinate s is an approximately constant orbit property (if neglecting particle drifts, the particle remains on the same flux surface), as well as the kinetic energy, i.e. the particle velocity v (if HAGIS is used without taking collisions into account, as it is in this work). For simulating isotropic energetic particles (e.g. α particles), the distribution function can be described in the above way, as the fast particle population is isotropic in pitch space then. For ICRH-heated plasmas, this characterization however is not sufficient, as it does not describe the strong anisotropy in λ: it is wrong to weight λ independent from θ. For a combined λ and θ weighting, one has to use other coordinates that are constants of the motion.

[4] Source file *quiets.F*. Different loading schemes are possible, addressed by the *start0* option, such as via random generator or user input. However, these other loading schemes are not used throughout this chapter.

[5] *&MARKER_LOADING* in *hagis.dat*

[6] In the input parameter file, $[s_1, s_2]$ are given by *s_load[:]*, $\theta_{1,2}$ by *thICRH1,thICRH2*, $\Delta\theta$ by *epsthICRH*, $E_{\min,\max}$ by *ensmin, ensmax*, λ_0 is *lam0* and $\Delta\lambda$ is *dellam* in the parameter file. The pitch anisotropy is addressed only when setting the parameter *lamopt==4*.

[7] *&DISTRIBUTION_FUNCTION* in *hagis.dat*

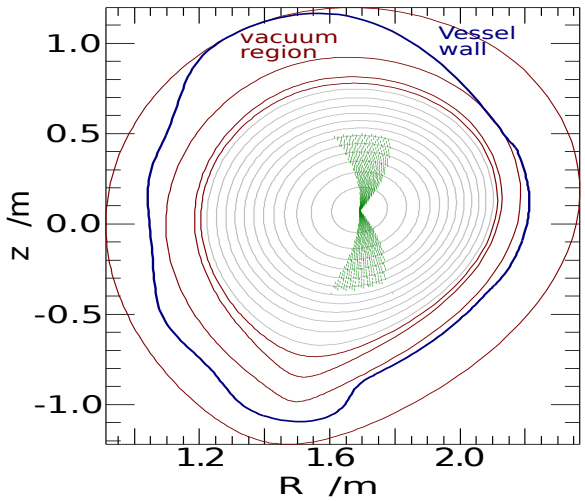

Figure 6.9: *The R-z plane of the MHD equilibrium used in the* HAGIS *simulations with the* ICRH*-type initial marker distribution (in green), i.e. showing the loading along the s and the θ coordinate. In this example,* $s \in [0.001, 0.70]$ *and* $\theta_1 = 1.26$, $\theta_2 = 5.09$, $\Delta\theta = 0.3$*, which transfer to* $\vartheta = \pm 90 \pm 17.2^o$ *in the shown torus coordinate system.*

ICRH-heated fast ions populate only a small area of pitch space around $\lambda = 0$. For NBI-heated plasmas, pitch space is populated highly anisotropic as well, but around $\lambda = \pm 1$. The pitch is not a conserved quantity and it is therefore not correct to just emphasize those markers (via a strong weight) that have $\lambda = 0$ (in the ICRH case), because this is only valid for certain θ angles. Instead, one has to search for a conserved quantity resulting from λ and θ, according to which the markers can then be weighted at any orbit position. The quantity Λ fulfills this condition: it is connected to the pitch λ, but in contrast to that, is not subject to changes along the orbit:

$$\Lambda = \frac{\mu\, B_{\mathrm{mag}}}{E_{\mathrm{tot}}} = \frac{B_{\mathrm{mag}}}{B}\left(1-\lambda^2\right), \tag{6.1}$$

where B_{mag} is the magnetic field at the magnetic axis, introduced as normalization, and B is the magnetic field at the respective position $B(s,\theta)$ and $\lambda = \lambda(s,\theta)$ the pitch at this position. In fig. 6.10d, the transformed distribution function is shown for three different flux surfaces. The blue lines in fig. 6.10c show the back transformed function dependent on λ.
Once the distribution functions along s, v, Λ are known, they can be implemented into HAGIS[8]. The choices for the simulations of this chapter are shown in blue in fig. 6.10.

[8] More precisely: in the *f0_method0.m* file, as a routine called *raddis* for the s direction, *veldis* for v and – in case of pitch anisotropy – *Lamdis* for Λ respectively. Several functions can be chosen via the input parameters *rflag, vflag, pitflag*.

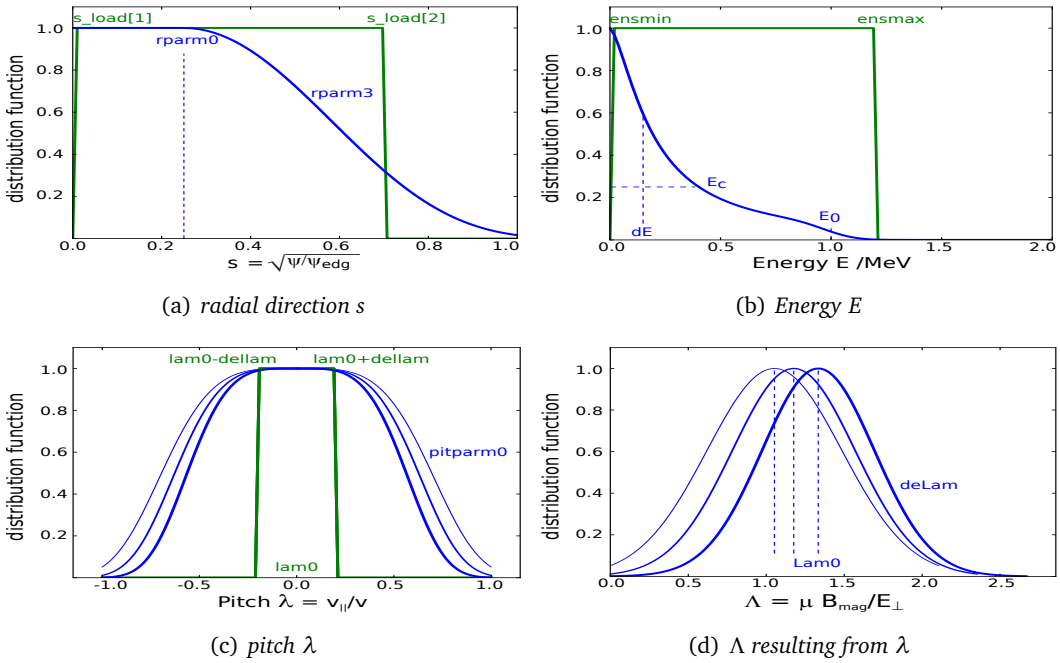

(a) *radial direction s* (b) *Energy E*

(c) *pitch* λ (d) Λ *resulting from* λ

Figure 6.10: *Regions where markers are loaded (green) in the different phase space directions and distribution functions for the unperturbed part* f_0 *and weighting (blue). Due to the weighting according to* Λ *instead of* λ*, the weight function in this direction becomes dependent on* (s,θ) *and is shown here for three different flux surfaces (the Gaussian is less steep for flux surfaces further outside).*

Due to the necessity of transforming λ coordinate into the constant of the motion Λ, one obtains one velocity space coordinate, Λ, dependent on the spacial coordinates: $\Lambda = B_{\mathrm{mag}}/B(s,\theta)(1-\lambda^2)$. As a consequence, when calculating the moments, the integration over the different phase space coordinates is not separable any more. Further, also the volume element has to be transformed into the new coordinate system,

$$\mathrm{d}\lambda = \mp \frac{B\mathrm{d}\Lambda}{2B_{\mathrm{mag}}\sqrt{1-\frac{B}{B_{\mathrm{mag}}}\Lambda}}. \tag{6.2}$$

Not only the volume element has become dependent on the spacial coordinates, but also the integration limits,

$$\begin{aligned}\Lambda_{\mathrm{min}} &= \frac{B_{\mathrm{mag}}}{B_{\mathrm{max}}}\left(1-|\lambda|^2_{\mathrm{max}}\right),\\ \Lambda_{\mathrm{max}} &= \frac{B_{\mathrm{mag}}}{B_{\mathrm{min}}}\left(1-|\lambda|^2_{\mathrm{min}}\right),\end{aligned} \tag{6.3}$$

with $B_{\mathrm{max/min}}$ being the maximum/minimum value of the magnetic field for a distinct s within the loading area $\theta_{1,2} \pm \Delta\theta$. For a general distribution function (with co- and counter-passing particles) the integration has to be performed over both branches of the square root in eq. (6.2), which are symmetric only in the case of $\lambda_0 = 0$, the typical ICRH distribution function.

'Educated Guess' for the ICRH Distribution Function

As the AUG #23824 discharge is ICRH minority-heated, it is a reasonable approximation to simulate the fast particle population as consisting of protons only. As in the previous chapter, the background plasma[9] (only important for the determination of the slowing-down parameter E_c in the energy distribution function) is chosen to consist of 94% deuterium ions and 6% protons. The fast particle population is simulated as protons (concerning mass and charge) with a volume averaged fast particle beta in the range of $\beta_{fp} \approx 0.05\%$. This can be estimated from the construction of the MHD equilibrium and different kinetic plasma profile measurements. However, the *volume averaged* β_{fp} does not alone determine the radial gradient of the distribution function, which governs the mode drive. For the most realistic modeling in the following sections, the β_{fp} value given above is reduced to $\beta_{fp} = 0.02\%$ to obtain mode amplitude saturation levels comparable to the experimental values. However, the larger β_{fp} value leads to a faster mode growing. In the indicated studies, it is chosen to save computational costs.

To get an idea of the fast particle distribution function, the TORIC-SSFPQL code [112] is considered, which calculates in a nonlinear loop algorithm the ICRH wave propagation (by TORIC, a linear full-wave code) and solves the Fokker-Planck equation (by SSFPQL, a nonlinear kinetic code). It provides a 3D function in radius, pitch and energy. However, to describe a fast particle distribution function including the higher energy range in SSFPQL, the loss mechanisms would have to be known quantitatively within the model. Therefore, energies $E > 400$ keV are neglected in the SSFPQL distribution function. In contrast, for the fast particle loss investigation with HAGIS, energies up to $E = 1200$ keV are considered. For the same reason of a missing loss mechanism, the radial distribution cannot be calculated self-consistently in SSFPQL, but strongly relies on AUG background profiles. Further, SSFPQL does not take the mirror effect ('trapping effect') nor a finite drift orbit width into account[10]. The drift orbit width can easily take values of around $\Delta s \approx 0.3$.

Both constraints (in the radial and energy direction) will lead to a radial pressure profile with underestimated radial width, as the broad orbits are missing. The red curve in fig. 6.11a shows the radial distribution function assumed by SSFPQL (from AUG data of the #23824 discharge, $t = 1.16$ s): for $s > 0.4$ there are no fast particles. Experimental observation of Alfvénic modes at up to $s \approx 0.7$ infers that a gradient in the fast ion population density exists also there. Ref. [114] addresses this problem by using different codes (amongst others the PSION code). These give a non-zero fast particle pressure at radial positions further outside. The differences are explained with the finite orbit width approximation. Thus, the radial distribution function for the simulations of this chapter is implemented to decrease to zero at $s_2 = 0.7$ (unless otherwise noted). The weighting function is implemented as constant for $s < 0.25$ and

[9] $n = 5.4 \cdot 10^{19}\ m^{-3}$, $T = 2$ keV

[10] The 'trapping effect' was taken into account in a very recent implementation, see ref. [113].

drops down according to a Fermi-like potential law for $s \geq 0.25$,

$$f(s) = \begin{cases} \text{const.} & \text{for } s < s_0 \\ (1-(s-s_0)^2)^a & \text{for } s \geq s_0, \end{cases} \quad \text{with} \quad s_0 = 0.25 \text{ and } a = 5 \tag{6.4}$$

It is depicted as blue curve in fig. 6.11a, where the line in turquoise gives the actual resulting numerical distribution (averaged over the remaining coordinates), which differs as it is also affected by the loading and (through the averaging) by the weighting in the other coordinates (E, λ).

Concerning the energy distribution $f(E)$, SSFPQL does not give information about the higher energy range. However, to fit (see red dashed line in fig. 6.11b) a slowing-down function [102, 103] to its values for all $E > 50$ keV (see red solid line) gives a quite reasonable fit. The function used in HAGIS is depicted as blue curve and matches well the fit. It reads:

$$f(E) = \frac{1}{E^{3/2} + E_c^{3/2}} \operatorname{erfc}\left(\frac{E - E_0}{\Delta E}\right), \\ \text{with} \qquad E_c = 19.34 \text{ keV}, \quad \Delta E = 149.9 \text{ keV}, \quad E_0 = 1.0 \text{ MeV}. \tag{6.5}$$

Within the energy range of interest, the resulting numerical function (turquoise line) does also not differ significantly from the SSFPQL result. This modeling has to be viewed in the light, that SSFPQL is designed for investigating particles at energies of a few tens of keV up to around 100 keV, whereas for the following simulations, merely particles at higher energies, as generated by ICRH, are of interest. Thus, the chosen energy range is $E \in [10, 1200]$ keV. Deviations from the SSFPQL distribution function in the lowest energy range are not crucial.

The distribution in Λ is determined by marker loading in poloidal angle (θ) and pitch (λ) space. Unless otherwise noted, markers start at pitches in

$$\lambda \in [0 \pm 0.2] \tag{6.6}$$

and at poloidal angles

$$\theta \in [90^o \pm 17.2^o] \qquad \text{and} \qquad \theta \in [270^o \pm 17.2^o] \tag{6.7}$$

(is 1.26 ± 0.3 rad, 5.09 ± 0.3 rad in HAGIS' Boozer coordinate system). A poloidal cut of the two initial cones, where the ICRH-generated fast particles are loaded is shown in fig. 6.9. A reasonable Λ weighting function is the Gaussian

$$f(\Lambda) = \exp\left\{\left((\Lambda - \Lambda_0)/\Delta\Lambda^{0.2}\right)^2\right\}, \tag{6.8}$$

where Λ_0 and $\Delta\Lambda$ result from λ_0 and $\Delta\lambda$ as well as from the (unperturbed) magnetic field $B(s,\theta)$ (according to eq. (6.1)) and are thus position-dependent. Transformed back to the pitch, $f(\lambda)$ is depicted as blue line in fig. 6.11c. For comparison, the SSFPQL result is shown in red, as well as a Gaussian fit to its data (red dashed).

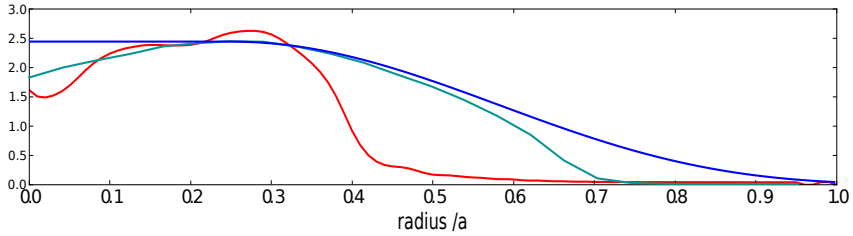

(a) *Radial distribution. Scaling: arbitrary.*

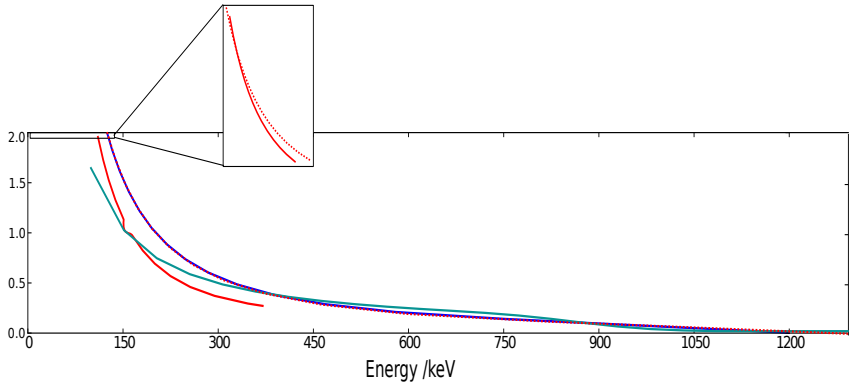

(b) *Energy distribution. Fit to slowing-down; scaling: fit matches weighting func.*

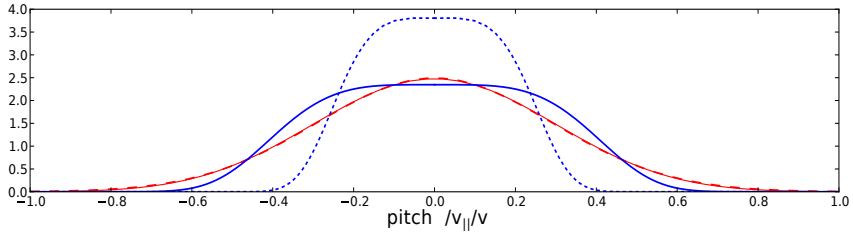

(c) *Pitch distribution (the blue dotted line gives the thinner alternative, eqs.* (6.9) *and* (6.10)*). Fit to Gaussian; scaling: integrals identical.*

Figure 6.11: *The implemented fast particle distribution functions for different coordinates: radius s, energy E and pitch λ. Blue curves depict the (analytical) weighting and turquoise curves the numerical distribution as a result from the loading and weighting scheme. For comparison, the distribution function from* AUG *data/calculated by* SSFPQL *is shown in red. The red dashed lines give a fit to this data.*

Note that the pitch distribution function is expected to be peaked stronger around $\lambda \approx 0$ than given by SSFPQL, since the given SSFPQL distribution function does not account for all particles in the higher energy range $E > 400$ keV. However, in this energy range, the ratio of particles at high pitches $\lambda \gtrsim \pm 0.5$ is smaller. The reason is, that the ICRH heating method produces high energy particles at low pitches, higher pitches result from collisions, which are less likely the higher the energy of a particle is. Further uncertainties enter the SSFPQL pitch distribution through the lack of the mentioned 'trapping effect': the given pitch is drift orbit averaged, but without finite orbit width

taken into account. Currently, SSFPQL is extended to include finite orbit width, thus it will be possible in the near future, to compare with a more realistic ICRH distribution function.
The chosen Λ weighting results in a relatively broad Λ distribution, which is realistic when considering also pitch angle scattering, but too broad to represent the instantaneous effect of the ICRH heating source. Therefore, the pattern of the losses appearing at the very beginning (prompt losses) is broader than what would be realistic. To investigate this pattern, additional simulations are carried out with marker loading in

$$\lambda \in [0 \pm 0.05] \tag{6.9}$$

and

$$\theta \in [90^o \pm 5^o] \qquad \text{and} \qquad \theta \in [270^o \pm 5^o]. \tag{6.10}$$

In sec. 6.2.2 it will be shown that the prompt losses are relatively sensitive to the distribution function, but cannot be determined quantitatively within the used model anyhow. The reason lies inherently in the code model, which does not calculate the establishing of the (unperturbed) fast particle distribution function, but considers a plasma situation, where the heating process is in a stationary state. More details will be discussed in sec. 6.3.6.
The non-prompt losses (i.e. those that appear in the presence of a mode) in contrast, are quite robust against minor changes in the radial and poloidal distribution function.

Results of Simulations with an ICRH-like Distribution Function

This section presents the results of the simulations performed with the ICRH-like distribution function as described above. They are based on the MHD equilibrium for AUG discharge #23824, $t = 1.16$ s, where the q profile is inverted. The radial structure of the magnetic perturbation data is given via analytic Gauss functions (fig. 6.12). The frequencies of the perturbation are chosen to match the experimentally determined frequencies, 120 kHz and 55 kHz. The fast particle beta value was set to β_{fp}=0.025%. Concerning numerical requirements, the minimum amount of markers, 120 000, needed for reasonable loss statistics provides sufficient convergence (tested against 1 000 000 and 1 500 000 markers).

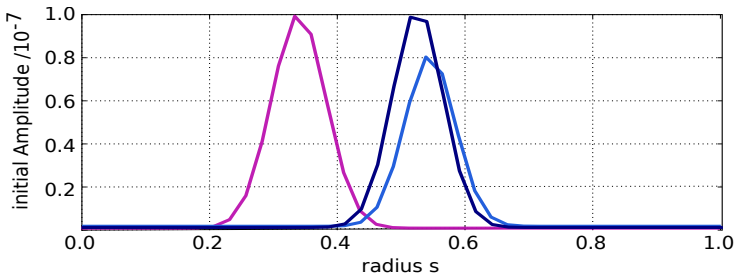

Figure 6.12: *Analytic perturbation $n = 4$ TAE of 120 kHz with two poloidal harmonics $m = 4, 5$ (dark and light blue) and the $n = 4$ RSAE of 55 kHz (pink).*

The results from the numerical study in chapter 5 still hold in the simulations with the ICRH-like distribution function (see fig. 6.13a): an amplitude oscillation is visible, at exactly the beat frequency of both modes. Stochastization sets in, as soon as the mode amplitude reaches the threshold. However, this appears to be slightly higher ($\delta B/B = 4 \cdot 10^{-3}$) compared to the simulations with an isotropic distribution function. The gradient driven double-resonance is clearly visible: as the RSAE redistributes particles to the TAE position, the TAE starts to grow (see fig. 6.13a and b). One can again distinguish three phases of the simulation: during the linear phase, the mode amplitudes grow with $\exp(\gamma t)$ (linear in the logarithmic plot). The resonant phase starts, when a first saturation level is reached, due to the depletion of the gradient in the fast particle distribution function due to resonant particle-mode interaction. If this level exceeds the stochasticity threshold, a stochastic phase sets in, allowing the mode to tap the energy of particles in a wider phase space range. The resulting mode amplitudes exceed the experimental measured values by a factor of 2 to 5, a mismatch that will be reduced by the use of more realistic eigenfunctions, shown in the next section.

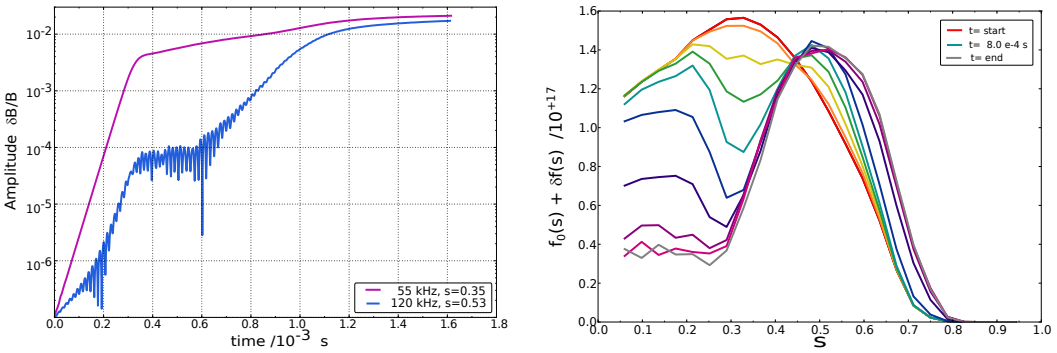

(a) *Mode amplitude evolution.*

(b) *Radial redistribution at different points in time.*

Figure 6.13: *Double-mode simulation of analytical modes as shown in fig. 6.12, in the inverted q profile equilibrium.*

A look at the changes in the particle distribution function in E-s space further confirms the picture drawn above: during the resonant phase, redistribution matches resonance lines very well (fig. 6.14a). In the stochastic phase, a broad redistribution sets in, especially in the lower energy range. The redistribution transports fast particles outwards, leading to particles crossing the loss boundary. During the resonant phase, this happens especially due to the $p = 2$ resonant mode interaction with both the RSAE and the TAE, thus at energies of ≈ 500 keV. In the stochastic phase, far more particles are redistributed across the loss boundary, especially in energy ranges of $E \in [250,500]$ keV and $E \in [750,1000]$ keV.

This redistribution pattern at different times is in accordance with the numerically obtained losses: fig. 6.15 shows the loss appearance over time at the first wall in energy space. One can clearly see the resonant losses at ≈ 500 keV. The (fewer) losses at higher energies emerge from the $p = 3$ resonance. Later, in the stochastic phase, a large number of lower energy losses appear between $E \in [250,500]$ keV, as well as

higher energetic losses, especially up to 900 keV. Prompt losses (white area) appear in the higher energy regime. However, their loss pattern can reach down to lower energies (with decreasing intensity), depending on the distribution function used.

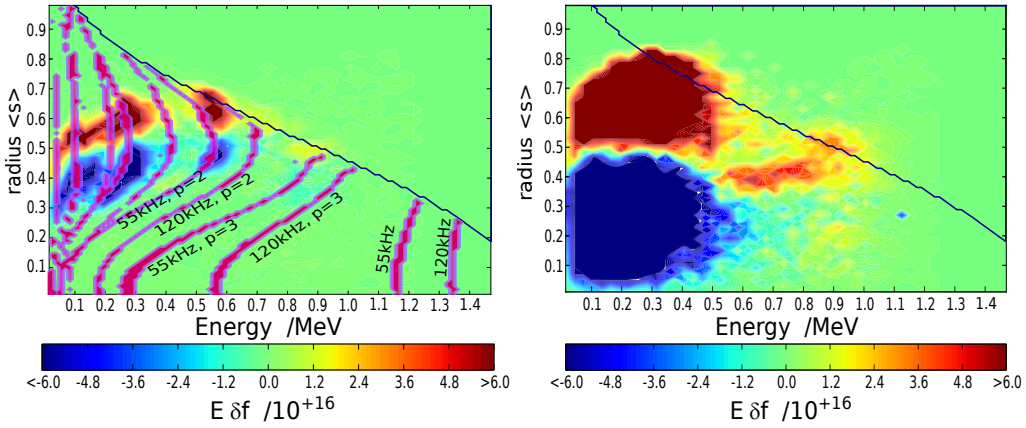

(a) *resonant phase,* $t = 4.3 \cdot 10^{-4} s$ (b) *stochastic phase,* $t = 1.4 \cdot 10^{-3} s$

Figure 6.14: *Redistribution in E-s space at different points during the simulation time: during the resonant phase (a), the redistribution (from blue to red) matches very well the resonance lines (pink). Once the stochastic phase is reached (b), a broad redistribution sets in. The dark line indicates the loss boundary.*

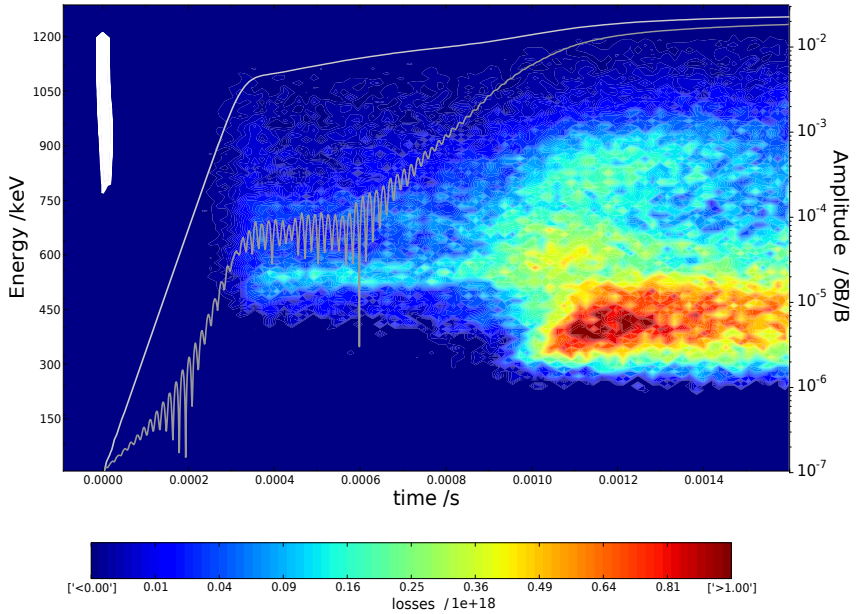

Figure 6.15: *Temporal evolution of loss appearance at the first wall in energy space for the inverted q profile simulation with analytic perturbation (fig. 6.12),* β_{fp}*=0.025%. The white area indicates the prompt losses, the gray lines depict the mode amplitude evolution for comparison.*

As the losses emerge very distinctively around 550 keV during the entire resonant phase, they are expected to show a correlation with either at least one of the mode frequencies or their beat frequency. Unfortunately, the amount of markers simulating the losses in this energy and time interval is not large enough for a reasonable statistics to carry out a Fourier analysis. Further, the TAE is, as long as it is still very subdominant, not resolved numerically well. Therefore, its frequency change is not calculated accurately. Without a constant frequency, frequency-correlated losses cannot be identified. However, plotting the time traces of losses shows only a very thin underlying offset of incoherent losses in this energy range (fig. 6.16a). The time integrated losses scale linear with the RSAE amplitude for amplitudes below $1.5 \cdot 10^{-2}$, indicating a resonant loss mechanism. For higher amplitudes, they scale quadratically, according to diffusive losses caused by stochastization (see fig. 6.17a).

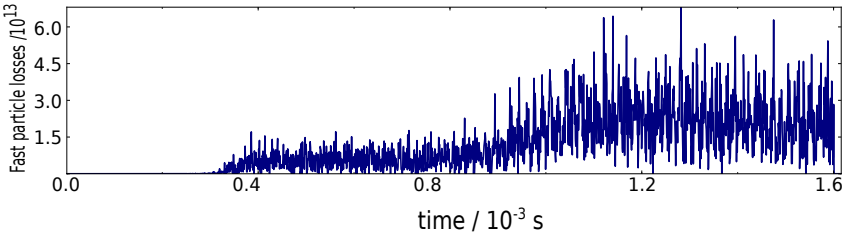

(a) *Resonant losses in the energy range from 500 to 580 keV).*

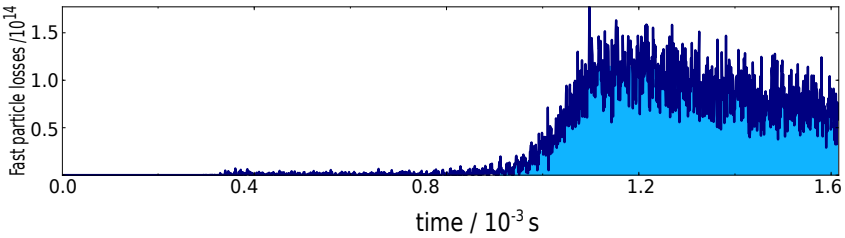

(b) *Stochastic losses in the lower energy range (300 to 500 keV).*

Figure 6.16: *Time traces of losses appearance in the inverted q profile simulation with analytic perturbation (fig. 6.12) for different energy ranges.*

The lower energetic losses in the energy range of 300 to 500 keV are ejected during stochastization. Their time trace reveals a significant underlying offset (light blue in fig. 6.16b). As the amount of losses is large, a Fourier analysis is possible. The resulting spectrum of these lower energetic losses exhibits a very small peak at the beat frequency. The time integrated losses show a quadratic dependence on the RSAE amplitude, as expected for stochastic losses.
In the high energy range of 800 to 1000 keV, losses appear as well in the non-prompt phase. They again have almost no underlying offset, and a significant peak in the Fourier spectrum at the modes' beat frequency, depicted in fig. 6.17b.

It is clear now, that losses in the lowest energy range (especially below 400 keV) are merely incoherent because they are caused by the modes' phase space stochastization. Prompt losses, which are also incoherent, appear in the higher energetic ranges. Their loss pattern, however, is quite sensitive to marker loading, as will be shown later.

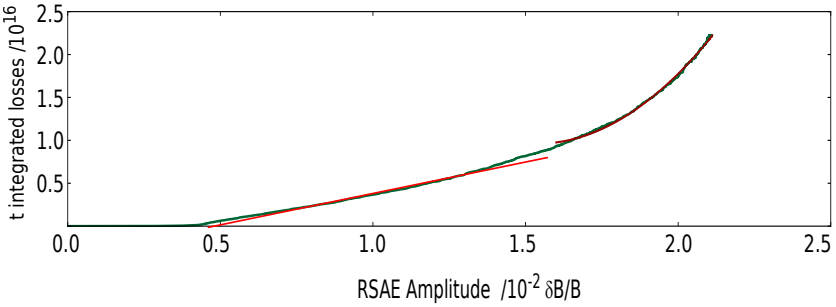

(a) *Time integrated resonant losses with $E \in [500,580]$ keV over RSAE amplitude (green) and a linear and quadratic fit (red).*

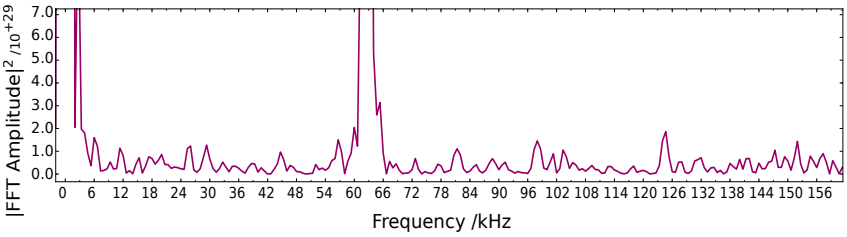

(b) *Fourier spectrum of higher energy losses with $E \in [500,580]$ keV.*

Figure 6.17: *Results of two different techniques to analyze the losses' time trace.*

For a preliminary comparison with the experimental FILD measurement, the loss pattern in pitch angle-energy space resulting from this simulation is shown in fig. 6.18: after accounting for the drift deviation as explained in sec. 6.1.2, prompt losses (a) appear in the energy range of $E \in [370\text{ keV}, 1300\text{ keV}]$ and in pitch of $\lambda^o \in [76^o,87^o]$, non-prompt losses (b) in $E \in [260\text{keV}, 1300\text{ keV}]$ and $\lambda^o \in [68^o,81^o]$. This position in phase space is already quite in accordance with experimental observation [33], where the loss pattern is located between $E \in [150\text{ keV}, 1400\text{ keV}]$ and $\lambda^o \in [65^o,81^o]$. However, the experimentally measured loss pattern reaches to both higher and lower energies. To miss the losses > 1300 keV in the simulation is not surprising, as no markers were loaded beyond this energy. Concerning the appearance of losses in the lowest energy range, it will turn out that one more step towards realistic simulation conditions has to be made.

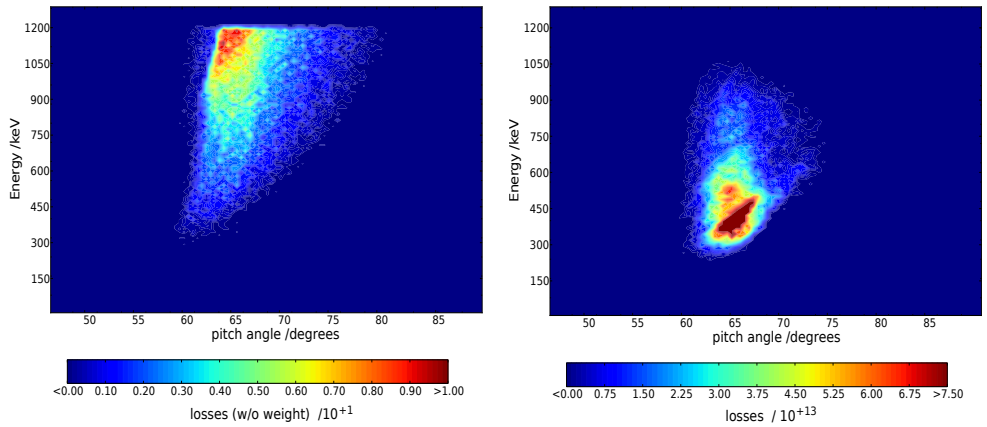

(a) *Prompt losses ($t < 10^{-4}$ s)* (b) *Non-prompt losses ($t > 10^{-4}$ s)*

Figure 6.18: *Losses at first wall in pitch angle-energy (λ^o-E) space for the simulation of two analytical modes (fig. 6.12) in the inverted q profile: prompt losses (a) and losses during mode activity (b).*

Robustness of the Results w.r.t. the Distribution Function

Due to the uncertainties in the distribution function, it is reasonable, to test the sensitivity of the model on the chosen distribution function. The ICRH characteristics enters the distribution function via θ and λ loading, but both are coupled, resulting in the constant Λ. Thus, it is sufficient to investigate one of these parameters, e.g. the poloidal loading $\Delta\theta$. The sensitivity of the model with respect to the radial distribution function is investigated since it affects strongly the prompt losses.

Radial distribution function

To investigate the importance of the radial distribution function, simulations with three different combinations of radial loading and weighting are performed, as shown in fig. 6.19a. The amplitude evolution depends on the radial distribution function both in the linear as well as in the saturation phase (fig. 6.19b): as expected (from eq. (3.37)), the steeper the radial distribution function, the higher is the linear growth rate. The saturation levels differ, since the energy that can be tapped by the mode depends on the radial profile of the energetic particle distribution function with respect to the radial mode structure. It is necessary to mention that due to the relatively high fast particle beta of β_{fp}=0.05%, the growth rates and final amplitudes of the modes reach levels that are close to the code's limits of validity. The reason for the choice is to save computational time, as it was found that simulations with lower β_{fp} give similar results, just on a larger time scale.

Looking at the loss pattern in pitch angle-energy space (fig. 6.20), one can see that the prompt losses are very sensitive to the initial fast particle distribution function: the further the radial distribution function reaches outside, the more the pattern broadens towards lower energies and higher pitch angle values $|\lambda^o|$.

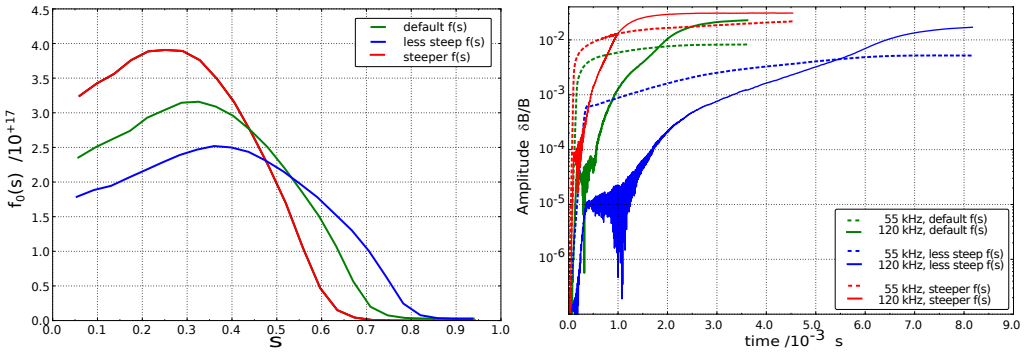

(a) *Initial radial distribution functions* (b) *Amplitude evolution*

Figure 6.19: *The amplitude evolution (b) of three double-mode simulations in the inverted q profile (mode radial structures and frequencies as explained later and shown in fig. 6.23, β_{fp}=0.05%). They differ in the applied radial distribution function what is shown in (a): the parameter s_0 in the weighting function eq. (6.4) takes the values 0.15, 0.25, 0.35, and the marker loading reaches out until $s_2 = 0.6$, 0.7 and 0.8 respectively (colored as red, green, blue).*

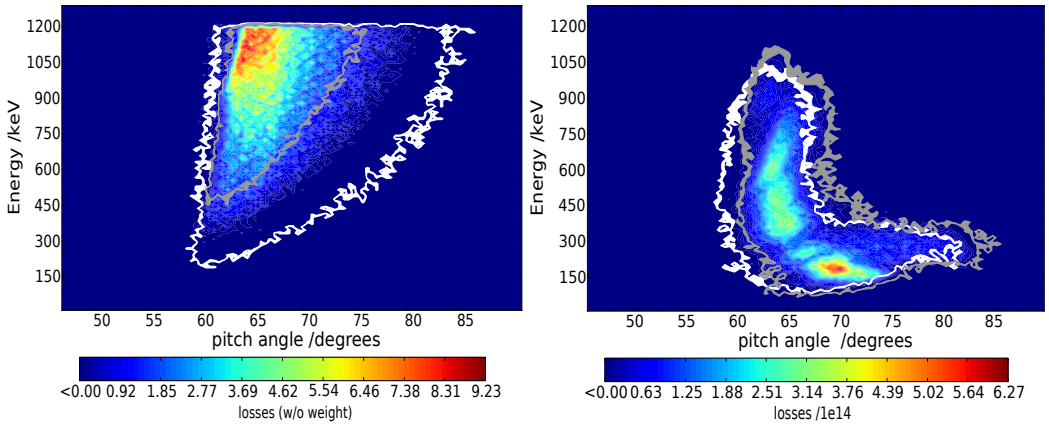

(a) *Prompt losses ($t < 10^{-4}$)* (b) *Resonant/diffusive losses*

Figure 6.20: *Losses at first wall in pitch angle-energy (λ^o-E) space for three double-mode simulations in the inverted q profile (modes as explained later and shown in fig. 6.23, β_{fp}=0.05%). The simulations differ in the radial distribution function: the color code gives the prompt (a) and later (b) losses for the intermediate distribution function in fig. 6.19b, the gray lines give the boundary of the pattern, when using the steeper distribution function; the white line gives the respective result for the less steep distribution function.*

However, as explained earlier, when considering prompt losses, all of the applied radial distribution functions are too broad in Λ space to represent a physically realistic picture of ICRH-heated ions before pitch angle scattering could smear out the Λ distribution. As a consequence, the extend of the prompt loss pattern is overestimated towards lower energies. Thus, when obtaining a large number of lower energetic losses, one will not expect them to be prompt in their majority. However, in the experimental measurement it is not possible to distinguish prompt losses from the incoherent diffusive losses. Concerning the non-prompt losses, which appear in all three cases mainly in the lower energy range below 400 keV, almost no dependence on the initial radial distribution function is found. Note: the spot looks different compared to fig. 6.18, because a different eigenmode structure was used. This will be discussed in more detail in sec. 6.2.3.

Poloidal distribution function

For the θ distribution function, a similar scan is performed: the default distribution function (as shown in green in fig. 6.21a) is compared with two similar simulations. One (blue) differs only in the width of the poloidal loading angle $\Delta\theta$, the second (red) additionally in the pitch loading range $\Delta\lambda$. (Note that $\Delta\theta$ and especially $\Delta\lambda$ enter the Λ weighting function.)

The modes' amplitude evolution (fig. 6.21b) reveals a difference only in the growth rate – giving higher growth rates, the narrower the loading range in θ and λ. This is expected (from eq. (3.37)), as the local β_{fp} value of potentially resonant particles is higher in the scenario with the narrower distribution function (to obtain the fixed volume averaged β_{fp}). In contrast, the amplitude saturation levels are independent of the poloidal distribution function, since the total energy that can be tapped from phase space is the same. This is different from the different radial distribution functions, where the radial energy reservoir that can be tapped is determined by the radial location and structure of a mode with respect to the radial gradient in the distribution function.

As expected, the prompt losses (fig. 6.22a) show a dependence on the poloidal distribution function. However, only for the extreme narrow poloidal loading the prompt loss pattern appears significantly smaller (mostly due to $\Delta\lambda$, affecting the weighting in Λ). The qualitative phase space position is the same. The non-prompt losses (fig. 6.22b) are very robust against changes in the poloidal distribution function. Only for the extreme narrow Λ function, the pattern is slightly smaller, missing the lowest pitch angles $|\lambda|$.

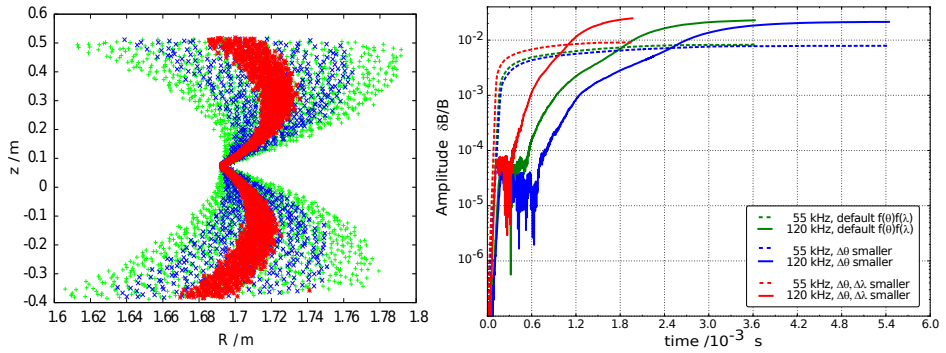

(a) *Initial poloidal distribution functions* (b) *Amplitude evolution*

Figure 6.21: *The amplitude evolution (b) of three double-mode simulations in the inverted q profile (modes as explained later and shown in fig. 6.23, β_{fp}=0.05%). They differ in the applied poloidal distribution function what is shown in (a): the marker are loaded in $\Delta\theta = \pm 17.2^o$ (green), $\pm 11.5^o$ (blue) and $\pm 2.5^o$ (red) respectively. The pitch loading is $\Delta\lambda = \pm 0.2$ (for both the green and blue case) and ± 0.05 (red case).*

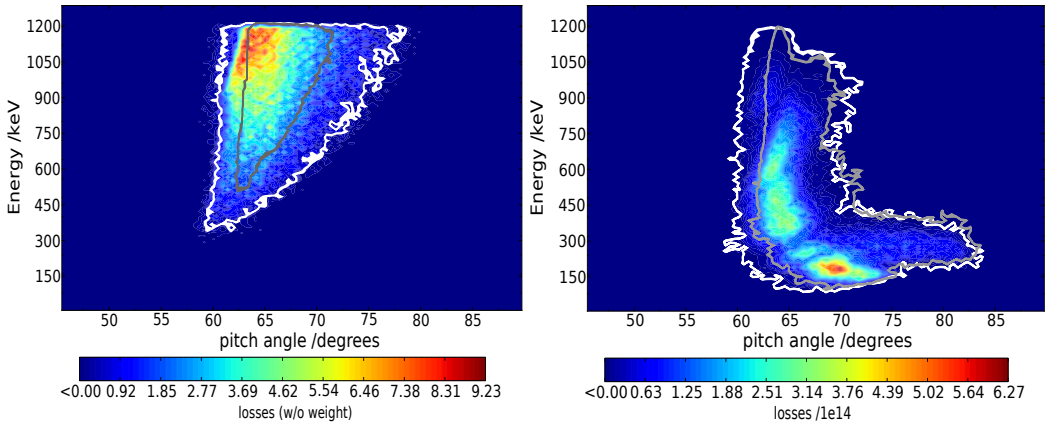

(a) *Prompt losses ($t < 10^{-4}$)* (b) *Resonant/diffusive losses*

Figure 6.22: *Losses at first wall in pitch angle-Energy (λ^o-E) space for two double-mode simulations in the inverted q profile (modes as explained later and shown in fig. 6.23, β_{fp}=0.05%). The simulations differ in the Λ distribution function: the color code gives the prompt (a) and later (b) losses for the $\Delta\theta = \pm 17.2^o, \Delta\lambda = \pm 0.2$ marker loading, the white lines give the boundary of the pattern, when using $\Delta\theta = \pm 11.5^o, \Delta\lambda = \pm 0.2$ loading, the gray lines for $\Delta\theta = \pm 2.5^o, \Delta\lambda = \pm 0.05$.*

6.2.3 More Realistic Simulation Conditions – MHD Eigenfunctions

In the previous section, the simulation conditions were adapted towards more realistic fast particle distribution functions. In this section, the input perturbation data is improved, as explained in the following.
The MHD equilibrium of AUG discharge #23824 (at $t = 1.16$ s and $t = 1.51$ s) is calculated by the Grad-Shafranov solver HELENA [84], under the constraint of the location of rational surfaces. These are known due to the experimental measurement of the modes' radial positions (via Soft-X ray) and the toroidal mode numbers n (via Mirnov coils). Based on the resulting MHD equilibrium (based on CLISTE calculations [85, 86, 115, 116]), the radial structure and frequency of the perturbation is calculated numerically with the linear gyrokinetic eigenvalue solver LIGKA [93]. As explained before, there are two dominating modes, which are seen in the experiment (see fig. 6.7) at $t = 1.16$ s around the radial positions $s \approx 0.3$ and $s \approx 0.5$ with frequencies of 120 kHz ($n = 4$) and 55 kHz ($n = 4$) respectively. At the later time point, the frequencies have evolved upwards, resulting in 160 kHz ($n = 5$) and 70 kHz ($n = 4$). The numerical LIGKA results are shown in fig. 6.23 and fig. 6.24. The higher frequency mode is identified as TAE, the lower as RSAE (=AC) at $t = 1.16$ s but as BAE at $t = 1.51$ s.

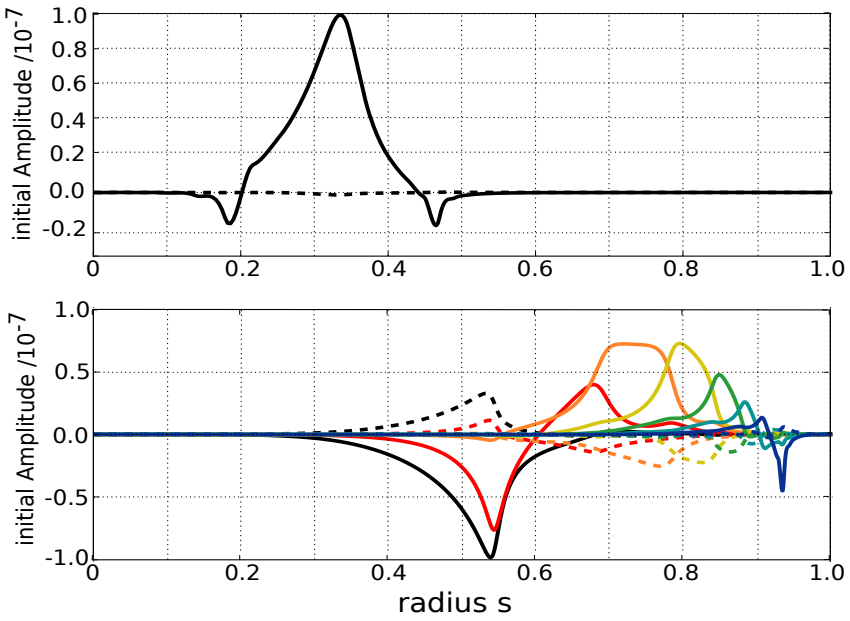

Figure 6.23: *The radial structure including poloidal harmonics with $m = 4...10$ (from black to blue) of the $n = 4$ TAE (120 kHz) (lower) and the $n = 4$, $m = 4$ RSAE (55 kHz) (upper) as calculated by* LIGKA *[117] for the* AUG *discharge #23824 equilibrium at $t = 1.16$ s. The given perturbation amplitude refers to the real (solid lines) and the imaginary (dashed lines) part of the electric perturbation potential $\tilde{\Phi}$. The values are normalized, such that unity corresponds to the initial value of $\delta B/B = 10^{-7}$.*

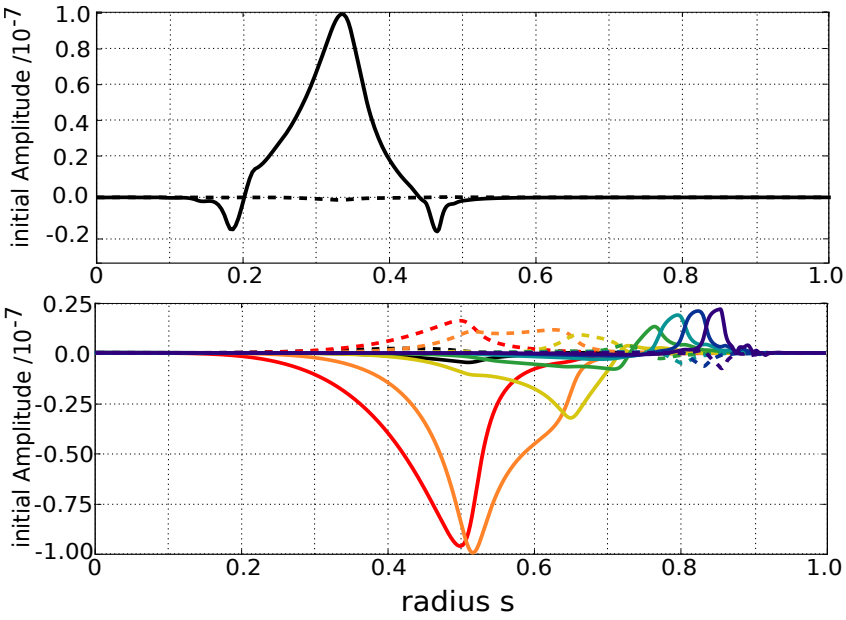

Figure 6.24: *The radial structure including poloidal harmonics with $m = 4...11$ (from black to violet) of the $n = 5$ TAE (160 kHz) (lower) and the $n = 4$, $m = 4$ BAE (70 kHz) (upper) as calculated by* LIGKA *[117] for the* AUG *discharge #23824 equilibrium at $t = 1.51$ s. The given perturbation amplitude refers to real (solid lines) and the imaginary (dashed lines) part of the electric perturbation potential $\tilde{\Phi}$. The values are normalized, such that unity corresponds to the initial value of $\delta B/B = 10^{-7}$.*

HAGIS is not only able to read analytically given radial perturbation structures of the electric perturbation's real part, but was extended to handle perturbation structures given by LIGKA[11]. Thereby, one can either only consider the electric perturbation (real and imaginary part) and obtain the magnetic perturbation from the relation eq. (4.66), i.e. neglecting any parallel electric field. The other way is to take both electric and magnetic perturbation from LIGKA and thus simulating with a non-vanishing parallel electric field $\tilde{E}_{\parallel}$, calculated from eq. (4.67). The latter possibility would effectively include a damping term into the wave equations. The imaginary part of the electric perturbation results in a phase shift of the modes only. In the present scenario, the observed perturbations are either purely Alfvénic (TAE, RSAE), and therefore characterized by damping rates well below 1%, or weakly damped (BAE) with damping rates of $\approx 1\%$. Therefore, it is not necessary to take the computational effort for the inclusion of $\tilde{E}_{\parallel}$ within the study of this chapter.
The simulations were performed again with 250 000 markers to obtain good statistics with the ejected losses.

[11] These options are addressed via the input parameter *spcpet==4* (analytic perturbation), *14, 15* (given by LIGKA with and without the magnetic potential).

To test the newly implemented HAGIS feature of using eigenfunctions given by LIGKA, quite simple simulations were carried out, comparable to those of chapter 5. The single-mode simulations with isotropic marker loading and β_{fp}=1% in the inverted q profile equilibrium were repeated with the mode structure given by LIGKA, adapted to the position of the modes used in the numerical study (TAE at $s = 0.4$, RSAE at $s = 0.35$). The structures can be seen in fig. 6.27.
This test reveals an almost identical mode growth for the RSAE mode (pink vs. red in fig. 6.25), whereas the TAE grows significantly slower with the structure given by LIGKA and saturates at lower amplitudes (light blue vs. green in fig. 6.25). However, this effect is partially compensated when using all LIGKA calculated poloidal harmonics for the TAE ($m = 4,...,10$) (dark blue).

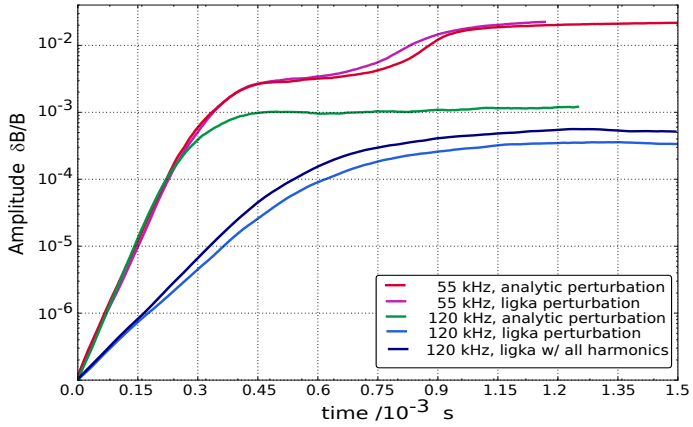

Figure 6.25: *Amplitude evolution in the single-mode simulations (inverted q profile equilibrium, β_{fp}=1%, isotropic marker loading) to compare modes given by* LIGKA *(pink and light blue for RSAE and TAE) with similar analytical Gaussians (red and green for RSAE and TAE). The mode peaks are at $s = 0.4$ (TAE) and $s = 0.35$ (RSAE). The mode structures are given in fig. 6.27. The dark blue curve shows the mode evolution of the TAE with all harmonics given by* LIGKA.

The reason for the lower drive must be given solely by the different structure of the waves: the more realistic eigenmodes given by LIGKA are spread more widely over the radius, but are characterized by a smaller mode width around their peak region. This leads to a lower impact on the resonant particles, which results in a less effective energy exchange. In this example, one can see the influence of the mode structure on the quantitative amplitude evolution, which emphasizes the need to implement a mode structure evolution into HAGIS via coupling it to the LIGKA code, as explained in sec. 4.5.

The first multi-mode simulations using the ICRH-like distribution function and eigenfunctions given by LIGKA including all poloidal harmonics (fig. 6.23) reveal that the double-resonance effect still holds in this realistic case (fig. 6.26): the broad radial redistribution of the RSAE enhances the TAE's drive. Also, one can clearly see an oscillation superimposed on the mode amplitude evolution, although it is less regular than in the simulations of the theoretical study presented in chapter 5, or even those of the previous section (sec. 6.2.2).

The three phases, linear phase, resonant phase and stochastic phase, however, are not as clearly separable any more, compared to the simulations with the analytical perturbation function. Therefore, it is difficult to say at which amplitude the modes reach the stochastization level, but a phase space analysis, as it will be described below (sec. 6.3.1) reveals that the threshold is reduced to $1 \cdot 10^{-3} \delta B/B$ for the first mode reaching it, and might even be lower for the subdominant mode (see fig. 6.31).

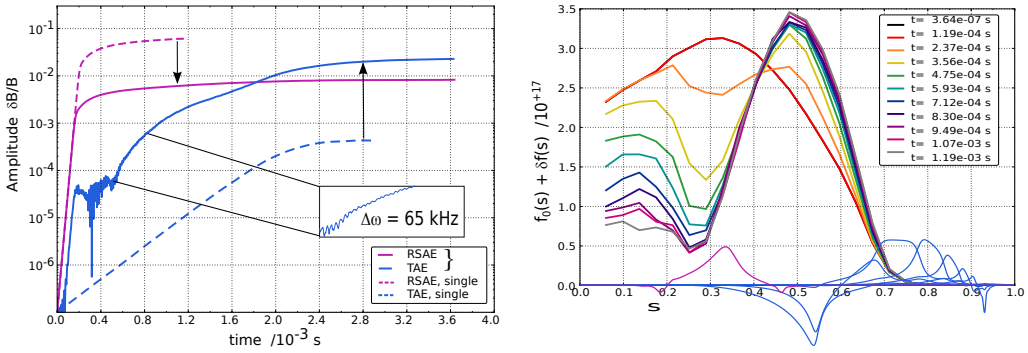

(a) *Mode amplitude evolution over time.*

(b) *Single RSAE radial redistribution at different times.*

Figure 6.26: *Amplitude evolution (a) of a $n = 4$ RSAE (55 kHz, pink solid) and a $n = 4$ TAE (120 kHz, blue solid) as shown in fig. 6.23, simulated with β_{fp}=0.05% in the inverted q profile equilibrium. For comparison, both modes were simulated alone as well (dashed). One can see clearly the double-resonance effect: the inner RSAE is lowered, while the outer TAE is enforced strongly, due to the redistribution caused by the RSAE, until reaching the stochastization threshold. In the nonlinear phase, the primarily weaker TAE outstrips the RSAE. The RSAE's radial redistribution at different time points is shown in (b). To point out its effect on the TAE, both mode structures are plotted over the radial axis (blue: TAE, pink: RSAE).*

Although the simulations with the perturbation structure given by LIGKA show the same double-resonance mechanism as found in the numerical study of chapter 5, they exhibit a lower growth rate and also lower saturation levels compared to the same scenario with a similar analytical Gaussian perturbation (fig. 6.27), as can be seen in fig. 6.28. It is remarkable that, compared to the single-mode investigation with the mode structure given by LIGKA, in the double-mode scenario it is the RSAE mode and not the TAE, which differs significantly from the result with the analytical mode structure. This can be explained by double-resonance effects: as a single-mode, the broader TAE given by LIGKA grows slower, as explained above. The presence of a second mode, however, leads to an energy transfer via gradient-driven double-resonance towards the TAE. Especially once the stochastic regime is reached, the thin peak region in the TAE structure of the LIGKA given mode is not so important any more, since the resonances have not to be met exactly. In contrast, the broad overall radial extent of this mode becomes crucial: since it overlaps stronger with the RSAE structure (compared to the Gaussian modes), it reduces the RSAE's drive through local gradient-flattening.

Using the eigenmodes given by LIGKA with all TAE poloidal harmonics results in an even slower growth rate of the TAE, but similar amplitude levels are reached. This can be understood when taking into account that the total wave energy is higher, the more poloidal harmonics the wave has. The mode grows slower, as the energy transfer needs to include all TAE harmonics, as can be seen from the sum over m in eq. (4.105). Since the energy reservoir to tap is wider due to the broader radial structure, the saturation levels are comparable.

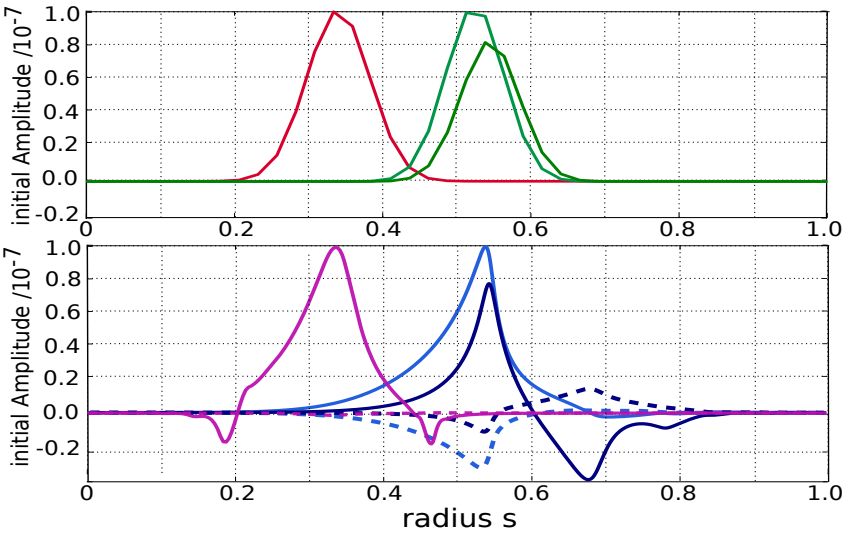

Figure 6.27: *Radial structure of the electric perturbation for two modes, a $n = 4$ RSAE of 55 kHz and two poloidal harmonics ($m = 4, 5$) of a $n = 4$ TAE of 120 kHz. The modes given by* LIGKA *(lower: RSAE in pink, TAE in blue; the solid lines depict the real part, the dashed lines the imaginary part of $\tilde{\Phi}$) are compared with their analytical approximation via Gaussians (upper: RSAE in red, TAE in green).*

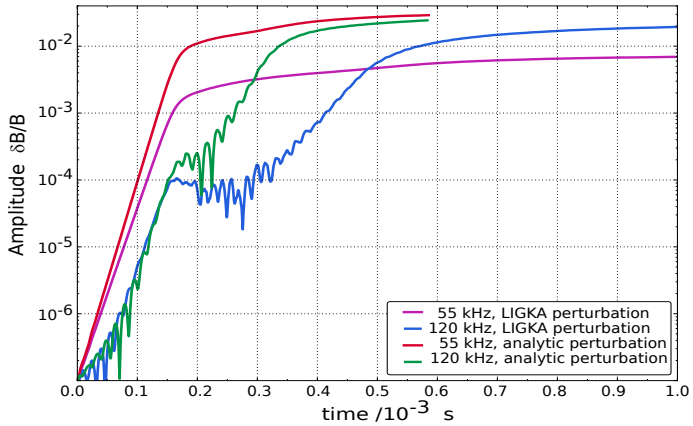

Figure 6.28: *Mode amplitude evolution in the double-mode simulations (inverted q profile equilibrium, β_{fp}=0.05%) to compare the eigenmodes given by* LIGKA *(pink and blue for RSAE and TAE) with similar analytical Gaussians (red and green for RSAE and TAE). Details on the modes are given in fig. 6.27.*

6.2.4 The Importance of the HAGIS Vacuum Extension

For the energetic particle loss investigation, the use of HAGIS with its vacuum extension [55] might be crucial, depending strongly on the scenario that is to be simulated. As can be seen from fig. 6.29, there is almost no difference in the losses' energy spectra resulting from simulations without using the vacuum extension (red curves) compared to the ones including it (black curves). The amount of lost markers is 99% of those in the simulation with the vacuum extension.

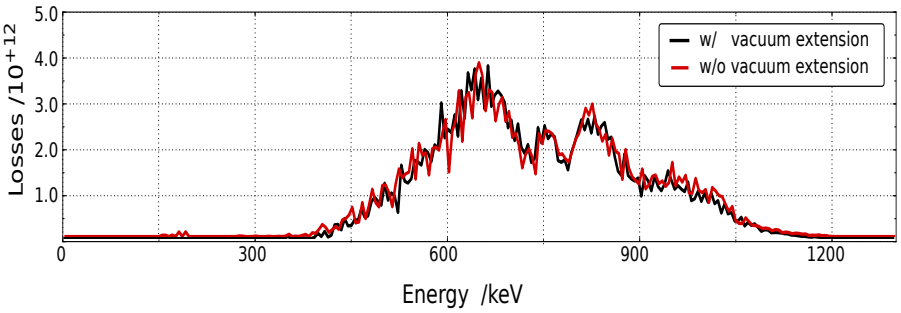

Figure 6.29: *Energy spectra of losses simulated in the monotonic q profile with eigenmodes given by* LIGKA *(see fig. 6.24) using* HAGIS *with its vacuum extension (black curve) and without (red). The amplitudes for these simulations were fixed at* $\delta B/B = 5.1 \cdot 10^{-3}$. *The losses shown appeared in a time interval starting after approximately 10 RSAE wave periods (*$t \in [0.2,1.5] \cdot 10^{-3}$ *s), to avoid the prompt losses.*

But the situation is quite different in scenarios with many lower energetic losses, as they appear e.g. in all inverted q profile simulations throughout this chapter. Fig. 6.30 visualizes the difference in the losses' energy spectra obtained with (black curve) and without (red curve) the vacuum extension – if simulating without it, the lower energetic losses are massively overestimated.

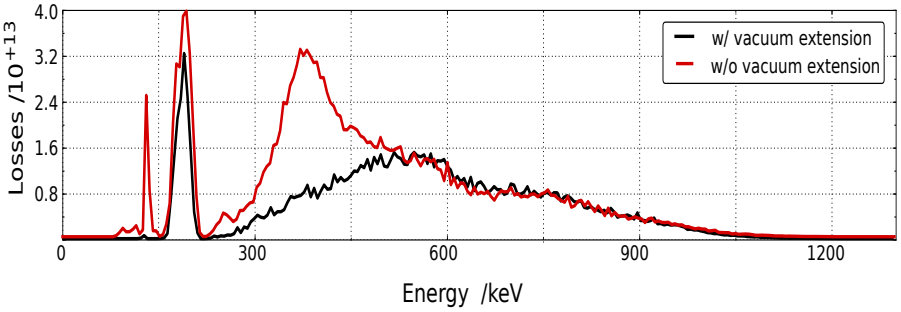

Figure 6.30: *Energy spectra of losses simulated in the inverted q profile with the eigenmodes given by* LIGKA *(see fig. 6.23) using* HAGIS *with its vacuum extension (black curve) and without (red). The amplitudes for these simulations were fixed at* $\delta B/B = 5.1 \cdot 10^{-3}$. *The losses shown appeared in a time interval starting after approximately 10 RSAE wave periods (*$t \in [0.2,1.5] \cdot 10^{-3}$ *s) to avoid the prompt losses.*

The overestimation results from to the fact, that particles are considered lost, as soon as they cross the separatrix. However, particles with very small gyroradii (i.e. low perpendicular energies), often re-enter the plasma and are not lost. The overestimation of lost markers if simulating without the vacuum extension is over 130% in the given example. ICRH-generated fast particles are characterized by relatively low pitches $\lambda = v_{\parallel}/v$, thus, they have low perpendicular energies only if their total energy is in a lower range. These particles have small gyroradii, and therefore a higher probability to re-enter the plasma. Further, the distance between the separatrix and the first wall is important, which depends on the given equilibrium in the particular fusion device. The vacuum extension allows particles to travel through the vacuum and checks[12] if the particle hits the machine specific first wall through assuming a 'tube' around its guiding center with the radius of the gyroradius.

6.3 Numerically Modeled vs. Experimentally Observed Losses

This section is dedicated to the simulation of fast particle redistribution and losses under realistic simulation conditions with the vacuum extended version of HAGIS. Therefore, the original eigenmodes given by LIGKA are used with all their poloidal harmonics, as depicted in fig. 6.23 for the MHD equilibrium of AUG discharge #23824 at $t = 1.16$ s (inverted q profile) and in fig. 6.24 for the time point $t = 1.51$ s (monotonic q profile). For the rest of this chapter, the two equilibria will be referred to as "scenario1.16" and "scenario1.51" respectively. In the following, the ICRH-like distribution function is used, and the fast particle beta value was chosen as β_{fp}=0.02%, a quite realistic value, that leads to mode amplitudes comparable to those measured experimentally [33], or slightly higher ($\delta B/B \in [5 \cdot 10^{-3}, 2 \cdot 10^{-2}]$).

6.3.1 Internal Transport Study in Two Different q profile Equilibria

This section examines the internal fast particle transport and also aims to find out when the stochastization sets in. The mode amplitude evolution in both equilibria are shown in fig. 6.31: in scenario1.16, one can see again clearly the double-resonance effect leading a superimposed oscillation (insert), and also to the TAE (blue curve) exceeding the initially much faster growing RSAE (pink curve) in the late nonlinear phase. The examination below (fig. 6.33) confirms that both modes reach the stochasticity threshold. In scenario1.51, the TAE (green curve) grows much faster than the low frequency mode (in this case a BAE, red curve), but both grow slower and saturate at a lower amplitude compared to scenario1.16. The TAE's stochasticity threshold is reduced by the stochastization due to the BAE. Since the simulated time scale in this case is only one order of magnitude below the slowing-down time, the effect of energy dissipation becomes slightly visible with the TAE amplitude decreasing at the end of the simulation. Beyond this time point, the model is valid only when accounting for a fast particle source term and damping mechanisms.

[12] routine gyro_check

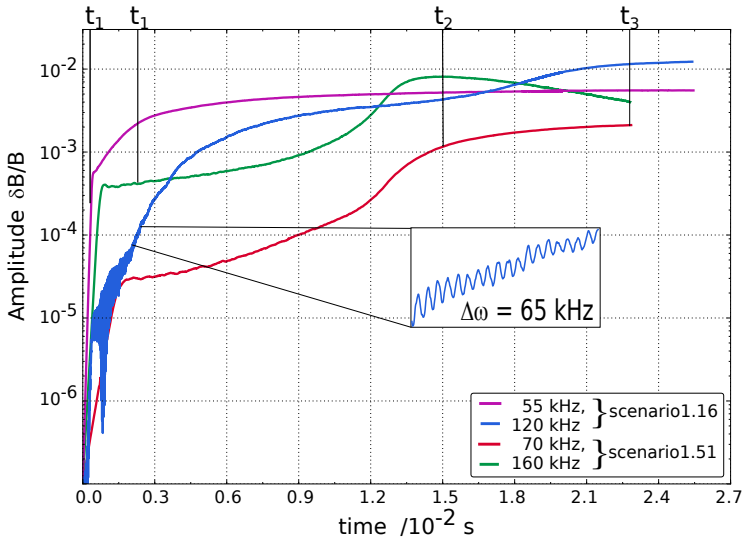

Figure 6.31: *Amplitude evolution in two double-mode simulations with different MHD equilibria of the* AUG *discharge #23824 (β_{fp}=0.02%): pink and blue: $n = 4$ RSAE (55 kHz) and $n = 4$ TAE (120 kHz) as shown in fig. 6.23, simulated in in the equilibrium at $t = 1.16$ s, red and green: $n = 4$ BAE (70 kHz) and $n = 5$ TAE (160 kHz) as shown in fig. 6.24 in the equilibrium at $t = 1.51$ s. The marker are loaded as a Fermi-like radial distribution, slowing-down energy distribution, and* ICRH*-type pitch and poloidal angle distribution.*

To understand the mode-particle interaction in the different stages of the mode evolution, it is helpful to look at the processes in phase space. In fig. 6.32, redistribution in *E-s* space is shown during the mode's resonant phases, for both, scenario1.16 (a), and scenario1.51 (b). The color code represents the change of the fast particle pressure ($E \cdot \delta f$) with respect to the equilibrium state. The pink color denotes the resonance lines, the blue areas the loss boundary, as given by the resonance plot (fig. 6.8). In this phase, the redistribution in phase space takes place along the resonance lines, from higher energies and lower radial positions to lower energies further outside. As the modes in scenario1.51 stay longer in the resonant phase, the redistribution pattern is better visible in this case.

When the modes, or at least one of both, reach the stochastization level, a massive radial gradient depletion takes place over the whole energy space. No resonance pattern is visible any more, as visualized in fig. 6.33. This happens in both scenarios, however much later in scenario1.51 around $t \approx 1.5 \cdot 10^{-2}$ s whereas at $t \approx 1.5 \cdot 10^{-3}$ s in scenario1.16. In both cases, at lower energies ($E \in [50,200]$ keV), the resonance regions are still slightly visible in the redistribution pattern. However, only in scenario1.16 does the redistribution (along the $p = 0$, 1 resonance lines of both modes) cross the loss boundary.

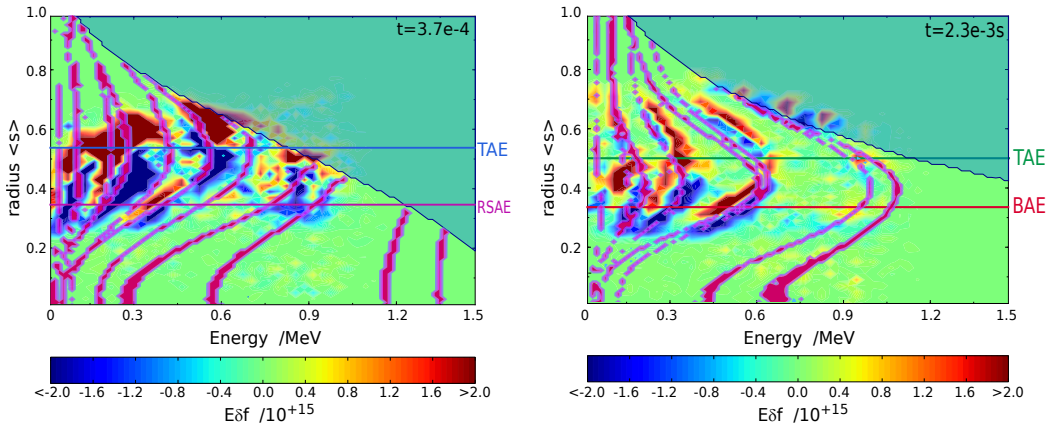

(a) *scenario1.16,* $t_1 = 3.7 \cdot 10^{-4}$ *s.* (b) *scenario1.51,* $t_1 = 2.3 \cdot 10^{-3}$ *s.*

Figure 6.32: *Redistribution in energy and radial position space during the resonant phase for both scenarios. Red indicates particle accumulation, blue means particles move away. The pink lines give the resonance lines for trapped particles, the blue areas the loss region. The horizontal lines denote the modes' radial positions. One can see clearly the redistribution caused by the wave-particle resonance along the resonance lines in the mode regions.*

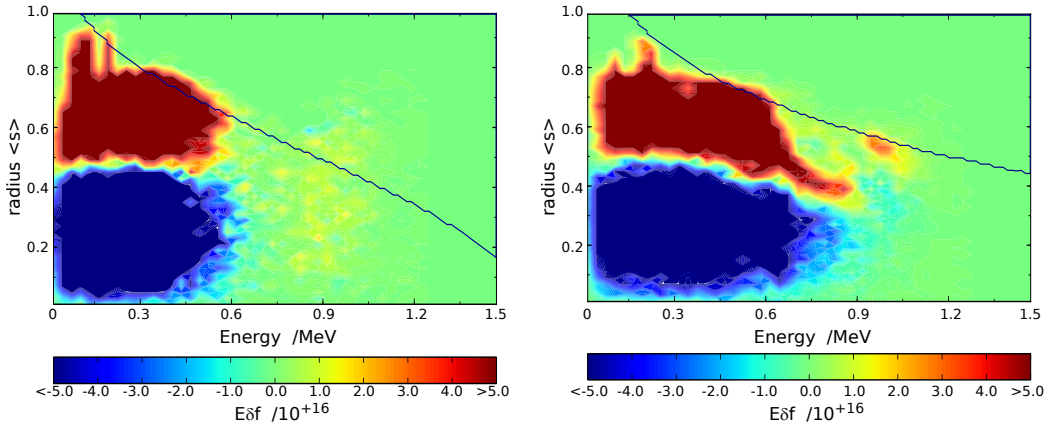

(a) *scenario1.16* (b) *scenario1.51*

Figure 6.33: *Redistribution in energy and radial position space in the stochastic phase* ($t_2 = 1.5 \cdot 10^{-2}$ *s) for both scenarios. Red indicates particle accumulation, blue means particles move away. The dark blue lines give the loss boundaries. The radial gradient depletion is taking place over a broad energy range.*

The redistribution takes place independently on the energy, but once the radial gradient is depleted in in the energy region of $E \in [400,600]$ keV, the redistribution is radially broadened at lower energies. In sec. 6.3.4, it will be seen that this broad radial redistribution is caused by the outer poloidal harmonics of the TAE. Once the process is coming to an end, the lowest resonance regions are again distinguishable, but only in scenario1.16, as shown in fig. 6.34.

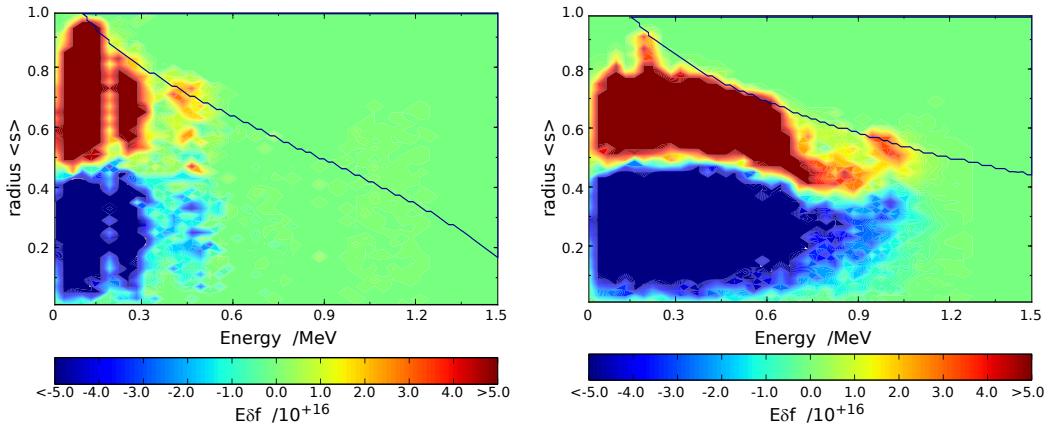

(a) *scenario1.16* (b) *scenario1.51*

Figure 6.34: *Redistribution in energy and radial position space in a later stochastic phase ($t_3 = 2.3 \cdot 10^{-2}$ s) for both scenarios. Blue means particles move away, red means they accumulate. The dark blue lines give the loss boundaries. In scenario1.16, the radial gradient depletion has come to an end in the medium energy range.*

6.3.2 Fast Particle Losses in Two Different q profile Equilibria

The redistribution plots already indicate fewer losses in scenario1.51, due to the smaller loss area, and the weaker redistribution especially in the lower energy range. In fact, scenario1.16 gives much more losses – prompt (i.e. appearing before any influence of the mode) as well as losses in the later phase of the simulation (compare fig. 6.35 a and b). In scenario1.51, there are no losses with an energy below 300 keV at all. This is in accordance with the redistribution pattern of this case, giving no redistribution across the loss boundary for $E < 300$ keV, due to the smaller loss area. The prompt losses appear in both cases in the higher energy range. They reach down to 600 keV (scenario1.16) and 750 keV (scenario1.51).
As the resonant phase is not distinguishable very clearly in scenario1.16, it is difficult to find resonant losses at very distinct energies. However, it is still visible, that losses in this phase have energies that match with the resonant phase space redistribution across the loss boundary (shown in fig. 6.32). In scenario1.16, these are at $E \in [450,700]$ keV and $\in [750,950]$ keV. In scenario1.51, these are very few losses around 400 keV, 550 keV, 700 keV and 850 keV.
When stochastization sets in, lower energetic losses appear, due to the broad redistribution across the loss boundary over a large energy range. In scenario1.16, this redistribution (see fig. 6.33 and fig. 6.34) is a caused by the fact that most of the relevant phase space is covered by overlapping resonances. As will be described in sec. 6.3.5, a *domino effect* is triggered: first, energies $E \in [300,600]$ keV are redistributed until the radial gradient in this energy area has flattened and the redistribution continues in $E \in [200,400]$ keV. In the loss spectrum over time (fig. 6.35), the successive transport across the loss boundary can be recognized as losses. Due to the many poloidal har-

monics resulting in a very broad radial structure of the TAE (as will be shown in sec. 6.3.4), even a very low energy resonance is able to transport particles across the loss boundary, that in turn appear as a thin loss peak at $E \in [100,150]$ keV, once the TAE has reached the stochastization level.

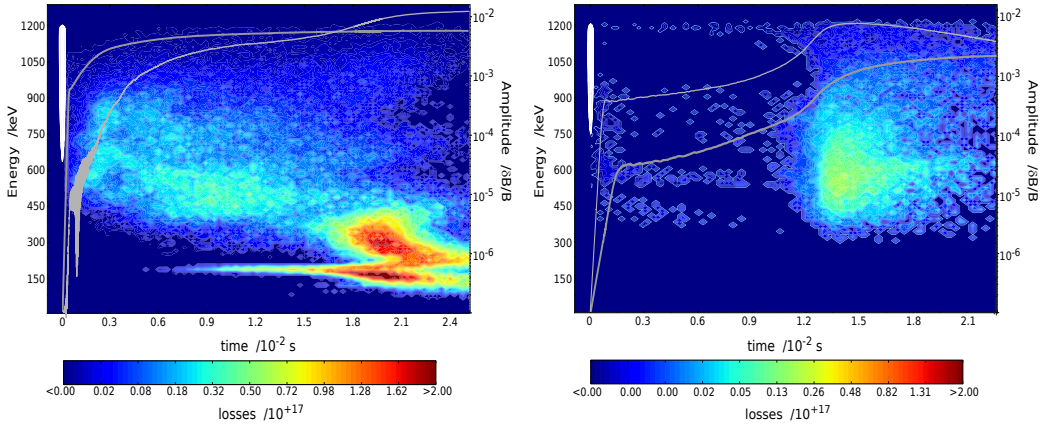

(a) *scenario1.16* (b) *scenario1.51*

Figure 6.35: *Temporal evolution of losses appearance at the first wall in energy space for the two different scenarios. The white areas indicate the prompt losses as carried out in an extra simulation with a thinner Λ distribution function eq. (6.9) and eq. (6.10), as explained before. The gray lines give the mode amplitude evolution as shown in detail in fig. 6.31.*

In scenario1.51, where the loss region is smaller, the TAE is not broad enough, to redistribute particles with $E < 350$ keV across the loss boundary. Although one reason for this is the lower amplitude levels reached in scenario1.51 (compared to scenario1.16), the main reason for the missing of the lowest energetic losses (around ≈ 180 keV) and the small amount of losses in the whole range of $E \in [300,600]$ keV is found in the different equilibrium, i.e. the smaller loss region and the larger distance between the resonance lines. This is proved by simulating the same TAE and RSAE eigenmode structures of scenario1.16 in both equilibria with a fixed mode amplitude of $\delta B/B = 5.1 \cdot 10^{-3}$ (an experimentally realistic value): as shown in fig. 6.36, even with the same mode amplitude, structure, mode number n and frequency, the monotonic q profile case leads to far fewer losses. No losses at all are observed in $E \in [300,600]$ keV. The complete inhibition of the very low energy peak around 180 keV however, is caused by a combination of the monotonic q profile equilibrium and the corresponding eigenmode.

The drop in the height of the very low energy peak not only results from the smaller loss area in the monotonic q profile [13], but also from a different redistribution: due to the less dense resonances in phase space around $E \in [100;600]$ keV, the redistribution

[13] Note that the resonances for the scenario resulting in the red curve differ from what is shown in fig. 6.8b, because as mode frequencies, the values from the modes in the inverted q profile equilibrium were used.

in the monotonic q profile is less intense but spreads wider towards higher energies. This can be seen in fig. 6.37, where the difference in the redistribution between the inverted and the monotonic q profile scenario (using the same perturbations) is shown. In combination with the different loss boundaries, this leads to the missing of losses in the energy range of $E \in [300,600]$ keV: one can see clearly the missing redistribution across the loss boundary in this energy range in the monotonic q profile (black circle). In contrast, the transport is stronger at energies around 600 keV and around 200 keV (red circles), but still does not reach into the smaller loss region. The higher the energy is, the smaller is the effect of the equilibrium on the loss spectrum. This is quite logical, as the orbit width is increasing with energy, reducing the relative impact of the equilibrium on the orbit width.

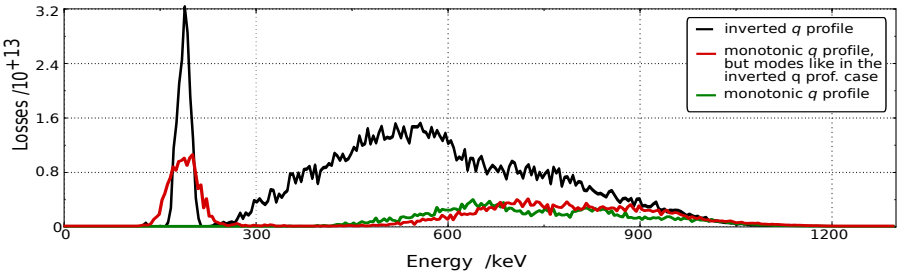

Figure 6.36: *Energy spectra of losses as numerically calculated within scenario1.16 (black curve), within scenario1.51 (green curve) and as simulated within the monotonic q profile equilibrium, using the eigenmodes given by* LIGKA *for the inverted q profile equilibrium (fig. 6.23) (red curve). The amplitudes for these simulations were fixed at* $\delta B/B = 5.1 \cdot 10^{-3}$. *The losses shown appeared in a time interval starting after c.a. 10 RSAE wave periods (*$t \in [0.2,1.5] \cdot 10^{-3}$ *s).*

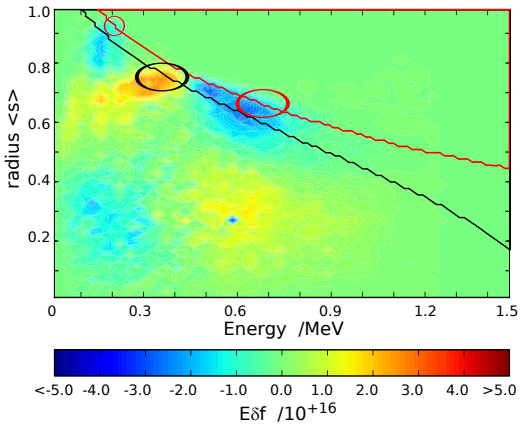

Figure 6.37: *Phase space redistribution (at* $t = 1.5 \cdot 10^{-3}$ *s) in the inverted q profile simulation subtracted from the redistribution of the same simulation within monotonic q profile equilibrium. In both simulations, the eigenmodes were used as given by* LIGKA *for the inverted q profile (fig. 6.23), with amplitudes fixed at* $\delta B/B = 5.1 \cdot 10^{-3}$. *The lines give the loss boundary for the inverted (black) as well as the monotonic q profile (red).*

6.3.3 Frequency Correlation between Losses and Modes

In the previous section, one could see that the prompt losses' energy range (white areas in fig. 6.35) does not reach to energies below 600 keV (in scenario1.16) and 750 keV (in scenario 1.51) respectively. Thus, the lower energy losses can only be either resonant or stochastic. However, at this point of the numerical investigation, the higher energetic losses that are measured experimentally can be explained to be either prompt or wave-correlated. To find out about the nature of the losses that occur in the presence of modes, the loss signature over time is investigated in the following: the frequency correlation to any of the modes or their beat frequency indicates resonant (*coherent*) losses, whereas a signal with no frequency signature but significant underlying offset indicates stochastic – also called 'diffusive' – losses, which are *incoherent*.

Fig. 6.38 shows the losses' time traces of scenario1.16 for three different energy ranges. In the intermediate energy range $E \in [450,700]$ keV (b), no offset is visible, the losses appear with a certain frequency, thus are rather coherent. In the higher energy range (a), significantly less losses appear (note that the energy range chosen is wider), because the highest energetic particles have already been ejected (incoherently) as prompt losses.

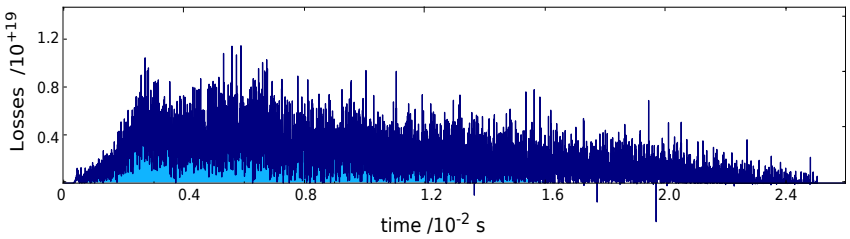

(a) *Energy range 700...1300 keV*

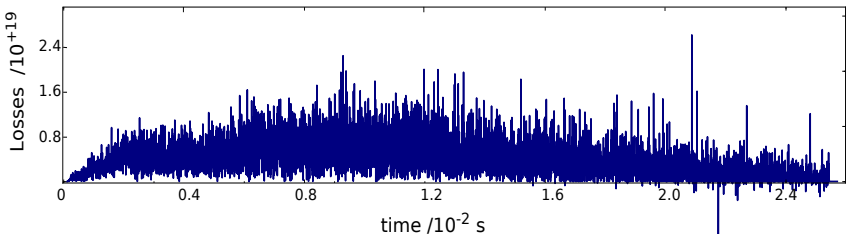

(b) *Energy range 450...700 keV*

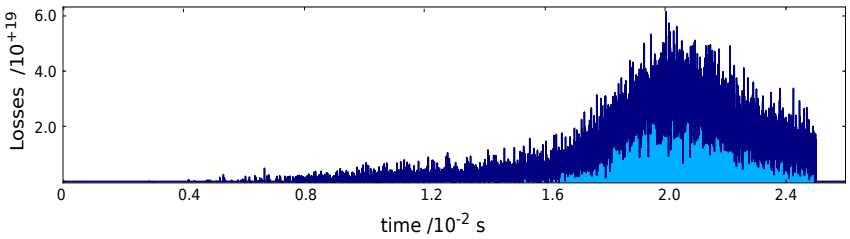

(c) *Energy range 90...350 keV*

Figure 6.38: *Time traces of the losses at the first wall in scenario1.16.*

During the phase when only the RSAE has reached the stochastization, a small underlying offset of incoherent losses is visible (light blue area in a) in the highest energy range. In the lower energy range, a large offset of incoherent losses appears (light blue in c), as soon as both modes reach the stochastization level.

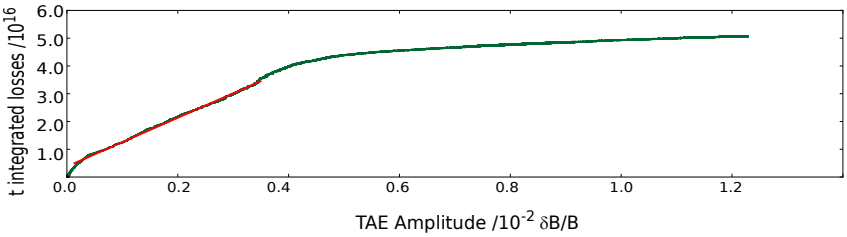

(a) *Time integrated losses of $E \in [700,1300]$ keV over TAE amplitude (green) and linear fit (red).*

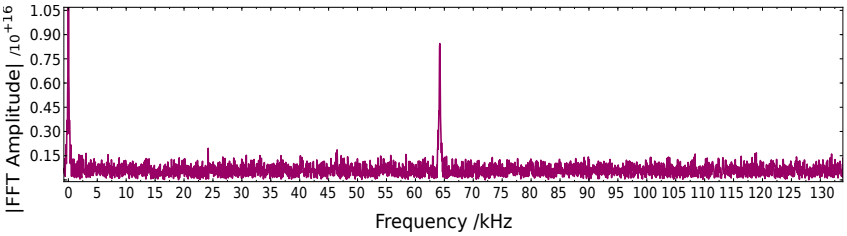

(b) *Fourier Analysis of the losses of $E \in [450,700]$ keV.*

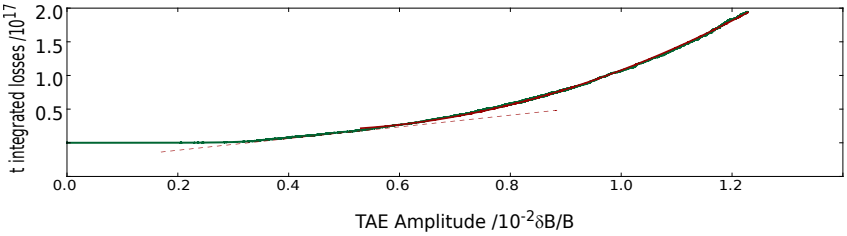

(c) *Time integrated losses of $E \in [90,350]$ keV over TAE amplitude (green) and quadratic fit (red).*

Figure 6.39: *Time integrated loss signal (a+c) and a Fourier analysis of the losses' time signature (b) for scenario1.16 in different energy ranges: high (a), intermediate (b) and low (c).*

In the following, the losses' time traces are Fourier analyzed to find a correlation between the ejection signature and the mode frequencies. However, for the higher energy range, the amount of losses is not large enough to provide good statistics for the Fourier analysis in a very thin energy interval. Especially at high energies, this is important, as different particle velocities would smear out any frequency correlation with the mode. In this part of phase space, it is only possible, to plot the time integrated losses over the mode amplitude. This results in a linear dependence with the TAE, as long as it is still below the stochasticity threshold (shown in fig. 6.39a), indicating a coherent loss mechanism due to the interaction with the TAE. At high TAE amplitudes, the losses saturate, as this corresponds to a late time point within the simulation, where most

particles of this energy are already lost. Comparing the time integrated losses in this energy interval to the RSAE amplitude, the losses scale quadratically with the RSAE amplitude, a characteristics for diffusive (incoherent) loss, which is also the dominant mechanism in the lowest energy range (shown in fig. 6.39c). In this range, however, the quadratic scaling is with respect to the TAE amplitude, as the losses appear only when this mode is reaching stochastization. The amount of losses allows for a Fourier analysis, which does not show a correlation with either mode, nor with their beat frequency. This confirms the classification of the lower energy losses as stochastic, thus incoherent. For the intermediate energy range, the Fourier analysis is possible as well, showing a strong frequency correlation to the beat frequency of both modes ($\approx$ 65 kHz). The peak is slightly shifted downwards, as the both modes' frequencies decrease slightly with time ($\Delta\omega_{\mathrm{TAE}} \approx -0.6$).

6.3.4 Influence of the Poloidal Harmonics

Next, the effect resulting from the many poloidal harmonics of the TAE is investigated. By calculating the eigenmodes with the LIGKA solver, the poloidal harmonics are known and can be used within the HAGIS simulation. Comparing two simulations – one with the poloidal harmonics $m = 4$ and $m = 5$ only, the other one with all harmonics (from $m = 4$ to $m = 10$) as shown in fig. 6.23 – shows a similar qualitative mode amplitude evolution (see gray lines in fig. 6.40) with similar mode saturation levels. However, the TAE growth rate is lower if simulating with all poloidal harmonics, as the energy has to be distributed over more poloidal harmonics. In the saturation phase, this effect is compensated by the wider radial range, i.e. the mode with all poloidal harmonics is able to tap energy from the radial gradient also radially further outside.

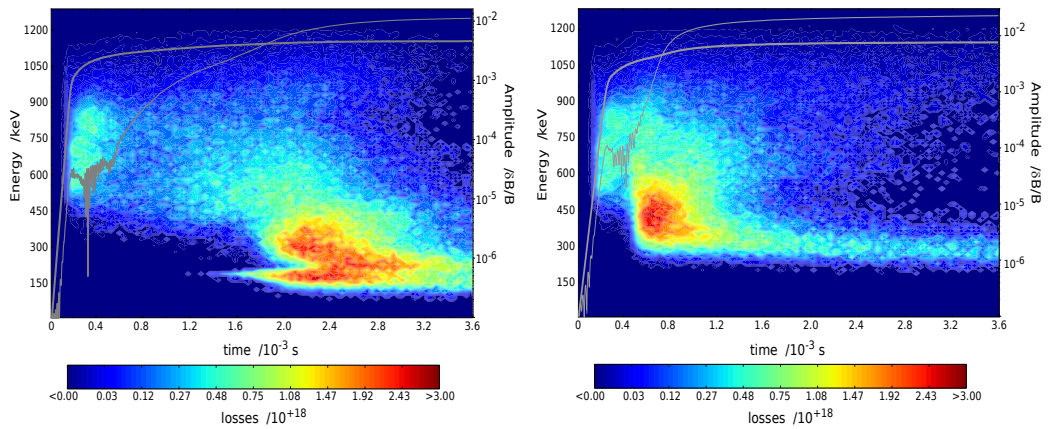

(a) *Modes as in fig. 6.31* (b) *same but only first 2 poloidal harmonics of TAE*

Figure 6.40: *Temporal evolution of losses appearance at the first wall in energy space in the inverted q profile simulation (β_{fp}=0.05%). Although the amplitudes (gray lines) reach the same levels (however, slower in the case with many harmonics), the lowest energy losses appear only in the case with many harmonics.*

This effect is well visible in the redistribution (fig. 6.41): only if all poloidal harmonics are present, the TAE redistributes particles at very low energies (around $E \approx 100$ keV) and far outside radial positions ($s > 0.8$). This redistribution results in the observed low energy losses of $E < 200$ keV, that are not observed in the simulation with only two poloidal harmonics (compare fig. 6.40 a and b).

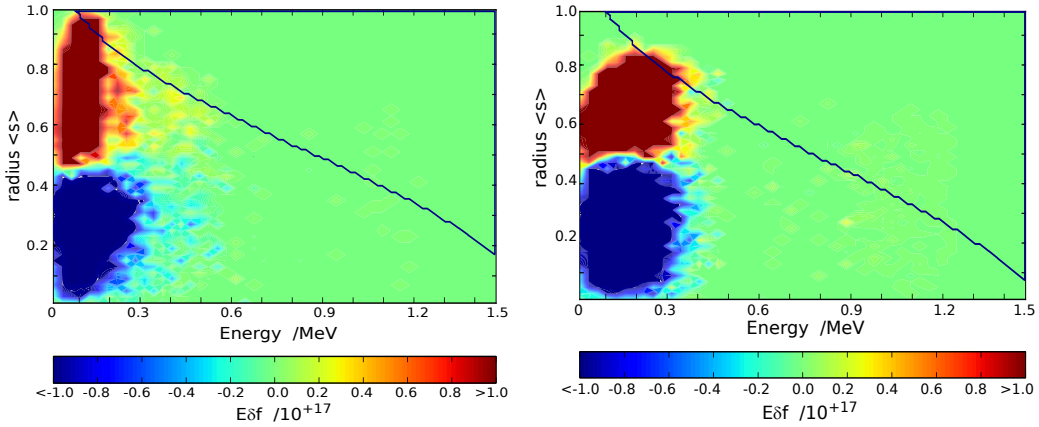

(a) *Modes as in fig. 6.31*

(b) *with only first 2 poloidal harmonics of TAE*

Figure 6.41: *Redistribution (blue means particles move away, red means they accumulate) in energy and radial position space at the end ($t = 3.6 \cdot 10^{-3}$ s) of two simulations in the inverted q profile (β_{fp}=0.05%): in (a) the modes are taken as given by* LIGKA *(see fig. 6.23), whereas in (b), the same modes are chosen, except that the TAE is simulated with only its first two poloidal harmonics. The blue line gives the loss boundary (as explained in fig. 6.8a).*

Summarized, it is clear now, that the losses with $E < 200$ keV result from the combination of the broad TAE with many harmonics and the large loss region appearing in the inverted q profile equilibrium. However, it was shown above (see fig. 6.36), that significantly less of these losses appear when simulating the same modes at the same amplitudes in the monotonic q profile, due to the smaller loss region. Concerning the losses in the lower energy range between around 300 keV up to c.a. 600 keV, it was found that these are due to the dense resonance lines meeting the loss boundary in the inverted q profile scenario, quite independent of the mode structure. In the monotonic q profile, these losses do therefore not occur.

6.3.5 Double-Mode Effect

To understand the loss mechanism with respect to multiple mode-particle interaction, it is important to find these losses that are caused by the fact that multiple modes are present. Multi-mode scenarios result in more losses for several reasons: first, amplitudes grow higher due to double-resonances, especially gradient-driven double-resonance (this has been investigated in detail in chapter 5 and earlier in this chapter). Second, a *domino effect* can transport particles outwards, caused by the inner mode delivering new particles to the outer mode's position. The outer mode in turn ejects the particles eventually. This second possibility was described on a theoretical basis in ref. [106] and is to be investigated numerically in the following.

As the mode amplitudes in the nonlinear saturation are known now from simulations with consistent mode evolution, HAGIS is run with these mode amplitudes kept fixed. This offers the possibility to investigate the losses caused by each of the modes alone vs. the losses caused by double-mode interaction, but without the additional effect that different amplitudes are reached in single-mode simulations compared to double-mode simulations. Fig. 6.42 shows the energy spectra of the losses appearing in such double-mode simulation (black curve), as well as those obtained, when simulating both modes individually (blue for the TAE and pink for the RSAE).

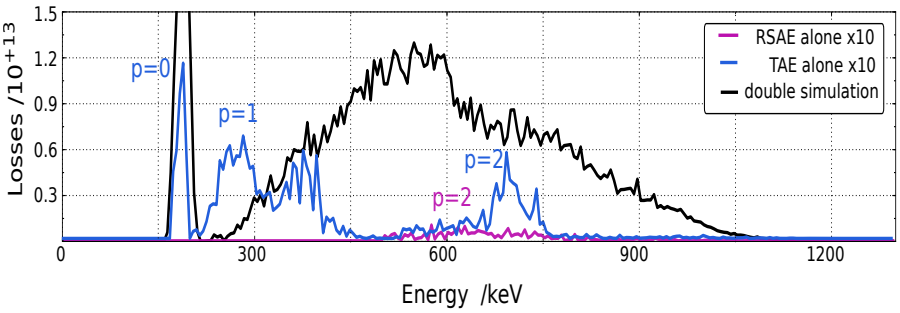

Figure 6.42: *Energy spectra of losses in three different simulations with fixed mode amplitudes at* $\delta B/B = 5.1 \cdot 10^{-3}$ *for a time interval starting after approximately 10 RSAE wave periods (*$t \in [2.0,1.2] \cdot 10^{-3}$ *s): the pink and the blue curves give the loss spectrum of the RSAE and TAE single-mode simulation, stretched by a factor of 10. The black curve gives the losses appearing if simulating both modes together (modes as shown in fig. 6.23).*

Note that the loss spectra curves obtained in the single-mode simulations are shown multiplied by a factor of 10. For each of the three spectra, the same time interval is chosen, starting after approximately 10 wave RSAE periods, to avoid the effect of prompt losses. All mode amplitudes are fixed at $\delta B/B = 5.1 \cdot 10^{-3}$, which is a reasonable value, when comparing to experimentally measured amplitudes. Further, it is of the order of the minimum saturation level reached in the previous simulations with consistent mode evolution. Although both modes are now fixed at the same amplitude level, it is not surprising that the more core-localized RSAE causes significantly fewer losses than the TAE, which is broad and located at a higher radial position. However, for

both single-mode simulations, the losses' energy spectra exhibits clearly the different resonances: losses appear at energies, where resonance lines meet the loss boundary (see fig. 6.8a). In fig. 6.42, the bounce harmonic number p is given to identify the individual resonance lines. But the most interesting fact is found, when looking at the double-mode simulation's losses: they do by far exceed the sum of the losses of the single-mode simulations, although the amplitude levels are the same. The redistribution in phase space is consistent with the appearance of losses in the double-mode simulation versus the single-mode simulations. Fig. 6.43 shows the radial redistribution for both modes simulated individually (blue for TAE, pink for RSAE) and for the double-mode scenario (black curve). For comparison, the initial distribution function of all three simulations is given (black dashed). As well as the losses, also the redistribution in the double-mode simulation exceeds by far those of the single-mode cases. Thus, the large number of losses in multi-mode situations is not only caused by the higher mode amplitudes that are possibly reached then (as was shown in chapter 5). The same reason that leads to higher mode amplitude levels – the lowering of the stochastization threshold – also causes more losses, because the redistribution is enhanced by the stochastization. If the loss boundary is large, as in the inverted q profile equilibrium, this redistribution leads to a large number of losses.

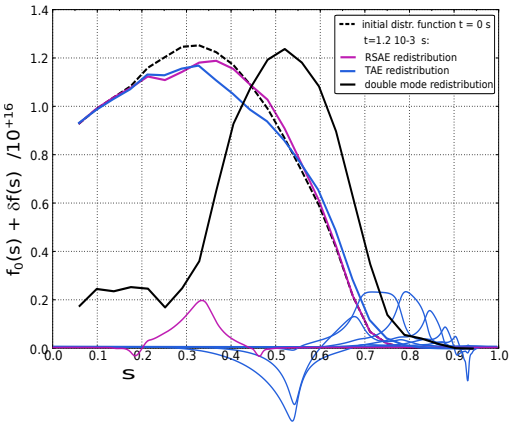

Figure 6.43: *Radial redistribution caused by the TAE (blue) and the RSAE (pink) alone and in the double-mode simulation (black), all in the inverted q profile equilibrium. The modes did not evolve in time in this simulation, but were both fixed at* $\delta B/B = 5.1 \cdot 10^{-3}$. *The radial mode structures are illustrated on the s axis (pink for the RSAE, blue for the TAE).*

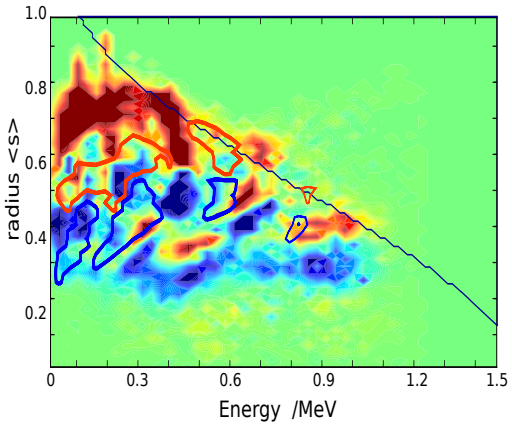

Figure 6.44: *Redistribution in energy and radial position space caused by the TAE (color code) and the RSAE (boundary lines) in the fixed amplitude simulation (at* $\delta B/B = 5.1 \cdot 10^{-3}$*). Red indicates particle accumulation (higher* $E\delta f$*), blue that particles move away (lower* $E\delta f$*). The dark line gives the loss boundary of the inverted q profile equilibrium.*

In the double-mode scenario, stochastization is enhanced due to the dense coverage of phase space with both resonance lines and perturbation structure. In fig. 6.44, this effect can be observed clearly: the RSAE transports energetic particles into phase space areas from where they are further redistributed by the TAE. Since this effect also occurs vice versa, both modes mutually refill the phase space areas with particles, where the other mode redistributes them away from. Through such nonlinear *domino effect*, not

only a high loss amount can be triggered, but also modes might be possibly destabilized that would otherwise be stable on the basis of linear stability [106].

Fig. 6.45a illustrates the orbit of such a particle together with the mode positions (pink for RSAE, blue for TAE) for the given particle energy. In (b), the particle's radial position and energy over time are shown. The little jags in the energy time trace clearly indicate the stochastic interaction, as discussed already in chapter 5 (fig. 5.12). Because of the stochastization, the mode-particle interaction does not occur due to the specific resonances any more, but the influence of the different modes can still be seen on the radial scale: the particle is trapped between the two modes until it is finally lost.

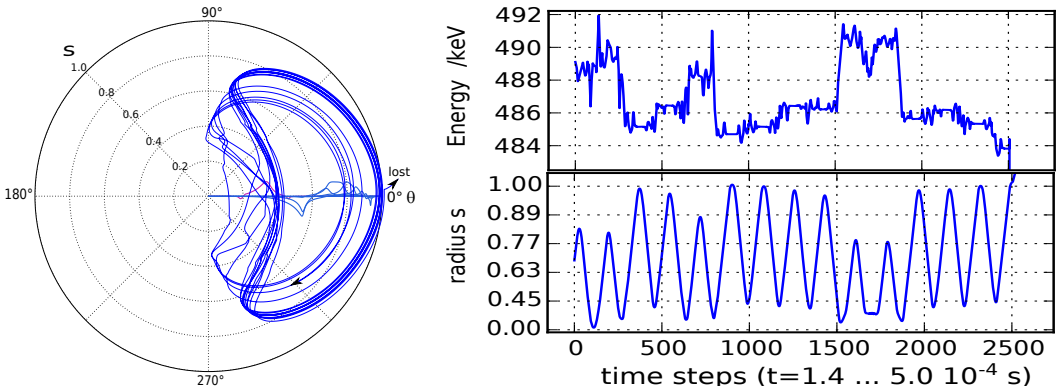

(a) *A representative particle orbit (with the modes plotted onto the s axis) ...*

(b) *... its radial position and energy time trace.*

Figure 6.45: *Representative orbit (a) of a particle that is trapped between two modes. In (b), its radial position and energy is shown over time.*

The described domino-like loss mechanism is a nonlinear phenomenon, since it is governed strongly by the interplay of different modes and the resulting phase space redistribution, which is significantly different compared to single mode redistribution. However, the scenario is still in a *weakly nonlinear regime*. In contrast, it is possible that an energetic particle distribution function (mostly its radial gradient) destabilizes the strongly damped energetic particle modes (EPM, [118]). In such system far above the stability threshold, fast particle transport can occur in avalanche-like events [119–122]. The regime is *strongly nonlinear* as the radial gradient and the mode structure change on a very fast time scale, before orbit stochastization can become relevant. To investigate scenarios like this requires to account for a damping mechanism, which is now possible within the HAGIS model due to the implementation of $\tilde{E}_{\parallel}$ described in chapter 4 and will be object of future studies, especially as application for the planned HAGIS-LIGKA hybrid model.

6.3.6 Summary & Comparison with the Experimental Loss Measurement

In this chapter, different causes for losses were discussed, depending on energies or ejection frequencies as a consequence of a certain loss mechanism. For the first time, a realistic scenario has been modeled numerically by implementing a consistent ICRH-like distribution function and kinetically calculated perturbation structures.

Summary of the most important findings

- The lowest energy losses around 180 keV ($\rho \approx 35$ mm) appear mainly due to the very broad radial mode structure of the TAE, and only in the inverted q profile equilibrium. They are the highest peak in the energy spectrum, and do not show any correlation to either one of the mode's frequencies, nor their beat frequency, and scale quadratically with the mode amplitude. Therefore, they can be classified as *incoherent diffusive* losses.

- In the low energy range of $E \in [200;350]$ keV ($\rho \in [40;50]$ mm), the high amount of losses is caused by the combination of a large loss area and dense resonance lines in phase space, in the inverted q profile equilibrium. Therefore, these losses do not occur in the monotonic q profile. Resonant losses do not appear in great number in this energy range, as the orbits are too small to be unconfined. Only the interaction of multiple modes can cause theses losses, leading to a strong phase space stochastization and non-resonant energetic particle transport. The modes grow to high amplitudes and to large scale particle redistribution and ejection. Thus, these losses are *incoherent* as well – appearing only when both modes reach the stochasticity threshold, uncorrelated to any mode or beat frequency. As *diffusive* losses, they scale quadratically with the mode amplitude.

- In the intermediate energy range of $E \in [450;700]$ keV ($\rho \in [55;70]$ mm), losses occur in the inverted q profile equilibrium, as well as in the monotonic one. The amount of losses is smaller than in the lower energy range (in the inverted q profile), however, they appear earlier in the simulation, even before both modes reach the stochasticity threshold. Their ejection is correlated to the beat frequency of both modes, and in a single-mode scenario or the monotonic q profile case, the distinct energies where the resonance lines meet the loss boundary are visible. They scale linearly with the TAE mode amplitude. All these characteristic strongly indicate a *resonant* (=*coherent*) loss mechanism.

- In the highest energy range of $E \in [700;1300]$ keV ($\rho \in [70;90]$ mm), losses appear mainly due to their large orbits, and thus as *prompt* losses, which are inherently *incoherent*. However, to identify *resonant* loss mechanisms in this energy range is difficult, due to the insufficiently amount of losses within a reasonably small energy interval to perform a Fourier analysis. It can be assumed, that these energetic particles can easily become unconfined by any resonant or non-resonant energy exchange with a wave, due to their large orbit width. In the view of transport studies in large fusion devices (like ITER), the characterization of these losses is not relevant, since such large-orbit particles do not exist.

Limitations of the Model

The simulations with the extended version of HAGIS give fast particle losses that are quite comparable to the experimental measurements, concerning the position in pitch angle and energy space, and the relative changes between different q profile equilibria. This will be shown in the next section. Before, several reasons, why a comparison on a quantitative level is difficult, will be discussed.

Throughout the last section, it was assumed, that the losses arriving at the FILD position are a representative subset of all losses hitting the machine's first wall, which might not be the case. Unfortunately it is not possible within HAGIS to investigate the **impact position of the losses** exactly: the model assumes perfect toroidal symmetry, thus the first wall is given in 2D, integrated over the toroidal angle. As a consequence, unconfined particles tend to hit the first wall earlier on their orbit than in reality. Since the orbit direction of losses is usually going upwards on the LFS, the z coordinate of their impact position is slightly underestimated and sensitive to the wall geometry. The exact wall geometry as well as further edge effects are addressed by other models, such as the ASCOTT code [123].

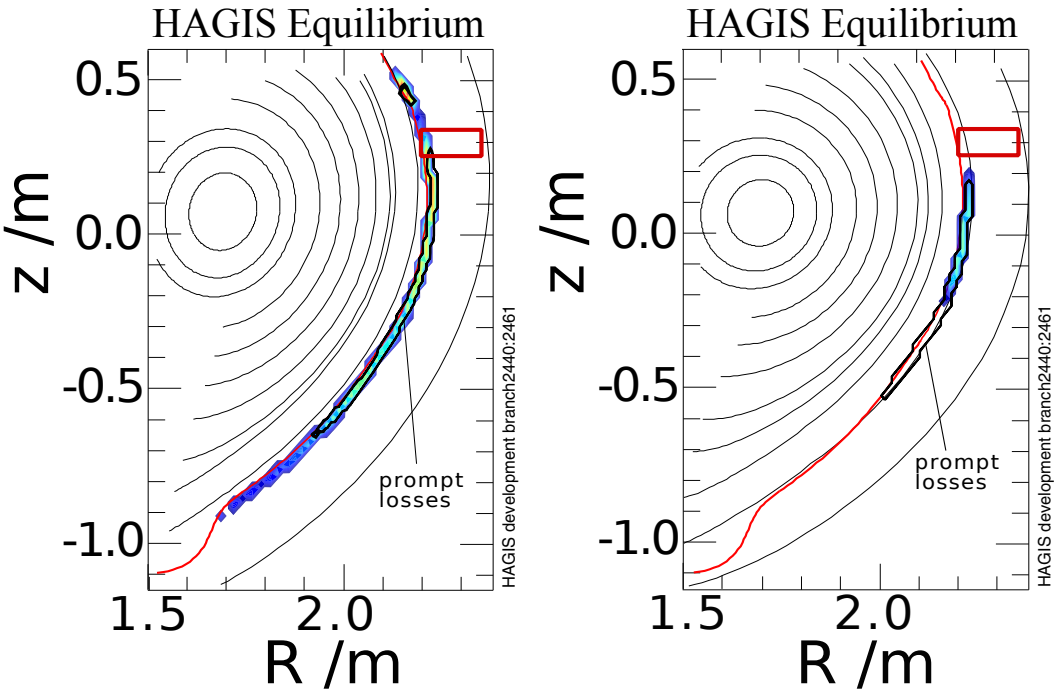

(a) *Equilibrium at* $t = 1.16$ *s*

(b) *Equilibrium at* $t = 1.51$ *s*

Figure 6.46: *Appearance of prompt* ($t < 10^{-4}$ *s) losses (indicated black lines) and non-prompt* ($t > 10^{-4}$ *s) losses (colors – from blue to red represent the losses according to increasing density) at first wall (red line) in the simulations of* AUG *discharge #23824. The red box depicts the approximate* FILD *position, the thin curved lines the plasma equilibrium reconstruction.*

The location of the FILD is at around $z \approx 300$ mm above the outboard midplane [108]. In fig. 6.46, a histogram of the loss appearance in R-z space is plotted onto the equilibrium used by HAGIS, that includes the vacuum region and also the first wall (red line). The great part or even the majority of losses hits the first wall slightly above the outboard midplane. In scenario1.16 (a), quite a representative fraction of losses appears at the detector position (red box). The area in gyroradius (ρ)-pitch (λ^o) space that this subset of losses covers does not differ from the one covered by the whole set of losses, except for the missing of very high pitch angles $|\lambda^o| > 82^o$. However, within the ρ-λ^o pattern, the peak in the lower energy range is under-represented in the set of losses restricted to the detector position. In scenario1.51 in contrast, all the numerical losses hit the first wall below the detector position, which is quite unrealistic, as a small amount of losses was measured in this equilibrium at the FILD.

It should further be mentioned, that the FILD is insensitive to different masses. Although, due to minority heating, most fast particles are protons, there is a fraction of **fast deuterium ions** as well ($< 10\%$), that were not taken into account in the simulations. At the same measured gyroradius, their energy is lower by a factor of two. Thus, the deuterium ions are slower, compared to the protons, and smear out the experimentally measured time signature of the losses. The incoherent loss fraction is therefore expected to be slightly overestimated by the FILD. A similar smearing effect is further caused by **magnetic field ripple** [124, 125] at the plasma edge, that alter the particle energy.

Another important limitation of the model is, that **prompt losses are not given quantitatively** within the HAGIS model, as explained in the following. Therefore, it is not possible, to quantify the ratio of incoherent to coherent losses in the higher energy range.

In a heated fusion plasma, the **energetic particle distribution function** results from the continuous balancing between energy input (source of fast ions) and the dissipation of this energy via collisional processes with the background plasma. Further transport channels within the slowing-down process are turbulence, transport due to non-axis symmetric components of the magnetic equilibrium, e.g. magnetic field ripple, and finally, the interaction with global plasma waves. In the HAGIS model, a stationary distribution function is assumed, neglecting all effects except the flattening due to mode-particle interaction. There is no source term implemented so far, nor the various dissipation mechanisms. As long as the simulated time is significantly below the fast particle slowing-down time [98] (≈ 0.1 s), the initial distribution function represents a stationary state of the energetic particles. Its form is justified by resulting mode amplitude levels in the range of the experimentally observed values. The evolution of the distribution function is caused purely by wave-particle interaction, leading to a flattening in the radial gradient, and to energetic particle losses. The modes grow and eventually saturate through this mechanism alone.
The reasons that allow to neglect different damping mechanisms were already discussed in sec. 3.2.1. Concerning the various energy dissipation mechanisms, it was found, that turbulent transport of fast particles is in the most relevant regimes two

orders of magnitude lower than thermal transport [126, 127], and ripple losses affect only the plasma edge. In the plasma core, the fast particle-wave interaction is the most important transport process. This justifies the limitation of the model to assume a stationary distribution function as non-perturbed initial state. However, as a consequence, prompt losses can not be calculated quantitatively. Concerning the qualitative findings, the energy range of the appearing prompt losses was shown (sec. 6.2.2) to be relatively sensitive to the **fast particle distribution function**. Since the ICRH energy deposition is very localized, the applied distribution function gives an upper estimate for the energy range of prompt losses. The non-prompt losses are quite robust against uncertainties in the radial or pitch distribution. Thus, also the finding of a drastic enhancement of diffusive low energy losses in the presence of multiple modes with many poloidal harmonics, is quite robust.

Achievements of the Model

Now, it is discussed, which of the various experimental findings can be reproduced and explained within the numerical model.

The first striking statement of ref. [33] is the difference in the **total amount of losses** between the earlier time points, $t < 1.4$ s, when a large number of losses appears in the whole energy range, and later times, $t > 1.4$ s, when there are only few losses in the high energy channel and almost none in the low energy channel.

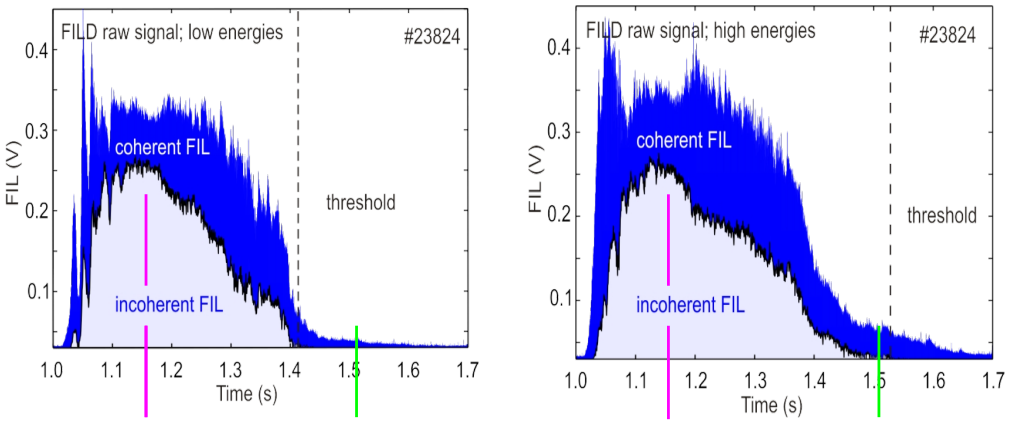

(a) *Low energy channel* $\rho \approx 40$ *mm*

(b) *High energy channel* $\rho \approx 70$ *mm*

Figure 6.47: *The* FILD *raw signal of losses over time during* AUG *discharge #23824 [33, 128] for different energy channels. The frequency correlated (coherent) losses are colored dark blue, the incoherent offset is shown in light blue. The vertical lines indicate the time points investigated numerically in this chapter (pink for the earlier, green for the later time).*

Focusing on the two time points $t = 1.16$ s and $t = 1.51$ s, shown in fig. 6.47 reveals: at $t = 1.16$ s (marked by pink lines), an equally high amount of losses is found in the low (a) and the high energy channel (b), whereas at $t = 1.51$ s (marked by green lines), no low energy losses appear – except for a general noise level (a), and fewer ($\approx 18\%$) in the high energy range (b). This result is well reproduced by the numerical simulations, as is found when interpreting the loss data shown in fig. 6.35: scenario1.16a gives a large number of losses in the lower and in the higher energy range, with quite comparable levels, relative to each other. In scenario1.51, no losses appear below $\rho \lesssim 45$ mm and a few for higher energies ($\rho \gtrsim 45$ mm), mostly within $\rho \in [65; 75]$ mm. The drop of losses in the higher energy range between the earlier and the later scenario is in the range of around 10% in the simulation, depending on the choice of the ρ range. However, to compare the losses quantitatively with the ones measured at the FILD is only possible in the lower energy channel. In the higher energy channel, prompt losses are expected. These prompt losses cannot be quantified within the model, as explained in the previous section. Despite the missing of the prompt losses, the numerically calculated difference between scenario1.16 and 1.51 is also one order of magnitude.

Next, the **nature of losses – incoherent or coherent** is discussed. The simulations for $t = 1.51$ s (see fig. 6.35b) give losses only in the high energy range. There are both prompt, i.e. incoherent losses and non-prompt losses, which show clearly an energy spectrum correlated to the resonance energies at the loss boundary. However, there is also a small amount of non-prompt incoherent losses (diffusive). Thus, the few incoherent losses seen also in the FILD signal fig. 6.47b can be both prompt or diffusive. But taking into account, that the mode amplitudes were slightly overestimated in the simulation, it can be concluded that in reality the diffusive losses are probably few.
In the experiment, the ratio of coherent to incoherent losses at $t = 1.16$ s is about 1:5 in the low and roughly 1:2.5 in the high energy channel. A possible overestimation of incoherent losses due to the smearing effects discussed in the previous section has to be taken into account. In the numerical simulation as well, both coherent and incoherent losses are found. In the lower energy range the ratio of coherent (resonant) to incoherent losses (caused by phase space stochastization, combined with the large loss area of the inverted q profile) is in the same order of magnitude (shown in fig. 6.38) as in the experiment. In the higher energy range, simulations indicate that the majority of incoherent losses are ejected as prompt losses: the non-prompt losses show coherent characteristics, but are too few to analyze the ratio of coherent to diffusive losses quantitatively. Further, the prompt losses do not allow a quantitative analysis for the reasons given above. Though, a rough estimate is, that a large fraction of the losses in this energy range is prompt: since no prompt losses occur in the low energy range, one can calculate a scaling factor between the experimental loss value and the simulated amount of losses. With this factor, the simulated losses in the high energy range can be compared to the measured ones. The difference gives the prompt losses, that are missing in the simulation. In the case of the most realistic simulation, this allows one to estimate, that between around 5% and 50% of the measured incoherent losses in the high energy channel would be prompt. However, this is only a rough estimate, due to the uncertainties that enter the comparison. Besides the limitations of the model

discussed above, these are the width of the energy channels, the FILD noise level, and the fact, that the scaling between experiment and simulation can depend on the energy, since the losses at different energies are caused by different loss mechanisms. If one considers smearing effects at the FILD, that overestimate the incohrent losses, the ratio of prompt losses are expected to be higher.

In the next step, the **energy-pitch angle characteristics** of the numerical losses is compared with the experimental measurement. As explained in sec. 6.1.2, the FILD gives a pattern in the space of gyroradius ρ and pitch angle λ^o. When comparing the numerically obtained values with the experimental ones, one has to bear in mind that the FILD measurement neglects the drift movement that takes place within the detector. Therefore, the numerically obtained values for ρ and λ^o are shifted about approximately $+6\%$ in ρ and $+9^o$ in $|\lambda^o|$, as explained in sec. 6.1.2 or ref. [55]. It is then found, that experimental (colored red in fig. 6.48, from ref. [33, 128]) and numerical loss pattern (blue and green lines) match very well in phase space. The numerical results indicate, that the higher energy (or gyroradius-) incoherent losses are prompt losses, whereas the lower energy (or gyroradius-) incoherent losses are caused by phase space stochastization due to the presence of multiple modes. The highest energies detected at the FILD do not appear in the simulation, as the maximum energy simulated was $E_{\text{max}} = 1.2$ MeV.

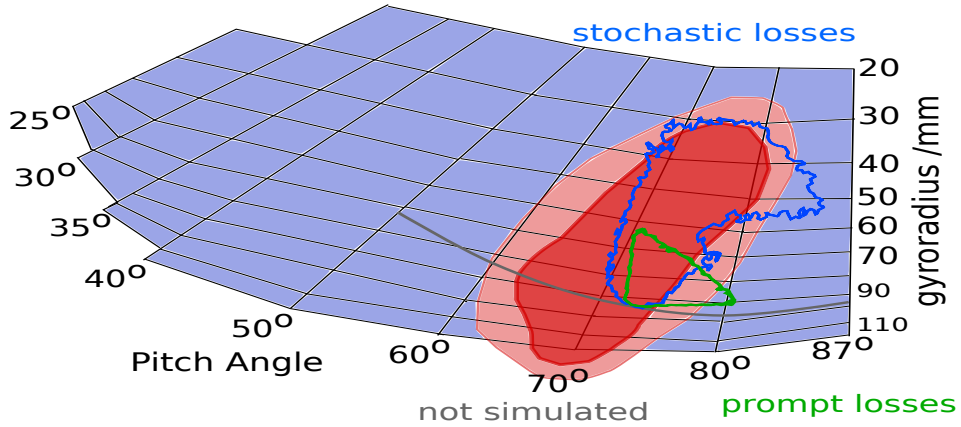

(a) *Inverted q profile MHD equilibrium of* AUG *#23824 ($t \approx 1.15$ s).*

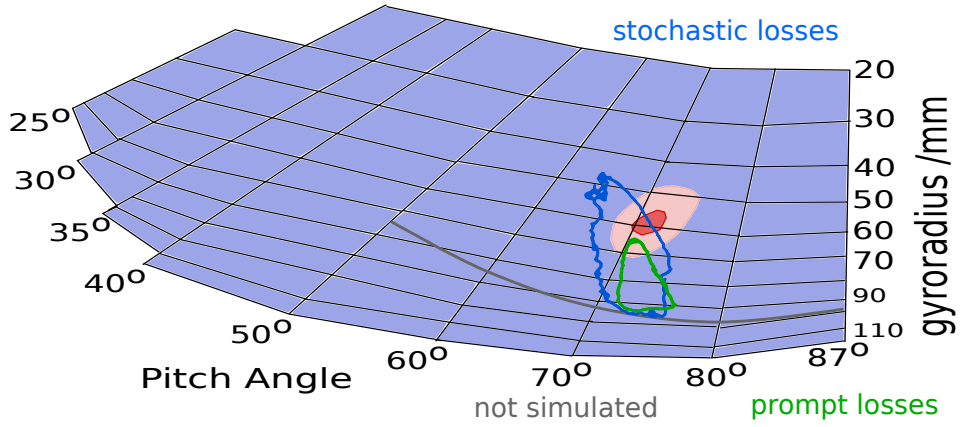

(b) *Monotonic q profile MHD equilibrium of* AUG *#23824 ($t \approx 1.5$ s).*

Figure 6.48: *Loss pattern (colored red) in phase space (gyroradius ρ over pitch angle λ^o) as measured at the* FILD *in* AUG *discharge #23824 at time $t \in [1.14,1.16]$ s (a, from ref. [128]) and $t \approx 1.52$ s (b, from ref. [33]). Further, the loss pattern as resulting from the simulation of an* ICRH*-generated fast particle distribution function in the MHD equilibrium of* AUG *#23824 at $t = 1.16$ s (a) and $t = 1.51$ s (b) with the corresponding perturbation given by* LIGKA *(see fig. 6.23 and fig. 6.24) is shown. For the distribution function see eqs. (6.6) to (6.8). The blue line gives the boundary of the non-prompt losses at the first wall – where the majority appears in the respective lower ρ part within the boundary. The green line depicts the boundary of the prompt losses' appearance at the first wall (simulated with the distribution function of eqs. (6.8) to (6.10)). The numerical values have been drift-corrected by +6% in ρ and $\approx +9^o$ in λ^o, as explained in sec. 6.1.2.*

CHAPTER 7

Conclusions and Outlook

In this thesis, nonlinear effects due to energetic particle driven Alfvén eigenmodes in a TOKAMAK plasma have been investigated. The simulations for this purpose have been performed with the HAGIS code [72]. The code has further been extended to be applicable to more realistic scenarios.

In chapter 5, the interaction of fast particles with Alfvén Eigenmodes of different frequencies were studied numerically with HAGIS in a simple, but physically realistic picture for two different MHD equilibria occurring during the ASDEX Upgrade discharge #23824. Double-resonant mode drive was compared with single mode scenarios, confirming previous findings of double-resonance mechanisms: gradient driven double-resonance [76] and inter-mode energy transfer [55]. The latter was observed to be significant only in low amplitude cases, enhancing the weaker mode at the expense of the dominant one. A beat frequency oscillation superimposed on both mode amplitudes was found, as well as higher linear growth rates – at least for one mode – compared to the single mode reference cases. The growth rate enhancement turned out to be fairly independent on the radial mode distance. The double-resonance can enhance the saturation amplitudes of the Alfvén Eigenmodes to reach the stochastic regime and can therefore lead to much higher saturation levels compared with the single mode scenarios, even if there is no radial mode overlap. However, close radial mode distances were found to stabilize linearly dominant modes when the nonlinear regime sets in. As a consequence, linearly weaker modes may become nonlinearly dominant. Thus, simulations revealed a complex nonlinear evolution of multi-mode scenarios, that is not just a simple continuation of the linear multi-mode behavior.

In chapter 6, simulations with ICRH-generated fast particles were performed with the extended HAGIS version [55]. They allowed to compare numerical fast particle losses with experimental measurements of the ASDEX Upgrade discharge #23824 [33] and lead to a deeper understanding of the transport processes. This was achieved through the investigation of the internal redistribution in combination with existing resonances, as well as phase space and frequency analysis of the losses. A useful diagnostic tool has been developed to allow the in-depth investigation of a large amount of simulation data.

At first, the importance of the extended HAGIS version, that includes the vacuum region was investigated. A difference in losses up to 30% was found, especially in scenarios with lower energetic losses. Further, the simulations have been carried out within a more realistic model in various respects: on the energetic particle side, a more general,

consistent ICRH-like distribution function was implemented, which applies the marker weighting on conserved quantities. The simulation results are quite robust against uncertainties in the radial and pitch distribution function, except for the prompt losses, i.e. those, that are unconfined solely due to their large orbit width – caused by a high birth energy – or a birth position radially far outside. On the perturbation side, HAGIS has been extended to use kinetic perturbation data from the eigenvalue solver LIGKA [93]. Differences in the mode amplitude evolution between the specific LIGKA given eigenmode structure and comparable analytical Gaussians were studied, stressing the importance of radially shaped eigenfunctions and the appropriate number of poloidal harmonics.

Next, the fast particle transport and losses, as simulated under these realistic conditions, were analyzed. The simulated losses' phase space pattern was found to coincide very well with the experimental one. Especially in multi-mode scenarios with different mode frequencies, stochastic redistribution sets in over a broad energy range, leading to lower energetic diffusive (incoherent) losses. Resonant losses appear from the late linear phase on, mainly in the intermediate to higher energy range, showing good coherence with the mode frequencies and especially their beat frequencies. The higher energetic part of experimentally measured incoherent losses has been identified as mainly prompt losses. The eigenmode structure given by LIGKA revealed that the lowest energetic losses result from a combination of two interconnected facts: first, the many poloidal harmonics of the toroidicity induced Alfvén eigenmode, which are caused by the gap alignment in the continuum of an inverted q profile equilibrium. Second, due to particle drift orbits that are radially extended on the size of the machine's small radius. In scenarios like this, especially in the presence of multiple modes with different frequencies, i.e. with complementary resonances, that densely fill the relevant phase space, a domino effect can occur: particles in the high energy range leave the plasma as prompt losses, followed by resonant and diffusive losses. At the same time, the redistribution caused by the core-localized mode refills the particles, that have been transported radially outwards by the outer mode. When the outer mode reaches the stochasticity threshold, low energy losses appear (down to $E = 300$ keV), and if many poloidal harmonics are present, they transport even very low energetic particles (down to $E = 100$ keV) across the loss boundary. This domino effect, caused by the presence of multiple modes, is clearly a nonlinear phenomenon, although the regime is still weakly nonlinear. Losses are enhanced by orders of magnitude.

Although the radial structure of the wave is very important, it is not yet allowed to evolve in time within the HAGIS model. HAGIS is a hybrid code, which calculates interaction with MHD or other perturbations self-consistently only concerning mode amplitude and frequency evolution. In the frame of this thesis, the coupling of HAGIS with the LIGKA code, which calculates the wave structures has been started. The future hybrid HAGIS-LIGKA model is planned to evolve the eigenmodes on a time scale slower than the eigenmode frequencies. For this purpose, the interface in HAGIS to the LIGKA given perturbation has been built. Also, a non-vanishing parallel electric field term $\tilde{\boldsymbol{E}}_{\parallel}$ has been included in HAGIS, and first successful consistency studies have been carried out. Previously, $\tilde{E}_{\parallel}$ was neglected, as in ideal MHD. With $\tilde{\boldsymbol{E}}_{\parallel}$, a damping enters the equations,

that has a radial structure and is different for each mode harmonic m. The new implementation will be used to study the nonlinear behavior of linearly stable modes and strongly damped modes, e.g. acoustic low-frequency electrostatic modes. Additionally, non-MHD-like modes will be investigated, such as energetic particle modes, which are strongly damped. In the strongly nonlinear regime, these modes can be destabilized by an energetic particle population and lead to an avalanche-like transport. It is still an open question, which conditions determine whether the regime is strongly or weakly nonlinear.

Appendix

Appendix A

List of Various Mag. Fusion Devices

Acronym/ name	stands for	institute/site	operation time	type
Alcator (C)	'Alto Campo Torus'	MIT (USA)	since 1975	T
ASDEX	'AxialSymmetrischesDivertor-Exper.'	IPP (Garching, D)	1980-90	T
ASDEX Upgrade	"	IPP (Garching, D)	since 1991	T
DIII-D	–	GA (San Diego, USA)	since 1980s	T
ITER	Formerly: 'Intern. Thermonuclear Experimental Reactor'	intern. project Cadarache (F)	scheduled D-T fusion in 2027	T
JET	'Joint European Torus'	EURATOM (Culham, UK)	since 1983	T
JT-60	'Japan Torus'	JAEA (Naka, Japan)	since 1985	T
LHD	'Large Helical Device'	NIFS (Nagoya, Japan)	since 1998	S
MAST	'Mega Ampere Spherical Tokamak'	UKAEA (Culham, UK)	since 1999	T
NSTX	'National Spherical Torus Exp.'	PPPL (Princeton, USA)	since 1999	T
TFTR	'Tokamak Fusion Test Reactor'	PPPL (Princeton, USA)	1992-97	T
Tore Supra	'Tore Supra'	CEA (Cadarache, F)	since 1988	T
T3, T10		Moscow (UdSSR)	in the 1960s	T
W7-AS	'Wendelstein7-AS'	IPP (Garching, D)	1988-2002	S
W7-X	'Wendelstein7-X'	IPP (Greifswald D)	scheduled start 2014	S

APPENDIX B

Useful Formula concerning Curvilinear Coordinate Systems

For derivations and explanations, see the book of d'Haeseleer [129] (Note: base vectors are not normalized there!).
Consider a one-to-one transformation R from one coordinate system (coordinates (u^1,u^2,u^3) or short: u^i) to the other (x_i):
$R(u^1,u^2,u^3) = (x_1(u^1,u^2,u^3), x_2(u^1,u^2,u^3), x_3(u^1,u^2,u^3))$.
The *tangent-basis vectors* or *covariant basis vectors* are defined as:

$$\boldsymbol{e}_i = \frac{\partial \boldsymbol{R}}{\partial u^i} \tag{B.1}$$

(in some notation normalized to unity length). They are tangential to the u^i coordinate curves.
The *reciprocal-basis vectors* or *contra-variant basis vectors* are defined as:

$$\boldsymbol{e}^i = \nabla u^i \tag{B.2}$$

(in some notation normalized to unity length as well). These are perpendicular to the coordinate surfaces $u^i = \text{const}$.

It holds $\boldsymbol{e}_i \cdot \boldsymbol{e}^j = \delta_i^j$, meaning that the set of vectors $\boldsymbol{e}^i$ forms a reciprocal set to those of $\boldsymbol{e}_i$. From this, it can be derived that any basis vector of one set can be calculated if the three vectors of the other set are known:

$$\boldsymbol{e}^i = \frac{1}{\mathfrak{J}}\, \boldsymbol{e}_j \times \boldsymbol{e}_k \tag{B.3a}$$

$$\boldsymbol{e}_i = \mathfrak{J}\, \boldsymbol{e}^j \times \boldsymbol{e}^k \tag{B.3b}$$

where i,j,k must be chosen as a cyclic permutation.
$\mathfrak{J}$ is the **Jacobian** of the transformation:

$$\mathfrak{J} = \frac{\partial \boldsymbol{R}}{\partial u^1} \cdot \frac{\partial \boldsymbol{R}}{\partial u^2} \times \frac{\partial \boldsymbol{R}}{\partial u^3} = \boldsymbol{e}_1 \cdot \boldsymbol{e}_2 \times \boldsymbol{e}_3 \tag{B.4a}$$

$$\mathfrak{J} = \frac{1}{\nabla u^1 \cdot \nabla u^2 \times \nabla u^3} = \frac{1}{\boldsymbol{e}^1 \cdot \boldsymbol{e}^2 \times \boldsymbol{e}^3} \tag{B.4b}$$

$\boldsymbol{A}$ denotes an arbitrary **vector**. It can be written with co-variant (A_i) or contra-variant (A^i) components:

$$\boldsymbol{A} = A_i \nabla u^i \qquad \text{i.e. with co-variant components,} \quad A_i = \boldsymbol{A} \cdot \boldsymbol{e}_i \tag{B.5a}$$

$$\boldsymbol{A} = A^i \boldsymbol{e}_i \qquad \text{i.e. with contra-variant components,} \quad A^i = \boldsymbol{A} \cdot \boldsymbol{e}^i \tag{B.5b}$$

Note the following geometric concepts in this notation:

The metric tensor:

$$\begin{aligned} g_{ij} &= \boldsymbol{e}_i \cdot \boldsymbol{e}_j \\ g^{ij} &= \boldsymbol{e}^i \cdot \boldsymbol{e}^j \qquad \text{(B.6a)} \\ &\Rightarrow A_i = g_{ij} A^j \\ &\Rightarrow A^i = g^{ij} A_j \qquad \text{(B.6b)} \end{aligned}$$

$$\begin{aligned} \mathfrak{g}_{ij} &= \boldsymbol{e}_i \cdot \boldsymbol{e}_j \\ &= -\mathfrak{J}^2 (\boldsymbol{e}^j \times \boldsymbol{e}^k) \cdot (\boldsymbol{e}^k \times \boldsymbol{e}^i) \\ &= \mathfrak{J}^2 \boldsymbol{e}^i \cdot [\boldsymbol{e}^k \times (\boldsymbol{e}^k \times \boldsymbol{e}^j)] \\ &= \mathfrak{J}^2 \boldsymbol{e}^i \cdot [\boldsymbol{e}^k (\boldsymbol{e}^k \cdot \boldsymbol{e}^j) - \boldsymbol{e}^j (\boldsymbol{e}^k)^2] \\ &= \mathfrak{J}^2 \left[\mathfrak{g}^{ik} \mathfrak{g}^{kj} - \mathfrak{g}^{ij} \mathfrak{g}^{kk}\right] \qquad \text{(B.7)} \end{aligned}$$

Gradient:

$$\nabla \Phi = \frac{\partial}{\partial u^i} \Phi \, \boldsymbol{e}^i \qquad \text{(B.8)}$$

Divergence:

$$\nabla \cdot \boldsymbol{A} = \frac{1}{\mathfrak{J}} \frac{\partial}{\partial u^i} (\mathfrak{J} A^i) \qquad \text{(B.9)}$$

Curl:

$$\nabla \times \boldsymbol{A} = \frac{\partial}{\partial u^j} A_i \, (\boldsymbol{e}^j \times \boldsymbol{e}^i) \qquad \text{(B.10)}$$

Parallel and perpendicular component of a vector A along B:

$$\boldsymbol{A}_{\parallel} = \frac{\boldsymbol{A} \cdot \boldsymbol{B}}{B} \qquad \boldsymbol{A}_{\perp} = -\frac{\boldsymbol{B}}{B^2} \times (\boldsymbol{B} \times \boldsymbol{A}) \qquad \text{(B.11)}$$

B.1 General Vector Identities

Scalar product:

$$\begin{aligned} \boldsymbol{c} &= \boldsymbol{a} \cdot \boldsymbol{b} = |a||b| \cos(\angle(a,b)) \\ c &= a^i a_j \qquad \text{(B.12)} \end{aligned}$$

Cross product:

$$\begin{aligned} \boldsymbol{c} &= \boldsymbol{a} \times \boldsymbol{b} \qquad \perp \boldsymbol{a}, \boldsymbol{b} \\ c_k &= a^i a^j \epsilon_{ijk} \qquad \text{(B.13)} \end{aligned}$$

Double cross product:

$$\boldsymbol{a} \times (\boldsymbol{b} \times \boldsymbol{c}) = \boldsymbol{b}(\boldsymbol{a} \cdot \boldsymbol{c}) - \boldsymbol{c}(\boldsymbol{a} \cdot \boldsymbol{b}) \tag{B.14}$$

Scalar triple product:

$$\begin{aligned} \boldsymbol{a} \cdot (\boldsymbol{b} \times \boldsymbol{c}) = \quad & \boldsymbol{b} \cdot (\boldsymbol{c} \times \boldsymbol{a}) = \quad \boldsymbol{c} \cdot (\boldsymbol{a} \times \boldsymbol{b}) \\ = -\boldsymbol{a} \cdot (\boldsymbol{c} \times \boldsymbol{b}) = & -\boldsymbol{c} \cdot (\boldsymbol{b} \times \boldsymbol{a}) = -\boldsymbol{a} \cdot (\boldsymbol{c} \times \boldsymbol{b}) \end{aligned} \tag{B.15}$$

Product rules with the nabla operator:

$$\nabla(\boldsymbol{a} \cdot \boldsymbol{b}) = (\boldsymbol{a} \cdot \nabla)\boldsymbol{b} + (\boldsymbol{b} \cdot \nabla)\boldsymbol{a} + \boldsymbol{a} \times (\nabla \times \boldsymbol{b}) + \boldsymbol{b} \times (\nabla \times \boldsymbol{a}) \tag{B.16}$$

$$\nabla \cdot (\boldsymbol{a} \times \boldsymbol{b}) = \boldsymbol{b} \cdot (\nabla \times \boldsymbol{a}) - \boldsymbol{a} \cdot (\nabla \times \boldsymbol{b}) \tag{B.17}$$

$$\nabla \times (\boldsymbol{a} \times \boldsymbol{b}) = \boldsymbol{a}(\nabla \cdot \boldsymbol{b}) - \boldsymbol{b}(\nabla \cdot \boldsymbol{a}) + (\boldsymbol{b} \cdot \nabla)\boldsymbol{a} - (\boldsymbol{b} \cdot \nabla)\boldsymbol{a} \tag{B.18}$$

APPENDIX C

Toroidal Geometry related Formula and Definitions

C.1 Poloidal and Toroidal Magnetic Fluxes

The magnetic flux is defined as the component of a magnetic field passing through a given surface.

Definition of the Toroidal Flux:
Independent on the coordinate system, the mathematical formulation of the magnetic flux definition is

$$\Psi_t = \iint_{A_{\zeta=\text{const.}}} \boldsymbol{B} \cdot \mathrm{d}A \tag{C.1}$$

The area $A_{\zeta=\text{const.}}$ is the surface of constant ζ angle, as shown in orange in fig. C.1. One can consider the following expression, where V is the volume enclosed by the flux surface A:

$$\iiint_V \boldsymbol{B} \cdot \nabla\zeta \, \mathrm{d}V.$$

Since $\nabla \cdot \boldsymbol{B} = 0$, one can write

$$= \iiint_V \nabla \cdot (\boldsymbol{B}\zeta)\mathrm{d}V,$$

and using Gauss's theorem :

$$= \oiint_A \boldsymbol{B}\zeta \cdot \mathbf{d}\boldsymbol{A},$$

$$= \iint_{A(\text{torus})} \boldsymbol{B}\zeta \cdot \mathbf{d}\boldsymbol{A} + \iint_{A(\zeta=0)} \boldsymbol{B}\zeta \cdot \mathbf{d}\boldsymbol{A} + \iint_{A(\zeta=2\pi)} \boldsymbol{B}\zeta \cdot \mathbf{d}\boldsymbol{A}. \tag{C.2}$$

The first integral on the right hand side vanishes by definition of a flux surface: $\boldsymbol{B}$ is tangent everywhere, thus perpendicular to the normal vector of A, i.e. $\boldsymbol{B} \cdot \mathbf{d}\boldsymbol{A} = 0$. On the surfaces $\zeta = 0$ and $\zeta = 2\pi$, ζ is constant and can be replaced by its value, leaving only

$$= 2\pi \iint_{A\zeta=2\pi} \boldsymbol{B} \cdot \mathbf{d}\boldsymbol{A}. \tag{C.3}$$

Combining eqs. (C.1) and (C.3), one obtains

$$\Psi_\mathrm{t} = \frac{1}{2\pi}\iiint_V \nabla\zeta \cdot \boldsymbol{B}\mathrm{d}V = \frac{1}{2\pi}\iiint_V B^\zeta \mathrm{d}V. \tag{C.4}$$

Analogously, the poloidal flux is defined.

Definition of the Poloidal Flux:

$$\Psi_\mathrm{p} = \iint_{A_{\theta=\mathrm{const.}}} \boldsymbol{B}\cdot\mathrm{d}\boldsymbol{A}. \tag{C.5}$$

The area $A_{\theta=\mathrm{const.}}$ is the surface of constant θ angle, as shown in green in fig. C.1. This expression can be written as

$$\Psi_\mathrm{p} = \frac{1}{2\pi}\iiint_V \nabla\theta \cdot \boldsymbol{B}\ \mathrm{d}V = \frac{1}{2\pi}\iiint_V B^\theta \mathrm{d}V. \tag{C.6}$$

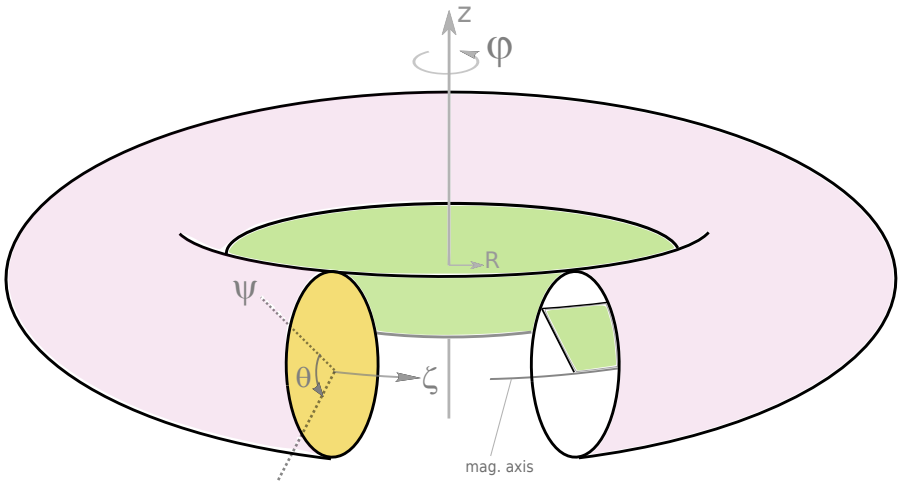

Figure C.1: *Schematic view of the torus, cylindrical (R,φ,z) and toroidal coordinate (ψ,θ,ζ) system, as well as surfaces of constant ζ (green), constant θ (orange), and constant ψ – a flux surface (pink).*

C.2 The Parallel Wave Vector $k_{\|}$ in the Cylindrical Limit

To consider the cylindrical limit of toroidal geometry, i.e. the wave equation in zeroth-order of the large-aspect ratio approximation, $a/R_{\mathrm{mag}} \ll 1$, let us assume a coordinate system as shown in fig. C.1: when bending up the torus towards a cylinder $R_{\mathrm{mag}} \to \infty$, the toroidal set of coordinates (ψ, θ, ζ) transfers to the common familiar cylindrical coordinate system $\psi \to r,\ \theta \to \varphi,\ \zeta \to z$, with z the coordinate along the magnetic axis. In this cylindrical coordinate system, the magnetic field reads

$$\begin{aligned} \boldsymbol{B} &= B_\varphi \boldsymbol{e}_\varphi + B_z \boldsymbol{e}_z \\ &= \frac{r}{R_{\mathrm{mag}}} \frac{B_z}{q}\, \boldsymbol{e}_\theta + B_z \boldsymbol{e}_z, \end{aligned} \tag{C.7}$$

as the safety factor q becomes $q = r/R_{\mathrm{mag}}\, B_z/B_\varphi$, because z equals the 'toroidal' direction, and φ the poloidal one. The factor r/R_{mag} is considered small, so one can assume the unity vector in the magnetic field direction is $\hat{\boldsymbol{b}} = \boldsymbol{B}/B \approx \boldsymbol{B}/B_z$
The parallel wave vector in this geometry can now be calculated via $\mathrm{i}k_{\|}\tilde{E}$ being the Fourier transform of $\nabla_{\|}\tilde{E} \equiv (\hat{\boldsymbol{b}} \cdot \nabla)\tilde{E}$, with $\tilde{E}$ the perturbation quantity. After executing the scalar product of $\hat{\boldsymbol{b}}$ with ∇ in cylindrical coordinates, one can directly read the expression for $k_{\|}$ as eq. (3.24):

$$\begin{aligned} \mathrm{i}k_{\|}\tilde{E} &= \hat{\boldsymbol{b}} \cdot \nabla \tilde{E} \\ &= \left(\frac{r}{qR_{\mathrm{mag}}} \boldsymbol{e}_\varphi + \boldsymbol{e}_z \right) \cdot \left(\boldsymbol{e}_r \frac{\partial}{\partial r} + \frac{1}{r} \boldsymbol{e}_\varphi \frac{\partial}{\partial \varphi} + \boldsymbol{e}_z \frac{\partial}{\partial z} \right) \tilde{E}, \end{aligned}$$

using the Fourier decomposition $\tilde{E} = \sum_m \tilde{E}_m(r) \exp(-\mathrm{i}m\varphi + \mathrm{i}n\, z/R_{\mathrm{mag}})$:

$$\mathrm{i}k_{\|m}\tilde{E} = \mathrm{i}\frac{1}{R_{\mathrm{mag}}} \left[n - \frac{m}{q} \right] \tilde{E}_m. \tag{C.8}$$

Thus, the parallel wave vector in the cylindrical limit is

$$k_{\|} = \frac{1}{R_{\mathrm{mag}}} \left(n - \frac{m}{q} \right).$$

APPENDIX D

Derivations Used for Introducing the Boozer Coordinates

D.1 A First Boozer Coordinate Representation of B

Flux coordinates are curvilinear coordinate systems, in which one of the coordinates, usually denoted ψ, the *flux label*, is constant over each flux surface. As the magnetic field lines lie within the surface, it holds[1] $\boldsymbol{B} \cdot \nabla\psi = 0$, in other words: the contravariant component of the magnetic field direction vanishes $B^\psi = 0$ and $\psi = \text{const.}$ defines a sequence of nested tori. The other two coordinates form a grid within each flux surface such that they close upon themselves once around the poloidal (θ) as well as the toroidal (ζ) direction, shown in fig. 4.2.
From these conditions, it follows for the co-variant basis vectors, using eq. (B.7):
$\boldsymbol{e}_\theta \cdot \boldsymbol{e}_\zeta = 0$ (implying $\mathfrak{g}_{\theta\zeta} = 0$) and $\boldsymbol{e}_\psi \cdot \boldsymbol{e}_\zeta = 0$ (implying $\mathfrak{g}_{\psi\zeta} = 0$).
However, one *cannot* take $\nabla\psi \cdot \nabla\theta = 0$ without losing the straightness of $\boldsymbol{B}$ lines. Therefore, $\mathfrak{g}^{\psi\theta} \neq 0$.
With these choices, it is possible, to express the magnetic field $\boldsymbol{B}$ as a composition of $\nabla\psi \times \nabla\theta$ and $\nabla\psi \times (\nabla\psi \times \nabla\theta)$, i.e. just like in eq. (4.8), but without using the $\nabla\zeta$ coordinate. The second term has been modified using eqs. (B.3a) and the metric tensor components $\mathfrak{g}_{\psi\theta} = \mathfrak{g}_{\theta\zeta} = 0$:

$$\begin{aligned}
\nabla\psi \times \nabla\zeta &= \nabla\psi \times [\boldsymbol{e}_\psi \times \boldsymbol{e}_\theta] \\
&= \nabla\psi \times [\mathfrak{g}_{\psi i}\boldsymbol{e}^i \times \mathfrak{g}_{\theta i}\boldsymbol{e}^i] \\
&= \nabla\psi \times [(\mathfrak{g}_{\psi\psi}\nabla\psi + \mathfrak{g}_{\psi\theta}\nabla\theta + 0\cdot\nabla\zeta) \times (\mathfrak{g}_{\theta\psi}\nabla\psi + \mathfrak{g}_{\theta\theta}\nabla\theta + 0\cdot\nabla\zeta)] \\
&= \nabla\psi \times (-\mathfrak{g}_{\psi\theta}^2 + \mathfrak{g}_{\psi\psi}\mathfrak{g}_{\theta\theta})(\nabla\psi \times \nabla\theta) \\
&= \text{const.}\ \nabla\psi \times (\nabla\psi \times \nabla\theta). \qquad \text{(D.1)}
\end{aligned}$$

The divergence-free nature of the magnetic field, $\nabla \cdot \boldsymbol{B} = 0$ (with the use of eqs. (B.3a)

[1] analogously: $\boldsymbol{j} \cdot \nabla\psi = 0$

and eqs. (B.6b) and (B.9)) leads to

$$
\begin{aligned}
0 &= \nabla\cdot[B_{\mathrm{h}}(\underbrace{\nabla\psi\times\nabla\theta}_{=\boldsymbol{e}_\zeta/\mathfrak{J}})] \;+\; \nabla\cdot[B_{\mathrm{O}}(\underbrace{\nabla\psi\times\nabla\theta}_{=\boldsymbol{e}_\zeta/\mathfrak{J}})\times \underbrace{\nabla\psi}_{=g^{\psi\psi}\boldsymbol{e}_\psi+g^{\psi\theta}\boldsymbol{e}_\theta+0\boldsymbol{e}_\zeta}] \\
0 &= \nabla\cdot\left[\frac{B_{\mathrm{h}}}{\mathfrak{J}}\boldsymbol{e}_\zeta\right] \;+\; \nabla\cdot\left[\frac{B_{\mathrm{O}}g^{\psi\psi}}{\mathfrak{J}}\mathfrak{J}\boldsymbol{e}^\theta - \frac{B_{\mathrm{O}}g^{\psi\theta}}{\mathfrak{J}}\mathfrak{J}\boldsymbol{e}^\psi\right] \\
0 &= \underbrace{\frac{1}{\mathfrak{J}}\frac{\partial}{\partial\zeta}B_{\mathrm{h}}}_{=0} + \nabla\cdot[B_{\mathrm{O}}g^{\psi\psi}\underbrace{\boldsymbol{e}^\theta}_{=g^{\psi\theta}\boldsymbol{e}_\psi+g^{\theta\theta}\boldsymbol{e}_\theta} - B_{\mathrm{O}}g^{\psi\theta}\underbrace{\boldsymbol{e}^\psi}_{=g^{\psi\psi}\boldsymbol{e}_\psi+g^{\theta\theta}\boldsymbol{e}_\theta}] \\
0 &= \nabla\cdot[B_{\mathrm{O}}\underbrace{(g^{\psi\psi}g^{\psi\theta}-g^{\psi\psi}g^{\psi\theta})}_{=0}\boldsymbol{e}_\psi \;+\; B_{\mathrm{O}}(g^{\psi\psi}g^{\theta\theta}-g^{\psi\theta}g^{\psi\theta})\boldsymbol{e}_\theta] \\
0 &= \frac{1}{\mathfrak{J}}\frac{\partial}{\partial\theta}[\mathfrak{J}(B_{\mathrm{O}}(\nabla\psi)^2(\nabla\theta)^2-(\nabla\theta\cdot\nabla\psi)^2)] \\
0 &= \frac{1}{\mathfrak{J}}\frac{\partial}{\partial\theta}[\mathfrak{J}B_{\mathrm{O}}(\nabla\psi\times\nabla\theta)^2] \\
&\Rightarrow\; B_{\mathrm{O}} \;=\; \frac{\Gamma(\psi)}{\mathfrak{J}(\nabla\psi\times\nabla\theta)^2}.
\end{aligned}
\tag{D.2}
$$

As mentioned above, equilibrium force balance implies $\boldsymbol{j}\cdot\nabla\psi = 0$, i.e. the plasma current is a flux function as well. Using Ampère's law $\boldsymbol{j} = \nabla\times\boldsymbol{B}$, B_{h} can be found:

$$
\begin{aligned}
0 &= (\nabla\times\boldsymbol{B})\cdot\nabla\psi = \nabla\cdot[\boldsymbol{B}\times\nabla\psi] \\
0 &= \nabla\cdot[B_{\mathrm{h}}\,(\nabla\psi\times\nabla\theta)\times\nabla\psi \;+\; B_{\mathrm{O}}\,((\nabla\psi\times\nabla\theta)\times\nabla\psi)\times\nabla\psi].
\end{aligned}
$$

The first term is analogous to the second term above.

$$
\begin{aligned}
0 &= \frac{1}{\mathfrak{J}}\frac{\partial}{\partial\theta}[\mathfrak{J}B_{\mathrm{h}}(\nabla\psi\times\nabla\theta)^2] \;+\; \nabla\cdot[\frac{B_{\mathrm{O}}}{\mathfrak{J}}g^{\psi\psi}(\underbrace{(\boldsymbol{e}_\zeta\times\boldsymbol{e}_\psi)}_{=\mathfrak{J}\boldsymbol{e}^\theta}\times\nabla\psi) + \frac{B_{\mathrm{O}}}{\mathfrak{J}}g^{\psi\theta}(\underbrace{(\boldsymbol{e}_\zeta\times\boldsymbol{e}_\theta)}_{=\mathfrak{J}\boldsymbol{e}^\psi}\times\nabla\psi)] \\
0 &= \frac{1}{\mathfrak{J}}\frac{\partial}{\partial\theta}[\mathfrak{J}B_{\mathrm{h}}(\nabla\psi\times\nabla\theta)^2] \;+\; \nabla\cdot[\frac{B_{\mathrm{O}}g^{\psi\psi}}{\mathfrak{J}}\boldsymbol{e}_\zeta + 0] \\
0 &= \frac{1}{\mathfrak{J}}\frac{\partial}{\partial\theta}[\mathfrak{J}B_{\mathrm{h}}(\nabla\psi\times\nabla\theta)^2] \;+\; \underbrace{\frac{1}{\mathfrak{J}}\frac{\partial}{\partial\zeta}[B_{\mathrm{O}}g^{\psi\psi}]}_{=0} \\
&\Rightarrow\; B_{\mathrm{h}} \;=\; \frac{g(\psi)}{\mathfrak{J}(\nabla\psi\times\nabla\theta)^2}.
\end{aligned}
\tag{D.3}
$$

With the knowledge of B_{h} and B_{O}, the magnetic field of eq. (4.10) can be written as

$$
\boldsymbol{B} = \frac{g(\psi)}{\mathfrak{J}(\nabla\psi\times\nabla\theta)^2}\,\nabla\psi\times\nabla\theta \;+\; \frac{\Gamma(\psi)}{\mathfrak{J}(\nabla\psi\times\nabla\theta)^2}\,(\nabla\psi\times\nabla\theta)\times\nabla\psi. \tag{D.4}
$$

One now chooses the poloidal flux Ψ_{p} to serve as flux label coordinate ψ, say $\psi = \Psi_{\mathrm{p}}/(2\pi)$. With this choice, the poloidal flux formula eq. (C.6) becomes

$$
\Psi_{\mathrm{p}} = \frac{1}{2\pi}\iiint_V \nabla\theta\cdot\boldsymbol{B}\;\;\mathfrak{J}\frac{\mathrm{d}\Psi_{\mathrm{p}}}{2\pi}\mathrm{d}\theta\mathrm{d}\zeta. \tag{D.5}
$$

From eq. (D.4), it can be seen that

$$\nabla\theta \cdot \boldsymbol{B} = \frac{\Gamma(\Psi_\mathrm{p})}{\mathfrak{J}}, \tag{D.6}$$

and therefore, $\mathfrak{J}$ cancels, and the angular integrations can be executed

$$\begin{aligned} \Psi_\mathrm{p} &= \frac{1}{2\pi}\int_V \Gamma(\Psi_\mathrm{p})\,\frac{\mathrm{d}\Psi_\mathrm{p}}{2\pi} 2\pi\, 2\pi \\ &\Rightarrow \Gamma(\psi) = 1. \end{aligned} \tag{D.7}$$

D.2 The Co-Variant Components of $\boldsymbol{B}$

The co-variant components of $\boldsymbol{B}$ are obtained by taking the scalar product of eq. (D.4) with the appropriate co-variant basis vector $\boldsymbol{e}_i$ (and making use of vector identities, such as eqs. (B.14) and (B.15)):

$$\begin{aligned} B_\psi &= \boldsymbol{B}\cdot\boldsymbol{e}_\psi \\ B_\psi &= \frac{1}{\mathfrak{J}(\nabla\psi\times\nabla\theta)^2}\left[g(\nabla\psi\times\nabla\theta)\cdot(\nabla\theta\times\nabla\zeta)\mathfrak{J} \;+\; 1\,[(\nabla\psi\times\nabla\theta)\times\psi]\cdot(\nabla\theta\times\nabla\zeta)\mathfrak{J}\right] \\ B_\psi &= \frac{1}{\mathfrak{J}(\nabla\psi\times\nabla\theta)^2}[g(\nabla\psi\times\nabla\theta)\cdot(\nabla\theta\times\nabla\zeta)\mathfrak{J} + \\ &\qquad + (\nabla\psi)^2\underbrace{\nabla\theta\cdot(\nabla\theta\times\nabla\zeta)}_{=0 \text{ as } \perp}\mathfrak{J} - (\nabla\theta\cdot\nabla\psi)\underbrace{\nabla\psi\cdot(\nabla\theta\times\nabla\zeta)}_{=1/\mathfrak{J}}\mathfrak{J}] \\ B_\psi &= \frac{1}{(\nabla\psi\times\nabla\theta)^2}\left[g(\nabla\psi\times\nabla\theta)\cdot(\nabla\theta\times\nabla\zeta) \;+\; \frac{\nabla\psi\cdot\nabla\theta}{\mathfrak{J}}\right]. \end{aligned} \tag{D.8}$$

Analogously, one obtains

$$\begin{aligned} B_\theta &= \boldsymbol{B}\cdot\boldsymbol{e}_\theta \\ B_\theta &= \frac{1}{(\nabla\psi\times\nabla\theta)^2}\left[g(\nabla\psi\times\nabla\theta)\cdot(\nabla\zeta\times\nabla\psi) \;+\; \frac{(\nabla\psi)^2}{\mathfrak{J}}\right], \end{aligned} \tag{D.9}$$

and very easily

$$\begin{aligned} B_\zeta &= \boldsymbol{B}\cdot\boldsymbol{e}_\zeta \\ B_\zeta &= g. \end{aligned} \tag{D.10}$$

D.3 The Contra-variant Components of $\boldsymbol{B}$

Analogously to the co-variant components, one obtains the contra-variant components of $\boldsymbol{B}$:

$$B^{\psi} = \boldsymbol{B} \cdot \nabla\psi = 0, \tag{D.11a}$$

$$B^{\theta} = \boldsymbol{B} \cdot \nabla\theta = \frac{1}{\mathfrak{J}}, \tag{D.11b}$$

$$B^{\zeta} = \boldsymbol{B} \cdot \nabla\zeta = \frac{1}{\mathfrak{J}(\nabla\psi \times \nabla\theta)^2} \left[\frac{g}{\mathfrak{J}} + (\nabla\psi \times \nabla\theta) \cdot (\nabla\psi \times \nabla\zeta) \right]. \tag{D.11c}$$

As Boozer coordinates are meant to be a type of straight field line coordinates, one wants the magnetic field lines to be straight in the $\boldsymbol{e}_\theta - \boldsymbol{e}_\zeta$ – plane, i.e. $B^\zeta / B^\theta = \text{const.}$ on one flux surface. This constant is named $q(\psi)$ in the following. The B^ζ component becomes then quite simple, using eq. (D.11b) in $B^\zeta = q\, B^\theta$:

$$B^{\zeta} = \frac{q}{\mathfrak{J}}.$$

Inserting eq. (D.11c) on the left side, one obtains

$$(\nabla\psi \times \nabla\theta) \cdot (\nabla\psi \times \nabla\zeta) = \frac{g}{\mathfrak{J}} - q(\nabla\psi \times \nabla\theta)^2. \tag{D.12}$$

Substituting this equation, eq. (D.12), and B^2, eq. (4.14), into the equation for B_θ, eq. (D.9), one obtains

$$B_\theta = I, \tag{D.13}$$

if I is defined as

$$I := \mathfrak{J} B^2 \; - \; qg. \tag{D.14}$$

D.4 Physical Meaning of the Co-variant Components of $\boldsymbol{B}$

To learn about the physical meaning of the angular co-variant components of $\boldsymbol{B}$, it is useful to compute the currents flowing in the device. According to Ampère's law, the current density is $\boldsymbol{j} = 1/\mu_0 \nabla \times \boldsymbol{B}$. Using eq. (4.20) and the curl in curvilinear coordinate systems, eq. (B.10), one obtains:

$$\boldsymbol{j} = \frac{1}{\mu_0}\left(\frac{\partial \delta}{\partial \theta}\nabla\theta \times \nabla\psi + \frac{\partial I}{\partial \psi}\nabla\psi \times \nabla\theta + \frac{\partial g}{\partial \psi}\nabla\psi \times \nabla\zeta\right). \tag{D.15}$$

Note: one can see very easily, that $\boldsymbol{j} \cdot \nabla\psi = 0$ is fulfilled.
The current penetrating one poloidal cross section $A_{\zeta=\text{const.}}$ (see orange area in fig. C.1) leads to the total toroidal current I_t:

$$\begin{aligned} I_\text{t} &= \iint \boldsymbol{j} \cdot \mathrm{d}\boldsymbol{A}_{\zeta=\text{const.}} = \frac{1}{\mu_0}\iint \nabla \times \boldsymbol{B} \cdot \mathrm{d}\boldsymbol{A}_{\zeta=\text{const.}} \\ &= \frac{1}{\mu_0}\int_{\psi,\zeta=\text{const.}} \boldsymbol{B} \cdot \mathrm{d}\boldsymbol{l} && \text{(Stoke's theorem)} \\ &= \frac{1}{\mu_0}\int_{\psi,\zeta=\text{const.}} \left[\delta\nabla\psi - I\nabla\theta + g\nabla\zeta\right] \cdot \boldsymbol{e}_\theta \mathrm{d}\theta && \text{(now use } \boldsymbol{e}^i \cdot \boldsymbol{e}_j = \delta^i_j\text{)} \\ I_\text{t}(\psi) &= \frac{2\pi}{\mu_0} I(\psi) \end{aligned} \tag{D.16}$$

Thus, I is closely related to the toroidal current within the flux surface.

Analogously, one can calculate the current penetrating one toroidal surface $A_{\theta=\text{const.}}$ (see green area in fig. C.1), leading to the total poloidal current I_p :

$$I_\text{p}(\psi) = \frac{2\pi}{\mu_0} g(\psi) \tag{D.17}$$

D.5 Straight Field Lines and q Factor

Calculating the toroidal magnetic flux according to eq. (C.4) reveals

$$\begin{aligned}\Psi_\mathrm{t} &= \frac{1}{2\pi}\iiint_V \frac{q(\psi)}{\mathfrak{J}}\mathfrak{J}\mathrm{d}\psi\mathrm{d}\theta\mathrm{d}\zeta \\ &= \frac{1}{2\pi}\int_V q(\psi)\,\frac{\mathrm{d}\Psi_\mathrm{p}}{2\pi}2\pi\,2\pi \\ \Rightarrow q(\psi) &= \frac{\mathrm{d}\Psi_\mathrm{t}}{\mathrm{d}\Psi_\mathrm{p}}\end{aligned} \tag{D.18}$$

Thus, the constant $q = B^\zeta/B^\theta$ is the familiar safety factor of eq. (2.4) in Boozer coordinates.

D.6 Vector Potential in Contra-variant Representation

With this representation of $\boldsymbol{B}$, it can be shown, that the following expression is valid as vector potential $\boldsymbol{A}$:

$$\boldsymbol{A} = \frac{\Psi_\mathrm{t}}{2\pi}\nabla\theta - \underbrace{\frac{\Psi_\mathrm{p}}{2\pi}}_{=:\psi}\nabla\zeta. \tag{D.19}$$

This is proved, using the curl in curvilinear coordinate systems, eq. (B.10):

$$\begin{aligned}&\boldsymbol{B} = \nabla\times\boldsymbol{A} \\ &\boldsymbol{B} = \underbrace{\frac{\partial\Psi_\mathrm{t}}{\partial\zeta}}_{=0}(\nabla\zeta\times\nabla\theta) + \underbrace{\frac{1}{2\pi}\frac{\partial\Psi_\mathrm{t}}{\partial\psi}}_{=q}(\nabla\psi\times\nabla\theta) - \underbrace{\frac{\partial\psi}{\partial\psi}}_{=1}(\nabla\psi\times\nabla\zeta) + \underbrace{\frac{\partial\psi}{\partial\zeta}}_{=0}(\nabla\theta\times\nabla\zeta) \\ &\boldsymbol{B} = \nabla\zeta\times\nabla\psi + q(\nabla\psi\times\nabla\theta).\end{aligned} \tag{D.20}$$

APPENDIX E

The Driftkinetic Lagrangian

E.1 Gyro-averaging the Driftkinetic Lagrangian

In chapter 2 and chapter 4, the driftkinetic particle Lagrangian is introduced.
As it is not necessary to retain the fast gyromotion within the equations, an averaging over the gyroangle is performed, indicated by '<>'. This so called *gyro-averaging* reduces the phase-space coordinates by eliminating the gyroangle ξ. The averaging within the Lagrangian yields

$$\begin{aligned}\mathscr{L} = e\underbrace{<\boldsymbol{A}(\boldsymbol{R})\cdot\dot{\boldsymbol{R}}>}_{\text{independent of }\xi} + e\underbrace{<(\rho\cdot\nabla)\boldsymbol{A}(\boldsymbol{R})\cdot\dot{\boldsymbol{R}}>}_{=0\ \text{(eq. (E.2))}} + e\underbrace{<\boldsymbol{A}(\boldsymbol{R})\cdot\dot{\boldsymbol{\rho}}>}_{=0\ \text{(eq. (E.3))}} + \underbrace{e<(\boldsymbol{\rho}\cdot\nabla)\boldsymbol{A}(\boldsymbol{R})\cdot\dot{\boldsymbol{\rho}}>}_{=-\mu B/\Omega\ \dot{\xi}\ \text{(eq. (E.4))}} \\ + \underbrace{m<\boldsymbol{v}\cdot\dot{\boldsymbol{R}}>}_{=mv_\parallel^2\hat{\boldsymbol{b}}\cdot\boldsymbol{R}\ \text{(eq. (E.6))}} + \underbrace{m<\boldsymbol{v}\cdot\dot{\boldsymbol{\rho}}>}_{=2\mu B/\Omega\ \dot{\xi}\ \text{(eq. (E.5))}} - \frac{1}{2}m\underbrace{<v_\parallel^2>}_{\text{indep. of }\xi} - \underbrace{<\mu B>}_{\text{indep. of }\xi} - e\underbrace{<\Phi(\boldsymbol{R})>}_{\text{indep. of }\xi}.\end{aligned} \tag{E.1}$$

The first and the three last terms are independent of ξ, and thus, the averaging brackets are obsolete. For the remaining terms, the averaging is performed in the following:

$$\begin{aligned}<(\rho\cdot\nabla)\boldsymbol{A}(\boldsymbol{R})\cdot\dot{\boldsymbol{R}}> &= \left\langle \rho\left[\begin{pmatrix}\cos\xi\\ \sin\xi\\ 0\end{pmatrix}\cdot\begin{pmatrix}\partial_x\\ \partial_y\\ \partial_z\end{pmatrix}\right]\begin{pmatrix}A_x\\ A_y\\ A_z\end{pmatrix}\cdot\begin{pmatrix}\dot{R}_x\\ \dot{R}_y\\ \dot{R}_z\end{pmatrix}\right\rangle \\ &= \rho[\underbrace{<\cos\xi>}_{=0}\partial_x A_z + \underbrace{<\sin\xi>}_{=0}\partial_y A_z]\,\dot{\boldsymbol{R}} \\ &= 0,\end{aligned} \tag{E.2}$$

$$\begin{aligned}<\boldsymbol{A}(\boldsymbol{R})\cdot\dot{\boldsymbol{\rho}}> &= \left\langle\begin{pmatrix}A_x\\ A_y\\ A_z\end{pmatrix}\cdot\begin{pmatrix}-\sin\xi\\ \cos\xi\\ 0\end{pmatrix}\rho\dot{\xi}\right\rangle \\ &= -A_x\underbrace{<\sin\xi>}_{=0}\rho\dot{\xi} + A_y\underbrace{<\cos\xi>}_{=0}\rho\dot{\xi} \\ &= 0,\end{aligned} \tag{E.3}$$

$$
\begin{aligned}
e<(\boldsymbol{\rho}\cdot\nabla)\boldsymbol{A}(\boldsymbol{R})\cdot\dot{\boldsymbol{\rho}}> &= e\left\langle \rho\left[\left(\begin{pmatrix}\cos\xi\\ \sin\xi\\ 0\end{pmatrix}\cdot\begin{pmatrix}\partial_x\\ \partial_y\\ \partial_z\end{pmatrix}\right)\begin{pmatrix}A_x\\ A_y\\ A_z\end{pmatrix}\right]\cdot\begin{pmatrix}-\sin\xi\\ \cos\xi\\ 0\end{pmatrix}\rho\dot{\xi}\right\rangle \\
&= e<\rho^2\dot{\xi}\,[-\underbrace{<\sin\xi\cos\xi>}_{=0}\partial_x A_x \;+\; \underbrace{<\cos^2>}_{=1/2}\partial_x A_y \\
&\qquad -\underbrace{<\sin^2\xi>}_{=1/2}\partial_y A_x \;+\; \underbrace{<\sin\xi\cos\xi>}_{=0}\partial_y A_y]> \\
&= e<\frac{1}{2}\rho^2\dot{\xi}\underbrace{(\partial_y A_x-\partial_x A_y)}_{=-B_z}> \\
&= -\frac{\mu B}{\Omega}\dot{\xi}, \qquad\qquad (E.4)
\end{aligned}
$$

$$
\begin{aligned}
m<\boldsymbol{v}\cdot\dot{\boldsymbol{\rho}}> &= m\left\langle\begin{pmatrix}v_x\\ v_y\\ v_\parallel\end{pmatrix}\cdot\begin{pmatrix}-\sin\xi\\ \cos\xi\\ 0\end{pmatrix}\rho\dot{\xi}\right\rangle \\
&= m<\boldsymbol{v}_\perp\rho\dot{\xi}> = m<\boldsymbol{v}_\perp^2/\Omega\,\dot{\xi}> \\
&= 2\frac{\mu B}{\Omega}\,\dot{\xi}, \qquad\qquad (E.5)
\end{aligned}
$$

$$
\begin{aligned}
m<\boldsymbol{v}\cdot\dot{\boldsymbol{R}}> &= m<v_\parallel>\hat{\boldsymbol{b}}\cdot\dot{\boldsymbol{R}} \;+\; m\underbrace{<\boldsymbol{v}_\perp>}_{=0}\cdot\dot{\boldsymbol{R}} \\
&= mv_\parallel\hat{\boldsymbol{b}}\cdot\dot{\boldsymbol{R}}. \qquad\qquad (E.6)
\end{aligned}
$$

The vector $\hat{\boldsymbol{b}}=\boldsymbol{B}/B$ is a unit vector in the direction of the equilibrium magnetic field. This leads to a Lagrangian of the form

$$
\mathscr{L} \;=\; (mv_\parallel\hat{\boldsymbol{b}} \;+\; e\boldsymbol{A}(\boldsymbol{R}))\cdot\dot{\boldsymbol{R}} \;+\; \frac{\mu B}{\Omega}\dot{\xi} \;-\; \frac{1}{2}mv_\parallel^2 \;-\; \mu B \;-\; e\Phi(\boldsymbol{R}). \qquad (E.7)
$$

E.2 The Equations of Motion for the Guiding Center

The driftkinetic equations of motion for the guiding center $\boldsymbol{R}$ can be obtained via the Euler-Lagrange method:

$$
0=\frac{\mathrm{d}}{\mathrm{d}t}\frac{\partial\mathscr{L}}{\partial\dot{\boldsymbol{R}}}-\frac{\partial\mathscr{L}}{\partial\boldsymbol{R}}. \qquad (E.8)
$$

With the driftkinetic Lagrangian, eq. (E.7), one calculates

$$
0=\frac{\mathrm{d}}{\mathrm{d}t}\left(mv_\parallel\hat{\boldsymbol{b}}+e\boldsymbol{A}\right)-mv_\parallel\frac{\partial}{\partial\boldsymbol{R}}\left(\dot{\boldsymbol{R}}\cdot\hat{\boldsymbol{b}}\right)-e\frac{\partial}{\partial\boldsymbol{R}}\left(\dot{\boldsymbol{R}}\cdot\boldsymbol{A}\right)+\mu\frac{\partial B}{\partial\boldsymbol{R}}+e\frac{\partial\Phi}{\partial\boldsymbol{R}},
$$

and with the magnetic field assumed temporarily constant, the time derivation applies on the quantities $x = v_\parallel$, $\boldsymbol{A}$, and $\boldsymbol{R}$ according to the chain rule $\mathrm{d}x/\mathrm{d}t = \dot{x} + \partial x/\partial \boldsymbol{R}\,\dot{\boldsymbol{R}}$. With the potential definition $\boldsymbol{E} = e\nabla\Phi + e\dot{\boldsymbol{A}}$, above equation becomes

$$0 = m\dot{v}_\parallel \hat{\boldsymbol{b}} + e(\dot{\boldsymbol{R}}\cdot\nabla)\boldsymbol{A}^* - e\boldsymbol{E} - e\nabla(\dot{\boldsymbol{R}}\cdot\boldsymbol{A}^*) + \mu\nabla B,$$

where the modified vector potential was introduced as

$$\boldsymbol{A}^* := m/e\; v_\parallel \hat{\boldsymbol{b}} + \boldsymbol{A}. \tag{E.9}$$

After expanding the gradient of the scalar product (with eq. (B.16), where, since $\dot{\boldsymbol{R}}$ is not a field, the 1st and 3rd term on the right hand side vanish) and with defining

$$\begin{aligned} \boldsymbol{B}^* &:= \nabla\times\boldsymbol{A}^* \\ \boldsymbol{B}^* &= \boldsymbol{B} + \frac{mv_\parallel}{e}(\nabla\times\hat{\boldsymbol{b}}), \end{aligned} \tag{E.10}$$

one obtains

$$0 = m\dot{v}_\parallel \hat{\boldsymbol{b}} - e\dot{\boldsymbol{R}}\times\boldsymbol{B}^* - e\boldsymbol{E} + \mu\nabla B. \tag{E.11}$$

This equation is multiplied by $\hat{\boldsymbol{b}}\times$ on both sides. Expanding the triple cross product (eq. (B.15)), one can solve for $\dot{\boldsymbol{R}}$:

$$\dot{\boldsymbol{R}} = \frac{1}{B_\parallel^*} v_\parallel \boldsymbol{B}^* + \frac{1}{B_\parallel^*}\left(\frac{1}{B}\boldsymbol{E}\times\boldsymbol{B} + \frac{\mu}{e}\hat{\boldsymbol{b}}\times\nabla B\right)$$

(where $B_\parallel^* := \hat{\boldsymbol{b}}\cdot\boldsymbol{B}^*$). The remaining $\boldsymbol{B}^*$ in the nominator is split into its parallel and perpendicular part, $\boldsymbol{B}^* = B_\parallel^*\hat{\boldsymbol{b}} + mv_\parallel/e(\nabla\times\hat{\boldsymbol{b}})_\perp$, where it was used, that $\boldsymbol{B}_\perp = 0$. Substituted into the previous equation yields

$$\dot{\boldsymbol{R}} = v_\parallel\hat{\boldsymbol{b}} + \frac{B}{B_\parallel^*}\left(\frac{1}{B^2}\boldsymbol{E}\times\boldsymbol{B} + \frac{\mu}{eB^2}\boldsymbol{B}\times\nabla B + \frac{mv_\parallel^2}{eB}(\nabla\times\hat{\boldsymbol{b}})_\perp\right),$$

which is the equation of motion for the guiding center position. It consists of a part parallel to the magnetic field (first term), and a 'drift' part (terms in bracket). The drifts are called as follows:

$$\mathrm{E}-\mathrm{cross}-\mathrm{B\ drift}: \qquad \boldsymbol{v}_{\mathrm{E}\times\mathrm{B}} = \frac{1}{B^2}\boldsymbol{E}\times\boldsymbol{B}, \tag{E.12a}$$

$$\mathrm{grad}-\mathrm{B\ drift}: \qquad \boldsymbol{v}_{\nabla\mathrm{B}} = \frac{\mu}{eB^3}\boldsymbol{B}\times\nabla B, \tag{E.12b}$$

$$\mathrm{curvature\ drift}: \qquad \boldsymbol{v}_{\mathrm{curv}} = \frac{mv_\parallel^2}{eB^4}\boldsymbol{B}\times(\boldsymbol{B}\cdot\nabla)\boldsymbol{B} \;\equiv\; -\frac{m\boldsymbol{v}_\parallel^2}{eB^3}(\nabla B\times\boldsymbol{B}). \tag{E.12c}$$

For the curvature drift, it was used that $(\nabla\times\hat{\boldsymbol{b}})_\perp = \hat{\boldsymbol{b}}\times(\hat{\boldsymbol{b}}\cdot\nabla)\hat{\boldsymbol{b}}$, which results from $\hat{\boldsymbol{b}}$ being a unit vector, thus $0 = \nabla(\hat{\boldsymbol{b}}\cdot\hat{\boldsymbol{b}}) = (\hat{\boldsymbol{b}}\cdot\nabla\hat{\boldsymbol{b}}) + \hat{\boldsymbol{b}}\times(\nabla\times\hat{\boldsymbol{b}})$ (used eq. (B.16)). This

equation is then multiplied with $\hat{\boldsymbol{b}}\times$ and after eq. (B.14), only the perpendicular terms remain. Therefore, it is

$$\begin{aligned}(\nabla\times\hat{\boldsymbol{b}})_\perp &\overset{eq.\,(B.11)}{=} \hat{\boldsymbol{b}}\times(\hat{\boldsymbol{b}}\cdot\nabla)\hat{\boldsymbol{b}}\\ &= \frac{1}{B^2}\,\boldsymbol{B}\times(\boldsymbol{B}\cdot\nabla)\frac{\boldsymbol{B}}{B}\\ &= \frac{1}{B^2}\,\boldsymbol{B}\times(\boldsymbol{B}\cdot\nabla)\boldsymbol{B} + \frac{1}{B^2}\,\underbrace{\boldsymbol{B}\times(\boldsymbol{B}\,(\boldsymbol{B}\cdot\nabla)\frac{1}{B})}_{=0 \text{ as } \parallel}.\end{aligned}$$

The alternative formulation for the curvature drift is derived in the following:

$$\begin{aligned}(\nabla\times\hat{\boldsymbol{b}})_\perp &= (\nabla\times\boldsymbol{B}/B)_\perp\\ &= \left(\frac{1}{B}(\nabla\times\boldsymbol{B}) + \boldsymbol{B}\times\frac{1}{B^2}\nabla B\right)_\perp,\end{aligned}$$

which is, after using Ampère's law $\nabla\times\boldsymbol{B}=\mu_0\boldsymbol{j}$,

$$\overset{eq.\,(B.11)}{=} -\hat{\boldsymbol{b}}\times\left[\hat{\boldsymbol{b}}\times\left(\frac{\mu_0\boldsymbol{j}}{B}+\frac{1}{B}\hat{\boldsymbol{b}}\times\nabla B\right)\right].$$

With the static MHD equilibrium condition eq. (3.1b), $\boldsymbol{j}\times\boldsymbol{B}=\nabla p$, this reads

$$\overset{eq.\,(B.14)}{=} \hat{\boldsymbol{b}}\times\frac{\mu_0\nabla p}{B^2}+\hat{\boldsymbol{b}}\times\frac{\nabla B}{B},$$

and after using the definition of β eq. (3.15):

$$= \frac{\beta}{2}\,\frac{\boldsymbol{B}}{B}\times\frac{\nabla p}{p}+\frac{1}{B^2}\boldsymbol{B}\times\nabla B. \tag{E.13}$$

For low-β scenarios, the first term is negligible.

The equation of motion for the guiding center velocity can be derived either from the particle's energy conservation, $\mathrm{d}/\mathrm{d}t(m/2v_\parallel^2+\mu B+e\Phi)=0$, or from eq. (E.11) as well, by multiplying $\dot{\boldsymbol{R}}$ onto it: with $\dot{\boldsymbol{R}}\cdot\hat{\boldsymbol{b}}$, this gives

$$\dot{v}_\parallel = \frac{\dot{\boldsymbol{R}}}{mv_\parallel}\left(e\boldsymbol{E}-\mu\nabla B\right). \tag{E.14}$$

APPENDIX F

Calculating the Derivatives of ψ_p and $\rho_{\|}$

Note: g, I and ψ_t are flux coordinates, and thus functions of ψ_p alone.
ψ_p in turn depends, as well as $\rho_{\|}$, on θ, ζ, p_θ and p_ζ:
$\psi_p = \psi_p(\theta, \zeta, p_\theta, p_\zeta)$ and $\rho_{\|} = \rho_{\|}(\theta, \zeta, p_\theta, p_\zeta)$.
Furthermore, for canonical variables, it holds:

$$\frac{\partial q_i}{q^j} = \delta_i^j, \qquad \frac{\partial p_i}{p^j} = \delta_i^j, \qquad \frac{\partial p_i}{q^j} = \frac{\partial q_i}{p^j} = 0. \tag{F.1}$$

Here, it is $q_i \in [\theta, \zeta, \xi]$ and $p_i \in [p_\theta, p_\zeta, p_\xi]$.
The prime $'$ indicates a derivation with respect to ψ_p.

F.1 The derivatives of ψ_p

To calculate the derivatives of ψ_p with respect to θ, ζ, p_θ and p_ζ, one starts from eq. (4.47), which is obtained out of the expressions for the canonical momenta, eqs. (4.45):

$$g(p_\theta - e\psi_t - e\tilde{A}_\theta) = I(p_\zeta + e\psi_p - e\tilde{A}_\zeta).$$

In the following, the total derivative of this expression **with respect to** θ is performed and solved for the derivative of ψ_p:

$$\begin{aligned} &g' \frac{\partial \psi_p}{\partial \theta} \left(p_\theta - e\psi_t - e\tilde{A}_\theta\right) + g\left(0 - e\frac{\partial \psi_t}{\partial \psi_p}\frac{\partial \psi_p}{\partial \theta} - e\frac{\partial \tilde{A}_\theta}{\partial \theta} - e\tilde{A}'_\theta \frac{\partial \psi_p}{\partial \theta}\right) \\ &= I' \frac{\partial \psi_p}{\partial \theta} \left(p_\zeta + e\psi_p - e\tilde{A}_\zeta\right) + I\left(0 - e\frac{\partial \psi_p}{\partial \theta} - e\frac{\partial \tilde{A}_\zeta}{\partial \theta} - e\tilde{A}'_\zeta \frac{\partial \psi_p}{\partial \theta}\right). \end{aligned} \tag{F.2}$$

Knowing that the safety factor q in Boozer coordinates reads

$$q = \frac{\partial \psi_t}{\partial \psi_p}, \tag{F.3}$$

and re-arranging the terms, one obtains

$$\begin{aligned} &\frac{\partial \psi_p}{\partial \theta}\left[g'(p_\theta - e\psi_t - e\tilde{A}_\theta) + eg(-q - \tilde{A}'_\theta)\right] - eg\frac{\partial \tilde{A}_\theta}{\partial \theta} \\ &= \frac{\partial \psi_p}{\partial \theta}\left[I'(p_\zeta + e\psi_p - e\tilde{A}_\zeta) + eI(1 - \tilde{A}'_\zeta)\right] - eI\frac{\partial \tilde{A}_\zeta}{\partial \theta}. \end{aligned} \tag{F.4}$$

From the expression for the conjugate momenta, eqs. (4.45), one knows, that $(p_\theta - e\psi_t - e\tilde{A}_\theta) = e\rho_\parallel g$ and $(p_\zeta + e\psi_p - e\tilde{A}_\zeta) = e\rho_\parallel I$.

$$\frac{\partial \psi_p}{\partial \theta}\left[\rho_\parallel(gI' - g'I) + I + qg - I\tilde{A}'_\zeta + g\tilde{A}'_\theta\right] = \left[I\frac{\partial \tilde{A}_\zeta}{\partial \theta} - g\frac{\partial \tilde{A}_\theta}{\partial \zeta}\right]. \tag{F.5}$$

Now, it is useful, to define

$$D \equiv \rho_\parallel(gI' - g'I) + I + qg - I\tilde{A}'_\zeta + g\tilde{A}'_\theta.$$

Thus, one obtains

$$\frac{\partial \psi_p}{\partial \theta} = \frac{1}{D}\left[I\frac{\partial \tilde{A}_\zeta}{\partial \theta} - g\frac{\partial \tilde{A}_\theta}{\partial \theta}\right]. \tag{F.6}$$

Analogously, the derivation **with respect to** ζ leads to:

$$\frac{\partial \psi_p}{\partial \zeta} = \frac{1}{D}\left[I\frac{\partial \tilde{A}_\zeta}{\partial \zeta} - g\frac{\partial \tilde{A}_\theta}{\partial \zeta}\right] \tag{F.7}$$

The the derivation **with respect to** p_θ leads to:

$$\begin{aligned} &g'\frac{\partial \psi_p}{\partial p_\theta}\underbrace{(p_\theta - e\psi_t - e\tilde{A}_\theta)}_{=e\rho_\parallel I} + g(1-0-0) + g(0 - e\underbrace{\frac{\partial \psi_t}{\partial \psi_p}}_{=q}\frac{\partial \psi_p}{\partial p_\theta} - e\tilde{A}'_\theta\frac{\partial \psi_p}{\partial p_\theta}) \\ &= I'\frac{\partial \psi_p}{\partial p_\theta}\underbrace{(p_\zeta + e\psi_p - e\tilde{A}_\zeta)}_{=e\rho_\parallel g} - I(0-0-0) + I(0 + e\underbrace{\frac{\partial \psi_p}{\partial \psi_p}}_{=1}\frac{\partial \psi_p}{\partial p_\theta} - e\tilde{A}'_\zeta\frac{\partial \psi_p}{\partial p_\theta}) \end{aligned} \tag{F.8}$$

$$\Leftrightarrow \frac{\partial \psi_p}{\partial p_\theta} e\underbrace{[\rho_\parallel(gI' - g'I) + I + qg - I\tilde{A}'_\zeta + g\tilde{A}'_\theta]}_{=D} = g \tag{F.9}$$

Resulting in

$$\frac{\partial \psi_p}{\partial p_\theta} = \frac{g}{eD}. \tag{F.10}$$

The the derivation **with respect to** p_ζ is performed analogously, giving

$$\frac{\partial \psi_p}{\partial p_\zeta} = -\frac{I}{eD}. \tag{F.11}$$

Summarized, it was found:

$$\frac{\partial \psi_\mathrm{p}}{\partial \theta} = \frac{1}{D}\left[I\frac{\partial \tilde{A}_\zeta}{\partial \theta} - g\frac{\partial \tilde{A}_\theta}{\partial \theta}\right], \tag{F.12a}$$

$$\frac{\partial \psi_\mathrm{p}}{\partial \zeta} = \frac{1}{D}\left[I\frac{\partial \tilde{A}_\zeta}{\partial \zeta} - g\frac{\partial \tilde{A}_\theta}{\partial \zeta}\right], \tag{F.12b}$$

$$\frac{\partial \psi_\mathrm{p}}{\partial P_\theta} = \frac{g}{eD}, \tag{F.12c}$$

$$\frac{\partial \psi_\mathrm{p}}{\partial P_\zeta} = -\frac{I}{eD}. \tag{F.12d}$$

F.2 The derivatives of $\rho_\parallel$

One can start from the expressions for the canonical momenta, eqs. (4.45):

$$\begin{aligned} p_\theta &= e\rho_\parallel I + e\psi_t + e\tilde{A}_\theta, \\ p_\zeta &= e\rho_\parallel g - e\psi_p + e\tilde{A}_\zeta, \\ p_\xi &= \mu. \end{aligned}$$

Differentiation of the first **with respect to** θ gives:

$$\underbrace{\frac{\partial p_\theta}{\partial \theta}}_{=0} = e(\frac{\partial \rho_\parallel}{\partial \theta} I + \rho_\parallel I' \frac{\partial \psi_p}{\partial \theta} + \underbrace{\frac{\partial \psi_t}{\partial \psi_p}}_{=q} \underbrace{\frac{\partial \psi_p}{\partial \theta}}_{\text{use eq. (F.12a)}} + \frac{\partial \tilde{A}_\theta}{\partial \theta} + \tilde{A}'_\theta \frac{\partial \psi_p}{\partial \theta})$$

$$-I\frac{\partial p_\theta}{\partial \theta} = (q + \rho_\parallel I' + \tilde{A}'_\theta)\left[\frac{1}{D} I\frac{\partial \tilde{A}_\zeta}{\partial \theta} - g\frac{\partial \tilde{A}_\theta}{\partial \theta}\right] + \frac{\partial \tilde{A}_\theta}{\partial \theta}$$

$$-I\frac{\partial p_\theta}{\partial \theta} = \frac{1}{D}\left[(qI + \rho_\parallel I' I + I\tilde{A}'_\theta)\frac{\partial \tilde{A}_\zeta}{\partial \theta} - (qg + \rho_\parallel I' g + g\tilde{A}'_\theta - D)\frac{\partial \tilde{A}_\theta}{\partial \theta}\right]. \tag{F.13}$$

Filling in D leads to

$$\frac{\partial \rho_\parallel}{\partial \theta} = \frac{-1}{D}\left[\left(1 - \rho_\parallel g' - \tilde{A}'_\zeta\right)\frac{\partial \tilde{A}_\theta}{\partial \theta} + \left(q + \rho_\parallel I' + \tilde{A}'_\theta\right)\frac{\partial \tilde{A}_\zeta}{\partial \theta}\right]. \tag{F.14}$$

Differentiating analogously the second momentum, eq. (4.45b) **with respect to** ζ gives:

$$\frac{\partial \rho_\parallel}{\partial \zeta} = \frac{-1}{D}\left[\left(1 - \rho_\parallel g' - \tilde{A}'_\zeta\right)\frac{\partial \tilde{A}_\theta}{\partial \zeta} + \left(q + \rho_\parallel I' + \tilde{A}'_\theta\right)\frac{\partial \tilde{A}_\zeta}{\partial \zeta}\right]. \tag{F.15}$$

Differentiating again the first momentum, eq. (4.45a) **with respect to** p_θ reads:

$$\underbrace{\frac{\partial p_\theta}{\partial p_\theta}}_{=1} = e(\frac{\partial \rho_\parallel}{\partial p_\theta} I + \rho_\parallel I' \frac{\partial \psi_p}{\partial p_\theta} + \underbrace{\frac{\partial \psi_t}{\partial \psi_p}}_{=q} \underbrace{\frac{\partial \psi_p}{\partial p_\theta}}_{\text{use eq. (F.12c)}} + \tilde{A}'_\theta \frac{\partial \psi_p}{\partial p_\theta})$$

$$eI\frac{\partial \rho_\parallel}{\partial p_\theta} = \frac{1}{D}(D - \rho_\parallel I' g - gq - \tilde{A}'_\theta g). \tag{F.16}$$

Filling in D in the numerator leads to

$$\frac{\partial \rho_\parallel}{\partial p_\theta} = \frac{1}{eD}\left[1 - \rho_\parallel g' - \tilde{A}'_\zeta\right]. \tag{F.17}$$

Analogously differentiating the second momentum, eq. (4.45b) **with respect to** p_ζ gives:

$$\frac{\partial \rho_\parallel}{\partial p_\zeta} = \frac{1}{eD}\left[q + \rho_\parallel I' + \tilde{A}'_\theta\right]. \tag{F.18}$$

Summarized, it was found:

$$\frac{\partial \rho_\parallel}{\partial \theta} = \frac{-1}{D}\left[\left(1 - \rho_\parallel g' - \tilde{A}'_\zeta\right)\frac{\partial \tilde{A}_\theta}{\partial \theta} + \left(q + \rho_\parallel I' + \tilde{A}'_\theta\right)\frac{\partial \tilde{A}_\zeta}{\partial \theta}\right], \tag{F.19a}$$

$$\frac{\partial \rho_\parallel}{\partial \zeta} = \frac{-1}{D}\left[\left(1 - \rho_\parallel g' - \tilde{A}'_\zeta\right)\frac{\partial \tilde{A}_\theta}{\partial \zeta} + \left(q + \rho_\parallel I' + \tilde{A}'_\theta\right)\frac{\partial \tilde{A}_\zeta}{\partial \zeta}\right], \tag{F.19b}$$

$$\frac{\partial \rho_\parallel}{\partial p_\theta} = \frac{1}{eD}\left[1 - \rho_\parallel g' - \tilde{A}'_\zeta\right], \tag{F.19c}$$

$$\frac{\partial \rho_\parallel}{\partial p_\zeta} = \frac{1}{eD}\left[q + \rho_\parallel I' + \tilde{A}'_\theta\right]. \tag{F.19d}$$

F.3 Derivation of the Equations of Motion for the Guiding Center

Having derived the partial derivatives of ψ_p and $\rho_\parallel$ with respect to the canonical variables $x = \theta, \zeta, p_\theta$ and p_ζ, it is now possible, to obtain the equations of motion via the Hamiltonian formalism, as recalled in eq. (4.46), using the chain rule:

$$\frac{\partial \mathscr{H}}{\partial x} = \frac{\partial \mathscr{H}}{\partial \psi_\mathrm{p}}\frac{\partial \psi_\mathrm{p}}{\partial x} + \frac{\partial \mathscr{H}}{\partial \rho_\parallel}\frac{\partial \rho_\parallel}{\partial x}. \tag{F.20}$$

Beginning with the differentiation of the Hamiltonian, eq. (4.43), with respect to $x = \theta$, using eq. (F.12a) and eq. (F.19a):

$$\dot{p}_\theta = -\left[(\rho_\parallel^2 B + \mu)B' + \tilde{\Phi}'\right]\frac{\partial \psi_\mathrm{p}}{\partial \theta} \tag{F.21}$$

$$- \rho_\parallel B^2 \frac{1}{D}\left[-\left(1 - \rho_\parallel g' - \tilde{A}'_\zeta\right)\frac{\partial \tilde{A}_\theta}{\partial \theta} - \left(q + \rho_\parallel I' + \tilde{A}'_\theta\right)\frac{\partial \tilde{A}_\zeta}{\partial \theta}\right], \tag{F.22}$$

using the dependency of the fields on θ,

$$B' = \frac{\partial B}{\partial \psi_\mathrm{p}} = \frac{\partial B}{\partial \theta}\frac{\partial \theta}{\partial \psi_\mathrm{p}} \qquad \tilde{\Phi}' = \frac{\partial \tilde{\Phi}}{\partial \psi_\mathrm{p}} = \frac{\partial \tilde{\Phi}}{\partial \theta}\frac{\partial \theta}{\partial \psi_\mathrm{p}}, \tag{F.23}$$

one obtains

$$\dot{p}_\theta = -(\rho_\parallel^2 B + \mu)\frac{\partial B}{\partial \theta} - \frac{\partial \tilde{\Phi}}{\partial \theta} + \rho_\parallel B^2 \frac{1}{D}\left[\left(1 - \rho_\parallel g' - \tilde{A}'_\zeta\right)\frac{\partial \tilde{A}_\theta}{\partial \theta} + \left(q + \rho_\parallel I' + \tilde{A}'_\theta\right)\frac{\partial \tilde{A}_\zeta}{\partial \theta}\right]. \tag{F.24}$$

The differentiation of the Hamiltonian with respect to $x = \zeta$, using eq. (F.12b) and eq. (F.19b) is exactly analogous, except for the vanishing of one term due to $\partial B/\partial \zeta = 0$ (assumption of toroidal symmetry of the magnetic field):

$$\dot{p}_\zeta = -\frac{\partial \tilde{\Phi}}{\partial \zeta} + \rho_\parallel B^2 \frac{1}{D}\left[\left(1 - \rho_\parallel g' - \tilde{A}'_\zeta\right)\frac{\partial \tilde{A}_\theta}{\partial \zeta} + \left(q + \rho_\parallel I' + \tilde{A}'_\theta\right)\frac{\partial \tilde{A}_\zeta}{\partial \zeta}\right]. \tag{F.25}$$

Differentiating $\mathscr{H}$ with respect to p_θ, using using eq. (F.12c) and eq. (F.19d), gives:

$$\dot{\theta} = \frac{1}{eD}\left[\rho_\parallel B^2 \left(1 - \rho_\parallel g' - \tilde{A}'_\zeta\right) + g\left((\rho_\parallel^2 B + \mu)B' + \tilde{\Phi}'\right)\right],$$

and analogously with respect to p_ζ, using eq. (F.12d) and eq. (F.19d):

$$\dot{\zeta} = \frac{1}{eD}\left[\rho_\parallel B^2 \left(q + \rho_\parallel I' - \tilde{A}'_\theta\right) - I\left((\rho_\parallel^2 B + \mu)B' + \tilde{\Phi}'\right)\right].$$

The equations of motion derived above describe completely the guiding center motion, however, they do not provide the easiest numerical scheme to implement. This is due to the fact, that the expressions for the momenta (eqs. (4.45)) have to be inverted to obtain ψ_p and $\rho_\parallel$. From the numerical point of view, it is more convenient to evolve ψ_p and $\rho_\parallel$ directly from their own equations of motion. These are derived in the following: $\dot{\psi}_\mathrm{p}$ is obtained from using the chain rule and substituting eqs. (F.12) into it:

$$\begin{aligned}
\dot{\psi}_\mathrm{p} &= \frac{\partial \psi_\mathrm{p}}{\partial \theta}\dot{\theta} + \frac{\partial \psi_\mathrm{p}}{\partial \zeta}\dot{\zeta} + \frac{\partial \psi_\mathrm{p}}{\partial p_\theta}\dot{p_\theta} + \frac{\partial \psi_\mathrm{p}}{\partial p_\zeta}\dot{p_\zeta} \\
\dot{\psi}_\mathrm{p} &= \frac{1}{D}\left[\left(I\frac{\partial \tilde{A}_\zeta}{\partial \theta} - g\frac{\tilde{A}_\theta}{\partial \theta}\right)\dot{\theta} + \left(I\frac{\partial \tilde{A}_\zeta}{\partial \zeta} - g\frac{\tilde{A}_\theta}{\partial \zeta}\right)\dot{\zeta} + \frac{g}{e}\dot{p}_\theta - \frac{I}{e}\dot{p}_\zeta\right].
\end{aligned}$$

As $\dot{\psi}_\mathrm{p}$ is known now, one obtains $\dot{\rho}_\parallel$ easily from either of the expressions for the momenta, eq. (4.45a or b), by differentiating it with respect to time:

$$\begin{aligned}
\dot{p}_\theta &= e\dot{\rho}_\parallel I + e\rho_\parallel I'\dot{\psi}_\mathrm{p} + e\underbrace{\frac{\partial \psi_\mathrm{t}}{\partial \psi_\mathrm{p}}}_{=q}\dot{\psi}_\mathrm{p} + e\dot{\tilde{A}}_\theta + e\frac{\partial \tilde{A}_\theta}{\partial \psi_\mathrm{p}}\dot{\psi}_\mathrm{p} + e\frac{\partial \tilde{A}_\theta}{\partial \theta}\dot{\theta} + e\frac{\partial \tilde{A}_\theta}{\partial \zeta}\dot{\zeta} \\
\dot{\rho}_\parallel &= \frac{1}{I}\left[\dot{p}_\theta - e\frac{\partial \tilde{A}_\theta}{\partial \theta}\dot{\theta} - e\frac{\partial \tilde{A}_\theta}{\partial \zeta}\dot{\zeta} - e\dot{\tilde{A}}_\theta - e(q + \tilde{A}'_\theta + \rho_\parallel I')\dot{\psi}_\mathrm{p}\right].
\end{aligned}$$

APPENDIX G

Expansion of the Potential

in Powers of the Slowly Varying Amplitude and Frequency Shift

Via

$$\chi_k = A_k(t)\ \hat{\chi}_k\ \mathrm{e}^{-\mathrm{i}\omega_k t - \mathrm{i}\sigma_k(t)} \tag{G.1}$$

(see sec. 4.4.1) the slowly varying complex amplitude term A is made explicit, as well as the small frequency shift σ. It is therefore possible, to set up an ordering for χ in powers of the small fractions $\dot{A}_k/(\omega_k A_k)$ and σ_k/ω_k. χ_k is of 0th order, its first temporal derivative yields

$$\begin{aligned}
\frac{\partial \chi_k}{\partial t} &= \dot{A}_k\ \hat{\chi}_k\ \mathrm{e}^{-\mathrm{i}\omega_k t - \mathrm{i}\sigma_k(t)} - A_k\ \hat{\chi}_k\ \mathrm{i}(\omega_k + \dot{\sigma}_k)\ \mathrm{e}^{-\mathrm{i}\omega_k t - \mathrm{i}\sigma_k(t)} \\
\frac{\partial \chi_k}{\partial t} &= \left[\underbrace{\frac{\dot{A}_k}{\omega_k A_k}}_{\text{1st order}} - \mathrm{i}\,(\underbrace{1}_{\text{0th}} + \underbrace{\frac{\dot{\sigma}_k}{\omega_k}}_{\text{1st order}}) \right] \omega_k \chi(t).
\end{aligned} \tag{G.2}$$

Its quadrature:

$$\begin{aligned}
\left|\frac{\partial \chi_k}{\partial t}\right|^2 &= \left[\frac{\dot{A}_k}{\omega_k A_k} - \mathrm{i}\,(1 + \frac{\dot{\sigma}_k}{\omega_k}) \right]^2 \omega_k^2 |\chi|^2(t) \\
&= \left[\left(\frac{\dot{A}_k}{\omega_k A_k} \right)^2 + 1 + 2\frac{\dot{\sigma}_k}{\omega_k} + \left(\frac{\dot{\sigma}_k}{\omega_k} \right)^2 \right] \omega_k^2 \chi^2(t) \\
&= \underbrace{\omega_k^2\ |\chi_k|^2}_{\text{0th order}} + \underbrace{2\frac{\dot{\sigma}_k}{\omega_k}\omega_k^2\ |\chi_k|^2}_{\text{1st order}} + \underbrace{\left(\left(\frac{\dot{A}_k}{\omega_k A_k} \right)^2 + \left(\frac{\dot{\sigma}_k}{\omega_k} \right)^2 \right) \omega_k^2\ |\chi_k|^2}_{\text{2nd order}}.
\end{aligned} \tag{G.3}$$

The quadrature of the perpendicular gradient of its temporal derivative:

$$\begin{aligned}
\left|\nabla_\perp \frac{\partial \chi_k}{\partial t}\right|^2 &= \left[\frac{\dot{A}_k}{\omega_k A_k} - \mathrm{i}\,(1 + \frac{\dot{\sigma}_k}{\omega_k}) \right]^2 \omega_k^2 |\nabla_\perp \chi|^2(t) \\
&= \underbrace{\omega_k^2\ |\nabla_\perp \chi_k|^2}_{\text{0th order}} + \underbrace{2\frac{\dot{\sigma}_k}{\omega_k}\omega_k^2\ |\nabla_\perp \chi_k|^2}_{\text{1st order}} + \underbrace{\left(\left(\frac{\dot{A}_k}{\omega_k A_k} \right)^2 + \left(\frac{\dot{\sigma}_k}{\omega_k} \right)^2 \right) \omega_k^2\ |\nabla_\perp \chi_k|^2}_{\text{2nd order}}.
\end{aligned} \tag{G.4}$$

Symbols & Abbreviations, Index

Bibliography

[1] J. M. Durão Barroso, *Speech* (2008), http://ec.europa.eu/commission_barroso/president/focus/energy-package-2008/index_en.htm.

[2] J. M. Durão Barroso, *Speech: 'Our energy future in an interdependent world'*, World Energy Congress Rome (2007), http://ec.europa.eu/commission_barroso/president/focus/energy-package-2008/index_en.htm.

[3] W. J. Nuttall, *Institute of Physics Report 'Fusion as an Energy Source: Challenges and Opportunities'*, Institute of Physics (2008), http://www.iop.org/activity/policy/Publications/file_31695.pdf.

[4] IPCC, 2007, in *Climate Change 2007*, edited by S. Solomon, D. Qin, M. Manning, Z. Chen, M. Marquis, K. Averyt, M. Tignor, and H. Miller (Cambridge University Press, 2007), http://www.ipcc.ch/pdf/assessment-report/ar4/wg1/ar4-wg1-spm.pdf.

[5] United Nations Environment Programme, *Climate in Peril – A popular guide to the latest IPCC reports* (2009), http://www.grida.no/_res/site/file/publications/ClimateInPeril.pdf.

[6] Shell International BV, *Shell energy scenarios to 2050* (2008), http://www-static.shell.com/static/aboutshell/downloads/our_strategy/shell_global_scenarios/SES%20booklet%2025%20of%20July%202008.pdf.

[7] International Energy Agency, *Renewables in Global Energy Supply – An IEA Fact Sheet* (2007), http://www.iea.org/textbase/papers/2006/renewable_factsheet.pdf.

[8] International Energy Agency (ED), *Highlights Section of the International Energy Outlook 2009 report*, Energy Information Administration, http://www.eia.doe.gov/oiaf/ieo/pdf/highlights.pdf.

[9] Deutsche Umwelthilfe, *Kohlekraftwerksprojekte in Deutschland* (2009), http://www.duh.de/fileadmin/user_upload/download/Projektinformation/Kohlekraftwerke/DUH-Liste_Kohlekraftwerke_Uebersicht_2012.pdf.

[10] World Nuclear Association, http://www.world-nuclear.org/info/inf23.html.

[11] P. H. Eichstaedt, *If you poison us – Uranium and Native Americans* (Red Crane Books, Santa Fee, 1994).

[12] D. J. MacKay, *Sustainable Energy – without the hot air* (2008), http://www.inference.phy.cam.ac.uk/withouthotair/.

[13] National Physics Laboratory, *Kaye&Laby-Table of Physical & Chemical Constants*, http://www.kayelaby.npl.co.uk/atomic_and_nuclear_physics/4_7/4_7_4a.html.

[14] J. Wesson, *Tokamaks* (Oxford Science Publications, 2004), 3rd ed.

[15] H. Breuer, *dtv-Atlas Chemie, Band 1* (Deutscher Taschenbuch Verlag, 2000).

[16] Institute of Ocean Energy, Saga University, Japan, *Lithium Occurence*, http://www.ioes.saga-u.ac.jp/ioes-study/li/lithium/occurence.html.

[17] World Nuclear Association, *World Nuclear Power Reactors 2008-09 and Uranium Requirements*, http://www.world-nuclear.org/info/reactors.html.

[18] *Kernfusion – Berichte aus der Forschung (Folge 2)* (2002), http://www.ipp.mpg.de/ippcms/de/pr/publikationen/pdf/berichte.pdf.

[19] J. Lawson, *Some Criteria for a Power Producing Thermonuclear Reactor*, Proceedings of the Physical Society. Section B 70 (1957).

[20] ITER website (2009), URL http://http://www.iter.org.

[21] H. W. M. Ralf Kleiber, ed., *IPP Summer University for Plasma Physics* (Max-Planck-Institut für Plasmaphysik, 2008).

[22] E. Leitner, U. Finckh, and F. Fritsche, *Das Lawson Kriterium* (2009), http://leifi.physik.uni-muenchen.de/web_ph12/umwelt_technik/11fusion/lawson.htm.

[23] J. Lyman Spitzer, *The Stellerator Concept*, Phys. Fluids **1**, 253 (1958), URL http://link.aip.org/link/?PFL/1/253/1.

[24] M. A. Gashev, G. K. Gustov, K. K. D'yachenko, E. G. Komar, I. F. Malyshev, N. A. Monoszon, A. V. Popkovich, B. K. Ratnikov, B. V. Rozhdestvenskii, N. N. Rumyantsev, et al., *The basic technical characteristics of the experimental thermonuclear device tokamak-3*, Journal of Nuclear Energy. Part C, Plasma Physics, Accelerators, Thermonuclear Research **7**, 491 (1965), URL http://stacks.iop.org/0368-3281/7/i=5/a=305.

[25] http://www.efda.org/fusion_energy/introduction_to_fusion.htm.

[26] http://www.ipp.mpg.de/ippcms/eng/pr/index.html.

[27] T. Stix, *Fast-wave heating of a two-component plasma*, Nucl. Fusion **15**, 737 (1975), URL http://stacks.iop.org/0029-5515/15/i=5/a=003.

[28] W. W. Heidbrink, K. H. Burrell, Y. Luo, N. A. Pablant, and E. Ruskov, *Hydrogenic fast-ion diagnostic using balmer-alpha light*, Plasma Phys. Control. Fusion **46**, 1855 (2004), URL http://stacks.iop.org/0741-3335/46/i=12/a=005.

[29] W. W. Heidbrink, *Fast-ion D alpha measurements of the fast-ion distribution (invited)*, Review of Scientific Instruments **81**, 10D727 (pages 8) (2010), URL http://link.aip.org/link/?RSI/81/10D727/1.

[30] M. N. Rosenbluth and P. H. Rutherford, *Excitation of Alfvén waves by high-energy ions in a tokamak*, Phys. Rev. Lett. **34**, 1428 (1975), URL http://link.aps.org/doi/10.1103/PhysRevLett.34.1428.

[31] N. Fisch and M. Herrmann, *Alpha power channelling with two waves*, Nucl. Fusion **35**, 1753 (1995), URL http://stacks.iop.org/0029-5515/35/i=12/a=I40.

[32] O. Gruber, M. Kaufmann, W. Köppendörfer, K. Lackner, and J. Neuhauser, *Physics background of the ASDEX Upgrade project*, Journal of Nuclear Materials **121**, 407 (1984), URL http://www.sciencedirect.com/science/article/pii/0022311584901533.

[33] M. García-Muñoz, N. Hicks, R. van Voornveld, I. G. J. Classen, R. Bilato, V. Bobkov, M. Brüdgam, H.-U. Fahrbach, V. Igochine, S. Jaemsae, et al., *Convective and diffusive energetic particle losses induced by Shear Alfvén waves in the ASDEX Upgrade tokamak*, Phys. Rev. Lett. **104**, 185002 (2010), URL http://link.aps.org/doi/10.1103/PhysRevLett.104.185002.

[34] M. A. V. Zeeland, W. W. Heidbrink, R. K. Fisher, M. M. García-Muñoz, G. J. Kramer, D. C. Pace, R. B. White, S. Aekaeslompolo, M. E. Austin, J. E. Boom, et al., *Measurements and modeling of Alfvén eigenmode induced fast ion transport and loss in DIII-D and ASDEX Upgrade*, Phys. Plasmas **18**, 056114 (2011), URL http://link.aip.org/link/?PHP/18/056114/1.

[35] M. García-Muñoz, P. Martin, H.-U. Fahrbach, M. Gobbin, S. Günter, M. Maraschek, L. Marrelli, H. Zohm, and the ASDEX Upgrade Team, *NTM induced fast ion losses in ASDEX Upgrade*, Nucl. Fusion **47** (2007), URL http://stacks.iop.org/0029-5515/47/i=7/a=L03.

[36] T. Boyd and J. Sanderson, *The Physics of Plasmas* (Cambridge University Press, 2003).

[37] A. G. Peeters, *The bootstrap current and its consequences*, Plasma Phys. Control. Fusion **42**, B231 (2000), URL http://stacks.iop.org/0741-3335/42/i=12B/a=318.

[38] T. G. Northrop, *The Adiabatic Motion of Charged Particles* (Interscience Publishers, John Wiley & Sons, 1963).

[39] R. G. Littlejohn, *Variational principles of guiding centre motion*, J. Plasma Phys. **29**, 111 (1983), ISSN 1469-7807, URL http://journals.cambridge.org/article_S002237780000060X.

[40] H. Goldstein, *Classical Mechanics* (Addison-Wesley series in Physics, 1980).

[41] B. Coppi, G. Rewoldt, and Massachusetts Institute of Technology. Research Laboratory of Electronics, *Collective Modes in Confined High Temperature Plasmas*, Plasma Research report (Massachusetts Institute of Technology, Research Laboratory of Electronics, 1974), URL http://books.google.de/books?id=LFT-GgAACAAJ.

[42] C. Nguyen, Ph.D. thesis, Ecole Doctorale de l'Ecole Polytechnique (2009).

[43] J. P. Freidberg, in *Ideal Magnetohydrodynamics* (Plenum Press,New York, NY, 1987), URL http://tinyurl.sfx.mpg.de/t3aq.

[44] H. Alfvén, *Existence of electromagnetic-hydrodynamic waves*, Nature **150**, 405 (1942).

[45] H. L. Berk, J. V. Dam, Z. Guo, and D. Lindberg, Tech. Rep., Texas Univ., Austin, TX (United States). Inst. for Fusion Studies (1991).

[46] P. Carl, *Finite element methods in linear ideal magnetohydrodynamics. R. Gruber and J. Rappaz. Springer-Verlag, Berlin-Heidelberg-New York-Tokyo, 1985; 180 pages, 103 figures: Springer Series in Computational Physics. Editors H. Cabannes, M. Holt, H. B. Keller, J. Killeen, S. A. Orszac, V. V. Rusanov*, Beiträge aus der Plasmaphysik **26**, 461 (1986), ISSN 1521-3986, URL http://dx.doi.org/10.1002/ctpp.19860260610.

[47] G. Y. Fu and J. W. V. Dam, *Excitation of the toroidicity-induced shear Alfvén eigenmode by fusion alpha particles in an ignited tokamak*, Phys. Fluids B **1**, 1949 (1989), URL http://link.aip.org/link/?PFB/1/1949/1.

[48] A. Hasegawa and L. Chen, *Plasma heating by alfvén-wave phase mixing*, Physical Review Letters **32**, 454 (1974), cited By (since 1996) 39.

[49] Ph. Lauber, *Superthermal particles in hot plasmas - kinetic models, numerical solution strategies, and comparison to tokamak experiments*, Elsevier (2013).

[50] C. Z. Cheng, L. Chen, and M. Chance, *High-n ideal and resistive shear Alfvén waves in tokamaks*, Ann. Phys. **161**, 21 (1985), URL http://www.sciencedirect.com/science/article/pii/0003491685903355.

[51] C. Z. Cheng and M. S. Chance, *Low-n shear Alfvén spectra in axisymmetric toroidal plasmas*, Phys. Fluids **29**, 3695 (1986), URL http://link.aip.org/link/?PFL/29/3695/1.

[52] H. L. Berk, J. W. V. Dam, Z. Guo, and D. M. Lindberg, *Continuum damping of low-n toroidicity-induced shear Alfvén eigenmodes*, Phys. Fluids B **4**, 1806 (1992), URL http://link.aip.org/link/?PFB/4/1806/1.

[53] F. Zonca and L. Chen, *Resonant damping of toroidicity-induced shear-Alfvén eigenmodes in tokamaks*, Phys. Rev. Lett. **68**, 592 (1992), URL http://link.aps.org/doi/10.1103/PhysRevLett.68.592.

[54] M. N. Rosenbluth, H. L. Berk, J. W. Van Dam, and D. M. Lindberg, *Continuum damping of high-mode-number toroidal Alfvén waves*, Phys. Rev. Lett. **68**, 596 (1992), URL http://link.aps.org/doi/10.1103/PhysRevLett.68.596.

[55] M. Brüdgam, Ph.D. thesis, Technische Universität München (2010).

[56] G. J. Kramer, S. E. Sharapov, R. Nazikian, N. N. Gorelenkov, and R. V. Budny, *Observation of odd toroidal Alfvén eigenmodes*, Phys. Rev. Lett. **92**, 015001 (2004), URL http://link.aps.org/doi/10.1103/PhysRevLett.92.015001.

[57] H. Kimura, Y. Kusama, M. Saigusa, G. Kramer, K. Tobita, M. Nemoto, T. Kondoh, T. Nishitani, O. D. Costa, T. Ozeki, et al., *Alfvén eigenmode and energetic particle research in JT-60U*, Nucl. Fusion **38**, 1303 (1998), URL http://stacks.iop.org/0029-5515/38/i=9/a=304.

[58] S. Sharapov, D. Testa, B. Alper, D. Borba, A. Fasoli, N. Hawkes, R. Heeter, M. Mantsinen, and M. V. Hellermann, *MHD spectroscopy through detecting toroidal Alfvén eigenmodes and Alfvén wave cascades*, Physics Letters A **289**, 127 (2001), ISSN 0375-9601, URL http://www.sciencedirect.com/science/article/pii/S0375960101005886.

[59] H. L. Berk, D. N. Borba, B. N. Breizman, S. D. Pinches, and S. E. Sharapov, *Theoretical interpretation of Alfvén cascades in tokamaks with nonmonotonic q profiles*, Phys. Rev. Lett. **87** (2001), URL http://link.aps.org/doi/10.1103/PhysRevLett.87.185002.

[60] B. N. Breizman, H. L. Berk, M. S. Pekker, S. D. Pinches, and S. E. Sharapov, *Theory of Alfvén eigenmodes in shear reversed plasmas*, Phys. Plasmas **10**, 3649 (2003), URL http://link.aip.org/link/?PHP/10/3649/1.

[61] A. D. Turnbull, E. J. Strait, W. W. Heidbrink, M. S. Chu, H. H. Duong, J. M. Greene, L. L. Lao, T. S. Taylor, and S. J. Thompson, *Global Alfvén modes: Theory and experiment*, Phys. Fluids B **5**, 2546 (1993), URL http://link.aip.org/link/?PFB/5/2546/1.

[62] W. W. Heidbrink, E. J. Strait, M. S. Chu, and A. D. Turnbull, *Observation of beta-induced Alfvén eigenmodes in the DIII-D tokamak*, Phys. Rev. Lett. **71**, 855 (1993), URL http://link.aps.org/doi/10.1103/PhysRevLett.71.855.

[63] F. Zonca, L. Chen, and R. A. Santoro, *Kinetic theory of low-frequency Alfvén modes in tokamaks*, Plasma Phys. Control. Fusion **38**, 2011 (1996), URL http://stacks.iop.org/0741-3335/38/i=11/a=011.

[64] Ph. Lauber, M. Brüdgam, D. Curran, V. Igochine, K. Sassenberg, S. Günter, M. Maraschek, M. García-Muñoz, N. Hicks, and the ASDEX Upgrade Team, *Kinetic Alfvén eigenmodes at ASDEX Upgrade*, Plasma Phys. Control. Fusion **51**, 124009 (2009), URL http://stacks.iop.org/0741-3335/51/i=12/a=124009.

[65] H. Sugama and T.-H. Watanabe, *Collisionless damping of geodesic acoustic modes*, J. Plasma Phys. **72**, 825 (2006), ISSN 1469-7807, URL http://journals.cambridge.org/article_S0022377806004958.

[66] A. Hasegawa and L. Chen, *Kinetic process of plasma heating due to Alfvén wave excitation*, Phys. Rev. Lett. **35**, 370 (1975), URL http://link.aps.org/doi/10.1103/PhysRevLett.35.370.

[67] A. Hasegawa and L. Chen, *Kinetic processes in plasma heating by resonant mode conversion of Alfvén wave*, Phys. Fluids **19**, 1924 (1976), URL http://link.aip.org/link/?PFL/19/1924/1.

[68] R. R. Mett and S. M. Mahajan, *Kinetic theory of toroidicity-induced Alfvén eigenmodes*, Phys. Fluids B **4**, 2885 (1992), URL http://link.aip.org/link/?PFB/4/2885/1.

[69] L. D. Landau, J. Phys. USSR **10**, 25 (1946).

[70] L. D. Landau, Zh. Eksp. Teor. Fiz. **16**, 574 (1946).

[71] A. Mikhailovskii, Sov.Phys.JETP **41**, 890 (1975).

[72] S. D. Pinches, Ph.D. thesis, University of Nottingham (1996), URL http://www.ipp.mpg.de/~Simon.Pinches/thesis/thesis.html.

[73] J. Candy, *Electron landau damping of toroidal Alfvén eigenmodes*, Plasma Phys. Control. Fusion **38**, 795 (1996), URL http://stacks.iop.org/0741-3335/38/i=6/a=002.

[74] N. N. Gorelenkov and S. E. Sharapov, *On the collisional damping of TAE-modes on trapped electrons in tokamaks*, Physica Scripta **45**, 163 (1992), URL http://stacks.iop.org/1402-4896/45/i=2/a=016.

[75] G. Y. Fu, C. Z. Cheng, and K. L. Wong (American Institute of Physics), *Stability of the toroidicity-induced Alfvén eigenmode in axisymmetric toroidal equilibria*, Phys. Fluids B **5**, 4040 (1993), URL http://link.aip.org/link/?PFB/5/4040/1.

[76] H. L. Berk, B. Breizman, and H. Ye, *Scenarios for the nonlinear evolution of alpha-particle-induced Alfvén wave instability*, Phys. Rev. Lett. **68**, 3563 (1992), URL http://link.aps.org/doi/10.1103/PhysRevLett.68.3563.

[77] B. N. Breizman and S. E. Sharapov, *Energetic particle drive for toroidicity-induced Alfvén eigenmodes and kinetic toroidicity-induced Alfvén eigenmodes in a low-shear tokamak*, Plasma Phys. Control. Fusion **37**, 1057 (1995), URL http://stacks.iop.org/0741-3335/37/i=10/a=001.

[78] H. Berk, B. Breizman, and H. Ye, *Finite orbit energetic particle linear response to toroidal Alfvén eigenmodes*, Physics Letters A **162**, 475 (1992), ISSN 0375-9601, URL http://www.sciencedirect.com/science/article/pii/037596019290009B.

[79] F. Porcelli, R. Stankiewicz, W. Kerner, and H. L. Berk, *Solution of the drift-kinetic equation for global plasma modes and finite particle orbit widths*, Phys. Plasmas **1**, 470 (1994), URL http://link.aip.org/link/?PHP/1/470/1.

[80] S. D. Pinches, V. Kiptily, S. Sharapov, D. Darrow, L.-G. Eriksson, H.-U. Fahrbach, M. García-Muñoz, M. Reich, E. Strumberger, A. Werner, et al., *Observation and modelling of fast ion loss in JET and ASDEX Upgrade*, Nucl. Fusion **46**, 904 (2006), URL http://stacks.iop.org/0029-5515/46/i=10/a=S06.

[81] H. Berk, B. Breizman, and M. Pekker, *Nonlinear dynamics of a driven mode near marginal stability*, Phys. Rev. Lett. **76**, 1256 (1996).

[82] M. K. Lilley, B. N. Breizman, and S. E. Sharapov, *Effect of dynamical friction on nonlinear energetic particle modes*, Phys. Plasmas **17**, 092305 (pages 10) (2010), URL http://link.aip.org/link/?PHP/17/092305/1.

[83] S. Pinches, L. Appel, J. Candy, S. Sharapov, H. Berk, D. Borba, B. Breizman, T. Hender, K. Hopcraft, G. Huysmans, et al., *The HAGIS self-consistent nonlinear wave-particle interaction model*, Comput. Phys. Commun. **111**, 133 (1998), ISSN 0010-4655, URL http://www.sciencedirect.com/science/article/pii/S0010465598000344.

[84] Huysmans G. T. A. et al, Conf. on Computational Physics Proc. World Scientific, Singapore (AIP, 1990).

[85] Mc Carthy P. J., *Analytical solutions to the grad–shafranov equation for tokamak equilibrium with dissimilar source functions*, Phys. Plasmas **6**, 3554 (1999), URL http://link.aip.org/link/?PHP/6/3554/1.

[86] Mc Carthy P. J. and the ASDEX Upgrade Team, *Identification of edge-localized moments of the current density profile in a tokamak equilibrium from external magnetic measurements*, Plasma Phys. Control. Fusion **54**, 015010 (2012), URL http://stacks.iop.org/0741-3335/54/i=1/a=015010.

[87] A. H. Boozer, *Plasma equilibrium with rational magnetic surfaces*, Phys. Fluids **24**, 1999 (1981), URL http://link.aip.org/link/?PFL/24/1999/1.

[88] A. H. Boozer, *Evaluation of the structure of ergodic fields*, Phys. Fluids **26**, 1288 (1983), URL http://link.aip.org/link/?PFL/26/1288/1.

[89] R. B. White and M. S. Chance, *Hamiltonian guiding center drift orbit calculation for plasmas of arbitrary cross section*, Phys. Fluids **27**, 2455 (1984), URL http://link.aip.org/link/?PFL/27/2455/1.

[90] J. M. Greene, Commun. Pure Appl. Math. **36**, 537 (1983).

[91] J. B. Taylor, *Equilibrium and stability of plasma in arbitrary mirror fields*, Phys. Fluids **7**, 767 (1964), URL http://link.aip.org/link/?PFL/7/767/1.

[92] W. Kerner, J. Goedbloed, G. Huysmans, S. Poedts, and E. Schwarz, *CASTOR: Normal-mode analysis of resistive MHD plasmas*, J. Comp. Phys. **142**, 271 (1998), ISSN 0021-9991, URL http://www.sciencedirect.com/science/article/pii/S0021999198959101.

[93] Ph. Lauber, S. Günter, A. Könies, and S. D. Pinches, *LIGKA: a linear gyrokinetic code for the description of background kinetic and fast particle effects on the MHD stability in tokamaks*, J. Comp. Phys. **226**, 447 (2007), ISSN 0021-9991, URL http://www.sciencedirect.com/science/article/pii/S0021999107001660.

[94] Y. Kusama, G. Kramer, H. Kimura, M. Saigusa, T. Ozeki, K. Tobita, T. Oikawa, K. Shinohara, T. Kondoh, M. Moriyama, et al., *Characteristics of Alfvén eigenmodes, burst modes and chirping modes in the Alfvén frequency range driven by negative ion based neutral beam injection in JT-60U*, Nucl. Fusion **39**, 1837 (1999), URL http://stacks.iop.org/0029-5515/39/i=11Y/a=324.

[95] W. W. Heidbrink, *Beam-driven chirping instability in DIII-D*, Plasma Physics and Controlled Fusion **37**, 937 (1995), URL http://stacks.iop.org/0741-3335/37/i=9/a=002.

[96] Y. Todo, K. Shinohara, M. Takechi, and M. Ishikawa, *Computer simulation of frequency sweeping of energetic particle mode in a JT-60U experiment*, Journal of Plasma and Fusion Research **79**, 1107 (2003).

[97] S. D. Pinches, H. L. Berk, M. P. Gryaznevich, S. E. Sharapov, and JET-EFDA Contributors, *Spectroscopic determination of the internal amplitude of frequency sweeping TAE*, Plasma Phys. Control. Fusion **46**, S47 (2004), URL http://stacks.iop.org/0741-3335/46/i=7/a=S04.

[98] L. Spitzer, *Physics of Fully Ionized Gases* (Interscience, New York, 1962), 2nd ed.

[99] H. L. Berk and B. N. Breizman, *Saturation of a single mode driven by an energetic injected beam. I. plasma wave problem*, Phys. Fluids B **2**, 2226 (1990), URL http://link.aip.org/link/?PFB/2/2226/1.

[100] H. L. Berk and B. N. Breizman, *Saturation of a single mode driven by an energetic injected beam. II. electrostatic "universal" destabilization mechanism*, Phys. Fluids B **2**, 2235 (1990), URL http://link.aip.org/link/?PFB/2/2235/1.

[101] H. L. Berk and B. N. Breizman, *Saturation of a single mode driven by an energetic injected beam. III. Alfvén wave problem*, Phys. Fluids B **2**, 2246 (1990), URL http://link.aip.org/link/?PFB/2/2246/1.

[102] J. D. Gaffey, *Energetic ion distribution resulting from neutral beam injection in tokamaks*, J. Plasma Phys. **16**, 149 (1976), URL http://journals.cambridge.org/production/action/cjoGetFulltext?fulltextid=4732304.

[103] W. Core, *A note on the calculation of NBI fast ion distribution functions*, Nucl. Fusion **33**, 829 (1993), URL http://stacks.iop.org/0029-5515/33/i=5/a=I13.

[104] H. L. Berk, B. N. Breizman, and H. Ye, *Map model for nonlinear alpha particle interaction with toroidal Alfvén waves*, Phys. Fluids B **5**, 1506 (1993), URL http://link.aip.org/link/?PFB/5/1506/1.

[105] D. Sigmar, C. Hsu, R. White, and C. Cheng, *Alpha-particle losses from toroidicity-induced Alfvén eigenmodes. Part II: Monte Carlo simulations and anomalous alpha-loss processes*, Phys. Fluids B **4**, 1506 (1992).

[106] H. Berk, B. Breizman, J. Fitzpatrick, and H. Wong, *Line broadened quasi-linear burst model [fusion plasma]*, Nucl. Fusion **35**, 1661 (1995), URL http://stacks.iop.org/0029-5515/35/i=12/a=I30.

[107] The ASDEX Upgrade Team, *ASDEX Upgrade discharge database*.

[108] M. García-Muñoz, H.-U. Fahrbach, H. Zohm, and the ASDEX Upgrade Team, *Scintillator based detector for fast-ion losses induced by magnetohydrodynamic instabilities in the ASDEX Upgrade tokamak*, Review of Scientific Instruments **80**, 053503 (2009), URL http://link.aip.org/link/?RSI/80/053503/1.

[109] V. Igochine, S. Günter, M. Maraschek, and the ASDEX Upgrade Team, *Investigation of complex MHD activity by a combined use of various diagnostics*, Nucl. Fusion **43**, 1801 (2003), URL http://stacks.iop.org/0029-5515/43/i=12/a=023.

[110] Ph. Lauber, the ASDEX Upgrade Team, *from the ASDEX Upgrade discharge database*.

[111] E. Fredrickson, R. Colchin, K. McGuire, W. Morris, and N. Sauthoff, *TFTR mirnov loop system*, Review of Scientific Instruments **57**, 2084 (1986), URL http://link.aip.org/link/?RSI/57/2084/1.

[112] R. Bilato, M. Brambilla, O. Maj, L. Horton, C. Maggi, and J. Stober, *Simulations of combined neutral beam injection and ion cyclotron heating with the TORIC-SSFPQL package*, Nucl. Fusion **51**, 103034 (2011), URL http://stacks.iop.org/0029-5515/51/i=10/a=103034.

[113] R. Bilato, M. Brambilla, and Z. Jiang, *Implementing zero-banana-width quasi-linear operator for fast ICRF simulations*, Journal of Physics: Conference Series **401**, 012001 (2012), URL http://stacks.iop.org/1742-6596/401/i=1/a=012001.

[114] K. Sassenberg, Ph.D. thesis, University College Cork (2009), URL http://physics.ucc.ie/~pjm/trachtais_macleinn/KarlSassenbergPhD2009.pdf.

[115] D. Curran, *private communication*.

[116] W. Schneider, *private communication*.

[117] Ph. Lauber, the ASDEX Upgrade Team, *LIGKA calculation, based on ASDEX Upgrade experimental data*.

[118] L. Chen, *Theory of magnetohydrodynamic instabilities excited by energetic particles in tokamaks*, Phys. Plasmas **1**, 1519 (1994).

[119] K. Shinohara, Y. Kusama, M. Takechi, A. Morioka, M. Ishikawa, N. Oyama, K. Tobita, T. Ozeki, S. Takeji, S. Moriyama, et al., *Alfvén eigenmodes driven by Alfvénic beam ions in JT-60U*, Nucl. Fusion **41**, 603 (2001), URL http://stacks.iop.org/0029-5515/41/i=5/a=313.

[120] K. Shinohara, M. Takechi, M. Ishikawa, Y. Kusama, K. Tsuzuki, K. Urata, H. Kawashima, K. Tobita, A. Fukuyama, C. Cheng, et al., *Energetic particle physics in JT-60U and JFT-2M*, Plasma Phys. Control. Fusion **46**, S31 (2004).

[121] S. Briguglio, G. Fogaccia, G. Vlad, F. Zonca, K. Shinohara, M. Ishikawa, and M. Takechi, *Particle simulation of bursting Alfvén modes in JT-60U*, Phys. Plasmas **14** (2007).

[122] G. Vlad, S. Briguglio, G. Fogaccia, and F. Zonca, *Consistency of proposed burning plasma scenarios with alpha-particle transport induced by Alfvénic instabilities*, Plasma Phys. Control. Fusion **46**, S81 (2004), URL http://stacks.iop.org/0741-3335/46/i=7/a=S06.

[123] J. Heikkinen, T. Kiviniemi, T. Kurki-Suonio, A. Peeters, and S. Sipilä, *Particle simulation of the neoclassical plasmas*, J. Phys. Chem. **173**, 527 (2001), ISSN 0021-9991, URL http://www.sciencedirect.com/science/article/pii/S0021999101968913.

[124] R. J. Goldston, R. B. White, and A. H. Boozer, *Confinement of high-energy trapped particles in tokamaks*, Phys. Rev. Lett. **47**, 647 (1981), URL http://link.aps.org/doi/10.1103/PhysRevLett.47.647.

[125] R. B. White and H. E. Mynick, *Alpha particle confinement in tokamaks*, Phys. Fluids B **1**, 980 (1989), URL http://link.aip.org/link/?PFB/1/980/1.

[126] C. Angioni and A. G. Peeters, *Gyrokinetic calculations of diffusive and convective transport of alpha particles with a slowing-down distribution function*, Phys. Plasmas **15**, 052307 (pages 15) (2008), URL http://link.aip.org/link/?PHP/15/052307/1.

[127] C. Angioni, A. Peeters, G. Pereverzev, A. Bottino, J. Candy, R. Dux, E. Fable, T. Hein, and R. Waltz, *Gyrokinetic simulations of impurity, he ash and α particle transport and consequences on iter transport modelling*, Nuclear Fusion **49**, 055013 (2009), URL http://stacks.iop.org/0029-5515/49/i=5/a=055013.

[128] M. García-Muñoz, H.-U. Fahrbach, V. Bobkov, N. Hicks, V. Igochine, S. Jaemsae, M. Maraschek, K. Sassenberg, and the ASDEX Upgrade Team, 11th IAEA Technical Meeting on Energetic Particles in Magnetic Confinement Systems (International Atomic Energy Agency, Kiev, 2009).

[129] W. D'haeseleer, W. Hitchon, J. Callen, and J. Shohe, *Flux Coordinates and Magnetic Field Structure* (Springer-Verlag, 1991).

Publications and Conference Contributions

Publications

Multi-mode Alfvénic Fast Particle Transport and Losses:
Numerical vs. Experimental Observation
M. Schneller, Ph. Lauber, R. Bilato, M. García-Muñoz, M. Brüdgam, S. Günter and the ASDEX Upgrade Team
Submitted to Nuclear Fusion (July 2013)

Nonlinear Alfvéic Fast Particle Transport and Losses
M. Schneller, Ph. Lauber, M. García-Muñoz, M. Brüdgam and S. Günter
Journal of Physics - Conference Series 401, 012022 (2012)

Double-resonant Fast Particle-Wave Interaction
M. Schneller, Ph. Lauber, M. Brüdgam, S.D. Pinches and S. Günter
Nuclear Fusion 52, 103019 (2012)

Anomalous Diffusion of Energetic Particles: Connecting Experiment and Simulations
M. J. Pueschel, F. Jenko, M. Schneller, T. Hauff, S. Günter, G. Tardini
Nuclear Fusion 52, 103018 (2012)

Alfvén Eigenmodes and Neoclassical Tearing Modes for Orbit-following Implementations
E. Hirvijoki, A. Snicker, T. Korpilo, Ph. Lauber, E. Poli, M. Schneller and T. Kurki-Suonio
Computer Physics Communications, Volume 183, Issue 12 (2012)

Core transport analysis of nitrogen seeded H-mode discharges in the ASDEX Upgrade
G. Tardini, R. Fischer, F. Jenko, A. Kallenbach, R.M. McDermott, T. Pütterich, S.K. Rathgeber, M. Schneller, J Schweinzer, A.C.C. Sips, D. Told, E. Wolfrum and the ASDEX Upgrade Team
Plasma Physics and Controlled Fusion, Volume 55, 015010 (2013)

Conference Contributions

Investigation of Fast Particle Transport due to Alfvénic Modes (Invited Talk)
M. Schneller, Ph. Lauber, M. García-Muñoz
13th IAEA Technical Meeting on Energetic Particles (09/2013, Beijing, China)

Investigation of Fast Particle Transport due to Alfvénic Modes (Poster)
M. Schneller, Ph. Lauber, M. Brüdgam
12th IAEA Technical Meeting on Energetic Particles (09/2011, Austin, USA)

Investigation of Fast Particle Transport due to Alfvénic Modes (Poster)
M. Schneller, Ph. Lauber, M. Brüdgam
Theory of Fusion Plasmas (08/2012, Varenna, Italy)

Acknowledgments

First and foremost, I want to thank my advisor, Dr. Philipp Lauber: he was always available for advice and consultation and his wise guidance was crucial for the outcome of this work. I am grateful for his enduring patience and his enthusiasm for physics, which was always a motivation for me. He deserves my gratitude for introducing me to the world of *fast particle* physics (both with respect to the models as well as the community), for finding the light at the end of the debug tunnel and for helping me with the interpretation of the results. At the same time, I appreciated the freedom to set my own emphases. I further thank him for proof-reading this thesis as well as our publications.
I want to express my gratitude to my supervisor Prof. Sibylle Günter, for giving me the opportunity to pursue a PhD project at IPP that is not only very interesting, but also considered relevant to the idea of nuclear fusion. I thank her for providing valuable advice with our publications and for proof-reading this thesis.
I thank my predecessor Michael Brüdgam for his very useful (yet challenging) legacy. Dr. Manuel Garía-Muñoz deserves my gratitude for making available and explaining his experimental results. I thank Dr. Simon Pinches and the people from the HAGIS repository in Culham for providing the HAGIS code and the access to its repository. I am grateful for the valuable discussions with Dr. Roberto Bilato and his data concerning the fast particle distribution function. I would further like to acknowledge the help of Dr. Christian Konz on the interfaces with equilibrium codes, as well as the help of Diarmuid Curran and Dr. Wolfgang Schneider with the plasma equilibria. Further, I want to thank the whole TOK department and its head, Prof. Karl Lackner.

A special thank deserve the former and actual members of the GENE group, who have been my social environment at IPP for a long time. I want to point out those who were there for me most often, be it for general code or computer problems, bureaucracy, health care (providing coffee!) or just for listening and for their company: a cordial thanks to Dr. Tobias Görler, to Dr. Daniel Told, and to Dr. Hauke Doerk.
I sincerely thank Dr. Matthias Hölzl for his support during the ups and downs of my PhD time and for the many things I learned. I express my thanks to Dr. Moritz Püschel for the cooperation before this thesis started, as well as for past and ongoing useful advice.

I also want to say thanks to all my office mates during my time as a PhD student, former and actual ones. “Thank you” to Andreas Stegmeir, Christoph Kowitz, Dr. David Hatch, Dr. Hauke Doerk, Dr. Stefanie Braun, Vasil Bratanov, Michael Oberparleiter, Andreas Volk and Dr. Andrés de Bustos Molina (especialmente por la lectura de algunos capítulos y la fruta quando trabajaba hasta tarde). I am grateful for interesting and sometimes challenging discussions, for the new ideas on various topics and, after all, for the lively atmosphere. Although never my office mate, Isabel Krebs deserves a “thank you” as well as Josefine Proll, for sharing the sorrows of PhD students, for their

advice and for their company, though at different distances.

Another thanks goes to the organizers of the HEPP graduate school for providing very interesting lectures and for encouraging the scientific exchange amongst the graduate students.

I thank the PR department for giving me the opportunity to present our interesting work to a wider audience. I not only consider this an important issue, but also learned a lot concerning presentation skills and guiding groups of people of all ages and gender compositions.

Many more people deserve my gratitude for their support in the fight against the all-day-life problems of a graduate student/TU student/theoretical physicist e.t.c.: thanks to our secretary Anja Baur and her colleagues for reducing bureaucracy to the necessary minimum. I thank Dr. Vittoria Belmondo, and especially Michael Huber and Josef Hausmann for their help with the supervision of the TU physics lab course. Thanks to the Studentenwerk München, especially to Marita Fries, for making life not only easier but also cheaper. Further I thank our cleaning lady for her service, for the plants and the interesting chats. I acknowledge the language support I got on very different occasions from Dr. David Hatch, Dr. Francis Casson, Dr. Alejandro Bañon Navarro, Dr. Andrés de Bustos Molina, Dr. Jéremie Abiteboul and Angelo Limone. For their help with computer and repository issues, I thank Dr. Klaus Reuter, Dr. Hajo Klingshirn, Dr. David Coster, Dr. Michael Kraus, and of course the people from Rechenzentrum Garching, Jülich and IFERC (Japan). The simulations for this thesis were run on the local Linux clusters and on HPC-FF in Jülich, as well as on HELIOS in Japan.